Cross-flow ultrafiltration of colloids : characterization of the mechanisms at nanometer length scales and enhanced by ultrasound

Yao Jin

UNIVERSITÉ DE GRENOBLE

THÈSE

Pour obtenir le grade de

DOCTEUR DE L'UNIVERSITÉ DE GRENOBLE

Spécialité : Mécanique des fluides, Energétique, Procédés

Arrêté ministériel : 7 août 2006

Présentée par

Yao JIN

Thèse dirigée par **Frédéric PIGNON**

préparée au sein du **Laboratoire Rhéologie et Procédés**
dans **l'École Doctorale I-MEP^2**

Procédés de séparation membranaire de colloïdes : caractérisation des mécanismes aux échelles nanométriques et intensification par ultrasons

Thèse soutenue publiquement le **17 Novembre 2014**,
devant le jury composé de :

M. Henri DELMAS
Professeur, Laboratoire de Génie Chimique, Toulouse (Président)
Mme Laurence RAMOS
DR-CNRS, Laboratoire Charles Coulomb, Montpellier (Rapporteur)
M. Philippe MOULIN
Professeur, Laboratoire M2P2, Marseille (Rapporteur)
Mme Martine MEIRELES
DR-CNRS, Laboratoire de Génie Chimique, Toulouse (Examinateur)
M. Theyencheri NARAYANAN
Senior Scientist, ESRF (Examinateur)
M. Frédéric PIGNON
DR-CNRS, Lab. Rhéologie et Procédés, Grenoble (directeur de thèse)
M. Nicolas HENGL
MCF, Lab. Rhéologie et Procédés, Grenoble (co-encadrant)
M. Stéphane BAUP
MCF, Lab. Rhéologie et Procédés, Grenoble (co-encadrant)

Abstract

This thesis studies an ultrasonic assisted cross-flow ultrafiltration process from macro to nano scales. Different types of colloids were investigated: synthetic and natural clay dispersions, casein micelles (skim milk) and starch or cellulose nanocrystal suspensions. Firstly, flow properties and the changes due to ultrasound (US) were investigated. Secondly, structural organizations at nanometer length scales in the vicinity of the membrane during filtration have been revealed for the first time by real-time *in-situ* Small Angle X-ray Scattering. The applied US increased significantly the permeate flux of ultrafiltration by an enhancement factor of 1.6 to 13.5, depending on the structural organization of the colloids. The applied US has led to three main effects: a removal of accumulated particle layer, a partial disruption or no change of the nano-organization. Thirdly, thanks to the obtained concentration profiles, a modeling approach has allowed a prediction of the permeate flux.

Key words: cross-flow ultrafiltration process, ultrasound, SAXS, rheology, fouling control, colloids, Laponite, natural swelling clay, casein micelle, skim milk, starch nanocrystals, cellulose nanocrystals

Résumé

Cette thèse étudie le procédé d'ultrafiltration tangentiel assisté par ultrasons aux échelles macro et nanométriques. Différentes dispersions colloïdales ont été filtrées (argiles, micelle de caséine, nanocristaux d'amidon et de cellulose). Les propriétés d'écoulement et les changements induits par les ultrasons (US) ont été caractérisés. Les organisations structurelles à proximité de la membrane ont été mises en évidence pour la première fois aux échelles nanométriques, lors de la filtration par diffusion de rayons X aux petits angles *in-situ*. L'application des US a permis une augmentation significative des flux de perméation d'un facteur 1,6 à 13,5, selon l'organisation structurale des colloïdes. Trois mécanismes induits par les US ont été identifiés : une érosion complète, une rupture partielle ou pas de changement (nanométrique) des couches de particules accumulées. Grâce aux profils de concentration obtenus, une approche de modélisation a permis une prévision du flux perméation.

Mots clés : procédé d'ultrafiltration tangentiel, ultrasons, SAXS, rhéologie, contrôle de colmatage, colloïdes, Laponite, argiles naturelles, micelles de caséine, lait écrémé, nanocristaux d'amidon, nanocristaux de cellulose

Knowledge is written as your legacy, knowledge itself is your future.

Remerciements

Cette thèse s'est déroulée au sein du Laboratoire Rhéologie et Procédés de Grenoble. Ce travail a abouti grâce à l'aide de plusieurs personnes. Je voudrais adresser mes sincères remerciements à tous les acteurs plus ou moins directs de cette expérience.

Je pense évidemment en premier lieu à mes encadrants de thèse, M. Frédéric Pignon, M. Nicolas Hengl et M. Stéphane Baup de m'avoir fait confiance pour mener à bien ce projet. J'ai été ravi de travailler avec eux ces trois dernières années. Merci à eux de m'avoir permis de grandir tant professionnellement que personnellement par le biais des diverses expériences vécues pendant ce temps. En débutant cette thèse, je ne savais pas que j'aurai la chance de rencontrer quelqu'un comme Frédéric Pignon, mon directeur de thèse. Les nombreux moments passés ensemble (discussions/apprentissage dans son bureau, nuits de manips à l'ESRF et ses concerts…) ont été d'une richesse indescriptible tant humainement que scientifiquement. J'ai eu également un véritable plaisir à rencontrer Nicolas Hengl et Stéphane Baup. Bien que chargés d'enseignement, ils ont consacré beaucoup de temps et d'énergie pour m'apprendre professionnellement grâce à leurs connaissances, leurs méthodes de travail et d'observation, ainsi qu'humainement lors de tous les bons moments partagés. Je ne les remercierai jamais assez pour la sérénité qu'ils m'ont apportée et l'enthousiasme sans borne qu'ils m'ont communiquée.

Impossible d'évoquer ces bons souvenirs et la chance d'avoir rencontré certaines personnes sans penser à M. Albert Magnin, M. Nicolas Gondrexon et M. Guillaume Maitrejean. J'ai toujours apprécié les échanges d'idées et leurs excellents conseils qui ont conduit à l'aboutissement de cette thèse.

Je tiens à remercier très sincèrement M. Theyencheri Narayanan pour plusieurs raisons, tout d'abord pour avoir accepté avec enthousiasme d'évaluer et de participer à l'issue de ce travail en tant que membre du jury, mais aussi pour avoir soutenu ce projet lors de manips à l'ESRF. Je remercie tous les membres du jury de me faire l'honneur de leur présence et de l'intérêt qu'ils portent à ces travaux. Merci à M. Henri Delmas pour avoir accepté de présider mon jury de thèse. Merci à M. Philippe Moulin et Mme Laurence Ramos d'avoir accepté le

travail de rapporteur. Merci également à Mme Martine Meireles pour son implication dans l'évaluation de ce travail.

Je voudrais remercier du fond du cœur toutes les personnes du Laboratoire, permanents et doctorants qui ont rendu ces trois années très conviviales. Je souhaite tout d'abord remercier M. Albert Magnin et Mme Nadia El Kissi pour m'avoir accueilli au sein du laboratoire. Je pense particulièrement aux personnels techniques, administratifs et informatiques du Laboratoire que j'ai souvent sollicités et qui se sont toujours rendus disponibles pour m'aider. Merci à Mohamed Karrouch, Didier Blésès, Hélène Galliard, Frédéric Hugenell, Eric Faivre, François Bergérot, Claudine Ly-Lap et Sylvie Garofalo. Merci également aux techniciens de l'ESRF, Michael Sztucki et Jacques Gorini pour leur accueil avec enthousiasme et les dépannages techniques.

Je tiens à remercier également les équipes de collaboration pour ce sujet de thèse. Je pense tout d'abord au LGP2. Un grand merci à Ahlem Romdhane, Agnès Guillet, Evelyne Mauret et Marc Aurousseau pour leur disponibilité en réunions, en session de rédaction d'article, etc. Merci également à Laurent Michot du LEM de se déplacer à l'ESRF ainsi qu'au Laboratoire pour nous aider lors de mesures et nous apporter des idées constructives; et à Geneviève Gésan-Guiziou de l'INRA-Agrocampus et Bernard Cabane de PMMH de nous avoir accordé du temps et des conseils avisés.

Merci également à Seydou Guinko que j'ai eu la chance d'encadrer et grâce à qui j'ai beaucoup appris sur les qualités humaines nécessaires à la diffusion de savoirs et à l'encadrement. Merci pour son travail et je lui souhaite bon courage dans sa future carrière.

Je souhaite remercier tous mes amis de Grenoble qui m'ont soutenu, encouragé et supporté depuis le début et bien au-delà. J'ai plus particulièrement des pensées vives pour tous les moments intenses partagés avec mes collègues et amis du bureau : Fiacre « tu sais, qu'on t'aime bien », Chong le petit filou, Hamdullah le grand conteur, Nabil le travailleur avec ses bananes noires, Abdulgadir monsieur loi/règlement, je n'oublierai pas les pots de vendredi ! J'ai également des pensées fortes pour Claudine la maman adoptive, Etienne « ju rhua din thon », Jérémy le petit PDG 'méchant', Yannick le grand frère, Nicolas mon interprète, Céline la tolérance, Anica qui rime, Benoit « nabeille m'aime trop… », Gabriel le vrai ingénieur,

Chourouk la grande cousine, Sasha l'aideur, Roy qui rit en toutes les blagues, Xiaoxiao « 你 ** 的 », Ning le grand timide avec son interprète ainsi que sa femme Yuan…

Merci à Charline de m'avoir accompagné.

Je remercie de tout mon cœur ma famille : mes grands-parents qui sont toujours fiers de moi, mes parents qui m'ont toujours fait confiance pour cette thèse, mes cousines, mon oncle et ma tante qui m'ont toujours encouragé. De même tous les autres membres de ma famille qui me soutiennent malgré la distance. Je vous aime. 公公婆婆，爸爸妈妈，大爸大妈，大姐二姐，谢谢你们在我读博期间给予的无条件支持，还有其他所有在远方关心我的亲人，我爱你们。

Table of Contents

General introduction

‘‘Procédés de séparation membranaire de colloïdes : caractérisation des mécanismes aux échelles nanométriques et intensification par ultrasons’’. The title reveals three key issues of this thesis: separation of colloids by membrane process (cross-flow ultrafiltration), process characterization at nanometer length scales and intensification by ultrasound (US).

Membrane separation processes are used to concentrate, purify or remove solute from solution. They have gained a prominent place in food, pharmaceutical, water purification and treatment of liquid fluent streams and are effective for a broad range of applications.

Cross-flow ultrafiltration is one of the most popular developments in membrane technology for separating and/or concentrating colloidal particles (colloidal humic matter, mineral colloids, macromolecular drugs, proteins, etc.). It is a complex process in which colloidal particles are simultaneously subjected to compression and shear flow, induced by transmembrane pressure and cross-flow rate, respectively. Such a process is mainly limited by the accumulation of matter on the membrane surface which leads to two phenomena: concentration polarization and membrane fouling. The events leading to the formation of a concentrated layer close to the membrane surface are taking place at a length scale of nanometers. The interactions between the particles at this scale are very important, which requires an understanding of colloidal interactions during such process.

Originating from various forces, colloidal interactions are responsible for strikingly influencing the transport properties of colloidal suspensions, such as gradient diffusivity, flow property and the thermodynamic properties such as the osmotic pressure. Those properties are considered to play important roles in the process of ultrafiltration of colloids. As a result, considerable research effort has been devoted to understanding this process by taking into account them appropriately.

However, understanding of cross-flow ultrafiltration is not yet complete so far. Modeling of this process has been studied since twenty years, several approaches have been proposed but they are all limited to monodisperse hard-sphere colloids, while the colloids encountered in the real world are often polydisperse, soft with various morphological characters. In addition, ample

of techniques have been employed to characterize this process but there is not yet any result that can provide a global version of the events occur during cross-flow ultrafiltration of diverse colloids, and especially in the vicinity of the membrane. In fact, what is desperately required for both modeling and fundamental understanding of the process is an accurate characterization that is non-destructive and which can provide real-time, *in-situ* observation of the concentrated particle layer during filtration.

Consequently, the first goal of this study is to characterize cross-flow ultrafiltration of colloids at multi-scales, especially at nanometer length scales by a non-destructive real-time *in-situ* measurement.

To reach such goal, small-angle X-ray scattering (SAXS) measurements were carried out at the European Synchrotron Radiation Facility (ESRF) with a custom designed filtration cell. Based upon elastic scattering, SAXS is often exploited to probe the microstructure and non-equilibrium dynamics of soft matter and related systems. It can give access to the particle mean size, shape and structural arrangement. More than that, it can also provide us the concentration information by appropriate analysis, which is the case of this study.

For a widely used process in industry, production demands better process performance. Approaches of a wide variety have been proposed to improve cross-flow ultrafiltration by controlling matter accumulation (often called fouling control). Among numerous fouling control techniques, ultrasound-related approach has gained a great attention. By now, a number of reports claim the effectiveness of ultrasound application in membrane cleaning and fouling control. Most of them employed either an ultrasonic bath for cross-flow filtration or an ultrasonic horn for dead-end filtration. Both of them present flaws, such as high level energy loss, no access to the effects in the vicinity of ultrasonic field (case of cross-flow filtration) or limited potential for industrial application (case of dead-end filtration). Therefore, a more in-depth, industrial-application-based investigation necessitates a design of ultrasonic coupled cross-flow filtration module.

The custom designed filtration cell mentioned above is thus upgraded by coupling an ultrasonic system in an appropriate way, which leads to the novel ‘‘SAXS Cross-Flow US-coupled Filtration Cell’’. Developed at the Laboratoire Rhéologie et Procédés, it allows, on one

hand, applying ultrasonic waves close to the membrane; on the other hand, getting access to, in real time, the *in-situ* structural organization of the concentrated layer at nano-scales by SAXS measurements.

Using this custom designed cell, **the second goal of this study is, therefore, to examine the effect of application of ultrasound on filtration performance and the structural changes in the concentrated layer during ultrasonic assisted cross-flow ultrafiltration.**

With these goals, we decided to investigate several colloids of various characters (nature, size, form, physico-chemical property) to widen the explored range and to deepen understanding of this process. Two model clay dispersions (a synthetic clay dispersions and two natural swelling clay dispersions) and two colloidal suspensions of great interest in industry (skim milk and polysaccharide nanocrystal suspenions) were involved in this study. It should be emphasized that cross-flow ultrafiltration process becomes more complex with the addition of US: aside from the internal interactions which can strongly influence the filtration performance, colloids in this case are simultaneously subjected to compression, shear flow as well as ultrasonic force, as shown in the figure below:

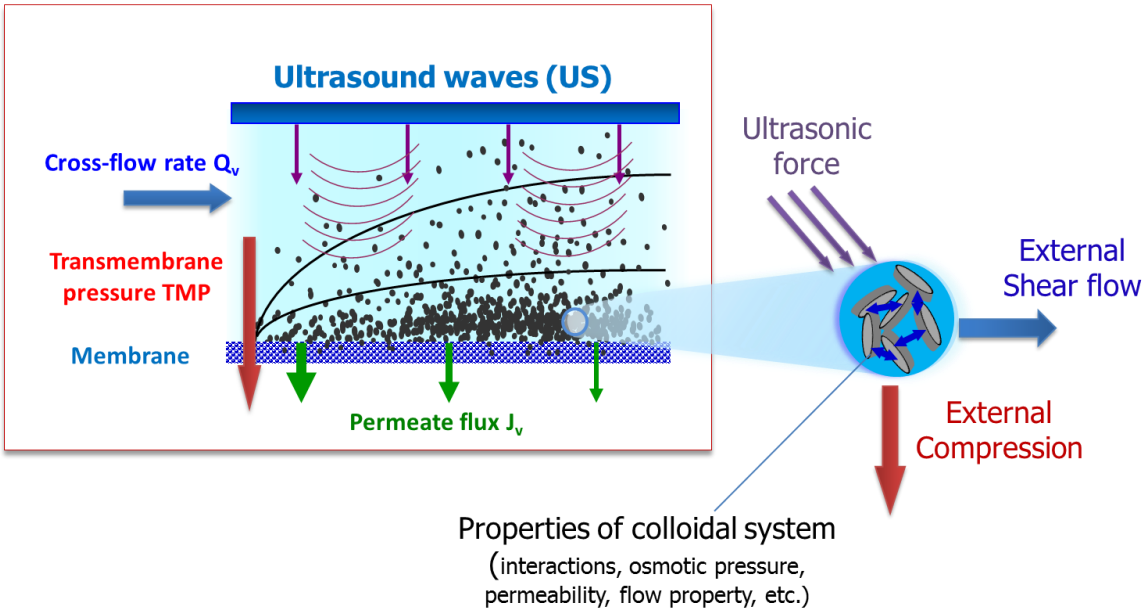

Colloids in ultrasonic assisted cross-flow ultrafiltration

In order to better present the key issues and the obtained results, this thesis is divided into 5 chapters.

In chapter 1, the principal techniques used in this study will be presented; basic principles or key elements that serve to understand this study are described. Some historical summaries are also included, such as the current methods of fouling characterization and fouling control, as well as the reported ultrasound-enhanced filtration examples.

In chapter 2, the materials and methods involved in this study will be presented. The investigated colloidal suspensions will be presented including their structural properties and preparation procedures. The experimental set-up and procedures, the characterization of used ultrasonic system and SAXS measurements will be described in details. All other analytical methods used in this study will also be presented.

In chapter 3, five different clay suspensions from two families during the process of ultrasonic assisted ultrafiltration at both macro-scales and nano-scales will be presented. Behaviors of Laponite dispersions in this process have been fully studied with different concentrations and different structural properties; their flow properties when submitted to ultrasound or pre-shearing have been also evaluated for better understanding of filtration phenomena. Two natural clay suspensions (Wyoming Montmorillonite (SWy-2) and Australia Nontronite (NAu-1)) were filtrated as well in order to consolidate the understanding of mechanism.

In chapter 4, four different colloidal suspensions from two families of great interest in industry are investigated: skim milk and polysaccharide nanocrytals. Effect of US on structural organization of skim milk will be discussed under different circumstances. It will also focus on the structural properties of starch nanocrystals (SNC) and cellulose nanocrystals (CNC) under this multi-forces field. Flow properties of them have been evaluated. In addition, some supplementary characterization such as microscopic observation of nanocrystals samples are presented.

In chapter 5, all the obtained results of this study will be reviewed, followed by an integrated analysis. A brief comparison between different colloidal suspensions will be given in

this chapter. Then some selected results will be analyzed in an integrated way: matter accumulation and yield stress chart of concentrated layer in the filtration channel will be calculated with the help of Matlab. At the end, a new approach of modeling has been conducted by combining our obtained results with previously studied concentration dependences of permeability and osmotic pressure for the concentrated layers. Permeate flux has been predicted and compared with the experimental one.

1

Review of general literatures

In this chapter, general introduction of the principal techniques used in this study will be presented; basic principles or key elements which will serve the next chapters are described. This chapter also includes some historical summaries, such as the current methods of fouling characterization and fouling control, as well as the reported ultrasound-enhanced filtration examples.

1. Membrane separation process

1.1 General presentation

1.1.1 Principle

Membrane separation is a process in which forces like pressure gradient, chemical or electrical potential leads to a separation through a semipermeable membranes. The compound which passes through the membrane, constituted of fluids (liquids or gases) and low molecular weight solutes, is called permeate, while the material which is retained by the selective barrier, constituted of suspended solids and solutes of high molecular weight, is called retentate. The separation process is purely physical and both fractions (permeate and retentate) can be used. This process is used in industry and research to purify or concentrate a dilute solution. Among the driving forces, it is the pressure gradient which is the most widely used in many different domains. Therefore, this study will focus on this type of driving force.

1.1.2 Classification of membrane processes

There are many processes available in membrane separation technology. Though based upon the same principle, their classification is not easy because of their disparity in driving forces, application fields and implementations. Usually, a general classification of this process is established on the basis of their separation threshold. As shown in Fig. 1.1, they are usually characterized by an effective pore-size or molecular weight cut-off (MWCO) and are divided into several distinct categories.

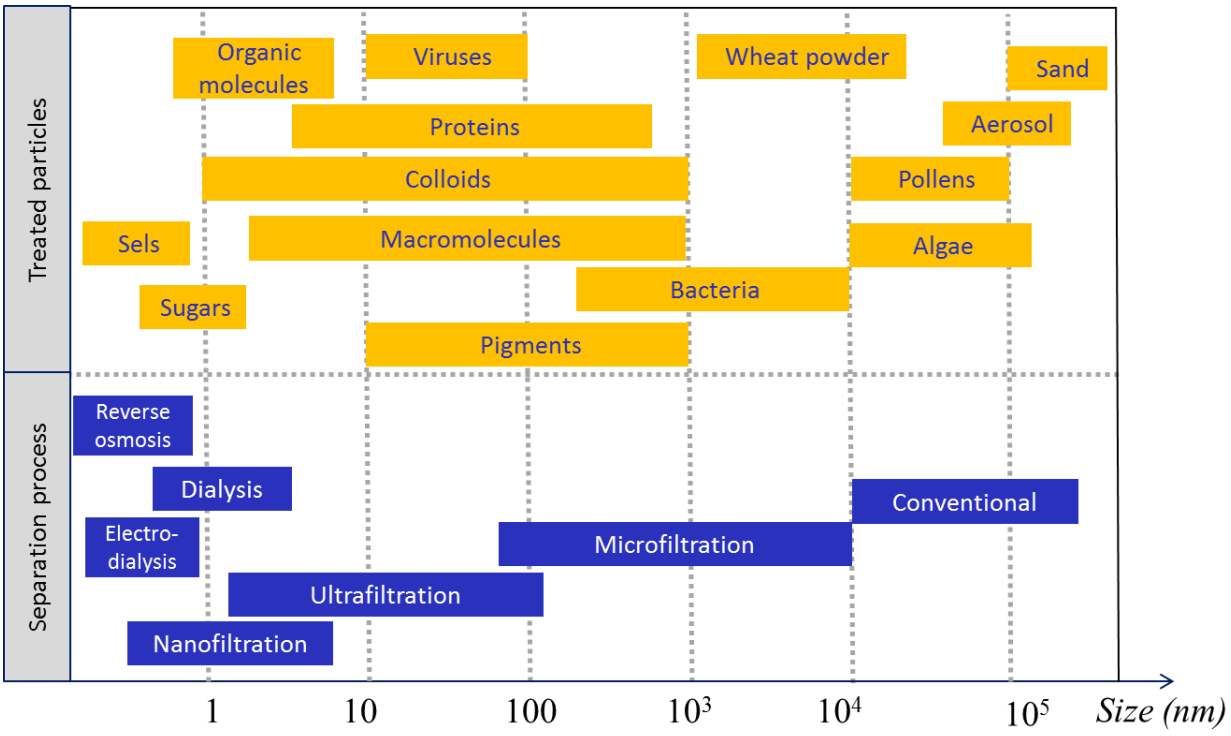

Fig. 1.1 *Classification of membrane process according to membrane pore-size and treated particle size (David, 2008; Jones, 2012; Simon, 1999; Thekkedath, 2007)*

Among those processes, electrodialysis is used to transport salt ions from one solution to another through ion-exchange membrane under an applied electric potential difference; while in dialysis the solutes diffuse through a neutral membrane under the influence of concentration gradient. In the processes as reverse osmosis (RO), nanofiltration (NF), ultrafiltration (UF) and microfiltration (MF), the application of different pressure between two sides of membrane allows to separate the fluids or low molecular weight solutes from the rest of the solutes through the membranes.

MF is generally used to separate particles in micrometer size range with pore diameters between 100 nm and 10 µm. It is typically used to remove turbidity and suspended solids in water treatment or to concentrate colloidal suspensions, bacteria, fat droplets and yeast cells, operated at relatively low transmembrane pressures (TMP, from 0.1 to 2.0 bar) (Cheryan, 1998).

As the major concerns of this study, UF uses smaller pore membranes than MF, which are typically in the range of 1-100 nm. With UF membranes, instead of particle size, it is standard to use the term ‘‘molecular weight cut-off’’, defined by the lowest molecular weight solute (in Dalton) in which 95% of the solute is retained by the membrane. This process is often used to purify and concentrate macromolecular (1 kDa to 1000 kDa) solutions, especially protein solutions. UF is becoming increasingly popular in water treatment industry since it can provide good quality drinking water thanks to its ability to remove turbidity, micro-organisms including viruses and macromolecules (Baker, 2004).

NF membranes have a pore-size range of about 0.5-2 nm which is just larger than that in RO. These two processes are operated at high TMP (5-50 bar) to counteract higher resistance and osmotic pressure. They are used to isolate low molecular weight solutions or small organic molecules, thus often applied in water treatment such as desalination of sea water or brackish water. (Mulder, 2000)

1.1.3 Filtration modes

Filtration can be carried out in different modes. There are two conventional modes used today, which are dead-end and cross-flow filtration (Mulder, 2000), as shown in Fig. 1.2.

In dead-end mode, the feed flows towards the surface of the membrane, and is forced to pass through the membrane perpendicularly (Fig. 1.2-a). In this mode, the convective flux towards the membrane leads to a continuous accumulation of solutes over time and consequently results in a regular decrease of productivity. This phenomenon can be attenuated by an additional agitation in the feed side. However, due to its instantaneous flux decline and limited productivity, this mode is not of practical interest for most filtration applications in industry.

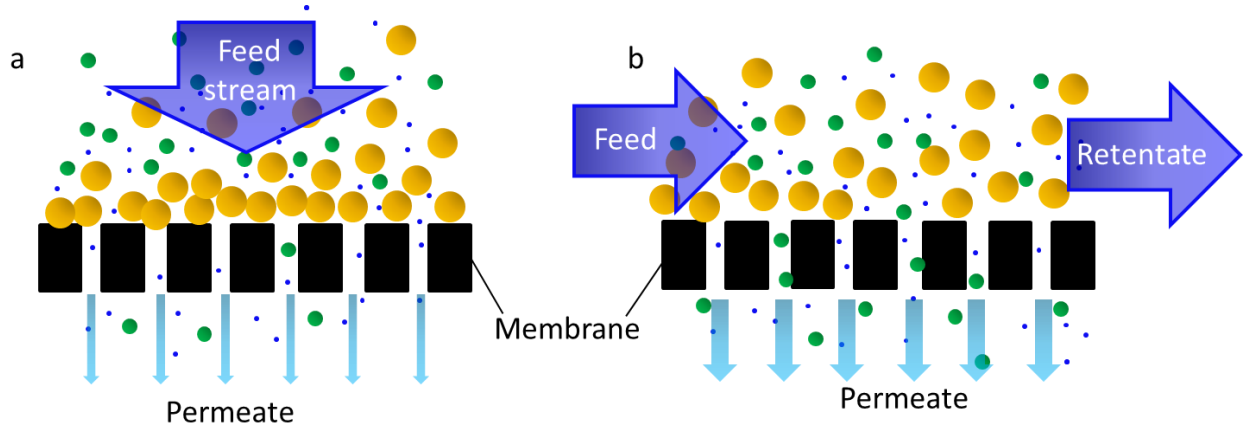

Fig. 1.2 *Filtration modes: a) dead-end filtration and b) cross-flow filtration*

In cross-flow mode, the feed flows parallel to the membrane surface with the inlet feed stream separating into permeate and retentate (Fig. 1.2-b). The principal advantage of this mode is that the permeate flux decline is much more reduced, compared to that of dead-end. In fact, the movement of retentate passing tangential to the surface can act as a washing role removing some built-up cake layer or even preventing its formation. Therefore, cross-flow filtration is widely used in large-scale pressure driven membrane plants.

In industry, four types of modules operating in cross-flow mode share the market: flat sheet, spiral wound, hollow fiber and tubular. Complete comparisons of advantages and drawbacks of each module have been carried out and further details are available in literature (Daufin *et al*., 1998; Cheryan, 1998).

1.2 Membrane of filtration

Membranes can be made of natural or synthetic materials such as porous organic polymers, ceramics or metals. Most membranes used in industry have an asymmetric structure, whereby the membrane consists of two layers. The top layer is a very thin dense layer (often from 0.1 to 1.5 µm, also called the top skin layer), and the bottom layer is a porous sub layer. The top dense layer is the key element of filtration performance while the porous sub layer provides the

membranes mechanical strength (Khulbe *et al*., 2008). An ideal membrane should have high porosity to ensure high permeate fluxes and a narrow pore size distribution to ensure good selectivity. As for the morphology of the top skin layer, two models have often been considered: model of capillaries or model of spheres-packing, which propose that the top layer consists of either some cylindrical channels or a packing of spheres, as shown in Fig. 1.3.

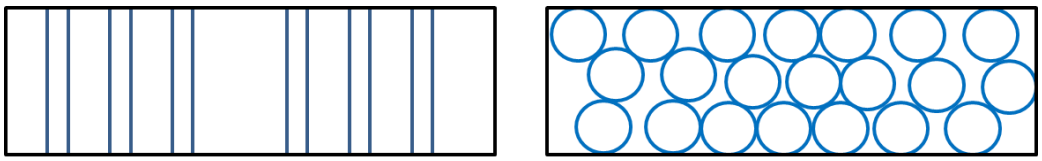

Fig. 1.3 *Models of membrane morphology (adapted from (Daufin et al., 1998))*

The membrane performances are principally assessed by their characteristics of permeability and selectivity. Their lifetime, resistance against pH, chemicals, temperature and pressure are also the important criteria.

1.2.1 Membrane permeability

Membrane permeability mainly depends on the structure of the top skin layer. It can be experimentally estimated by measuring the permeate flux of pure solvent (mainly water) under different transmembrane pressure. The variation is linear and follows Darcy's law:

$$J_w = L_p . TMP \qquad \textbf{\textit{Eq. 1.1}}$$

Where J_w is the specific volumetric flux of pure water that passes through the membrane ($m^3.m^{-2}.s^{-1}$), TMP is the transmembrane pressure (Pa) and L_p is the hydraulic permeability of tested membrane ($m^3.m^{-2}.Pa^{-1}.s^{-1}$).

The permeability of a membrane determines its reference state which we always hope to regain after every experiment for result comparison or better production. However, a progressive

decrease of permeability is often observed during membrane utilization, mainly due to membrane fouling which will be discussed later.

1.2.2 Membrane selectivity

Membrane selectivity corresponds to its efficiency as a barrier for certain substances in a solution. It can be determined by measuring the rejection rate (TR) of concerned substance, which is often expressed as:

$$TR = \left(1 - \frac{c_P}{c_b}\right) \times 100\ \% \qquad \textit{Eq. 1.2}$$

Where c_P and c_b are the concentrations of this substance in the permeate and in the feed solution, respectively. The rejection rate is an important parameter that provides information about the growth of fouling and the quality of product flux. When the selectivity is affected the product quality is compromised. This could have greater consequences than low production rates.

1.3 Transport mechanisms

Assuming that the membrane top layer consists of identical cylindrical pores (model of capillaries), then the pure water flux can be described by Poiseuille's law applied to porous medium (Daufin *et al*., 1998):

$$J_w = \frac{\pi . r^4 . N_p}{8 . \eta . e'} . TMP \qquad \textit{Eq. 1.3}$$

Where r is the pore radius (m), N_p represents the pore number per unit of surface (pores/m^2), η is the dynamic viscosity of fluid (Pa.s) and e' is the apparent thickness of membrane (m).

This law suggests that the pure water flux is directly proportional to the applied transmembrane pressure and inversely proportional to the fluid viscosity. The same suggestion was also proposed by Darcy:

$$J_w = L_p . TMP = \frac{TMP}{\eta . R_m} \qquad \textit{Eq. 1.4}$$

Where R_m represents the hydraulic resistance of membrane (m^{-1}). It is a constant assuming the physical properties of the membrane remains unchanged throughout.

When the feed solution contains some substances retained by the membrane, the convective flux through the membrane, called permeate flux (J_v), will be lower than that obtained with only pure water, J_w. A flux decline is often observed during solution filtration (Fig. 1.4a) with fixed TMP; in MF and UF this flux decline can be very severe, causing a change in the membrane properties. A number of reports have also shown that J_v does hardly vary with TMP linearly and becomes even independent in some circumstances (Fig. 1.4b). The value of applied TMP under which the limiting flux (J_{lim}) is reached depends on the operating conditions and the combination of feed solution and membrane.

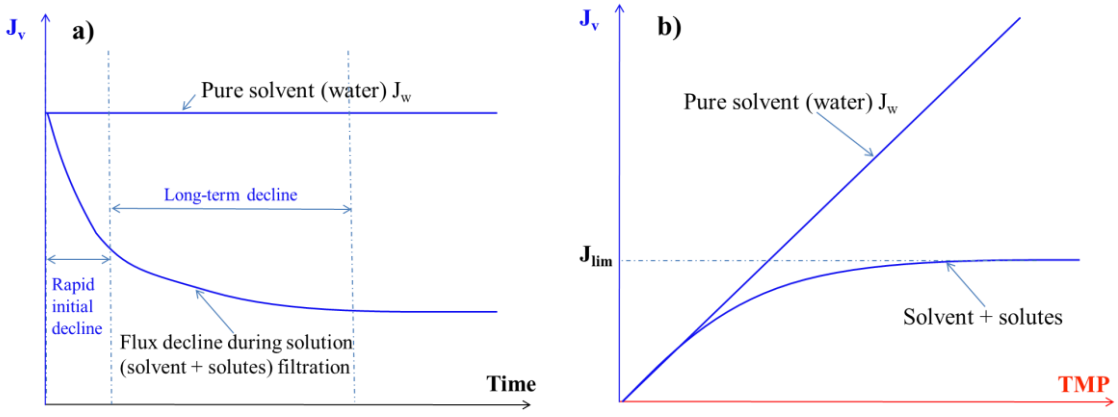

Fig. 1.4 *Classical filtration curves in different circumstances: a) evolution of permeate flux as a function of time at fixed TMP, b) Evolution of permeate flux as a function of TMP (adapted from (Simon, 1999))*

The flux decline originates from two well-known phenomena: concentration polarization and membrane fouling.

1.3.1 Concentration polarization and film theory model

While a solution is treated by filtration, the substances retained by the membrane tend to accumulate on its surface under the effect of the convective flux through the membrane. Consequently, the concentration on the membrane surface (C_m) increases and becomes higher than that in bulk of the solution. This concentration gradient generates a diffusive flow back to the bulk of the feed (Fick's first law). This phenomenon, known as concentration polarization, is built up very rapidly since the first moment of filtration and induces the rapid initial flux decline (Fig. 1.4a). After a period of time, a steady state can be reached. Mulder (2000) well describes the phenomenon: the convective solute flow to the membrane surface (J.C) is balanced by the solute flux through the membrane ($J.C_p$) plus the diffusive flow from the membrane surface to the bulk (J_d), as shown in Fig. 1.5.

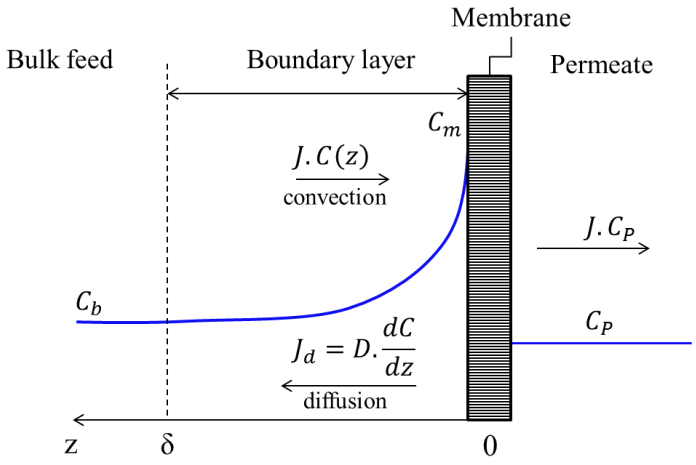

Fig. 1.5 *Concentration polarization: concentration profile under steady state conditions (adapted from (Mulder, 2000))*

On the basis of this knowledge, the mass balance of solute during filtration can be described as:

$$J.C(z) - D.\frac{dC}{dz} = J.C_P \qquad \textit{Eq. 1.5}$$

Where z is the distance from the membrane (m), C(z) is the concentration of solute within the boundary layer (kg.m^{-3}), D represents the coefficient of diffusion of solute (m^2.s^{-1}) and C_p is the concentration of solute in the permeate (kg.m^{-3}). Eq. 1.5 is often called "film theory model", the simplest and most broadly employed model, being proposed since 1960s' (Michaels and Bixler, 1968).

At steady state of filtration, the thickness of boundary layer of polarization is δ (m), then with the boundary conditions:

$$Z = 0 \rightarrow C = C_m$$

$$Z = \delta \rightarrow C = C_b$$

So Eq. 1.5 can be integrated and expressed as:

$$J_V = \frac{D}{\delta}.\ln\frac{C_m - C_p}{C_b - C_p} = M.\ln\frac{C_m - C_p}{C_b - C_p} \qquad \textit{Eq. 1.6}$$

Where M = D/δ, is termed the mass transfer coefficient (m.s^{-1}). When a complete rejection of solute occurs (C_p = 0), Eq. 1.6 can be simplified to:

$$J_V = M.\ln\frac{C_m}{C_b} \qquad \textit{Eq. 1.7}$$

1.3.2 Gel layer model

In 1970, Blatt *et al*. proposed a supplementary hypothesis based upon film model to explain the existence of limiting flux during filtration (Fig. 1.4b). According to them (Blatt *et al*., 1970), material accumulation close to the membrane is so severe that a gel layer could form with a concentration of C_g (kg.m^{-3}), as shown in Fig. 1.6. Increase of TMP leads to, no further increase of permeate flux but the growth of this gel layer. This layer reduces the membrane permeability and modifies its selectivity. In addition, it is not always reversible and often leads to membrane fouling. In this circumstance, Eq. 1.7 can be rewritten as:

$$J_V = M.\ln\frac{C_g}{C_b} \qquad \textit{Eq. 1.8}$$

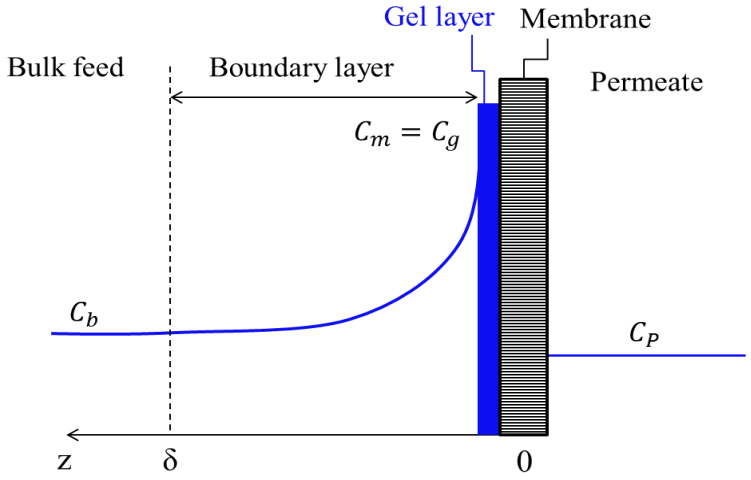

Fig. 1.6 *Concentration polarization with hypothesis of gel layer (gel layer model, adapted from (Blatt et al., 1970))*

The model assumes that the solute is fully retained and the concentration at the membrane surface is constant. According to Mulder, the gel layer concentration depends on the size, shape and chemical structure of solute but is independent of the bulk concentration (Mulder, 2000).

1.3.3 Osmotic pressure model

An osmotic pressure model has been developed and it assumes the osmotic pressure is generated by the retained macromolecules and the low molecular weight components permeate through freely. For high concentrations as those within the polarization layer in certain conditions, the osmotic pressure cannot be neglected (Elimelech and Bhattacharjee, 1998; Mulder, 2000). The model is based on Darcy's law, and the driving force through the membrane is given by the transmembrane pressure minus the osmotic pressure difference across the membrane, ΔΠ (Pa).

$$J_V = \frac{TMP - \Delta\Pi}{\eta . R_m} = \frac{TMP_{eff}}{\eta . R_m} \qquad \textbf{Eq. 1.9}$$

Where TMP_{eff} is the effective transmembrane pressure (Pa).

1.3.4 Resistance model

According to Darcy's law, the permeate flux is directly proportional to the transmembrane pressure and inversely proportional to the solution viscosity and the filtration resistances due to the clean membrane (R_m), gel formation (R_g), concentration polarization (R_{cp}) and internal fouling (R_{if}), as shown in Fig. 1.7.

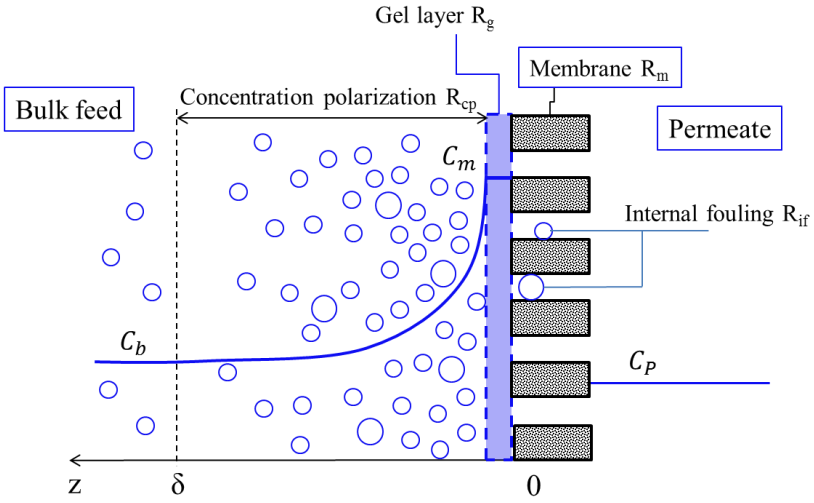

Fig. 1.7 *Overview of various types of resistance towards mass transport across a membrane (Adapted from (van den Berg and Smolders, 1990))*

Then for this model, the permeate flux can be expressed as:

$$J_V = \frac{TMP}{\eta . R_t} = \frac{TMP}{\eta . (R_m + R_g + R_{cp} + R_{if})} \qquad \textbf{Eq. 1.10}$$

1.4 Membrane fouling

As mentioned before, substance accumulation leads to, in certain circumstance, membrane fouling. Fouling is defined as the unwanted deposition (or growth) of suspended, dissolved or chemically generated species from process fluids on to a surface. Membrane fouling is a process where solute or particles deposit onto a membrane surface or into membrane pores in a way that degrades the membrane's performance. The formation of a deposit on a membrane surface can occur due to several mechanisms:

- Particulate fouling: accumulation of particulate matter originally suspended in the feed;
- Chemical precipitation: excess of solubility for some components when the feed stream becomes more concentrated;
- Reaction fouling: formation of foulants by chemical reaction either in the bulk or on/with the membrane surface;
- Colloidal fouling: deposit of material due to colloidal charge or size characteristics;
- Biological fouling: attachment of micro-organisms to the membrane.

If the filtration feed is of a complex nature multiple mechanisms can occur simultaneously or synergistically (Evans and Bird, 2006). Membrane fouling depends on the hydrodynamics of the filtration process and the interactions between the membrane and foulants (Marshall *et al*., 1993).

1.4.1 Mechanisms of membrane fouling

According to Tracey and Davis, there are two types of membrane fouling: external and internal, depending on where it takes place - on the external surface of the membrane or in the membrane pores (Tracey and Davis, 1994). External fouling induces the increase of the effective membrane thickness, blockage or constriction of pore entrance; while internal fouling leads to internal blockage or constriction of pores. Consequently, membrane fouling could alter both membrane hydraulic permeability and solute transmission characteristics.

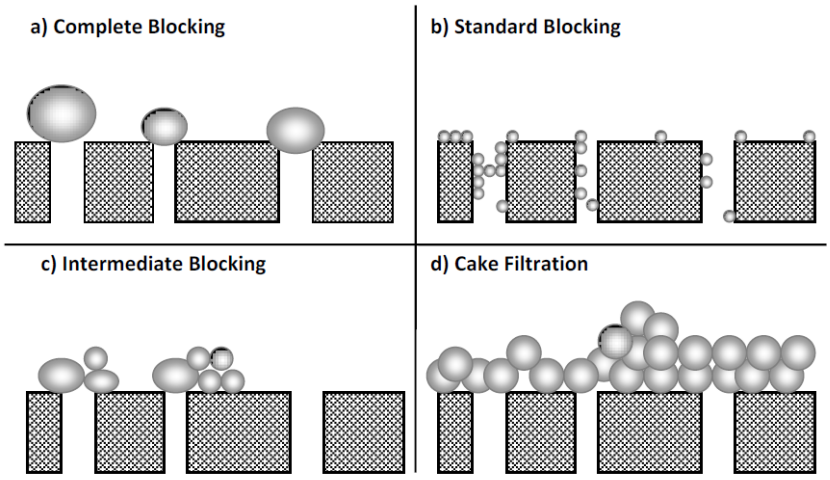

Fig. 1.8 *Membrane fouling mechanisms (Bowen et al., 1995)*

Four main mechanisms of membrane fouling can be distinguished (Bowen *et al*., 1995; Hermia, 1982; Shirato *et al*., 1979), as presented in Fig. 1.8:

a) Complete blocking (pore blocking): the pores are blocked by particles having very similar size to the pores and no further material can pass through the pores;
b) Standard blocking (pore constriction): the inner surface of the pores are covered by the particles which are much smaller than the pores, a result of direct adsorption of particles, which leads to reduction of pore volume;
c) Intermediate blocking (long term adsorption): every particle reaching a pore will contribute to blockage and particles accumulate on each other;
d) Cake filtration (boundary layer resistance): particles are retained without entering the pores; the deposit of particles on the membrane surface contributes to the boundary layer resistance.

1.4.2 Membrane cleaning

In industry, membrane cleaning is one of the most important steps for maintaining membrane performance, such as permeability and selectivity. All membranes will more or less foul during operation involving liquid. Although operational conditions and methods should be, and have been, studied first to reduce the fouling process, membrane cleaning is often inevitable.

Unfortunately, the cleaning procedure demands to interrupt the filtration and it often consists of some operations long, complex and very costly. Main difficulty is that there is no ‘‘universal procedure’’ of cleaning, and each situation should be considered properly in taking into account the membrane material and physico-chemical properties of foulants. Nowadays, cleaning can be summarized into four distinct methods (Bowen *et al*., 1989; Daufin *et al*., 1998; Trägårdh, 1989):

- Mechanical cleaning: methods such as removing deposits using turbulence or reversal of TMP, including back flushing (flow reversal), back pulsing (backpressure is applied at rapid pulses), rotating disks and secondary vortex flows.

- Chemical cleaning: a heterogeneous interaction between the detergent solution, the fouling layer and the membrane surface. With different feed requirement, both acid and alkaline agents could be used.

- Biological cleaning: an enzymatic cleaning step can be included in chemical cleaning, the operating conditions should be adapted for optimizing the enzyme’s action (pH, temperature).

- Electric cleaning: application of an electric field across the membrane under which charged particles or molecules will migrate in the direction of the electric field. This cleaning method does not need to interrupt the work cycle of the membrane.

1.5 Characterization of fouling on membranes

A fundamental understanding of fouling mechanisms is of paramount importance in order to mitigate or minimize fouling and promote cleaning. Therefore, this phenomenon has been investigated extensively by many authors using a variety of techniques attempting to understand the following three regions: (1) the membrane, (2) the fluid boundary layer and (3) the bulk fluid in the membrane module (V. Chen *et al*., 2004). *In-situ* methods are preferable because they allow monitoring the deposit or blockage without moving the sample from its original position. *In-situ* observation of membrane process can be classified into two categories: optical techniques and non-optical probes (J. C. Chen *et al.*, 2004; V. Chen *et al.*, 2004). Details of these techniques are described in the following section.

1.5.1 ‘‘Offline’’ characterization of fouling cake

The formed fouling cake can be analyzed by the techniques commonly used in material science, such as particle size analysis, microscopic observation or spectroscopy. Among them, scanning electron microscopy (SEM) could be the most used technique in literature to characterize the fouling cake.

Lamminen *et al.* have employed SEM to reveal the effectiveness of ultrasonic cleaning by showing the structure of fouled surface in different conditions (Lamminen *et al*., 2006, 2004). Meng *et al.* have analyzed the major components of cake layer in submerged membrane bioreactor systematically by particle size analyzer (PSA), SEM, confocal laser scanning microscopy (CLSM), X-ray fluorescence (XRF), energy dispersive X-ray analyzer (EDX), and Fourier transform infrared (FTIR) spectroscopy (Meng *et al*., 2007). Similarly, Lin *et al.* have used a series of analyses, including FTIR spectroscopy, EDX, CLSM, SEM, atomic force microscopy (AFM) and PSA to reveal the sludge cake structure formed in submerged anaerobic membrane bioreactors (Lin *et al*., 2009).

‘‘Offline’’ characterization can provide the structure properties of fouling cake and allow identifying the substances. However, it often requires sample treatment before measurements; therefore, the results can not exactly describe the fouling cake properties since the foulant could be already altered at the moment of measurement.

1.5.2 Imaging techniques

Imaging techniques refer to direct visualization of particle deposit. The direct observation through the membrane (DOTM) technique was first developed to observe particle deposition and interactions between the particles and the membrane during the cross-flow MF process. A DOTM set up includes an optical microscope attached with a Closed-circuit television (CCTV) video camera. This enables particles larger than 1µm to be identified. Li *et al*. first published the DOTM technique, whereby a microscope and video camera assembled above a cross-flow

filtration cell, in which the permeate flowed upwards through a transparent alumina membrane (Li *et al*., 1998). The major disadvantage of the DOTM technique is the need to use a relatively transparent membrane and the requirement of a relatively clear feed solution (J. C. Chen *et al*., 2004; V. Chen *et al*., 2004). The membrane channel was then modified where the microscope objective is mounted above the membrane to view particle deposition from the feed side *(*Kang *et al*., 2004; Mores and Davis, 2001). The limitation of these techniques is that the positioning of the microscope objective does not allow the observation of particle accumulation beyond a monolayer.

Direct visualization approach has recently developed more divisions. The group of Bacchin developed poly-dimethylsiloxane (PDMS) device for dead-end and cross-flow filtration to observe directly the clogging mechanisms of microchannels (Agbangla *et al*., 2012; Bacchin *et al*., 2014; Marty *et al*., 2014). The group of Schmitz carried out an *in-situ* 3D characterization of deposition on microsieve using Confocal Laser Scanning Microscopy (CLSM) (Ben Hassan *et al*., 2014a, 2014b, 2014c). These new techniques allow a better understanding of fouling build-up mechanisms; however, their results are limited in specific conditions. Pore sizes of microchannel are between 5 and 20 µm while that of microsieve are between 0.8 µm and 2 µm, therefore, their results are not suitable for other membrane process with smaller pore sizes, such as ultrafiltration.

Nuclear magnetic resonance (NMR) imaging was also employed to characterize particle accumulation phenomena in membrane process. Basically, NMR imaging involves the excitation and relaxation of protons in a specimen under the influence of an external magnetic field. This technique allows imaging of any selected plane within a complex sample and can image samples that are optically opaque. Additional advantages include a spatial resolution down to 10 µm or lower. Application of this technique can be found in literature for characterization of concentration polarization phenomena in hollow fiber membrane filtration (Airey *et al*., 1998; Yao *et al*., 1995). Application of NMR imaging in membrane process is limited by the size restrictions or “field of view” provided by conventional imaging apparatus (V. Chen *et al*., 2004).

Another imaging technique, X-ray computed tomography, has also been used by Frank *et al*. to show fiber packing and concentration distributions in commercial dialyzers (Frank *et al*., 2000). X-rays require distinct difference in electron density between components of interest and

can be used to determine concentration profiles within membrane module. As in medical applications, scanners comprise an X-ray source combined with an opposing detector on the other side of the sample. Reconstruction of the image in three dimensions is then carried out by the computed tomography. This technique provides lower spatial resolutions than NMR (V. Chen *et al*., 2004).

1.5.3 Techniques based on waves reflection and refraction

Characterization of accumulated particles layer could also be carried out using wave reflection/refraction based techniques. Laser-related and ultrasound-related techniques are the most common ones.

Altman and Ripperger studied the development of an accumulated particles layer on a membrane surface using laser triangulometry (Altmann and Ripperger, 1997). This technique is based on the reflection of laser beam off the membrane surface. The elevation of the surface changes with the formation of particle layer, thus the reflected beam captured by a CCD camera will shift. Measurement of the shift can then be directly related to the displacement of the elevation of the surface. During membrane filtration, laser triangulometry can be used to track the growth of an accumulated particles layer and to measure the thickness of this layer.

Laser refraction could also be used to investigate this phenomenon. Named refractometry, it is based on the principle that light is deflected when passing through a medium of continuously varying refractive index, with the deflection patterns determined by the gradient of the refractive index. Thus the concentration gradient in the polarized layer can be determined by this technique (Gowman and Ethier, 1997). However, this study concerns only dead-end filtration.

As for the ultrasound-related technique, ultrasonic time-domain reflectometry (UTDR) must be mentioned. This technique uses sound waves to measure the location of a moving or stationary interface and can provide information on the physical characteristics if the media through which the waves travel (J. C. Chen *et al*., 2004). Bond *et al.* first reported the use of UTDR to investigate membrane fouling and compaction with high-frequency transducers (Bond *et al*., 1995). This technique was then employed by numerous authors for *in-situ* measurement of

membrane fouling during different membrane process (J. C. Chen *et al*., 2004; Mendret *et al*., 2007). The results showed a good correlation between the ultrasonic response signals and the development of the fouling layer on the membrane surface. The UTDR technique is one of the non-invasive methods that could be applied to commercial-scale modules (J. C. Chen *et al*., 2004), however, its drawback is that the implementation is complex, and relies on a number of assumptions about the properties of both the foulant and the medium.

1.5.4 Light scattering techniques

Light scattering techniques such as static light scattering (SLS), small-angle X-ray scattering (SAXS) and small-angle neutron scattering (SANS) have been used to monitor filtration process. The scattered source is particle, electron cloud and nuclei for SLS, SAXS and SANS, respectively. Therefore, SLS can access to the structure of micrometer scale and both SAXS and SANS get access to the structure at nanometer length scale. All of them can provide real-time, *in-situ* observation of the fouling layer, including foulant structure as well as thickness, during filtration

Pignon *et al.* first presented SLS and SANS to quantify the inner structure of deposited colloid fouling layers on the membrane surface (Pignon *et al*., 2000). In their measurements, incident light or neutrons were directed through the cake layer resulting in scattering through the deposit; the scattering intensity was then related to the fractal dimension of the deposit.

Pignon *et al.* have advanced their previously described observation techniques using SAXS measurement to characterize the structure of particle deposits during dead-end ultrafiltration of different dispersions (Pignon *et al*., 2003, 2004). They have also applied a magnetic field to manipulate the orientations of charged particle for enhancing the filtration performance. More recently, they have designed a “SAXS cross-flow filtration cell” to characterize the structure organization of accumulated particle layer during cross-flow filtration (Pignon *et al.*, 2012). On the basis of their previous works, SAXS characterization was employed in this study and will be presented in details in section 5 of this chapter.

1.6 Fouling control

Method to prevent or control fouling is always highlighted before cleaning. Important considerations include pre-treatment of feed or membrane, changes of operational conditions, modifications of filtration module or application of additional field such as magnetic, electric or ultrasonic field.

1.6.1 Pre-treatment

Pre-treatment of the feed solution can cause great differences in flux and transmission. Methods employed include heat treatment, pH or ionic force adjustment, ultrasonication, chemical clarification and pre-filtration (Mulder, 2000; Muthukumaran *et al*., 2006). A number of reports (Almécija *et al*., 2009; Gésan-Guiziou *et al*., 1993; Koh *et al*., 2014; Lee and Merson, 1976) can be found in literature and the pre-treatment method and effectiveness depend strongly on the properties of feed solutions, and no further discussion is given here.

In spite of pre-treatment of feed solutions, the membrane surface can also be modified to make it less prone to fouling. The membrane properties can influence the structure of the initial fouling layer. Membrane chemistry can affect the adsorption rate of the first few layers of the deposited material (de Barros *et al*., 2003). Modification of the surface can be carried out by using surfactants, electron irradiation, UV irradiation, plasma treatment or some chemical modifications such as blending, coating and grafting (Bryjak *et al*., 2000; Huang *et al*., 2009; Pieracci *et al*., 2002; Pontié *et al*., 2005; Shim *et al*., 2001).

1.6.2 Operational condition changes

In industry, fouling is often controlled by the use of high cross-flow velocity. However, the high cross-flow velocity results in a relatively large pressure drop over the cross-flow channel, which causes a decreasing transmembrane pressure over the length of the tube. Therefore, the transmembrane pressure is compensated by a cross-flow at the permeate side, this method is called “uniform low transmembrane pressure (UTP) concept” (Saboyainsta and Maubois, 2000).

A flaw of this concept is the high energy demand as a result of the cross-flow at both sides of the membrane (Brans *et al*., 2004).

Besides the flow manipulation, the transmembrane pressure can also be manipulated to remove fouling during filtration. Backpulsing and comparable techniques, such as backwashing, backflushing and back-shocking are effective means (McLachlan *et al*., 2010; Redkar *et al*., 1996). In these procedures, the transmembrane pressure is temporarily inverted and part of the permeate flows back into the cross-flow channel. Deposits on the membrane are lifted and taken up by the cross-flow. The effectiveness of the pulse depends on the frequency, the duration and the pressure profile, and highly dependent on the feed composition.

Combined application of UTP concept and backpulsing is also reported by Guerra *et al.* (1997) with good results. Furthermore, pulsating or reversed feed flows can be used to control fouling by rapid velocity changes in the cross-flow channel (Curcio *et al*., 2002; Jaffrin *et al*., 1994).

1.6.3 Filtration module modifications

In order to control fouling, modifications of filtration module have been proposed on the basis of increasing shear rate close to the membrane. To reach such goal, some spacers or turbulence promoters, such as Dean vortices or micro-turbulences, can be inserted so that flow instabilities are created (Krstić *et al*., 2002; Moulin *et al.*, 1999; Winzeler and Belfort, 1993). A possible disadvantage of inserts is cleaning problems, because dead-zones will also be created. Other means of increasing shear rate close to the membrane is to use vibrating modules, such as VSEP (vibratory shear-enhanced processing system) (Al-Akoum *et al*., 2002), or rotating disk modules (Ding *et al*., 2002; Engler and Wiesner, 2000). These vibrating or rotating membrane equipment are difficult to scale up and expensive (Brans *et al*., 2004).

1.6.4 Other techniques

There are also other techniques being proposed to reduce the effect of fouling, including gas bubbling (Cui *et al*., 2003; Cui and Wright, 1996), scouring particles (Noordman *et al*., 2002) and the use of acoustic or ultrasonic waves and sonication. Gas bubbling and scouting particles increase shear rate and improve mixing close to the membrane surface, but they are not easy to control in large membrane systems (Brans *et al*., 2004).

Among these different techniques developed in order to reduce fouling, the use of ultrasound seems to be one of the most promising techniques (Lamminen *et al*., 2006; Muthukumaran *et al*., 2005). Therefore, the next section is dedicated to the understanding of ultrasound, presenting this technique in light of its fundamentals and potential use.

2. Ultrasound

2.1 Definition, classification and applications

Like the visible spectrum, the audio spectrum corresponds to the standard human receptor response function and covers frequencies from 20 Hz to 20 kHz. Ultrasound is defined as a sonic waves whose frequencies are above 20 kHz up to the MHz range and finally at around 1 GHz, which is conventionally called as hypersonic (Cheeke, 2002). This band is variable according to different researchers since it is also defined from 16 kHz to 10 MHz (Mason and Lorimer, 1988; Pétrier *et al*., 2008).

Ultrasound has many applications, covering a very broad range of disciplines. Taking into account two principal parameters which are the frequency and ultrasonic intensity, ultrasonic applications can be divided into two categories: high-power ultrasound, often with a frequency band from 20 kHz to 1 MHz, and low-power ultrasound often with a high or very high frequency (Fig. 1.9). The high-power ultrasound excites some chemical changes or produces significant effects by direct mechanical actions. It is often used in cleaning processes, emulsification or chemical reaction intensification. Conversely, when the ultrasonic power is low (< 1 W), there is no further interaction with the substance rather than vibration; hence no such properties modification is produced with its propagation. Consequently, the low-power ultrasound is often used as a diagnostic tool in medical domain, or underwater range finding, also known as Sonar. Another major application is non-destructive testing, used to find flaws in materials and to measure the thickness of objects.

Ultrasonication generates alternating low-pressure and high-pressure waves in liquids, leading to the formation and violent collapse of small bubbles. This phenomenon is termed cavitation and causes high speed impinging liquid jets and strong hydrodynamic shear-forces.

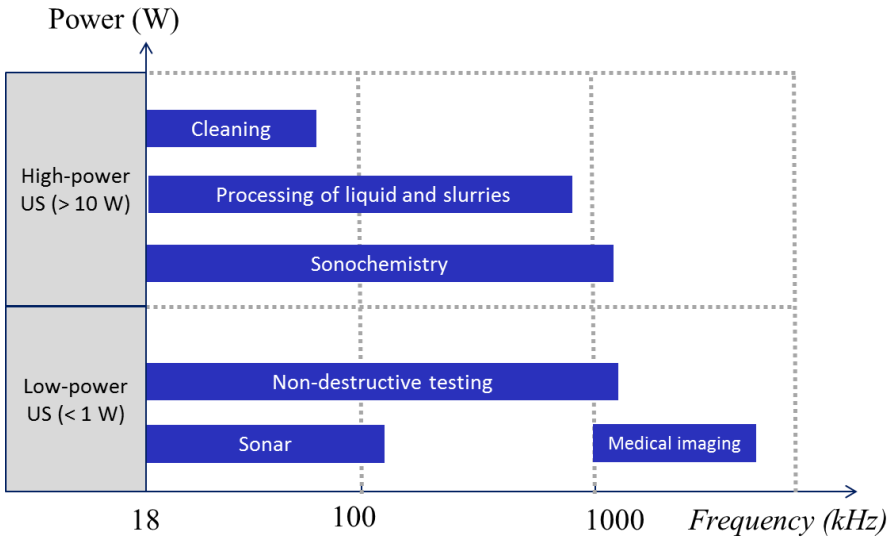

Fig. 1.9 *Common frequency and power range of ultrasound for various applications (adapted from (Pétrier et al., 2008))*

2.2 Generation and propagation

2.2.1 Generation

Ultrasonic waves are generated by a device called ultrasonic transducer that converts available energy (electrical or mechanical energy) into high frequency sound. There are three main types: gas driven, liquid driven and electromechanical (Mason, 1999).

The gas driven or liquid driven transducers convert mechanical energy in the form of air pressure or liquid motion into ultrasonic sound waves, for example the dog whistle. The commonly used one is electromechanical transducer, which is based on either the piezoelectric or the magnetostrictive effect. Magnetostrictive transducers were the first to be used on an industrial scale to generate high-power ultrasound. They make use of the shape or dimension change of ferromagnetic materials in a magnetic field to produce ultrasound.

The most common type of transducer used for both the generation and detection of ultrasound is the piezoelectric transducer. The piezoelectric effect is defined as a reversible process in which an interaction between the mechanical and the electrical state in certain

crystalline materials can be found. Application of an electrical field results in, therefore, a structure deformation (fluctuation in dimensions) of a piezoelectric material. This effect can be harnessed to transmit ultrasonic vibrations from such material through whatever medium with which it is in contact. Many materials, both natural and synthetic, exhibit piezoelectricity, such as quartz, some semi-conductors and some synthetic crystals or ceramics. Modern transducers are based on ceramics containing piezoelectric materials, among which lead zirconate titanate (also known as PZT) is the most frequently employed one.

2.2.2 Propagation

The ultrasonic waves propagate by longitudinal motion (compression/rarefaction), which induces simultaneously spatial and temporal pressure variation in which they travel. Leighton explained the wave propagation by a simple analogue consisting of a series of bobs of equal mass, connected in a line by massless, lossless springs (Leighton, 2007), as shown in Fig. 1.10. When a single-frequency longitudinal wave is passing through the medium, the bobs in the equilibrium position are displaced either to the left or right except those at the centers of the created rarefactions or compressions. Regions of high pressure (compression) correspond to the zones with more bobs, similarly, low-pressure regions (rarefaction) occur in zones with less bobs. This analogue demonstrates the particles movement in the medium where the ultrasonic waves pass through. Note that the wave propagation does not lead to a general medium movement, but only an oscillation of each particle around the equilibrium position.

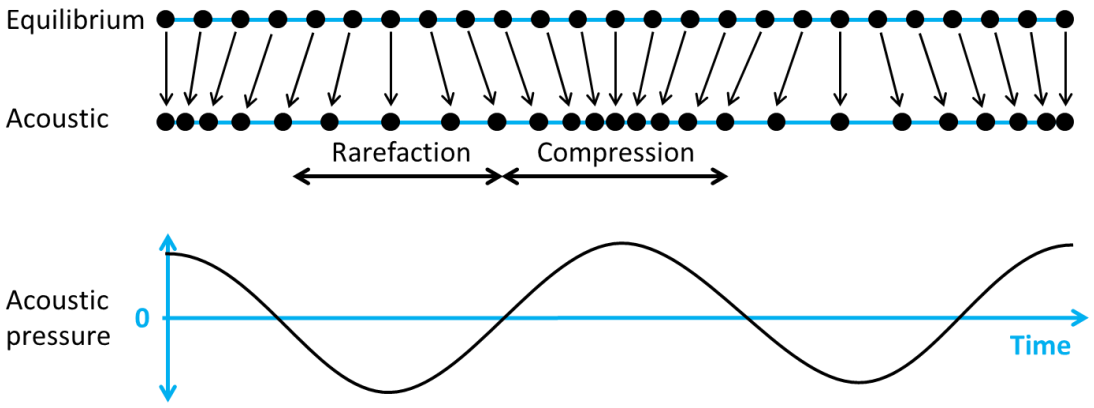

Fig. 1.10 *Schematic of ultrasonic waves' propagation (adapted from (Leighton, 2007))*

Evolution of the displacement, A, of one particle around this position, and the instantaneous acoustic pressure, P, in the medium where the longitudinal wave travels over time (t) can be expressed by:

$$A = A_m . \sin(\omega t) \qquad \textit{Eq. 1.11}$$

$$P = P_m . \sin(\omega t) \qquad \textit{Eq. 1.12}$$

Where A_m is the maximum of displacement amplitude (m) and P_m is the maximum of acoustic pressure amplitude (Pa), ω is the circular frequency defined by:

$$\omega = 2\pi f = \frac{2\pi c}{\lambda} \qquad \textit{Eq. 1.13}$$

With c the propagation speed of the longitudinal wave ($m.s^{-1}$), which can be calculated by the product of wavelength λ (m) and wave frequency f (Hz).

One principal parameter for the longitudinal wave is the acoustic impedance in the medium Z:

$$Z = \rho . c \qquad \textit{Eq. 1.14}$$

Where ρ is the density of the medium at equilibrium ($kg.m^{-3}$). According to Leighton, the acoustic intensity ($W.m^{-2}$) of a simple linear-propagated plane and spherical wave could be estimated by (Leighton, 2007):

$$I = \frac{P_m{}^2}{2Z} = \frac{(A_m . \omega . Z)^2}{2Z} = \frac{1}{2} . A_m{}^2 . \omega^2 . Z \qquad \textit{Eq. 1.15}$$

2.3 Phenomena associated with ultrasound propagation

Many phenomena may ensue from propagation of an ultrasonic wave in a liquid medium. The major ones include acoustic streaming, microstreaming, cavitation and thermal effect.

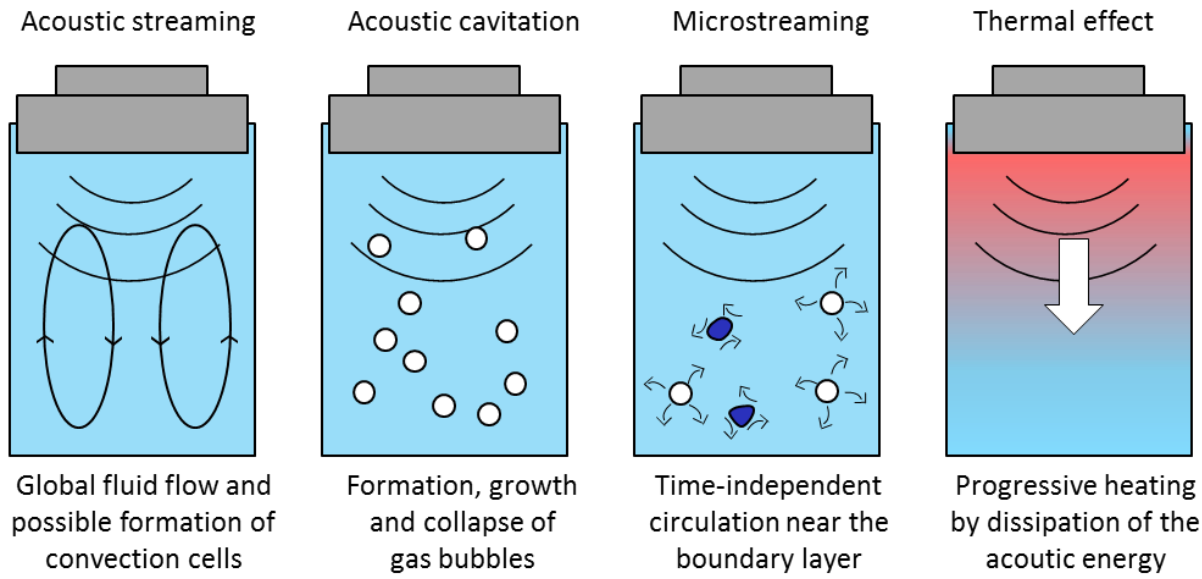

Fig. 1.11 *Major phenomena associated with ultrasound propagation (adapted from (Legay et al., 2011; Leighton, 2007))*

2.3.1 Acoustic streaming

Being investigated since over half a century (Leighton, 2007, 1994; Lighthill, 1978; Nyborg, 2005), acoustic streaming refers to a flow in the direction of sound field in a medium manifested by the momentum absorbed from the acoustic field when an acoustic wave travels through the medium. This phenomenon is usually considered as the consequence of an energy gradient in the direction of propagation when energy is absorbed from the wave during its propagation through an attenuating liquid. An energy gradient corresponds to a force, and when it acts upon the liquid a streaming flow is generated (Leighton, 2007). Acoustic streaming depends on the acoustic intensity and spatial attenuation in the medium; an increase of either parameter will increase the streaming. In addition, higher frequency ultrasound tends to have greater acoustic streaming due to higher energy absorption of the medium (Suslick, 1988). The effective range of acoustic streaming is on the order of centimeters to tens of centimeters (Lamminen *et al*., 2004), with the streaming velocity between 1 to 100 $cm.s^{-1}$ which may vary slightly with ultrasonic power and frequency (Loh *et al*., 2002; Nomura *et al*., 2002).

2.3.2 Acoustic cavitation

Microbubbles (cavities) can occur in a liquid that is subjected to rapid changes of pressure. It often occurs in hydraulic pumps, propellers, etc. As the name implies, acoustic cavitation refers to the formation, growth, oscillations and collapse of gas bubbles under the influence of an ultrasonic field in liquids.

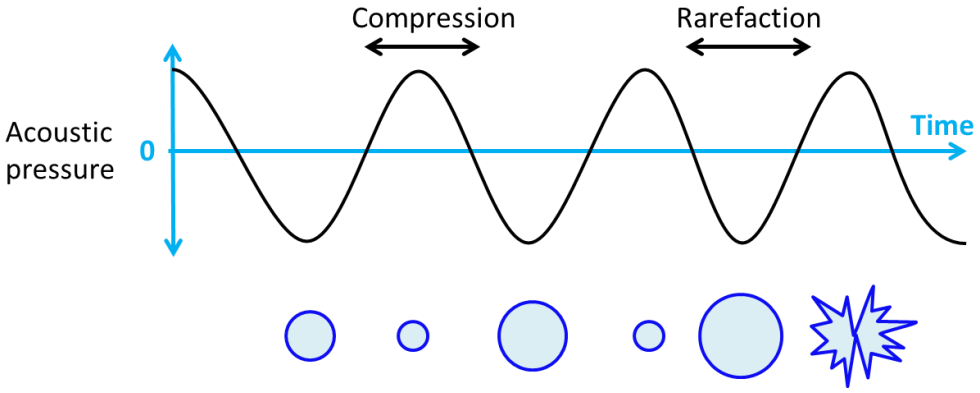

Fig. 1.12 *Schematic of the interaction of a cavitation bubble with a propagating sound wave (adapted from (Neppiras, 1980))*

Ultrasound is propagated via waves which alternately compress and stretch the particles, to be more exact, the molecular spacing, in the medium through which it passes (see Fig. 1.10). Thus the average distance between the molecules in a liquid will vary as the molecules oscillate about their equilibrium position. When a large negative pressure is applied to the liquid (during the rarefaction phase), the distance between molecules increases; if this pressure is low enough (below the vapor pressure) so that inter-molecules distance exceeds the critical value necessary to hold the liquid intact, the liquid will break down and voids will be created, i.e. cavitation bubbles will form (Mason, 1999). Once the bubble forms it can remain trapped in the acoustic pressure field and will grow in volume as solvent vapor and dissolved gases diffuse into the cavity (named rectified diffusion). After a period of time the bubble will grow to a size that is no longer stable. At this point the bubble will undergo implosive collapse, which generates the energy for chemical and mechanical effects. The whole process is schematized in Fig. 1.12.

The collapse of the cavitation bubbles results in the formation of a micro-scale ‘‘hotspot’’ which experiences high temperature (up to 6000 K) and pressure (up to 200 MPa) (Neppiras, 1980). These transient hotspots result in the formation of radicals which could provide conditions for many chemical applications, e.g. solvent lysis and degradation of molecules in solution.

Tab. 1.1 *Influence of external parameters on acoustic cavitation*

External parameters	Influence on acoustic cavitation
Frequency of ultrasound	It becomes more and more difficult to produce cavitation in liquids when the ultrasonic frequency is increased, due to the shortening of rarefaction phase at high frequency.
Power of ultrasound	High power ultrasound has higher wave amplitude which is in favor of cavitation production.
Physic properties of solvent (viscosity, surface tension, vapor pressure)	It is more difficult to produce cavitation in a viscous liquid while high surface tension and low vapor pressure make it even harder.
Nature of dissolved gas	Acting as nuclei for cavitation, presence of entrapped or dissolved gas, especially those with large ratio of specific heats (polytropic index) like He, Ar or Ne, promotes cavitation.
Operation conditions (applied pressure, temperature)	Increase of the applied pressure requires a greater rarefaction pressure to initiate cavitation, i.e. makes it more difficult to produce. Once initiated, raising external pressure will give rise to a larger intensity of cavitational collapse and consequently enhance the ultrasonic effect on medium. As for temperature, any increase of it will raise the vapor pressure of a medium resulting in easier cavitation but less violent collapse.

Usually the bubble implosion is assumed to be on the order of microseconds, and the bubble size is about 10^{-4} m, depending on frequency. Therefore, the order of magnitude of particle displacement velocity during bubble implosion can be estimated, which is on the order of

100 $m.s^{-1}$. Without surprise, this high velocity fluid movement if occurs near the solid-liquid interface, would disrupts thermal and velocity boundary layers which could reduce the resistance of heat transfer and mass transfer (Legay et al., 2011).

It is well known that external parameters have a great influence on acoustic cavitation. Here lists the most important ones (Mason, 1999) in Tab.1.1.

2.3.3 Microstreaming

There is another type of streaming occurring near small obstacles (gas bubble or solid surface) placed within a sound field arising from the frictional forces between the boundary and the medium (Leighton, 1994). Unlike acoustic streaming, this time-independent circulation occurs only in a small region of the fluid, often in the neighborhood of the boundary layer, it is therefore termed microstreaming.

Microstreaming can occur particularly when small vibrating gas bubbles are present (Leighton, 2007; Nyborg, 1982). Gentler than cavitation, microstreaming can also bring about a number of important effects; among which bioeffects have been reported the most in literature (Nyborg, 1982; Rooney, 2005; Williams and Slade, 1971). Collis *et al.* found that a variety of microstreaming patterns are possible around a microbubble and each pattern is associated with a particular oscillation mode of the bubble and generates a different shear stress distribution (Collis *et al*., 2010). Nyborg suggested that if the medium is a fluid, a circulatory flow occurs with particularly large velocity gradients near the boundaries; while strain fields can be produced in non-fluid media, especially when the material consists of a lattice-water combination, the consequent strains could lead to a disruption of the lattice structure if they exceed critical values (Nyborg, 1982).

Microstreaming can also occur in the viscous boundary layer of the waveguide and other present solid surfaces. Spengler *et al*. revealed the microstreaming velocity vector field of latex suspension by Particle Image Velocimetry (PIV) measurements and found an average microstreaming velocity of 450 $\mu m.s^{-1}$ for a 3.2 MHz ultrasonic wave with an acoustic pressure of about 0.5 MPa (amplitude) (Spengler *et al*., 2003).

2.3.4 Thermal effect

The absorption of ultrasonic wave by a medium will convert the acoustic energy ultimately into heat, which results in the thermal effect of ultrasound: medium heating, as shown in Fig. 1.11. This effect is the fundamental of calorimetric measurements proposed by Mason (Mason, 1991) for ultrasound dissipated power determination.

Most of these phenomena tend to induce local streaming and turbulence in a fluid system. Therefore, it is common that ultrasound has been applied to improve performance of certain processes; one of them is filtration process.

3. Ultrasound-enhanced filtration

3.1 Overview

Since 80s', when ultrasound (US) was applied for the first time to enhance membrane process (Okahata and Noguchi, 1983), more and more investigations can be found in literature reporting its effectiveness of membrane cleaning (Ahmad *et al.*, 2012; Chai *et al.*, 1999; Gonzalez-Avila *et al.*, 2012; Lamminen *et al.*, 2006) and fouling control (Ahmad *et al.*, 2012; Mirzaie and Mohammadi, 2012; Muthukumaran *et al.*, 2007), thanks to enormous actions induced by its propagation, such as particles vibrations, cavitation and acoustic streaming (Lamminen *et al.*, 2004). However, membrane damage and material denaturation have been occasionally reported (Masselin *et al.*, 2001; Villamiel and de Jong, 2000). In fact, principal cause of these unfavorable consequences is the high ultrasonic intensity, often with close US transducer-membrane distance (Kallioinen and Manttari, 2011). Otherwise, low US-intensity applications are promising for membrane process as far as we know, confirmed by majority of reports in literature.

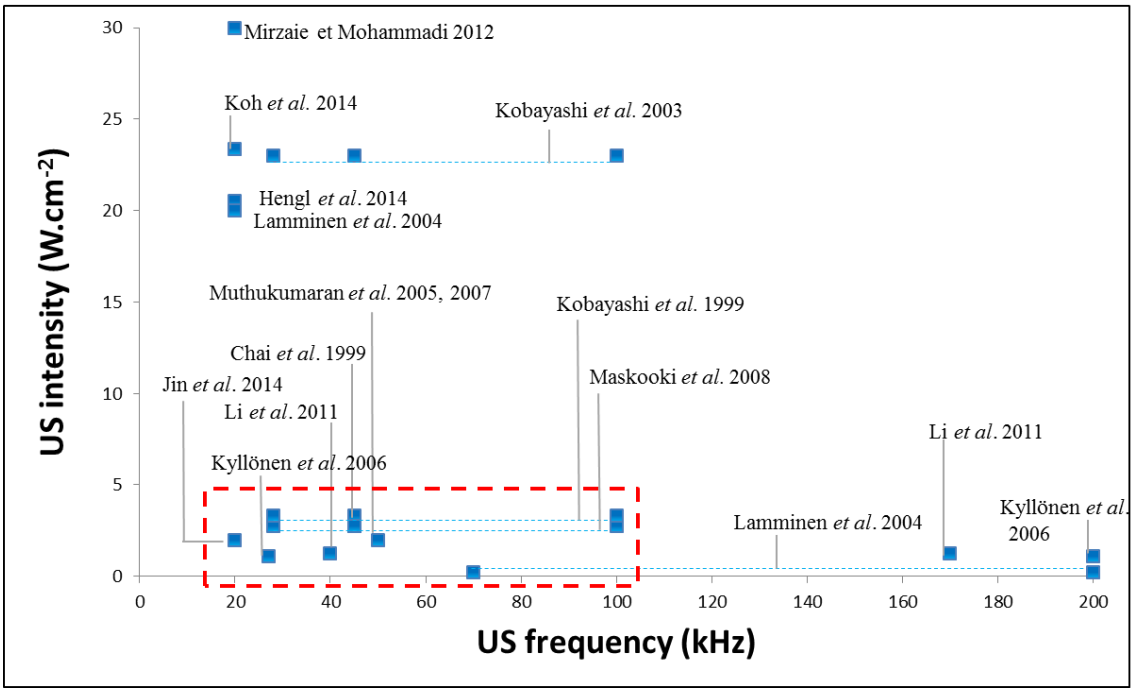

Fig. 1.13 *Literature review of intensity-frequency configurations in US enhanced membrane filtration*

Fig. 1.13 summarizes the available US intensity and frequency configurations in the literature that reported the effectiveness of US on membrane cleaning or fouling control without altering the membrane's intrinsic permeability. The presented range of US intensity and frequency in this figure is the most studied zone in literature, whereas the applied US intensity can be found up to 82.9 $W.cm^{-2}$ even higher using ultrasonic horn (Li *et al*., 2002; Simon *et al*., 2000); and the studied frequency stretched till 1 MHz (Lamminen *et al*., 2004). It is quite obvious that major studies were carried out at low US intensity, below 5 $W.cm^{-2}$, and at low frequency, from 20 to 100 kHz. The application of US in conventional membrane filtration can be divided into two categories: ''offline'' cleaning enhancements and ''online'' continuous fouling control.

3.2 ''Offline'' cleaning enhancements

In many cases, US was used to clean fouled membrane when filtration was stopped. Immersing the membranes inside an ultrasonic bath, Kobayashi *et al.* compared the cleaning performance of three US frequencies (28, 45 and 100 kHz) for UF and MF membranes and they have found that lower frequencies were more effective in cleaning fouled membranes (Kobayashi *et al*., 2003). This work was further investigated by Maskooki *et al.* analyzing more variables of this process (Maskooki *et al*., 2008). Lamminen *et al*. have developed a specific experimental setup to execute the cleaning procedure as well as to characterize the US cleaning performance (Lamminen *et al*., 2004). Combined of permeate flux measurement, gravimetric and SEM analysis, they have found that ceramic membranes may be effectively cleaned using US at frequencies from 70 kHz up to 620 kHz without damaging the membranes. Gonzalez *et al*. employed a tandem frequency method (220 kHz and 28 kHz) to remove the deposited particles from hollow fiber membrane and the bubble activity near the membrane was recorded using a high speed camera (Gonzalez-Avila *et al*., 2012). They have reported the efficiency of this method based upon the fact that a large number of cavitation bubbles created on the surface of the membrane.

3.3 ‘‘Online’’ fouling control enhancements

Otherwise, US was applied during filtration in order to control fouling formation. This ‘‘online’’ ultrasonication has already been applied in both cross-flow (Kobayashi *et al*., 1999; Kyllonen *et al*., 2006; Li *et al*., 2002, 2011; Muthukumaran *et al*., 2005; Ng *et al.*, 2012) and dead-end filtration (Mirzaie and Mohammadi, 2012; Simon *et al*., 2000), and great effectiveness was always reported. In most of these studies, the ultrasound devices are ultrasonic water baths, in which the loss of acoustic power is reported to be very high, about 90% (Cai *et al*., 2009). In order to have a better control of US, Simon *et al.*, Juang *et al.* and Mirzaie and Mohammadi used ultrasonic probe systems (all at a frequency of 20 kHz, estimated ultrasonic intensity from 30 to 110 $W.cm^{-2}$) to transmit ultrasonic waves directly to the feed medium in a dead-end filtration operation (Juang and Lin, 2004; Mirzaie and Mohammadi, 2012; Simon *et al*., 2000). Kyllönen *et al.* also developed a membrane module integrated with several sandwich type ultrasonic transducers to apply ultrasound (27 kHz, 1.1 $W.cm^{-2}$) in cross-flow filtration with little loss of ultrasonic efficiency (Kyllonen *et al*., 2006).

3.4 Mechanisms of ultrasound actions during filtration

Mechanisms of US actions during filtration have been discussed in the literature. It is thought that the acoustic cavitation may be able to remove parts of the foulant layer from the membrane surface and/or avoid the deposition of particles that lead to membrane fouling. During this acoustic cavitation, the aqueous stagnant diffusion layer at the membrane/solution interface is eliminated due to the physical effects generated (Bonggotgetsakul *et al*., 2010; Latt and Kobayashi, 2006). Latt *et al*. studied US-enhanced MF hollow fiber membrane process (US: 28 kHz) by means of reflection technique (Latt and Kobayashi, 2006). With the correlation of sound pressure intensity and luminal fluorescence intensity, they suggested that violent collapse of cavity bubbles could occur which supported the enhanced membrane permeability in ultrasound bath.

Lamminen *et al*. studied the cleaning of fouled ceramic membranes in a dead-end filtration cell by US (20-1062 kHz, 0.21-20 $W.cm^{-2}$) (Lamminen *et al*., 2004). According to them,

the cavitational mechanisms, i.e. microstreaming and micro-streamers (cavitation bubbles that form at nucleation sites within the liquid and are subsequently translated to a mutual location, i.e. antinodes), were important in detaching particles from the membrane surface while turbulence associated with ultrasound, i.e., acoustic streaming, played a role in the transport of particles away from the surface following detachment. In dead-end filtration with minor feed flow, the acoustic streaming effect can be more efficient than in cross-flow filtration where crossflow velocities can be several meters per second. Micro-jets (liquid jet, they are formed when a cavitation bubble collapses in the presence of an asymmetry, e.g. a surface or another bubble) did not appear to cause significant removal compared to microstreamers, although evidence of micro-jet pitting was visible in SEM images of the fouled surface.

4. Rheometry

4.1 General principles

Rheology describes the deformation of a body under the influence of stresses. ‘‘Body’’ in this context can be either solids, liquids, or gases. Ideal solids deform elastically. The energy required for the deformation is fully recovered when the stresses are removed. Ideal fluids such as liquids and gases deform irreversibly-they flow. The energy required for the deformation is dissipated within the fluid in the form of heat and cannot be recovered simply by removing the stresses (Gebhard Schramm, 1998).

Only a few liquids of technical or practical importance come close to ideal liquids in their behavior. The vast majority of liquids show a rheological behavior that classifies them to region somewhere between the liquids and the solids: they are in varying extents both elastic and viscous and may therefore be named ‘‘visco-elastic’’.

In order to determine the rheological properties of different liquids (also solids and gases, but they are not the major concern of this study), some experimental techniques are required, which are generically called rheometry. The measurement of the viscosity of liquids first requires the definition of the parameters which are involved in flow. Isaac Newton was the first to express the basic low of viscometry describing the flow behavior of an ideal liquid:

$$\tau = \eta \,.\, \dot{\gamma} \qquad \textbf{\textit{(Eq. 1.16)}}$$

Shear stress (Pa) = viscosity (Pa.s) . shear rate (s^{-1})

Therefore, in measurement, either shear stress or shear rate is applied and the other can be measured as a result. To carry it out, an instrument, often referring to a rheometer, is required. 4 types of shear induced flow in liquids can be applied in rheometers:

-Flow between two parallel flat plates

-Flow between a cone and a plate

-Flow in the annular gap between two concentric cylinders

-Flow through pipes, tubes, or capillaries

Fig. 1.14 presents a parallel-plates sensor where the upper plate is moved and the lower one is stationary. A force F (N) applied tangentially to an area S (m^2) being the interface between the upper plate and the liquid underneath, leads to a shear stress τ, which induces a flow in the liquid layer. Where

$$\tau = \frac{F}{S} \qquad \textit{(Eq. 1.17)}$$

A maximum flow speed V ($m.s^{-1}$) is found at the upper boundary and the speed drops across the gap between two plates whose height is H (m) and gets down to 0 at the lower boundary. The speed drop across the gap is named ‘‘shear rate’’, defined by:

$$\dot{\gamma} = \frac{dV}{dH} \qquad \textit{(Eq. 1.18)}$$

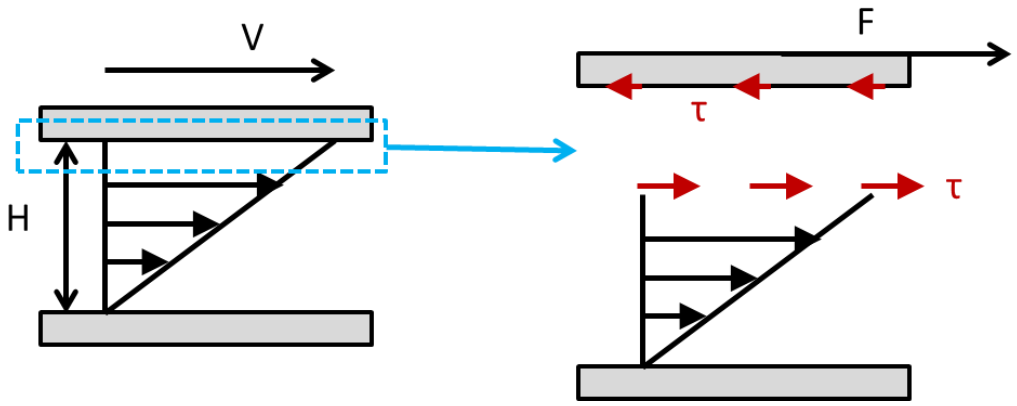

Fig. 1.14 *Schematic representation of rheological measurement (adapted from (David, 2008))*

4.2 Flow behavior of different types of liquids

The correlation between shear stress and shear rate can be graphically displayed in a diagram of τ as a function of $\dot{\gamma}$, called ‘‘flow curve’’, defining the flow behavior of a liquid. Another common curve is the ‘‘viscosity curve’’ where η is plotted versus $\dot{\gamma}$. In order to compare the flow behaviors of different liquids, flow curve or viscosity curve is often plotted at steady state of each applied shear stress. Fig. 1.15 shows the common types of flow behavior of liquids.

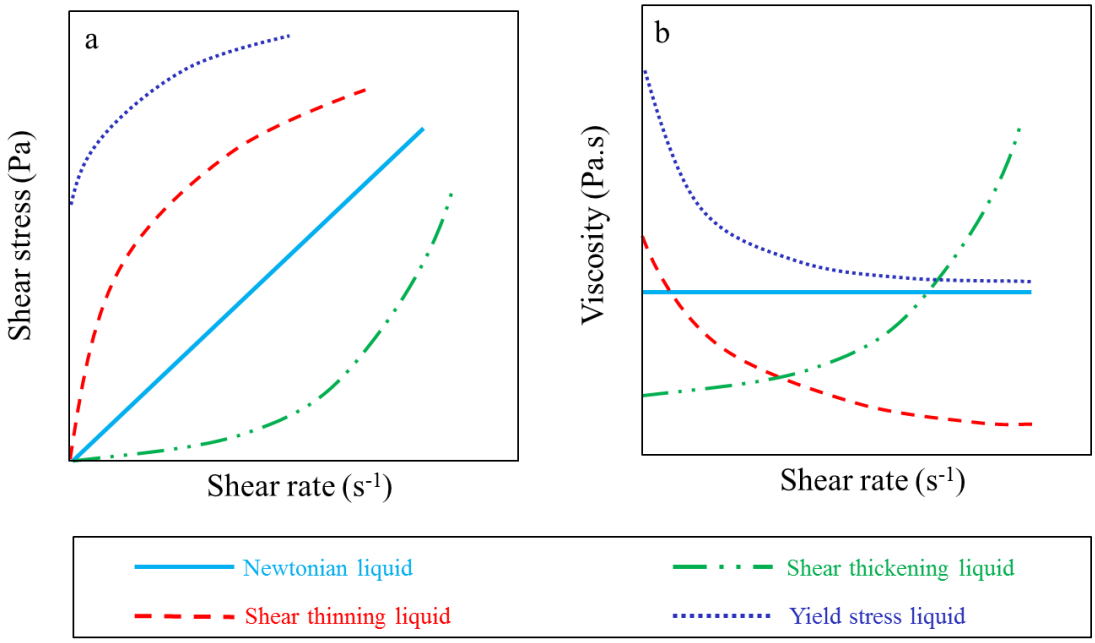

Fig. 1.15 *Four common types of flow behavior of liquids: a) flow curve, b) viscosity curve*

4.2.1 Newtonian liquids

As the ideal liquids which fit perfectly (Eq. 1.16), it is said that for the Newtonian liquids, the viscous stresses that arise from their flow, at every point, are proportional to the local shear rate (Batchelor, 2000). While no real fluid fits the definition perfectly, many common liquids, such as water and mineral oils, can be assumed to be Newtonian for practical calculations under ordinary conditions.

4.2.2 Non-Newtonian liquids

All other liquids not exhibiting this ‘‘ideal’’ flow behavior are called ‘‘Non-Newtonian liquids’’. Fig. 1.15 shows three common types of them: shear thinning liquids (also known as pseudoplastic liquids), shear thickening liquids (also known as dilatant) and yield stress liquids. The viscosity of shear thinning liquids—the measure of their resistance to flow—decreases with an increasing rate of shear stress, which is the opposite of shear thickening liquids. It exists some other liquids with a yield stress below which they won’t flow, once beyond this yield stress, they

will flow either like a Newtonian liquid (such as Bingham plastic liquid) or a Non-Newtonian liquid.

Several models are available to describe these non-Newtonian flow behaviors, power law and Herschel-Bulkley viscoplastic model (Macosko, 1994) are used in this study:

Power law: $$\tau = \kappa\dot{\gamma}^n$$ ***(Eq. 1.19)***

Herschel-Bulkley law: $$\tau = \tau_o + \kappa\dot{\gamma}^n$$ ***(Eq. 1.20)***

Where τ_o represents the yield stress, κ is the consistency, and n is the behavior index (n>1 for shear thickening liquids and 0<n<1 for shear thinning liquids, n = 1 for Newtonian liquids).

Shear thickening in liquids is rare and generally it is to be avoided in industry if at all possible since it leads to such problems as failure of mixer motors due to overloading or fouling pipes and spraying equipment, but occasionally a controlled amount might be useful (Barnes, 1989). Shear thickening behavior occurs when a colloidal suspension transitions from a stable state to a state of flocculation. Such behavior is currently being researched for use in body armor applications that stiffens under impact (Wagner and Brady, 2009). A large portion of the properties of these systems are due to the surface chemistry of particles in dispersion, known as colloids.

Many substances such as emulsions, suspensions, or dispersions of high technical and commercial importance are shear thinning. Examples of this group can be found easily in our daily life, such as ketchup, whipped cream, blood, paint, and nail polish. According to Barnes *et al.*, all materials that are shear thinning are thixotropic, referring to the reversible viscosity decrease when shaken, agitated, or otherwise stressed (Barnes, 1997). They reported that thixotropy comes about first because of a change in microstructure which is brought to a new equilibrium by competition between the processes of tearing apart by stress and flow-induced collision. When the flow stops, Brownian motion is able to move the elements of the microstructure around slowly to more favorable positions and rebuild the structure.

Suspensions, especially colloidal suspensions, can display all known rheological phenomena from shear thinning or thickening to time-dependent phenomena (thixotropic or its opposite-rheopecty) and strong extensional effects (Macosko, 1994). Wagner *et al*. revealed the

microstructure change of a specific colloidal dispersion in different flow regime (Wagner and Brady, 2009). As shown in Fig. 1.16, in equilibrium, random collisions among particles make them naturally resistant to flow. With increasing shear rates, particles become organized in the flow, which lowers their viscosity, exhibiting a shear thinning behavior. At yet higher shear rates, hydrodynamic interactions between particles are enhanced and induce hydroclusters (red) formation-transient fluctuations in particle concentration, hence shear thickening behavior appears.

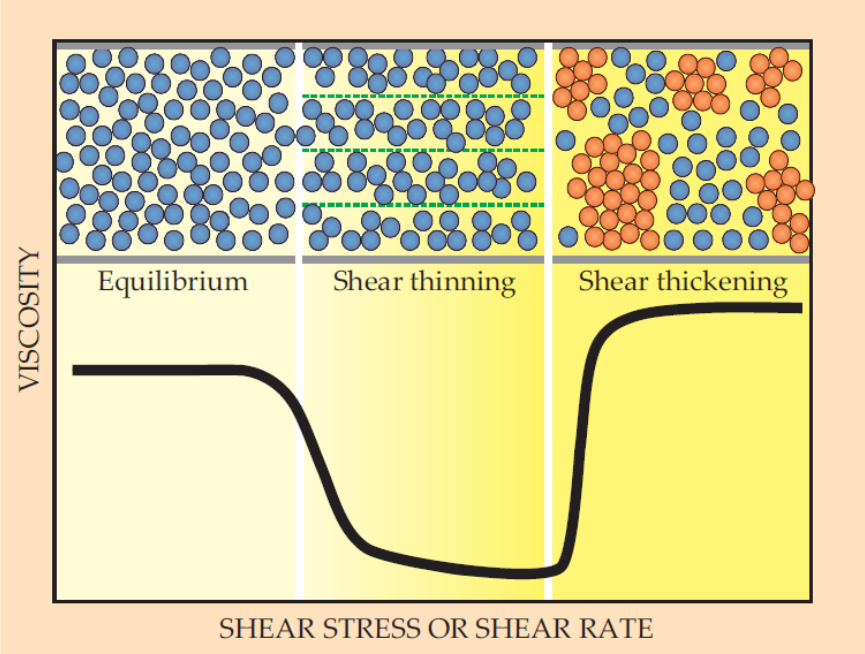

Fig. 1.16 *The change in microstructure of colloidal dispersion between different flow behaviors (captured from (Wagner and Brady, 2009))*

Some materials, among which the most famous should be mayonnaise, exhibit a yield stress behavior. A yield stress (τ_o) may be defined as the minimum shear stress required to initiate flow (Steffe, 1996), which is a significant factor in many industrial processes such as pumping, spreading and coating. Yield stress liquids are often shear-thinning liquids which additionally feature a yield point. They can be classified with good reasoning to belong to both groups of liquids and solids. They are mostly dispersions which at rest can build up an intermolecular/interparticle network of binding forces (polar forces, van der Waals forces, etc.). These forces restrict positional change of volume elements and give the substance a solid character with an infinitely high viscosity. Forces acting from outside, if smaller than those

forming the network, will deform the shape of this solid substance elastically. Only when the outside forces are strong enough to overcome the network forces – surpass the threshold shear stress called the ‘‘yield point’’, the network collapse. Volume elements can then change position irreversibly: the solid turns to a flowing liquid.

5. Small angle X-ray scattering (SAXS)

5.1 Synchrotron X-rays

X-rays are electromagnetic waves like visible light but situated at the high energy/short wavelength end of the electromagnetic spectrum, between ultraviolet light and gamma rays (Fig. 1.17). Most X-rays have a wavelength in the range of 0.01 to 10 nm, which is comparable to interatomic distances and makes X-rays suitable for the study of atoms and bonds.

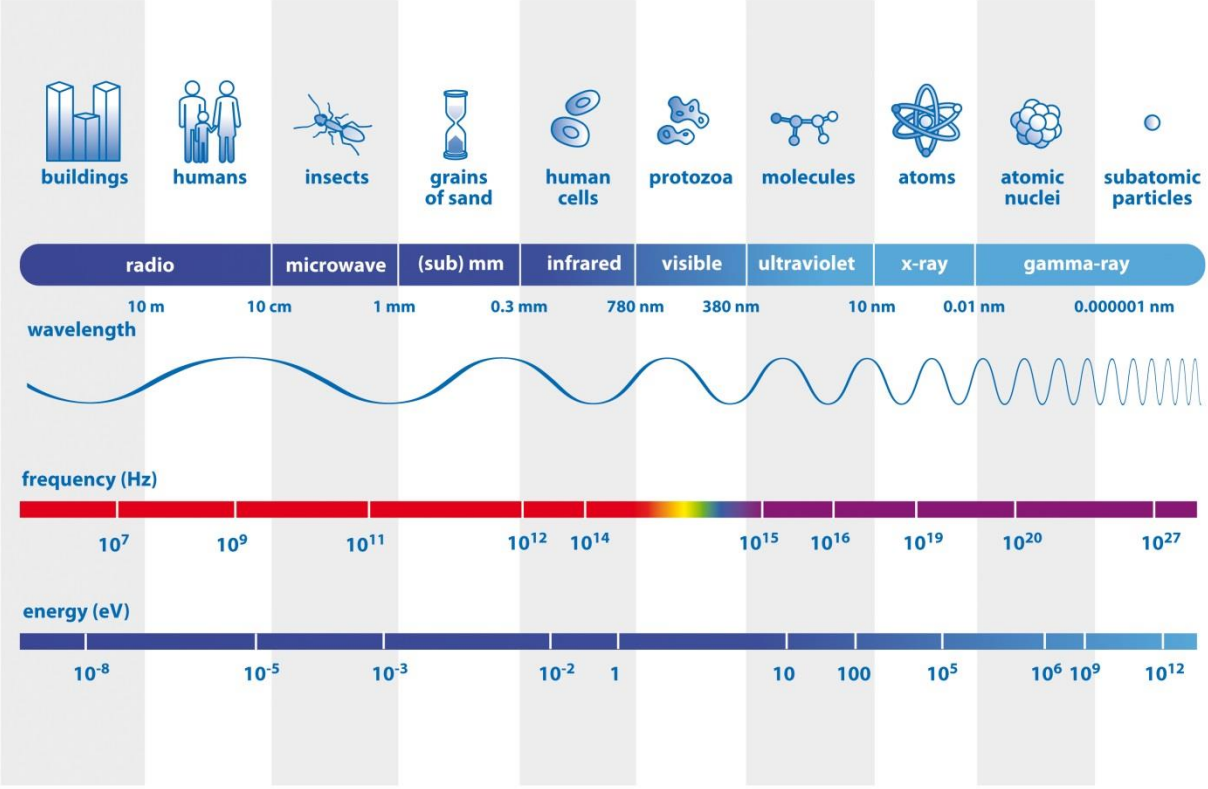

Fig. 1.17 *The electromagnetic spectrum (source: http://www.esa.int/ESA)*

Since a century, X-rays have been used extensively in medical imaging because they have a high penetration depth through materials and are selectively absorbed by the parts of the body with the highest electron density such as bones. The principal difference between synchrotron

light and the X-rays used in hospital is the brilliance (energy): a synchrotron source is ten thousand billion times brighter than a hospital X-ray source.

The European Synchrotron Radiation Facilities (ESRF) produces X-rays of high energy, called “hard” X-rays, which have wavelengths of 0.20 to 0.005 nm or energy in the range 6 to 200 keV. Synchrotron X-rays are a unique high-performance probe for non-destructive and non-contact materials analysis over a wide range of length scales, right down to the size of an atom. The special properties of synchrotron X-rays, including element-selectivity, offer a variety of analytical tools for the *in-situ* measurements, and often in real time, where traditional techniques cannot reach.

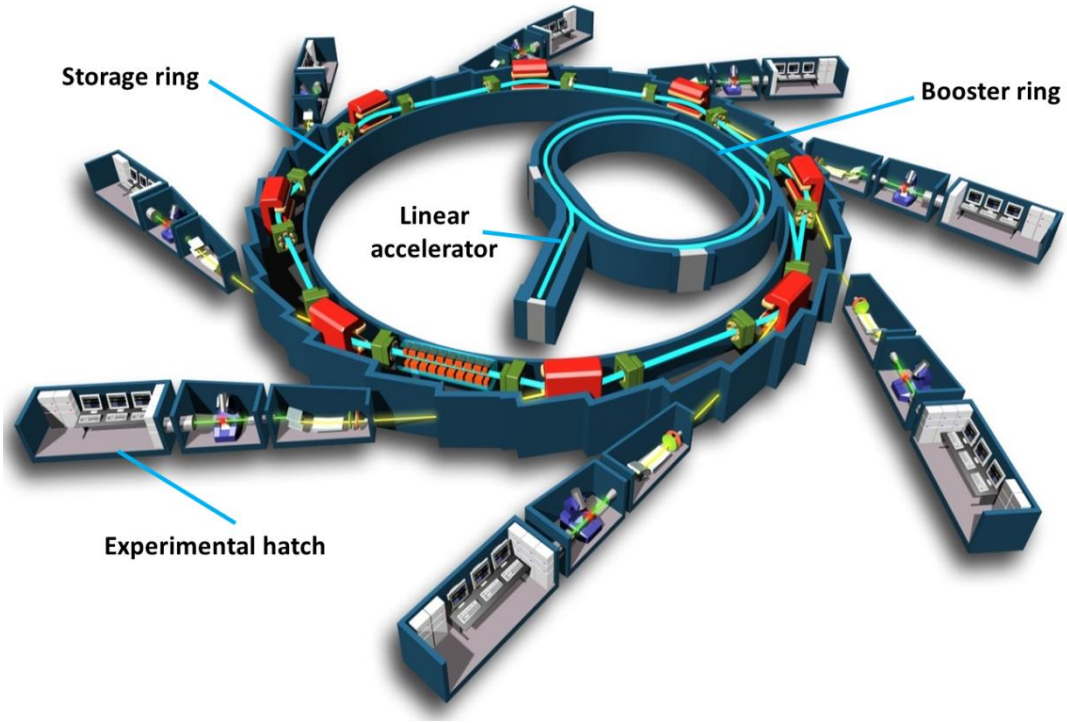

Fig. 1.18 *Schematic of synchrotron light production (source: Wikipedia)*

As shown in Fig. 1.18, synchrotron light starts with an electron gun. Electrons emitted are first accelerated in a linear accelerator and then transmitted to a circular accelerator (booster ring) where they are accelerated to reach an energy level of 6 billion electron volts (6 GeV). These high-energy electrons are then injected into a large storage ring where they circulate in a vacuum

environment, at a constant energy, for many hours. Each time these electrons pass through an undulator, a device consisting of series of alternating magnets, they emit X-rays, which are directed along the beamlines - the experimental stations.

5.2 Principle of SAXS

There are two main interactions of X-rays with matter: absorption and scattering. Scattering can occur with or without loss of energy, which means that the scattered radiation can have a different wavelength than the incident radiation, such as in Compton scattering (inelastic scattering) (Hubbell *et al*., 1975), or it can have the same wavelength, such as in Rayleigh or Thomson scattering [1] (elastic scattering) (Hubbell and O/verbo, 1979). SAXS is a small-angle scattering technique based upon Thomson scattering that is often exploited to probe the microstructure and non-equilibrium dynamics of soft matter and related systems (Glatter and Kratky, 1982).

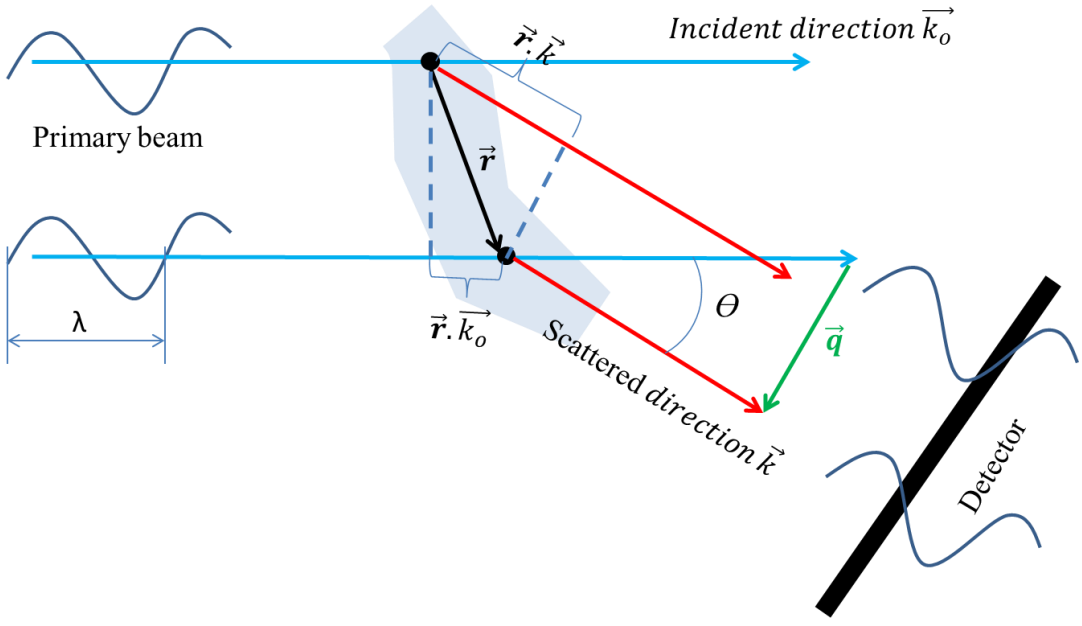

Fig. 1.19 *Schematic of elastic scattering*

[1] Rayleigh scattering is used when the incident radiation is visible light. Thomson scattering is used in the case of X-rays.

When X-rays are striking the atoms, all electrons will behave as if they are free since the energy level of an X-ray photon is very high compared with the binding energy of an atom. Therefore, every electron becomes the source of a scattered wave. The scattered waves (photons) from different electrons then produce interference patterns at the detector (Fig. 1.19).

The photons from different positions (e.g. with a distance of r) travel different paths to reach the detector creating a phase shift. As shown in Fig. 1.19, the path difference L can be expressed as $L = -\vec{r}.(\vec{k} - \overrightarrow{k_o})$, with $\overrightarrow{k_o}$ and $\vec{k}$ the unit vectors indicating the incident and scattered direction, respectively. The phase shift φ is:

$$\varphi = \frac{2\pi}{\lambda} L = -\frac{2\pi}{\lambda}.\vec{r}.\left(\vec{k} - \overrightarrow{k_o}\right) = -\vec{q}.\vec{r} \qquad \textbf{Eq. 1.21}$$

Where

$$\vec{q} = \frac{2\pi}{\lambda}(\vec{k} - \overrightarrow{k_o}) \qquad \textbf{Eq. 1.22}$$

$$q = |\vec{q}| = \frac{4\pi}{\lambda}.\sin(\frac{\theta}{2}) \qquad \textbf{Eq. 1.23}$$

Names for q, which can be found in literature, are ‘‘magnitude of the scattering vector’’ or ‘‘momentum transfer’’, which is usually used to describe the scattering patterns. Whatever the name, fact is that the dimension of q is one over length (nm^{-1}) and this explains that a scattering pattern is usually called ‘‘the structure in reciprocal space’’.

5.3 Form factor

The scattering of one particle can be explained as the interference pattern produced by all the waves sent to the detector from every electron/atom inside the particle. The intensity scattered by different electrons sums up.

It is well known that the scattered pattern of a sample can be simply described in terms of the reciprocal space. If we designate by $\rho_1(\vec{r})$ the electronic density of one single particle at a point defined by the vector $\vec{r}$, then the total scattering amplitude of this single particle $A_1(q)$ is

the sum of all the individual electrons with their corresponding phase shift ($e^{-i\vec{q}.\vec{r}}$) (Brumberger, 1994; Guinier and Fournet, 1955):

$$A_1(q) = \int_V \rho_1(\vec{r}).\, e^{-i\vec{q}.\vec{r}} d\vec{r} \qquad \textbf{\textit{Eq. 1.24}}$$

Eq. 1.24 is the Fourier transform of the electron density. The more electrons are placed in a sample volume (i.e. the higher the electron density), the more waves are scattered.

The scattered waves are coherent, indicating that the amplitudes are added, and the intensity is then given by the absolute square of the resulting amplitude. The amplitudes are of equal magnitude, and differ only by their phase, which depends on the position of the electron in space. In the case of one single particle of volume V_1 with an electron density of ρ_1, the total scattered intensity of this particle then amounts to

$$I_1(q) = |A_1(q)|^2 = {\rho_1}^2.{V_1}^2.P(q) \qquad \textbf{\textit{Eq. 1.25}}$$

Where P(q) is the form factor of the particle.

In practical applications many particles are illuminated at the same time and the observed scattering pattern corresponds to the form factor of one single particle only if the particles are all identical in shape and size (i.e. monodisperse sample) and if the particles are well separated from each other widely enough (i.e. dilute sample) (Glatter and Kratky, 1982; Narayanan, 2008).

For a dilute system, the inter-particle interactions can be neglected and $I_1(q)$ mainly depend on the shape and size of the particles. For the special case of a sphere (radius R) of uniform density the scattered intensity has been given by Rayleigh (1911) (Glatter and Kratky, 1982):

$$I_1(q) = {\rho_1}^2.{V_1}^2.\left[3.\frac{sin(qR) - qRcos(qR)}{(qR)^3}\right]^2 \qquad \textbf{\textit{Eq. 1.26}}$$

Then

$$P(q) = \left[3.\frac{sin(qR) - qRcos(qR)}{(qR)^3}\right]^2 \qquad \textbf{\textit{Eq. 1.27}}$$

The result is the square of a spherical Bessel function of the first kind which is characterized by successive oscillations and zeros at fixed qR values (qR = 4.493, 7.725…), as presented in Fig. 1.20. These zeros allow estimating the approximate size of the sphere from the scattering function.

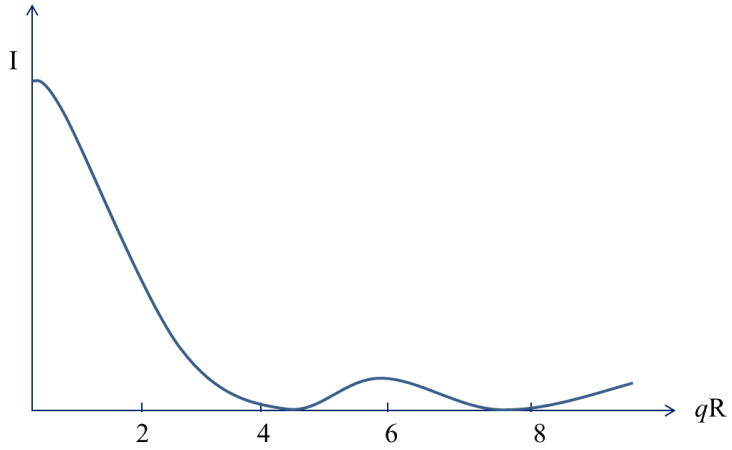

Fig. 1.20 *Scattering intensity of a sphere (adapted from (Glatter and Kratky, 1982))*

5.4 Structure factor

When particle systems become concentrated, the interparticle distances come into the same order of magnitude as the distances inside the particles. The interference pattern will therefore contain contributions from neighboring particles as well. This additional interference pattern multiplies with the form factor of the single particle and is called "structure factor". In the special case of monodisperse spherical particles with identical interparticle interactions, the scattered intensity can be separated into two terms as given in equation as follows (Lindner and Zemb, 2002):

$$S(q) = 1 + \frac{1}{N}\langle \sum_{i,j} e^{i\vec{q}\cdot(\vec{r_i}-\vec{r_j})} \rangle_N \qquad \textbf{Eq. 1.28}$$

Where N is the number of particles, $\vec{r_i}$ and $\vec{r_j}$ are the positions of particles i and j. In the SAXS profile, the structural effect becomes visible at small q-values by the formation of an additional wave (Fig. 1.21), when $q = \infty$, S(q) = 1.

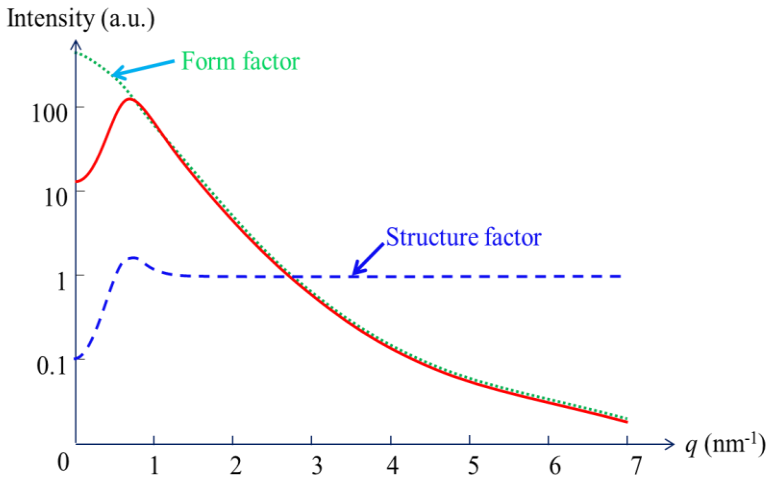

Fig. 1.21 *The SAXS profile (red) of a concentrated particle dispersion: a product of the form factor (dotted green) of one single particle with the structure factor (dashed blue) of the neighboring particles*

5.5 Scattering intensity

SAXS pattern of one sample is the result of all the scattered waves from every particle, which is also affected by the particle interaction, as well as the medium. Particles embedded in a matrix material (the medium) must have an electron density different from that of the matrix in order to become visible in SAXS pattern. The visibility increases with the difference in electron density between the two phases. If the electron density of the particles were the same as that of the medium, then the particles could not be distinguished from their environment and the SAXS pattern would be the same as that of the medium. For a monodisperse sample, Eq. 1.25 should be modified to describe the total scattered intensity (q) :

$$I(q) = N.\Delta\rho^2.{V_1}^2.P(q).S(q) \qquad \textbf{Eq. 1.29}$$

Where $\Delta\rho = \rho_1 - \rho_m$, called contrast that represents the electron density difference between the particle and the medium. Therefore, for a defined particle-solvent system at high q-values range where S(q) =1, the scattered intensity is proportional to the number of particles per unit volume.

Conclusions

This chapter dealt with the process, the techniques and the principal characterization methods in this study. The basic principles of membrane separation processes have been reviewed and the fouling issue has been particularly discussed: what's the mechanism of fouling, how to characterize it and how to control it even avoid it.

Ultrasound has then been introduced and the phenomena induced by its propagation have been discussed in details. Brief historical summary on ultrasound-enhanced filtration has also been made: a lot of successful examples can be already found in literature.

Finally, two principal characterization methods in this study have been presented: rheometry and SAXS. It contains the general principles of rheometry and different flow behaviors which will be discussed in the result parts. As for SAXS, the principle and the key elements/parameters that will serve the following chapter have been introduced and discussed briefly.

2

Materials and methods

This chapter presents the materials and methods involved in this study. Firstly, the investigated colloidal suspensions will be presented including their general structure properties and preparation procedures. More of their structure properties will be discussed in the next chapters aiming for explaining the phenomena revealed. In this chapter, the experimental set-up and procedures will then be described in details. The fourth section will focus on the characterization of used ultrasonic system. In section 5, SAXS measurements will be presented in details including the instrument, measurement installation and the used methods to analyze SAXS results. Finally, all other analytical methods will be depicted.

1. Colloids and membranes of interest

1.1 Laponite suspensions

1.1.1 General description of structural properties

The synthetic clay used in this study, Laponite XLG, is manufactured by Laponite Industries. Its chemical composition is as follows: 66.2 % SiO_2, 30.2 % MgO, 2.9 % Na_2O and 0.7 % Li_2O, which corresponds to the following chemical formula:

$$Si_8[Mg_{5.5}Li_{0.4}H_{4.0}O_{24.0}]^{0.7-}{Na_{0.7}}^{0.7+}$$

The clay suspension consists of small platelets or disc-shape particles with a diameter of about 30 nm and thickness of 1 nm (Avery and Ramsay, 1986; Ramsay *et al.*, 1990). The particles have a density of 2.53 $g.cm^{-3}$ (Rosta and von Gunten, 1990). The disc-shape particles have marked anisotropy and exhibit positive surface charges on their edges and negative surface charges on their sides, thereby making an edge-to-face interaction favorable (Lockhart, 1980). Consequently, the arrangement of the particles within the aqueous medium will be strongly influenced by the particle volume fraction, by the pH and by the ionic strength of the surrounding aqueous medium. Depending on these three parameters the suspensions can have different states: a stable colloidal solution, an elastic gel, a plastic paste or even separate solid and liquid phases. The gel state is reached above a volume fraction ϕ_v^*, for a given ionic strength, pH and gelation time t_p.

The phase diagram of these suspensions (Gabriel *et al*., 1996; Mourchid *et al*., 1998, 1995), the sol-gel transition and the structure formation (Kroon *et al*., 1998; Morvan *et al*., 1994; Mourchid *et al*., 1995; Pignon *et al*., 1997, 1996; Ramsay *et al*., 1990; Ramsay and Lindner, 1993; Ruzicka and Zaccarelli, 2011) of this gel has already been widely studied. By combining scattering measurements of various radiation types (x-rays, neutrons and light), Pignon *et al.* summarized the structure of Laponite dispersion at rest, as shown in Fig. 2.1. They suggest that the structure of the dispersions at rest consists of sub-units measuring a few tens of nanometers, which is organized under the effect of attraction and repulsion forces acting between the particles. They then combine to form dense aggregates measuring about 1 µm. At larger length scales, these micrometer-sized aggregates are rearranged to form a continuous three-dimensional isotropic structure that has a fractal behavior of dimension F_D, giving the gel its three-dimensional structure that is responsible for the occurrence of a yield stress (Pignon *et al*., 1998).

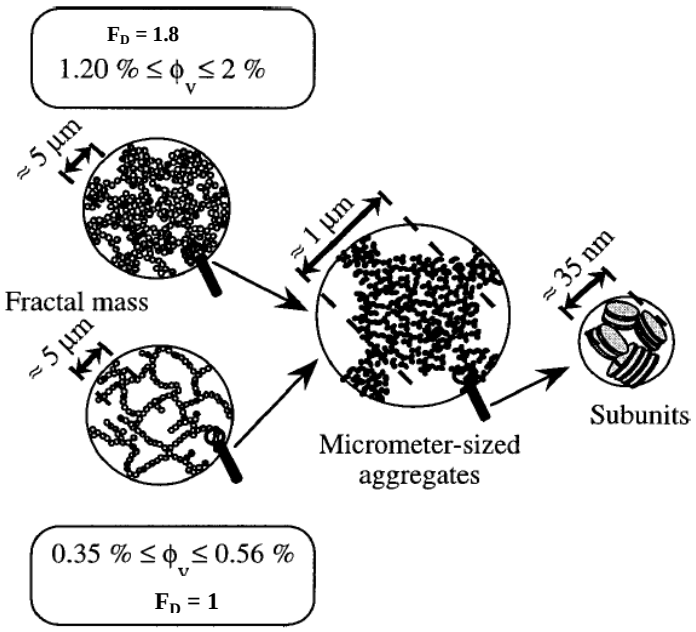

Fig. 2.1 *Schematic representation of structure of Lapnite suspension at rest. (Pignon et al., 1998)*

In a volume fraction domain close to the sol–gel transition (0.35 vol % ≤ ϕ_v≤ 0.56 vol %), the micrometer-sized aggregates form bundles (F_D = 1±0.05), giving the gels a mechanically fragile fibrous texture. In a high volume fraction domain (1.20 vol % ≤ ϕ_v≤ 2 vol %), the

structure is more heterogeneous, with zones of dense and less dense particle concentrations (F_D = 1.8±0.01). Between these two volume fraction domains, there is a transition zone, with the fractal dimension from 1 to 1.8, where the micrometer-sized aggregate fibers become entangled to produce an increasingly dense structure (Fig. 2.1).

Peptizers are commonly used to control the edge-to-face interactions (Martin *et al*., 2002). The peptizer used in this study was tetrasodium diphosphate (abbreviated to tspp hereafter). Its chemical formula is $Na_4P_2O_7$, $10H_2O$ with a molecular mass of 446 g.mol^{-1}. The effect of this peptizer on the structure, rheological behavior, osmotic pressure and frontal filtration performance of the Laponite dispersions has been studied previously (Martin *et al*., 2006, 2002; Pignon *et al*., 2000). In water, it releases $P_2O_7{}^{4-}$ groups which bind to the positive surface charged edges of the Laponite platelets. Consequently, the strength of edge-face and edge-edge attractions between the particles has been reduced. The result of this reduction in attractive forces between the particles is a partial disruption of the network. Depending on the volume fraction and aging time t_p, different rheological behaviors could be reached. In this study, two peptizer concentrations (C_{tspp}) have been investigated (0 % and 6 %) as percentages of the dry clay mass. The addition of tspp in this work has led to a transformation of the flow properties from yield stress gels (C_{tspp} = 0 %) to shear-thinning fluids (C_{tspp} = 6 %).

Thompson and Butterworth (Thompson and Butterworth, 1992) showed that there is significant dissolution of magnesium silicate with pH values of less than 7 and the disappearance of such dissolution at pH values above 9. Therefore, the pH of all the samples used in this study was adjusted to 10 in order to avoid any dissolution of the material.

Changes in the viscoelastic properties and structural characteristics of this gel could be observed over time. This is due, in part, to the osmotic swelling caused by repulsion between the double layers and also to the progressive organization of the particles into fractal aggregates over larger length scales (Pignon *et al*., 1997). The long-term gelation of these Laponite suspensions has also been studied by Mourchid and Levitz (Mourchid and Levitz, 1998). They have shown that under ambient atmosphere, Mg^{2+} is released from Laponite, implying that carbon dioxide from the atmosphere promotes acidification of the dispersions, leading to a gradual Laponite dissolution and a slow increase of the ionic strength. The release of divalent cations Mg^{2+} can

enhance aggregative processes resulting in the observation of fractal structural above some micrometers.

In order to take into account these structural and mechanical changes in the dispersions, the time t_p that elapsed between the end of preparation and the investigations will always be indicated in this study.

1.1.2 Sample preparation

The suspensions used in this study were prepared as follows. When peptizer was not used, the clay powder was added gradually into a solution of 10^{-3} M NaCl-deionized water at 20 °C. The mixing was under stirring of 800 rpm and it took about 20 min when all the powder was added. Then the mixture was kept being stirred of 200 rpm for 1h. When the peptizer-tspp was used, its powder was firstly mixed in a solution of 10^{-3} M NaCl-deionized water at 20 °C under stirring of 800 rpm for 5 min. The clay was then added into the mixture and the same procedure of mixing was used as the case without tspp. This preparation procedure ensures that the suspensions were completely homogeneous.

Dispersions to be filtered were prepared at initial volume fractions of ϕ_v = 0.48 % and 1%, corresponding to mass fraction of 0.0121 g.cm^3 and 0.0253 g.cm^3, respectively. The dispersions were then aged in closed vessels for 12-26 days before the filtration experiments. The pH value of the dispersions remained stable during this aging time and equal to 10 during the measurement, which indicates that there is no further dissolution of material since pH was always above 9 (Thompson and Butterworth, 1992).

1.2 Skim milk suspensions

1.2.1 General description of structural properties

Milk is a constituent of many foods and food products. Milk can be considered as an emulsion of fat globules in an aqueous phase. The aqueous phase consists of suspended and

dissolved components, such as casein micelles, serum proteins, lactose and salts. Besides the major components fat, casein and lactose, milk contains valuable minor components that can be interesting for specific isolation. When the milk is defatted (the cream is removed), the remaining aqueous phase is called skim milk.

The total protein component of milk is composed of numerous specific proteins. The primary group of milk proteins is the casein. There are 3 or 4 caseins in the milk of most species; the different caseins are distinct molecules but are similar in structure, which form a multi-molecular, granular structure called casein micelles. All other proteins found in milk are grouped together under the name of whey proteins. The major whey proteins in cow milk are β-lactoglobulin (β-LG) and α-lactalbumin (α-LG).

The structure of casein micelles has been studied for more than half century. Here presents the principal ones. The first ‘‘classic’’ model represents the structure in terms of casein sub-micelles which are approximately spherical with sizes from 10 to 20 nm and are primary made up of casein molecules. These sub-micelles aggregate into a larger micelle by means of calcium phosphate clusters bridging them together. The sub micelle composition varies with the inner ones mainly built of $\alpha_s -$ and $\beta -$caseins, while the outer ones primarily made of $\alpha_s -$ and $\kappa -$caseins. The C-terminal ends of $\kappa -$caseins stick out of the sub-micelles, forming a ‘‘hairy layer’’ that prevents - by steric and electrostatic repulsion - any further aggregation of the sub-micelles, as shown in Fig. 2.2.

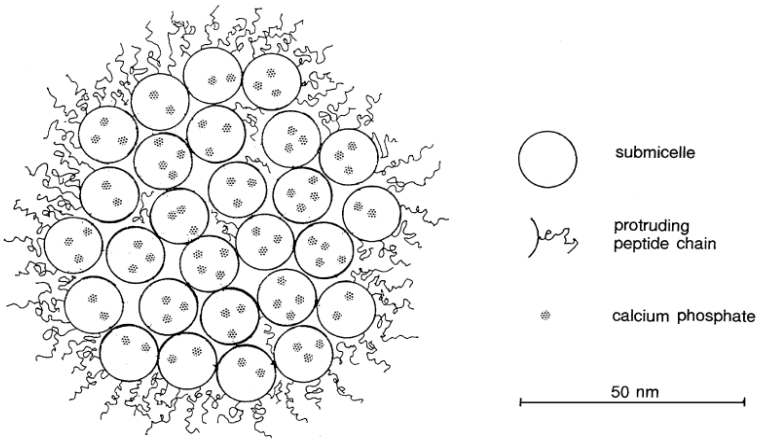

Fig. 2.2 *Schematic representation of the casein micelles structure according to the sub-micelle model proposed by Walstra (1999).*

Based upon the same principle, Horne proposed the dual bonding model (Horne, 2006). Bonding occurs between the hydrophobic regions of different molecules: α_s- caseins, $\beta-$caseins and $\kappa-$caseins, shown as rectangular bars in Fig. 2.3, and by linkage of hydrophilic regions containing phosphoserine clusters to colloidal calcium phosphate clusters (CCP). Molecules of $\kappa-$caseins limit further micelle growth, which become part of the surface structure of the micelle.

The more recent model of casein micelles is the nanocluster model proposed by De Kruif *et al*.. In this nanocluster model, the CCP is dispersed as small 'cherry stones' in a homogeneous protein matrix (a nanogel) (Kruif and Holt, 2003). The basis of the nanocluster model is the idea that phosphorylated caseins bind to the growing nanoclusters so as to prevent calcification of the mammary gland. The protein tails sticking out of the nanoclusters associate with other proteins through a collection of weak interactions to form a more or less homogeneous protein matrix. Used as a collective term, weak interactions refer to hydrophobic interactions, hydrogen bonding, ion bonding, weak electrostatic interactions and other factors (but not the strong calcium phosphate interaction) leading to self-association. The heterogeneity of the casein proteins could be taken as an indication for heterogeneity of the weak interactions. Invariable as the two former models, $\kappa-$casein is thought to limit the process of self-association, called ''hairy layer'', leading to stabilization of the native casein micelle. This model is supported by small-angle neutron and X-ray scattering and static light scattering spectrum (SANS, SAXS, SLS) which suggest that this nanocluster model captures the main features of the casein micelle (de Kruif *et al*., 2012).

Size of this casein micelle has also been characterized, often by scattering measurements like SAXS or SANS. The CCP nanoclusters are dispersed as very small ''cherry stones'' with a diameter from 1.7 to 2.5 nm (de Kruif *et al*., 2012; Marchin *et al*., 2007); the casein micelles were estimated by different techniques to have a radius from 60 to 100 nm and often polydisperse (de Kruif *et al*., 2012; Pignon *et al*., 2004).

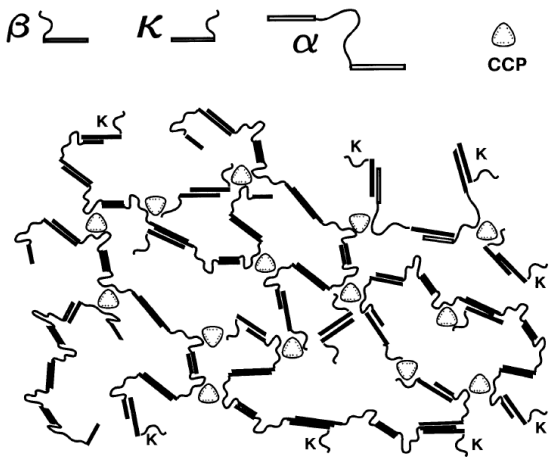

Fig. 2.3 *Schematic representation of the casein micelles structure according to the dual bonding model proposed by (Horne, 1998).CCP represents the colloidal calcium phosphate.*

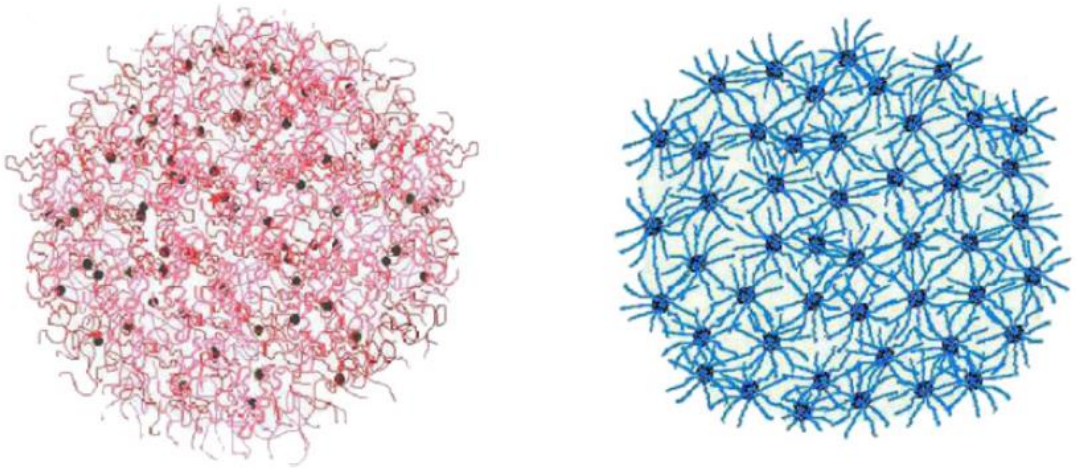

Fig. 2.4 *Schematic representation of the casein micelles structure according to the nanocluster model proposed by De Kruif (de Kruif et al., 2012; Kruif and Holt, 2003).*

1.2.2 Sample preparation

Different suspensions were prepared in this study. The suspensions for filtration are skim milk suspensions. They were prepared from 'low heat' Bovine Skim Milk Powder containing soluble proteins and mineral salts in addition to casein micelles, the major protein of milk. This powder was provided by ''UMR 1253 INRA Agrocampus Ouest, STLO Science et Technologie

du Lait et de l'Œuf'' Rennes, France (Schuck *et al.*, 1994). To prevent the development of bacteria, sodium azide (0.2 $g.L^{-1}$) was added to the suspension. The casein micelle content of standard skim milk suspension is about 27 $g.L^{-1}$ (26 $g.kg^{-1}$). The equivalent mass of the 'low heat' powder (about 95.8 g) was dispersed in deionized water under steady stirring at a fixed temperature of 45 °C to obtain a 1 kg milk with a standard concentration in casein micelles. Mixing time was adapted according to the desired concentrations in order to produce homogeneous suspensions and sufficient hydration of casein micelles (30 min for standard concentration and until 2 h for concentrated suspensions). To simplify the interpretation of results, a relative concentration C/C_o was presented in this study, where C is the casein micelle concentration of sample suspension and C_o corresponds to the casein micelle concentration of standard skim milk (27 $g.L^{-1}$).

Other casein micelle suspensions were also used in the study of flow properties (section 3.1). They were obtained by dissolution of a standard commercial ''high protein content powder'' (Promilk 852B, Ingrédia, 62, Arras, France) in aqueous phase. The same suspensions have already been used in precedent work (David *et al*., 2008). The content of casein micelles in this powder is higher, about 75 % (w/w), compared to that of ''low heat'' powder, about 26 % (w/w). Therefore, the equivalent mass of powder is 35.2 g for 1 kg of suspension correspondent to the casein micelle concentration of standard skim milk. The preparation protocol is the same as that of ''low heat'' powder. In order to reveal the eventual difference of flow properties of casein micelle suspensions in different ionic equilibriums, three types of aqueous phase were exploited. The casein micelles were dispersed either in deionized water, in ultrafiltrate (UFP) or microfiltrate (MFP). The microfiltrate was obtained by microfiltration (0.1 µm) of skim milk. It contains some dissolved proteins, lactose and some minerals. The ultrafiltrate was acquired by ultrafiltration (8 kDa) of the obtained microfiltrate, it contains only lactose and minerals. The suspensions of casein micelles dispersed in MFP could be considered as an equivalent of skim milk.

1.3 Nanocrystal suspensions

1.3.1 General description of structural properties

a)

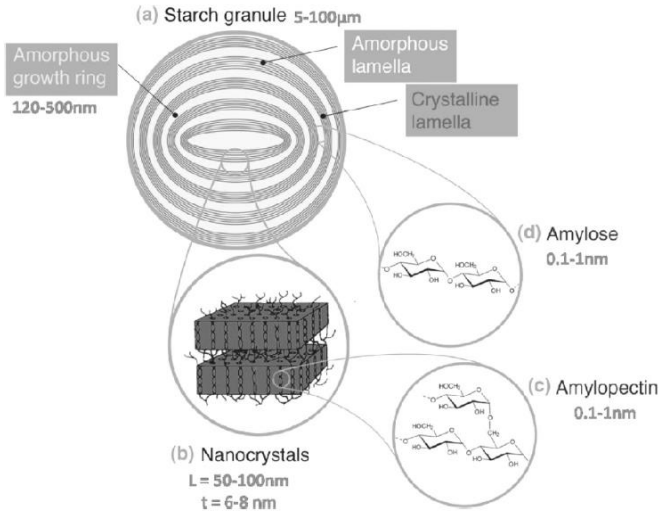

b)

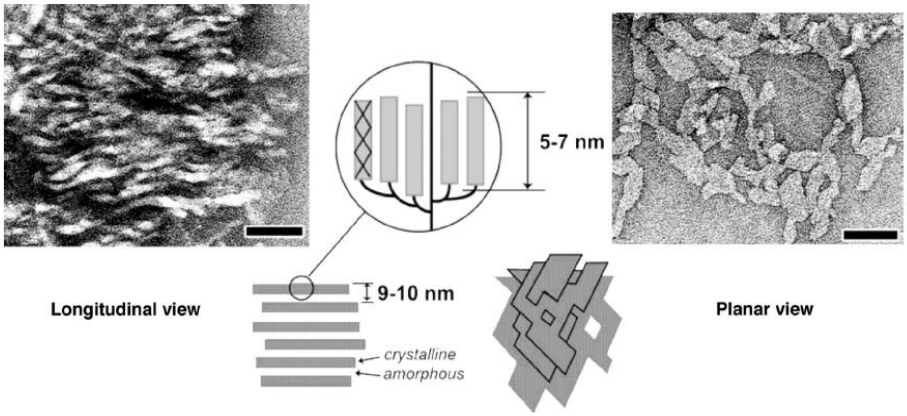

Fig. 2.5 *a.Starch granule structure; b. Transmission electron microscopy (TEM) observations of starch nanocrystals (SNC): longitudinal view and planar view. (LeCorre et al., 2011)*

As shown in Fig. 2.5a, starch has a concentric semicrystalline multiscale structure that allows the production of starch nanocrystals (SNC) resulting from the disruption of amorphous domains from semicrystalline granules by acid hydrolysis (LeCorre *et al*., 2011; LeCorre *et al.*, 2010). Putaux *et al*. revealed the morphology of nanocrystals resulting from the disruption of the waxy maize starch granules by acid hydrolysis (Putaux *et al*., 2003). After 6 weeks of hydrolysis,

transmission electron microscopy (TEM) observations (Fig. 2.5b) showed a longitudinal view of lamellar fragments consisting of a stack of elongated elements with a width of 5-7 nm and a planar view of an individualized platelet with a length of 20-40 nm and a width of 15-30 nm. However, more recent publications report bigger SNC, from 40 to 100 nm with round edges and even are found as grape-like aggregates of 1-5 μm (LeCorre *et al*., 2010). The heterogeneity in particle size could be explained by the differences in starch types and also by the difficulty to obtain well-defined pictures of non-aggregated nanocrystals. Contrary to cellulose nanocrystals, starch nanocrystals are not almost 100% crystalline, but rather 45% crystalline, with variations depending on the botanic origin (LeCorre *et al*., 2011).

Cellulose nanocrystals (CNC) derived from acid hydrolysis of native cellulose possesses different morphologies depending on the origin and hydrolysis conditions. Generally, they are rigid rod-like crystals with diameter in the range of 10–20nm and lengths of a few hundred nanometers (Fig. 2.6); e.g. crystallites from tunicates and green algae have lengths in the range of a few micrometers and crystallites from wood and cotton have lengths of the order of a few hundred nanometers, while some spherical shape CNC were also produced during the acid treatment (Wang *et al*., 2008; Zhang *et al*., 2007). Therefore, the relative degree of crystallinity and the geometrical aspect ratio, i.e. the length-to-diameter (L/d) are very important parameters controlling the properties of CNC-based materials. An important characteristic of CNC, when prepared in sulphuric acid, is that they possess negative charges on their surface due to the formation of sulphate ester groups during acid treatment, which enhances their stability in aqueous solutions.

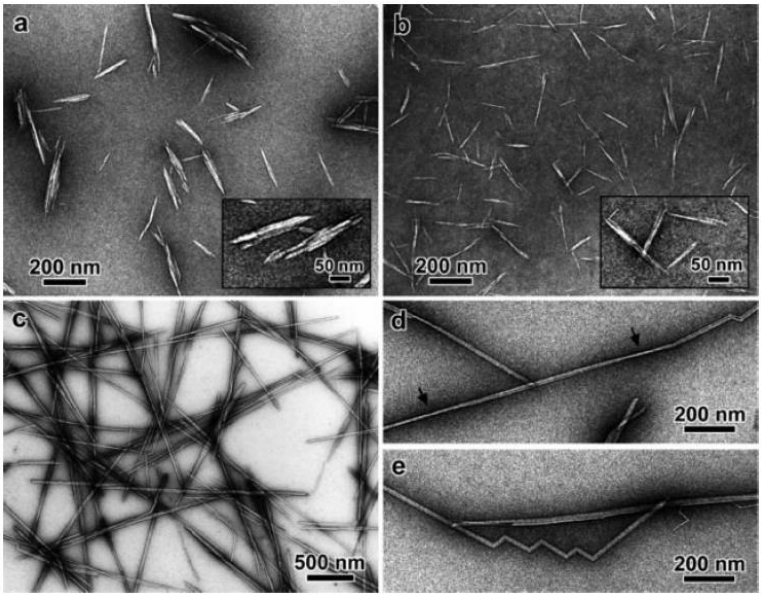

Fig. 2.6 *Transmission electron microscopy (TEM) micrographs of nanocrystals obtained by sulfuric acid hydrolysis of (a) cotton (b) avicel (c-e) tunicate cellulose. (Elazzouzi-Hafraoui et al., 2008)*

CNC derived from sulphuric acid hydrolysis can disperse in aqueous solutions due to their negative charged surfaces. It should be noted that CNC are very polar and attract each other by hydrogen bonding thus they have tendency to form bundles or aggregates (Lu and Hsieh, 2010; Marcovich *et al.*, 2006). At low concentration, CNC particles are randomly oriented in aqueous suspension as an isotropic phase, and when the concentration reaches a critical value, they form a chiral nematic ordering, where CNC suspensions transform from an isotropic to an anisotropic chiral nematic liquid crystalline phase (Revol *et al*., 1992). As the concentration increased further, aqueous CNC suspensions showed a shear birefringence phenomenon. The critical concentration for sulphated CNC typically ranges between 1 and 10% (w/w), which is a function of aspect ratio of CNC, charge density and osmolarity. Theories based on different parameters have been studied to explain the phenomena (Stroobants *et al*., 1986).

1.3.2 Sample preparation

SNC made from waxy maize starch were prepared using the optimized procedure of Angellier et *al*. (2004). 147 g of starch particles were mixed with 1 L of H_2SO_4 at 3.16 mol L^{-1} during a 5 days period under constant heating at 40 °C. Then, the suspension was washed by successive centrifugations (centrifuge 6K-15C, Sigma) at 10 000 rpm (16211 g) in deionized water. Seven to eight centrifugation steps were needed to reach neutral pH. At each step SNC were re-dispersed using Ultra Turrax to avoid aggregates formation. The centrifuged suspension was then dialyzed for 5 days to eliminate remaining salts and then filtered on a Nylon filter (40 µm and 1 µm) before storage at 5 °C.

CNC were isolated from microcrystalline cellulose (Avicel®, Sigma Aldrich, France) based on the optimized protocol reported by Bondeson *et al*. (2006). Controlled acid Hydrolysis was achieved at 50 °C with 65wt% sulphuric acid for about 44 min, using mechanical stirring at 500 rpm. Fiber content during all of the chemical treatment was 10% (w/w). Afterwards, the suspension was diluted with deionized ice cubes and washed until neutrality by 5 successive centrifugations at 10 °C for 10 min each step, in order to inhibit the acid hydrolysis. During about 5 days and until the water conductivity is stabilized, the suspension was dialyzed against deionized water. Subsequently, CNCs were dispersed by using a light sonication treatment (500 J/g). At the end of the production, the suspension was filtered on a 1 µm membrane. A small quantity of Chloroform (0.01 wt%) was added to the suspension to prevent microbial growth in the material which was stored at 5 °C.

1.4 Natural clay suspensions

Two types of naturally occurring swelling clay minerals are investigated in this study, both of them are diocthaedral smectites: (i) Wyoming Montmorillonite (SWy-2), (ii) Australia Nontronite (NAu-1). They were purchased from the Source Clays Minerals Repository of the Clay Mineral Society of Purdue University. All these clay dispersions were produced and provided by the team of Laurent Michot (Laboratoire Environnement et Minéralurgie, Nancy) Their structural formulas are shown as below:

SWy-2 $(Si_{7.74}Al_{0.26})(Al_{3.06}Fe^{3+}_{0.42}Fe^{2+}_{0.03}Mg_{0.48})O_{20}(OH)_4Na_{0.77}$

NAu-1 $(Si_{6.98}Al_{0.95}Fe^{3+}_{0.07})(Al_{0.36}Fe^{3+}_{3.61}Mg_{0.04})O_{20}(OH)_4Na_{1.05}$

These high aspect ratio (20-1000) layered aluminosilicate compounds are typically formed from two tetrahedral layers (Si, Al, and Fe) encompassing an octahedral one (Al, Mg, and Fe). Consisting of these platelets, the structure of these gels and the mechanisms responsible for gelation have been debated since the 1930s with two conflicting views: (i) the so-called "house of cards" model based on the electrostatic attraction between the edges and faces of the platelets, leading to a tridimensional network and (ii) the stabilization of the gel structure by a repulsion between the interacting electrical double layers of the platelets. (Avery and Ramsay, 1986; Callaghan and Ottewill, 1974; Norrish, 1954; Ramsay, 1986) Making use of both models, Abend and Lagaly proposed a general phase diagram for sodium montmorillonites, showing a repulsive gel at low ionic strength (<10^3 M) and high volume fraction, whereas at higher ionic strength only attractive interactions were involved whatever the clay concentration (Abend and Lagaly, 2000). In addition, numerous experimental measurements (Baravian *et al.*, 2003; Michot *et al.*, 2006; Ramsay and Lindner, 1993; ten Brinke *et al.*, 2007) and simulation works (Agra *et al.*, 2004; Delville, 1994; Jönsson *et al.*, 2008; Spitzer, 1989) have pointed out the relevance of repulsive interactions in natural clay suspensions due to double-layer electrostatic forces.

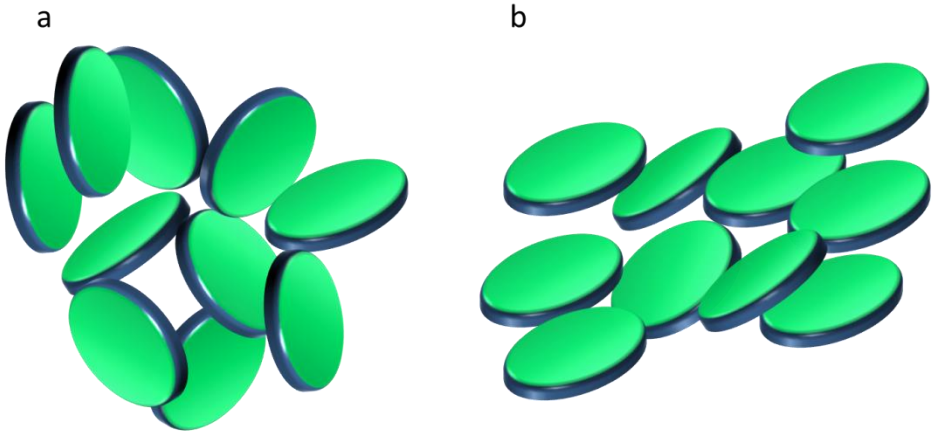

Fig. 2.7 *Schematic representation of swelling clay suspensions: a:isotropic liquid phase; B:nematic phase.*

One of the most important properties of swelling clay minerals is their ability to form yield stress materials when dispersed in water. Their aqueous suspensions can exhibit an isotropic/nemetic transition, that the nematic phase displays strong orientational order, and that it can be aligned in modest magnetic fields, a distinctive feature of liquid-crystal phase transition before the sol-gel transition (Michot *et al*., 2006). The schematic representation of these clay suspensions is shown in Fig. 2.7.

Before use, these natural clay samples were purified of accessory minerals such as quartz, feldspar, and oxyhydroxides and sodium exchanged. A size fractionation procedure was then applied by successive centrifugation as described by Michot *et al.* (2006) and Paineau *et al.* (2011), and four size fractions were obtained, referenced as T1 to T4, the third one (T3) was used in this study. The morphological parameters of each size fraction were determined by transmission electron microscopy (TEM) using a CM12 Philips microscope operating at 80 kV. The results are reported in Tab. 2.1, for the two suspensions used in this work.

Tab. 2.1 *Morphological parameters of Montmorillonite and Nontronite Clays used in this study*

Parameters	SWy-2 T3	NAu-1 T3
Average diameter (nm)	100	/
Polydispersity diameter (%)	45	/
Average length (nm)	/	350
Polydispersity length (%)	/	47
Average width (nm)	/	54
Polydispersity width (%)	/	35
Average thickness (nm)	0.75	0.76
Ionic strength (M)	10^{-5} [NaCl]	10^{-4} [NaCl]
Specific mass $g.cm^{-3}$	2.7	2.9
Concentration of the filtered dispersions ($g.L^{-1}$)	12.70	11.64
Volume fraction of the filtered dispersions	0.47 %	0.40 %

1.5 Membranes

The membranes used in this study are flat polyethersulfone (PES) ultrafiltration membranes (MWCO = 100 kD, PleyadeRayflow x100, Rhodia Orelis). The top skin layer of the membrane is made of porous organic polymers-polyethersulfone- that are fixed above a supportive film, resulting in an average membrane thickness of 200 µm. These membranes are supplied in the form of flat sheets, and are immersed in a solution of sodium azide (NaN_3) at 0.2 $g.L^{-1}$ to avoid bacterial growth. The membranes are then stored at 4°C in a closed container away from direct light before using.

2. Experimental set-up

2.1 'SAXS Cross-Flow US-coupled Filtration Cell'

Previously, a 'SAXS Cross-Flow Filtration Cell' was developed to measure *in-situ* the concentration and structural organization of colloids as a function of time at different distances z from the membrane surface (Pignon *et al.*, 2012). This cell is made of transparent polycarbonate and contains a flat polyethersulfone ultrafiltration membrane (MWCO = 100 kD, PleyadeRayflow x100, Rhodia Orelis). The design of this filtration cell was modified in order to combine an ultrasound system: a thin titanium vibrating blade was embedded in the feed compartment and placed above the flat membrane at a distance of 8 mm. This blade is connected to a sonotrode consisting of a piezoelectric transducer attached to a metal rod, which generates ultrasonic waves at a 20 kHz frequency and at an applied amplitude of 1.6 µm (SODEVA TDS, France), as shown in Fig. 2.8a. The input electric power stretches from 2 W to 10 W, corresponding to power intensity from 0.57 W.cm^{-2} to 2.86 W.cm^{-2} (the input power per unit area of the blade surface). The feed channel is 100 mm long in tangential flow direction and 4 mm × 8 mm (width ×height) in the flow section. Three windows of 3 mm × 5.5 mm × 0.3 mm (width × height × thickness) are opened into the wall located upstream, in the middle and downstream in the feed compartment with a distance of 43 mm from each other (Fig. 2.8b).

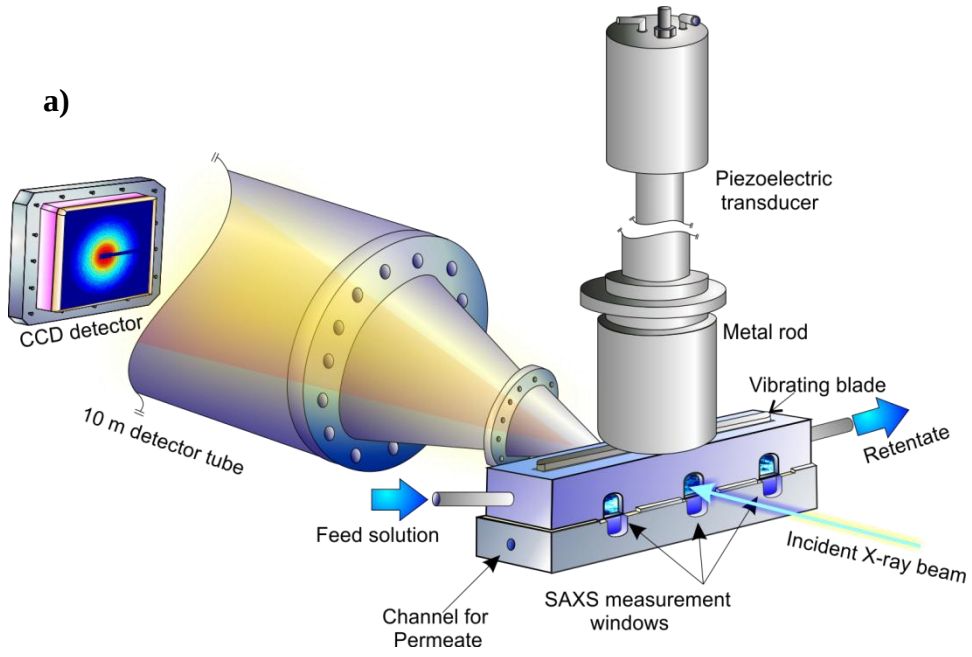

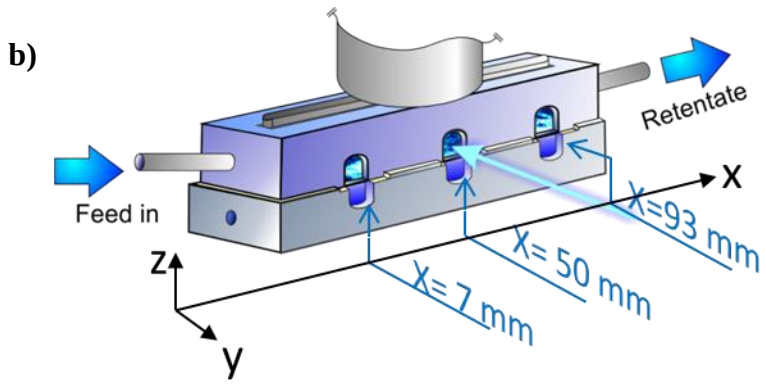

Fig. 2.8 *a) Schematic of ''SAXS Cross-Flow US-coupled Filtration Cell''; b) front view of filtration cell*

2.2 Filtration installations

As shown in Fig. 2.9, during filtration, the feed suspensions, denoted as retentate, are pumped (Mono pump LF series) from a high pressure resistant vessel (Millipore, capacity: 5L) to the filtration cell and the cross-flow rate is quantified constantly by a magnetic flow meter (Optiflux 6300C, Krohne). The pressure is applied via purified compressed air, and is monitored by two pressure gauges (FP 110 FGP Sensors & Instrument) at both the inlet and outlet of the filtration cell. The filtration temperature is maintained at 25°C by a thermostatic bath (Thermo &Scientific SC 150 A25, HAAKE) and it is verified constantly by two sensors (YC-747D with K thermocouples) at both inlet and outlet of the filtration cell. The permeate flux J_v is monitored by measuring the mass variation in the reservoir vessel every 5 s with an accuracy of 0.001 g (Balance Precisa 400M).

a)

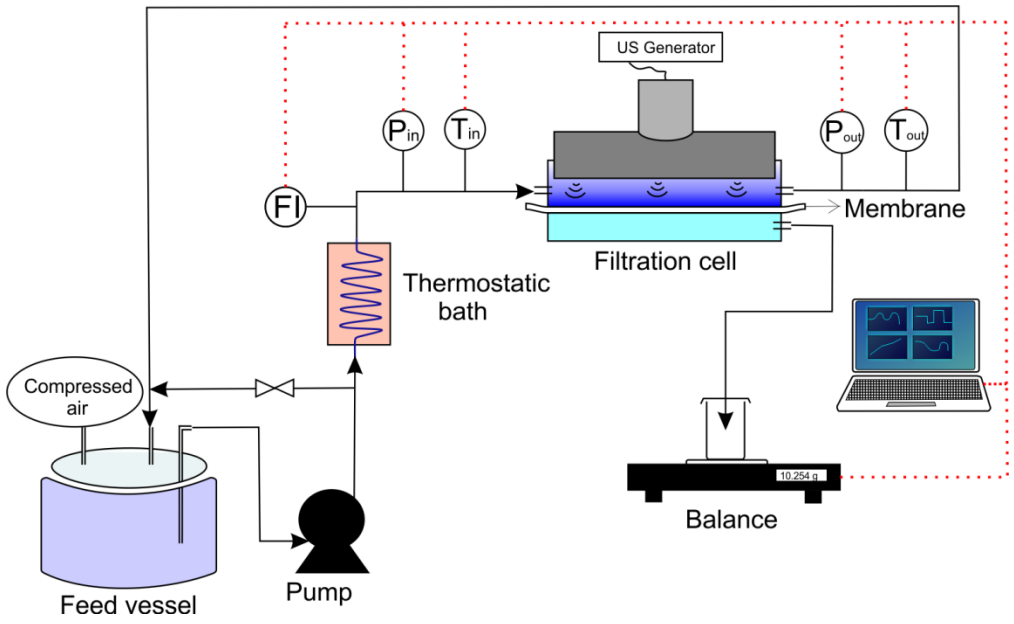

b)

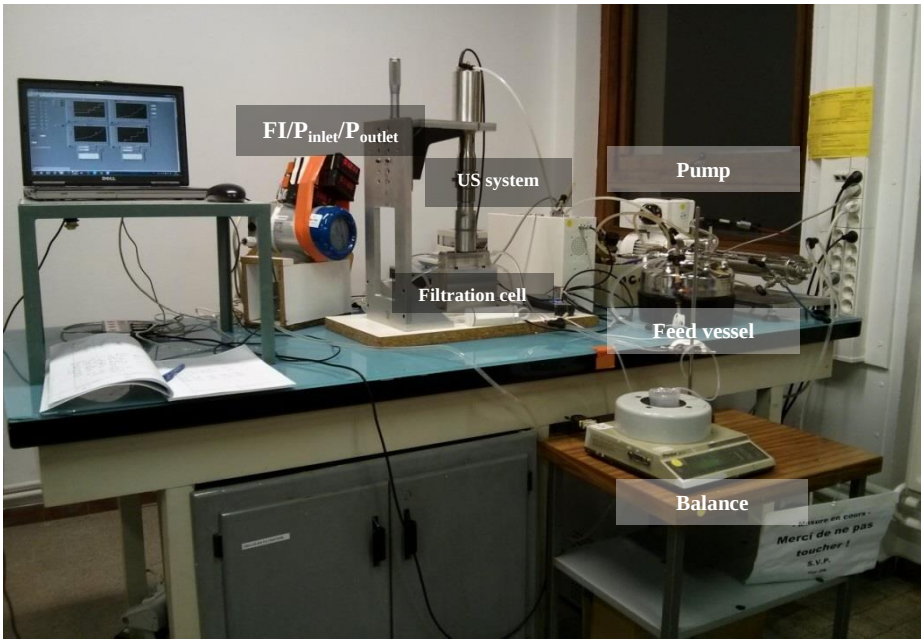

Fig. 2.9 *Overview experimental setup of cross-flow filtration. a) schematic, b) photo captured in Laboratoire Rhéologie et Procédé.*

3. Experimental procedures

3.1 Membrane conditioning

Before utilization, the membrane was cut delicately from the sheet to adapt the filtration channel with a dimension of 8 mm × 200 mm (width × length). Then the membrane conditioning should be carried out immediately, which consists of three steps: rinsing, immersing and compaction.

For the first two steps, deionized water and ethanol solution were used to condition the membranes, removing the glycerin preservative with which new membranes are coated during manufacture. Firstly, the membrane was thoroughly rinsed with large amounts of deionized water for 5 min. Then it was immersed in ethanol solution and deionized water successively for 5 min every time; the operation was repeated three times. Finally, the membrane was rinsed again with abundant deionized water to finish the immersing step.

Afterwards, the membrane was mounted into the filtration module and compaction was carried out. This step necessitates deionized water of 3 L as the feed solvent. Then a filtration run was executed at TMP = $1.5.10^5$ Pa for 1 hour. This step then allowed shaping a definitive inner porous structure of the membrane.

3.2 Determination of membrane hydraulic permeability

Membrane hydraulic permeability was measured at least twice for each filtration run: one before the run and the other after cleaning cycles. Deionized water was used to determine the membrane hydraulic permeability. A stepped-up TMP procedure was followed from $0.2.10^5$ Pa to $1.1.10^5$ Pa, at T= 25 °C and cross-flow rate Q_v = 0.45 $L.min^{-1}$. The steady-state values of permeate flux (J_v) were then picked up for each TMP step to plot the curve of J_v versus TMP, whose slope represents the membrane hydraulic permeability (L_p).

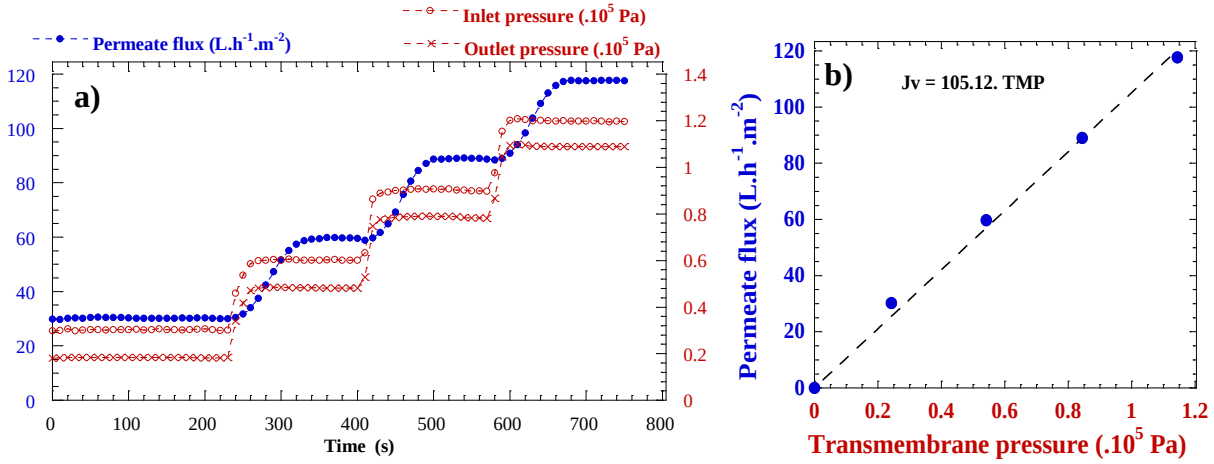

Fig. 2.10 *Determination of membrane hydraulic permeability. a) permeate flux Jv, inlet and outlet pressure of filtration module over time; b) Steady state curve of Jv as a function of transmembrane pressure TMP (averaged pressure between inlet and outlet pressure)*

As shown in Fig. 2.10, the filtration curve over time (a) is interpreted as steady state curve of Jv versus TMP (b) that allows determining the membrane hydraulic permeability L_p = 105.12×10^{-5} $L.h^{-1}.m^{-2}.Pa^{-1}$ by curve fitting (correlation coefficient R>0.99), according to Eq.1.1.

3.3 Filtration procedure and data acquisition

Filtration runs were carried out in different modes as needed. Three major procedures were used in this study: (i) Espinasse method, (ii) stepped-up TMP method and (iii) TMP constant filtration.

Espinasse method refers to an alternating increase-decrease TMP filtration procedure, proposed by Espinasse et *al.* (2002). Using such a procedure, reversible fouling can be distinguished from deposit at the range of applied pressure. It also illustrates critical flux and limiting flux, which reveals the filtration performance of a given dispersion. Stepped-up TMP method simplifies Espinasse method and allows determining the critical flux and limiting flux of concerned filtrate. TMP constant filtration, just as its name implies, refers to a fixed TMP

filtration, which was often employed to compare the filtration performance at multi-scales with and without US. Schematic of the two first procedures is demonstrated in Fig. 2.11.

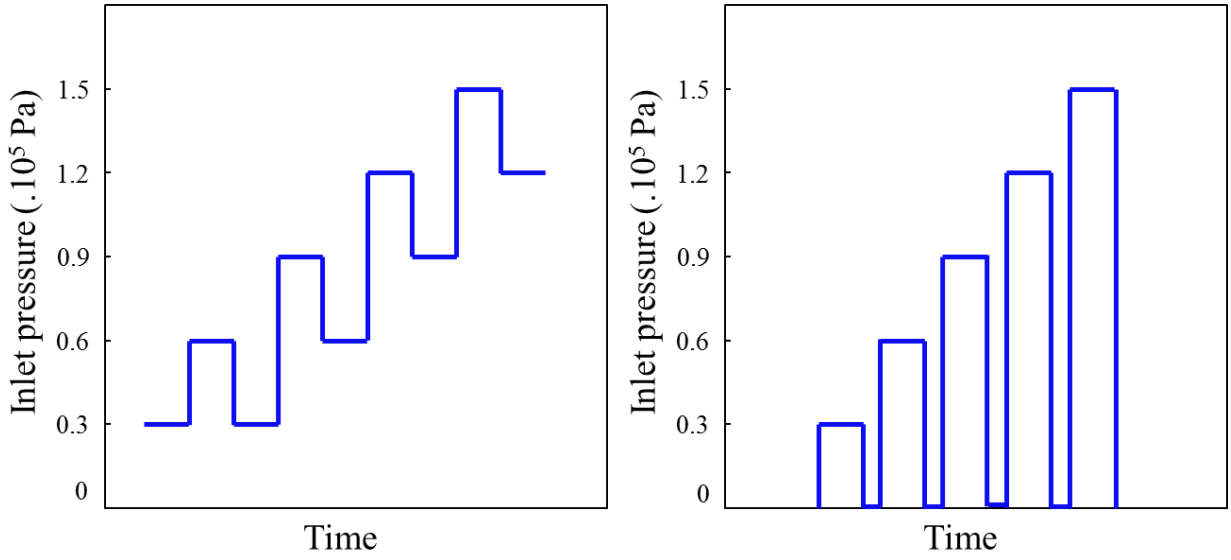

Fig. 2.11 *Schematic of filtration procedures. a) Espinasse procedure, b) stepped-up TMP procedure*

For every filtration process, permeate flux is a key parameter that requires a measurement as accurate as possible. In this study, permeate flux was determined by mass variation (Δm, g) at certain interval of time (Δt, s), described by following equation:

$$J_V(\Delta t) = \frac{1}{\rho_p . S_m} . \frac{\Delta m}{\Delta t} \qquad \textbf{Eq. 2.1}$$

Where ρ_p is the density of permeate, equal to that of water in most cases (kg.m^{-3}), S_m is the effective surface of membrane (m^2), $J_V(\Delta t)$ is the permeate flux within this time interval Δt (m^3.m^{-2}.s^{-1}).

The permeate mass was recorded every 5 s by the balance, instantaneous permeate flux was calculated based upon 10-values averaged mass, described by:

$$J_V(t_n) = \frac{1}{\rho_p . S_m} . \frac{\sum_{i=n}^{n+10} m(t_i) - \sum_{j=n-10}^{n} m(t_j)}{\sum_{i=n}^{n+10} t_i - \sum_{j=n-10}^{n} t_j} \quad (n \geq 10) \qquad \textit{Eq. 2.2}$$

Where $J_V(t_n)$ is instantaneous permeate flux at t = t_n, with $t_{n+1} - t_n = 5\ s$. This method allows minimizing the flux fluctuation due to small time interval thus can provide a steadier curve thanks to the statistical consideration (David, 2008). Otherwise, the statistical permeate flux starts at t = t_{10} (50 s), implying that the values from t_o (0 s) to t_9 (45 s) are not available. This omission is negligible compared to the filtration time which is at least 2h.

3.4 Cleaning conditions

At the end of each filtration run when the data acquisition was stopped, the set-up was emptied and rinsed with large amounts of fresh tap water (10 L) at Q_v = 1 L.min^{-1}, T = 25 °C. Following cleaning procedures depend on feed dispersions.

For gel-like dispersions, including Laponite and the natural clay gel dispersions, mechanical cleaning was adopted: the set-up was emptied again and refilled with 5L of fresh tap water, which circulated at high cross-flow velocity (Q_v = 1 L.min^{-1}) in the installation via counter-current (inverse of inlet and outlet of the installation) during 20 min. Then the set-up was emptied again, the filtration module was dismounted and was particularly cleaned by brush and tap water; the membrane which was still mounted in the module was delicately cleaned by water jetting in order to remove all the attached gel on the surface. Finally, the filtration module was re-mounted and the set-up was refilled with deionized water. So far, the set-up was ready for the after-filtration measurement of membrane hydraulic permeability.

For the dispersions of organic matter, such as skim milk and nanocrystals, chemical cleaning was employed: after the first rinse by fresh tap water, the set-up was emptied again and refilled with 1.5 L of cleaning agent solution, called Ultrasil 10, at 4 g.L^{-1} (P3, Ecolab, France). This cleaning agent then circulated in the installation at 50 °C for 1 h, while the permeate side of filtration module was also filled with this agent. The next step was to empty the set-up and rinse

it with 10 L of fresh tap water at ambient temperature to ensure the total removal of this cleaning agent. At last, tap water was evacuated and renewed by deionized water.

4. Characterization of ultrasound system

4.1 Vibration determination

Ultrasound propagates in the form of vibration, which is, therefore, the first parameter to be characterized. Vibrometry was employed to achieve this goal. As shown in Fig. 2.12, vibrometry system consists of a sensor head (OFV 353, Polytec), a velocity decoder (OFV3001, Polytec) and an oscilloscope (DPO 3014, Tektronix). The beam of a helium neon laser was focused on the vibrating blade of ‘‘SAXS Cross-Flow US-coupled Filtration Cell’’ directed by a mirror, scattered back from there and coupled back into the interferometer in the sensor head. The interferometer compared the phase and frequency of the return beam with those of the internal reference beam. The phase difference was proportional to the instantaneous position of the vibrating blade and the frequency difference was proportional to the instantaneous velocity.

In the controller, the resulting signal was decoded using the velocity decoder. A voltage signal was generated which was proportional to the instantaneous velocity of the vibrating blade. This voltage signal was then transmitted into the oscilloscope and was displayed. So far, the velocity amplitude of vibration ($\hat{v}$, $m.s^{-1}$) was obtained which can be converted to the displacement amplitude ($\hat{x}$, m) according to:

$$\hat{v} = 2\pi f . \hat{x} \qquad \textit{Eq. 2.3}$$

With f the vibration frequency (Hz).

Tab. 2.2 characteristics of velocity decoder OVD3001 at used ranges in this study

Velocity Range (mms^{-1}/V)	Full scale output peak to peak (mms^{-1})	Resolution μms^{-1}	Max.frequency kHz
5	100	0.6	50
25	500	0.8	
125	2500	1.0	

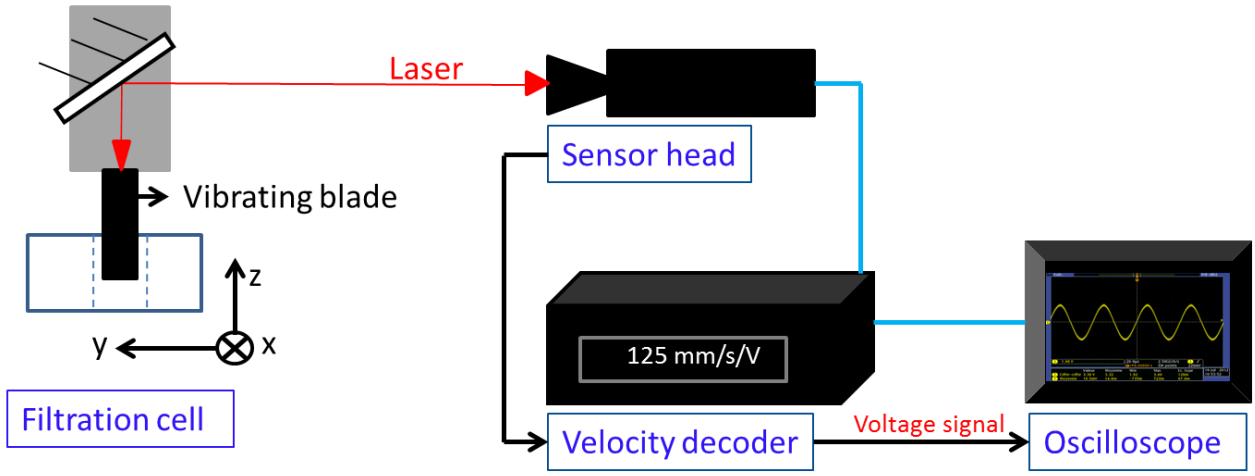

Fig. 2.12 *Schematic view of vibrometry installation*

In this measurement, different velocity ranges were used and their resolutions are shown in Tab. 2.2. In order to measure the vibration of different positions of the blade, the sensor head was fixed on a movable platform so that it can displace along x and y axis (see Fig. 2.12) with an accuracy of 0.01 mm. The displacement of the blade during filtration as a function of the distance from the two extremes is shown in Fig. 2.13. The displacement amplitude $\hat{x}$ of the blade is not homogeneous, and can be distinguished by four blocks. Block zero (B0) corresponds to the block below the sonotrode which could not be measured during filtration due to geometric barrier. B1 represents the blocks close to B0 where the displacement amplitude is almost constant with a value of 1.6 µm (US amplitude command = 100%). In the middle of each side of the blade, another block - B2, can be identified where a low point of $\hat{x}$ is found, suggesting a feebly vibration in this block. At the end of this block, $\hat{x}$ rebounds to the same level as B1, it then takes a gradual decay at the extremities of the blade, denoted as B3.

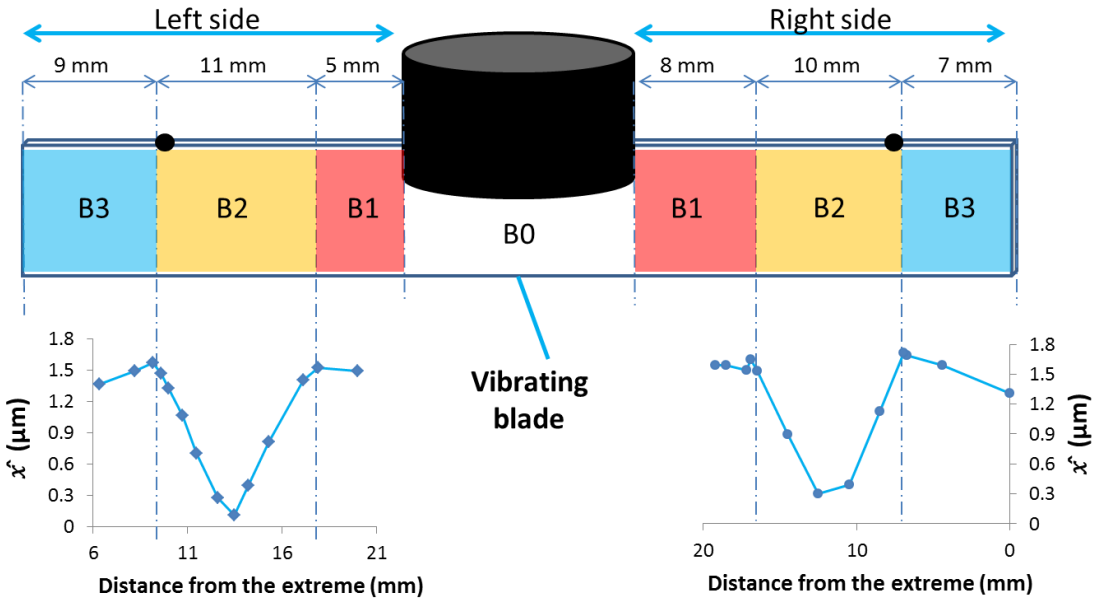

Fig. 2.13 *Schematic representation of displacement amplitude $\hat{x}$ of different positions of the vibrating blade during filtration (TMP = 1.1.10^5 Pa, US amplitude command = 100%). Four blocks can be distinguished. B0: block that was not measured; B1: block of constant high-level displacement; B2: block with a V-shape evolution of displacement; B3: block of gradual decrease of displacement.*

Fixed at 20 kHz, the US generator (SODEVA TDS, France) can itself produce the ultrasonic waves of different amplitude by commanding. Therefore, the displacement amplitude of different commanded US amplitudes (from 40% to 100%) was estimated. This measurement was carried out at fixed positions (indicated by the round dots in Fig. 2.13) where the displacement amplitude have the maximal value. Fig. 2.14 shows the measured $\hat{x}$ at different US amplitude commands at both sides of the blade as well as the averaged values. The averaged $\hat{x}$ at the measured positions varies from 1.09 µm to 1.58 µm when US amplitude command changes from 40 % to 100 %.

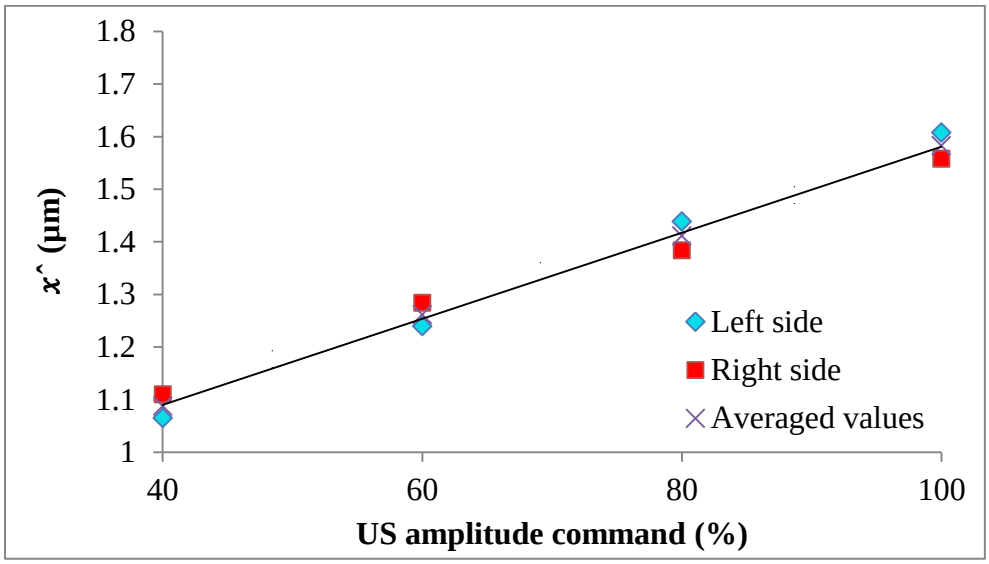

Fig. 2.14 *Measured displacement amplitude $\hat{x}$ versus US amplitude command at both sides of the blade. Averaged values are also presented and fitted, as the curve shows.*

4.2 Power estimation

4.2.1 Different US power terms

First of all, it is important to clarify the US power terms that could be used in this study. Firstly, an input electric power (P_{in}, W) is required to trigger the piezoelectric effect; then ultrasonic waves with certain amplitude are generated, which are the energy carrier. These ultrasonic waves are then transmitted into the feed suspension by the blade, along with energy loss by the means of heating, etc. Ultrasonic intensity is often used to quantify the ultrasonic power. Depending on different reference, they can be expressed as US power per unit area of the blade surface ($I_{in,b}$ W.cm^{-2}), US power per unit area of the membrane surface ($I_{in,m}$ W.cm^{-2}) or US power per unit volume of feed suspension ($I_{in,v}$,W.cm^{-3}). They are presented in Tab. 2.3.

Tab. 2.3 *Different terms for describing ultrasonic power in this study and its respective value*

Commanded amplitude (%)	P_{in} (W)	$I_{in,b}$ (W.cm^{-2})	$I_{in,m}$ (W.cm^{-2})	$I_{in,v}$ (W.cm^{-3})
40	2±1	0.57±0.29	0.50±0.25	0.63±0.31
60	4±1	1.14±0.29	1.00±0.25	1.25±0.31
80	7±1	2.00±0.29	1.50±0.25	2.19±0.31
100	10±1	2.86±0.29	2.50±0.25	3.13±0.31

4.2.2 Effective US power estimation

Effective ultrasonic power was estimated by calorimetry method, which involves a measurement of the initial rate of heating produced by US (Mason, 1999). In a pure liquid, one might assume that almost all the mechanical energy produces heat and so, via calorimetry, some estimation of the acoustic power entering the system can be obtained. This is a simple method of estimating the overall acoustic power entering a fluid system even when a thermally insulated vessel is not employed. In fact, acoustic power heats the liquid with partial loss towards the environment due to temperature difference between the liquid and environment. When liquid temperature is equal to environmental temperature, the energy loss towards environment may be neglected. Therefore, the dissipated acoustic power (P_{diss}, W) in the liquid can be described as:

$$P_{diss} = m.C_{p,liq}.\frac{dT}{dt} \ (\text{when } T = T_{amb}) \qquad \textit{Eq. 2.4}$$

Where m is the mass of liquid (kg), $C_{p,liq}$ is the heat capacity of the liquid (J.kg^{-1}.K^{-1}), T_{amb} is the environmental temperature (K) and $\frac{dT}{dt}$ represents the instantaneous temperature change around the T_{amb} at tiny time interval.

Calorimetric measurements were carried out by an acquisition system developed by Legay (2012). Before measurements, all the thermocouples were calibrated by being immersed in water tank with homogenous temperature. They were positioned as close as possible from each other so that the temperature difference due to location in the tank can be neglected. The average

temperature captured by each thermocouple was calculated (from T_{m_1} to T_{m_3}) which then was used to calculate the comon average (T_M, °C). This averaged temperature (T_M) was considered as the real temperature of water sample at each situation. Then the same procedure was carried out for 9 different water temperatures from about 5 °C to 30 °C. Afterwards, correlation curves were plotted between the averaged temperature of each thermocouple (T_{m_n}) and the common average (T_M). These correlations shown in Tab. 2.4 were used to adjust the measured temperatures of each thermocouple for the following investigation.

Tab. 2.4 *Correlations between the averaged temperature of each thermocouple (T_{m_n}) and the general average (T_M) at the range of 5-30 °C*

Thermocouple	Correlation
1	$T_M = 1.0002.T_{m\_1} - 0.2356$
2	$T_M = 0.9979.T_{m\_2} - 0.0206$
3	$T_M = 1.0019.T_{m\_3} + 0.2568$

For the calorimetric measurement, the three calibrated thermocouples were used. Two of them (denoted as TC1 and TC2) were placed in the water with a distance of about 3 cm from the vibrant blade and the other (TC3) placed in ambient condition. The vibrant blade and the two thermocouples were immersed in a plastic tank containing 300 g water wrapped by multi-layers aluminum sheets, as shown in Fig. 2.15a. When US was switched on, the temperature of tank water (T) was recorded against time (t), at intervals of 20 seconds. At the end of each measurement, a curve of instantaneous thermal power as a function of tank water temperature was plotted and fitted by linear law in the proximity of T_{amb}, which was then used to determine the dissipated acoustic power, as shown in Fig. 2.15b. The dissipated acoustic power was determined for different input electric powers (commanded amplitudes). Each measurement was repeated 3 times and average values are presented in Fig. 2.16 (standard deviation 15%). Effective ultrasonic intensities by different references (e.g. per unit area of the blade surface) are shown in Tab. 2.5.

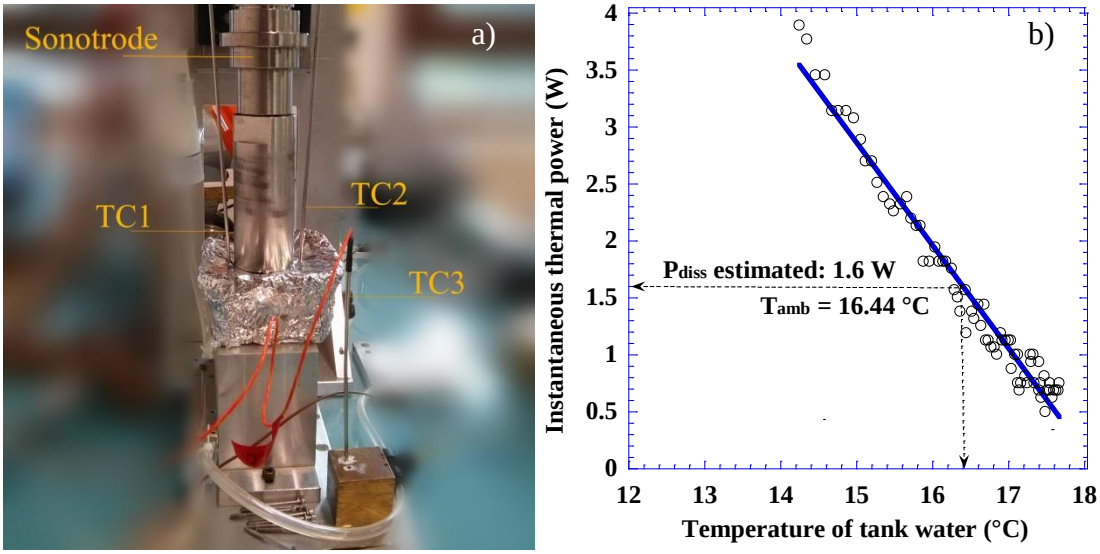

Fig. 2.15 *a) setup of calorimetric measurement; b) example of dissipated acoustic power determination (commanded amplitude: 40%, input electric power: 2 W)*

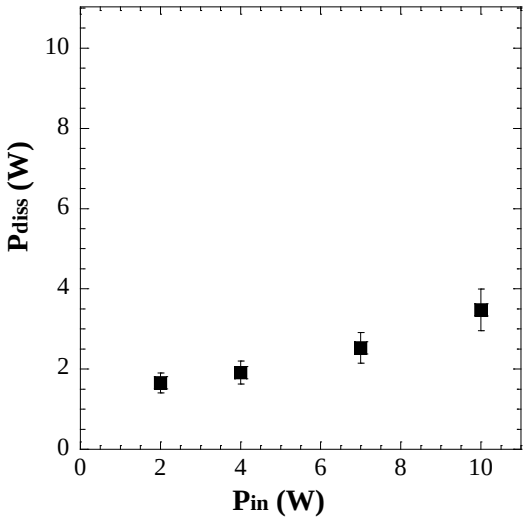

Fig. 2.16 *Dissipated acoustic powers (P_{diss}) of different input electric powers (P_{in}), estimated by calorimetric measurements.*

It shows that the dissipated acoustic power increases with input electric power, and the energy yield (denoted as η_E, dissipated power/input electric power, %) varies from 35 % to 83 %. Power loss seems to be more important at high-level input electric power (η_E = 35 % when the input power is 10±1 W) compared to that of low-level input power (η_E = 83 % when the input

power is 2±1 W). In this study, ultrasonic amplitude of 80 % (7±1 W) is often commanded and the energy yield is around 36 % in this circumstance.

Tab. 2.5 *Effective ultrasonic intensities of different input electric powers*

Commanded amplitude (%)	P_{in} (W)	P_{diss} (W)	η_E	$I_{in,b,effect.}$ ($W.cm^{-2}$)	$I_{in,m,effect}$ ($W.cm^{-2}$)	$I_{in,v,effect}$ ($W.cm^{-3}$)
40	2±1	1.66±0.32	83 %	0.47±0.09	0.42±0.08	0.52±0.10
60	4±1	1.91±0.34	48 %	0.55±0.10	0.48±0.09	0.60±0.11
80	7±1	2.53±0.26	36 %	0.72±0.07	0.63±0.06	0.79±0.08
100	10±1	3.48±0.53	35 %	0.99±0.15	0.87±0.13	1.09±0.17

4.3 Assessment of cavitation activity

4.3.1 Principle of assessment

Acoustic cavitation can generate a range of effects, both chemical and biological, but perhaps the earliest observables attribute to it were erosion (Leighton, 2007). Erosion of metal surfaces by ultrasonic cavitation is well known and has been used over half-century as a rapid method of assessing ultrasonic cavitation activity at low frequencies (Crawford, 1964; Dular *et al*., 2013; Krefting *et al*., 2004; Laguna-Camacho *et al*., 2013; Neppiras, 1968; Zeqiri *et al*., 2006).

In this context, erosion is taken to mean the mechanical disruption of the surface of a solid, related to the motion of the liquid surrounding the cavitation bubbles. The growth and collapse of cavitation bubbles near a rigid boundary is a focal point of cavitation research. Rayleigh considered the collapse of an isolated spherical cavity in a liquid under hydrostatic pressure. He suggested that the emission of shock waves upon the collapse of the bubble is responsible for the cavitation corrosion of rigid boundary (Rayleigh, 1917). Kornfeld and Suvorov suggested that cavitation bubbles might collapse asymmetrically and produce a liquid jet (commonly named micro-jet). The jet passes across the cavity and penetrates the far surface and

hits the boundary (Kornfeld and Suvorov, 1944). Based upon these two suggestions, it is now commonly thought that the observed erosion arise from inertial cavitation, whilst non-inertial cavitation generated by longer-lived, stable bubbles, leads to indentations or depressions in the solid surface (Zeqiri *et al*., 2006).

Erosion of homogeneous solids is very dependent on hardness, grain structure, purity, mechanical fatigue strength and surface finish (Neppiras, 1968). Methods of measuring are, for example vibratory determination or the usage of soft metal or paint coating of the submerged body as a sensor (Dular *et al.*, 2004). Soft material specimen is usually employed, such as foils of aluminum, tin or lead. There are two principles of using such specimen. First, one can observe just the earliest stages of cavitation damage, the formation of microscopic deformations, the so called pits. Second, one can observe the long term damage, i.e. material loss (Lohrberg and Stoffel, 2001). Aluminum foils are the most used due to some significant attractions for industry: it is cheap and simple to apply, provides minimal disturbance of the acoustic field and gives a permanent record of the cavitation distribution (Neppiras, 1968).

4.3.2 Cavitation erosion test

In this study, a qualitative method has been adopted to assess the cavitation activity within the filtration channel (as shown in Fig. 2.8) during ultrasonic assisted filtration. A 20 µm aluminum foil (TOUS LES JOURS, France) was used as erosion sensor. It was cut delicately into 8×150 mm^2 (the membrane size) to fit the filtration cell. The foil cuts were then mounted on the membrane to span the surface of the vibrating blade. Great care was taken to the application of aluminum foil in order to keep the foil surface as intact as possible, some imperfections could remain present. After cavitation erosion test (CET), the aluminum foil was demounted and back-lighted photos were taken by a digital camera (EX-FH25, CASIO, Japan) to detect whether there were some cavitation erosions (pits).

CET has been carried out using the filtration cell, and cross-flow rate was applied at 0.3 $L.min^{-1}$ in order to simulate the hydrodynamic regime of cross-flow filtration. During CET, four parameters were controlled: ultrasonic power, test pressure (P_{CET}, Pa), test duration (Dur., unit of

time) and the distance between the vibrating blade and aluminum foil, the erosion sensor (D_{sensor}, mm).

Fig. 2.17 and Fig. 2.18 present the back-lighted photos of test specimens. In Fig. 2.17, all the specimens were placed 8 mm below the vibrating blade, which is the blade-membrane distance during filtration and which is far shorter than the applied ultrasonic wave length (7.42 cm). At first, tests were carried out at different ultrasonic powers under atmospheric pressure. At the end of 2 h, cavitation pits can be observed only for the most important power (10±1 W), as shown in Fig. 2.17 d. The specimens remain intact (by this observing technique) at lower ultrasonic powers (7±1 and 4±1 W), as shown in Fig. 2.17 b and c. Further tests were performed with duration of 4 h, cracks are detected at the end of test for 7±1 W (Fig. 2.17 f), always no change of specimen for 4±1 W (Fig. 2.17 e). It should be noted that the incubation time of cavitation erosion is relatively long, compared to the reported ones in literature (Crawford, 1964; Dular *et al*., 2013; Leighton, 2007; Zeqiri *et al*., 2006), which is often in the order of magnitude of several seconds (in the same range of temperature). In addition, though exposed in the ultrasonic field for so long time, the specimens were not significantly eroded (for the eroded ones, specimen d and f): the eroded areas are very small compared to the reported ones (cited before). True, no definitive conclusion can be drawn from this simple comparison, but these results strongly suggest that the cavitation activity at D_{sensor} = 8 mm is feeble and it depends on ultrasonic power as well.

The specimens were then placed closer to the vibrating blade, at D_{sensor} = 4 mm. CET was performed again. As shown in Fig. 2.18 g-k, all the aluminum foils exposed at this distance present some cracks/ruptures or holes. The incubation time is also sharply reduced at this distance since at the end of 5 min, cracks can already be observed for specimen j while they appear only at the end of 4 h (specimen f) under the same conditions at D_{sensor} = 8 mm. Therefore, it is plausible to state that the cavitation activity is more pronounced at D_{sensor} = 4 mm than 8 mm.

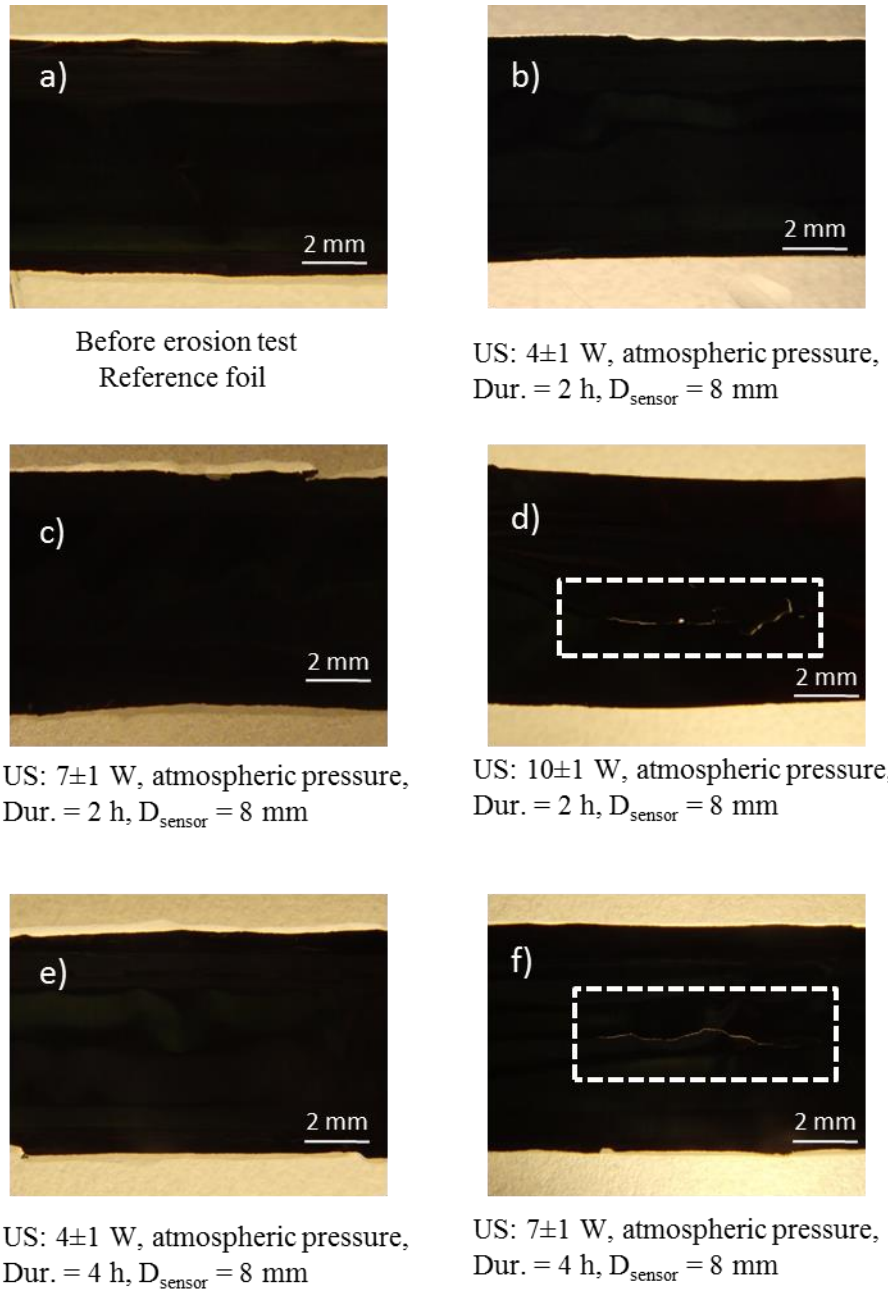

Fig. 2.17 *Back-lighted photos of aluminum foils in the cavitation erosion test (CET) under different conditions-series 1 (specimen a-f). The dark regions show where the foil is intact. The dashed boxes indicate where there are pits.*

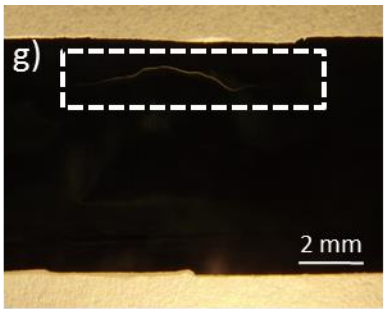

US: 2±1 W, atmospheric pressure, Dur. = 2 h, D_{sensor} = 4 mm

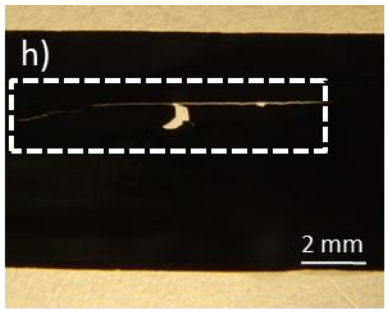

US: 4±1 W, atmospheric pressure, Dur. = 2 h, D_{sensor} = 4 mm

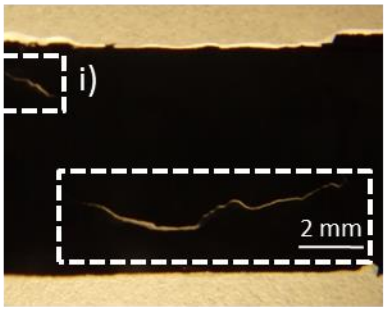

US: 7±1 W, atmospheric pressure, Dur. = 15 min, D_{sensor} = 4 mm

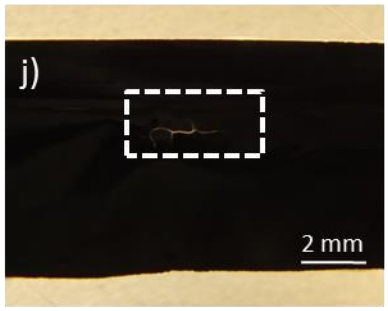

US: 7±1 W, atmospheric pressure, Dur. = 5 min, D_{sensor} = 4 mm

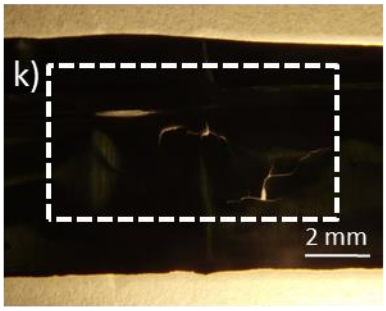

US: 7±1 W, P_{CET} = 1.2.10^5 Pa, Dur. = 4 h, D_{sensor} = 4 mm

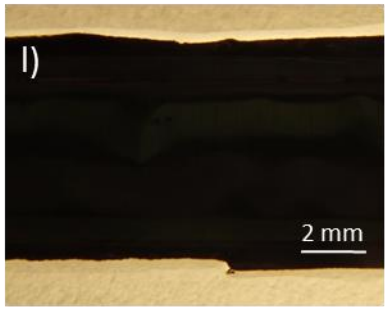

US: 7±1 W, P_{CET} = 1.2.10^5 Pa, Dur. = 4 h, D_{sensor} = 8 mm

Fig. 2.18 *Back-lighted photos of aluminum foils in the cavitation erosion test (CET) under different conditions-series 2 (specimen g-l). The dark regions show where the foil is intact. The dashed boxes indicate where there are pits.*

Such statement could be confirmed by another observation. Specimen k and l were tested when the applied pressure was higher than the atmospheric one (P_{CET} = 1.2.10^5 Pa, which is a most used TMP during filtration in this study) at these two distances. Erosions appear at D_{sensor} = 4 mm while no change can be observed at D_{sensor} = 8 mm at the end of 4 h. Bearing in mind that 8 mm is the blade-membrane distance during cross-flow filtration in this study, these results indicate that the main action zone of cavitation is in the bulk rather than at the membrane surface during filtration.

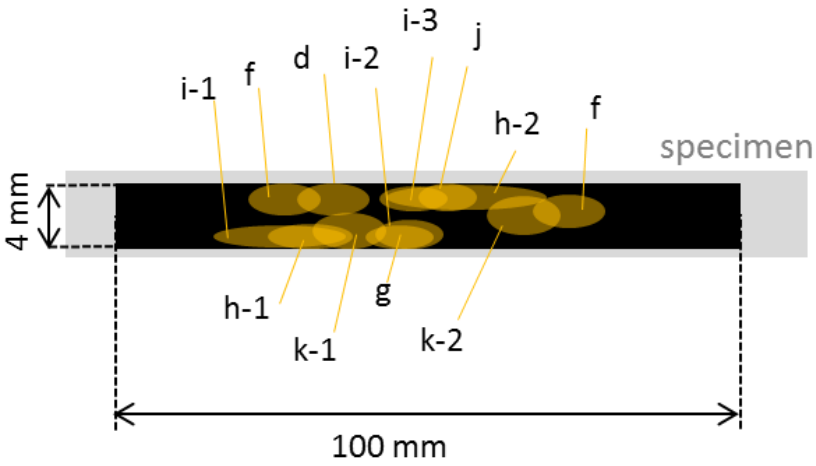

Fig. 2.19 *Zones of cavitation erosion on the specimens in CET. Roundel-covered zones represent the eroded areas of each specimen. Certain specimens present more than one eroded zones, they are distinguished by the followed number after specimen code, such as ‘‘i-1’’, ‘‘i-2’’.*

Based upon the locations of eroded areas on each specimen, Fig. 2.19 reveals the main zone of cavitation erosion in CET, which is in the vicinity of specimen center. This zone locates straightly below the sonotrode (see Fig. 2.8), it is therefore reasonable to state that ultrasonic power is relatively higher in the middle of the channel than the two ends where amplitude loss is more pronounced (as revealed in section 4.1 of this chapter).

5. SAXS measurements and analysis

5.1 Pinhole SAXS instrument

SAXS measurements were carried out at the ID2 High Brilliance SAXS/WAXS/USAXS Beamline (Narayanan *et al.*, 2001), at the European Synchrotron Radiation Facility (ESRF, Grenoble, France). Fig. 2.20 is a schematic overview of the high-brilliance beamline ID02 at ESRF. The X-ray beam with high photon flux and low divergence is provided by an undulator source. The beamline optics consist of a crypgenically (liquid nitrogen) cooled Si-111 channel-cut monochromator and a focusing torroidal mirror. The beamline is optimized for experiments using a fixed wavelength around λ = 0.1 nm (12.4 keV). The beam used in this study was collimated to 20 µm vertically and 200 µm horizontally using slits. There are two separate experimental stations, one for combined SAXS/WAXS and the other for USAXS.

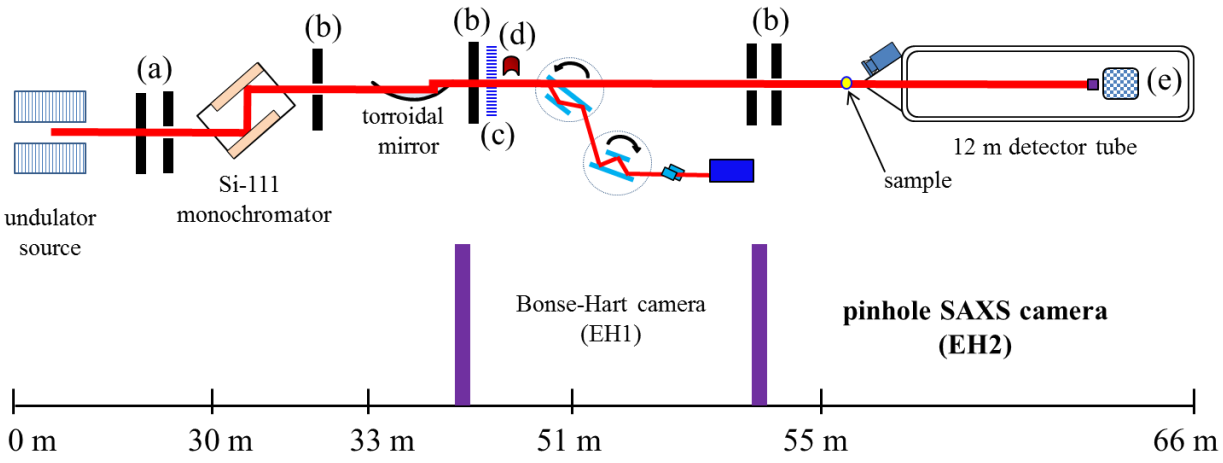

Fig. 2.20 *Schematic overview of the high brilliance beamline (ID2) at ESRF (adapted from ESRF ID2 website). The principal components are indicated in the figure. Other elements are: (a) primary slits, (b) secondary slits, (c) fast beam shutter, (d) beam intensity monitor, (e) 2-dimensional SAXS detector. The elements that are not concerned in this study are also presented in the figure but not described.*

The SAXS/WAXS setup consists of three slits, two collimation slits, one before the monochromator at 29 m and the other after the mirror at 50 m, as shown in Fig. 2.20. Two guard slits are located at 53 m and directly before the sample at 55 m. The micro slits block the region

around the primary beam in which diffuse parasitic scattering from the optics is visible. The SAXS detector is mounted on a wagon inside the 12 m evacuated detector tube. The sample-to-detector distance can be varied from 1 m to 10 m covering a wide scattering wave vector *q*-range, 6.10^{-3} nm^{-1} < *q* < 6 nm^{-1} for λ = 0.1 nm. The *q* resolution limited by the beam divergence (~25 μrad) and size (~100 μm) is about 3.10^{-3} nm^{-1}. However, the smallest *q* reachable at 10 m detector distance is also limited by the detector point spread function and the parasitic scattering to about 6.10^{-3} nm^{-1}.

The used SAXS detector is a fiber optically coupled FReLoN (Fast-Readout, Low-Noise) CCD based on Kodak KAF-4320 image sensor. The detector has an input field of 100mm x 100mm, and full frame readout rate of 3 frames/sec (2048 x 2048), but it can reach 15 frames/sec in high speed mode. This detector records the two-dimensional (2D) scattered intensity pattern of every measurement.

The raw 2D data are first corrected for detector artefacts (subtraction of dark current and readout noise, division by flatfield, and spatial distortion correction). In the second step, the pixel intensities are normalized to absolute scattering intensities (I_m):

$$I_m = \frac{1}{T_s}\frac{1}{t_s}\frac{\Delta I_s}{I_i}\frac{1}{\Delta\Omega} \qquad \textbf{\textit{Eq. 2.5}}$$

Where I_i is the incident flux, T_s is the sample transmission, t_s is the sample thickness, ΔI_s is the corrected pixel intensity and $\Delta\Omega$ is the solid angle defined by the pixel element. With the subtraction of the background from the sample container, the solvent and the parasitic scattering from the elements upstream, the absolute scattered intensities of the sample is obtained. The normalized two-dimensional scattering pattern is then transformed to the corresponding one-dimensional scattering curve by azimuthal averaging after masking the unusable regions of the pattern.

5.2 Combination of SAXS-filtration measurements

5.2.1 Installation

At the sample position in Fig. 2.20, the ‘‘SAXS Cross-Flow US-coupled Filtration Cell’’ was mounted in a motorized stage, which allows monitoring by SAXS the concentration and structural organization of suspensions at different distances from the membrane as well as at different positions along the membrane during filtration. All the devices described in Fig. 2.9 were installed in experimental hutch 2 (EH2) with respect of the operation manual of each device. The photos of overview setup and ‘‘SAXS Cross-Flow US-coupled Filtration Cell’’ captured in EH2 are shown in Fig. 2.21.

5.2.2 Determination of membrane position

In this study, colloidal organization neighborhood of the membrane surface was investigated, which requires at first the determination of membrane position along axis z (the distance from the membrane surface, as already shown in Fig. 2.8b). Therefore, the X-ray beam was accurately mapped through the filtration cell by transmitted intensity measurements. Fig. 2.22 shows a schematic view of the SAXS-filtration cell containing deionized water at rest and the transmitted intensity through it at different distances z from the membrane surface. Several zones have been identified as a function of z. The first zone (Z1) corresponds to the thick polycarbonate support below the membrane where the X-ray beam was completely absorbed. The end of the zone is defined by the increase of the transmitted signal (z = -200 µm) where the X-ray started to pass through the porous membrane. Hence, the second zone (Z2) represents the membrane which is 200 µm of thickness. The X-ray signal in the third zone (Z3) originated partially from the liquid sample but was affected by the membrane absorption. Depending on the beam width, this zone measured 20 µm. Finally, at Z4, the transmitted intensity was constant at high level, suggesting no further influence of membrane in this zone, which was, therefore, the SAXS measurements zone (from z = 20 µm to z = 2000 µm).

a)

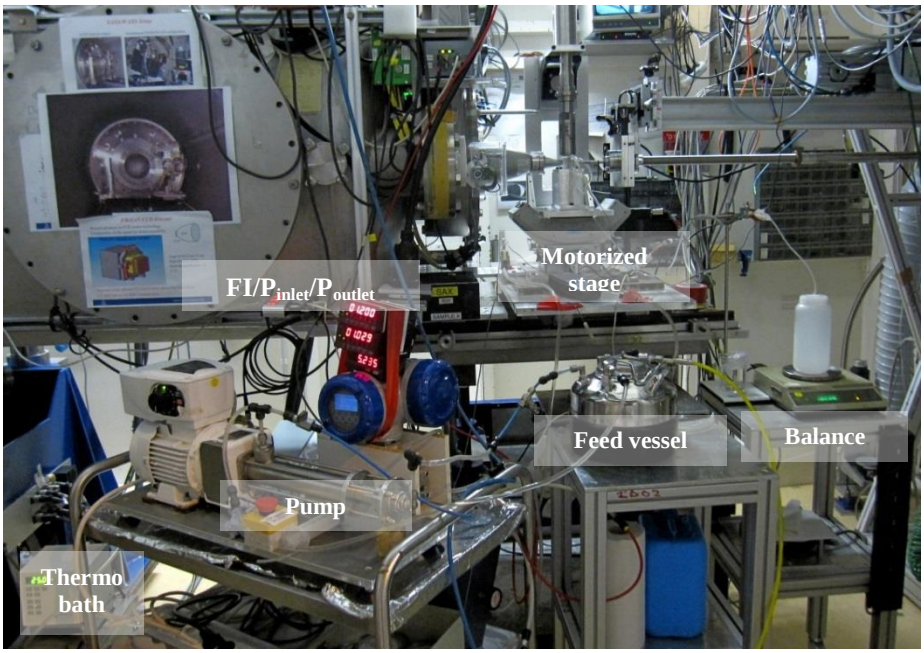

b)

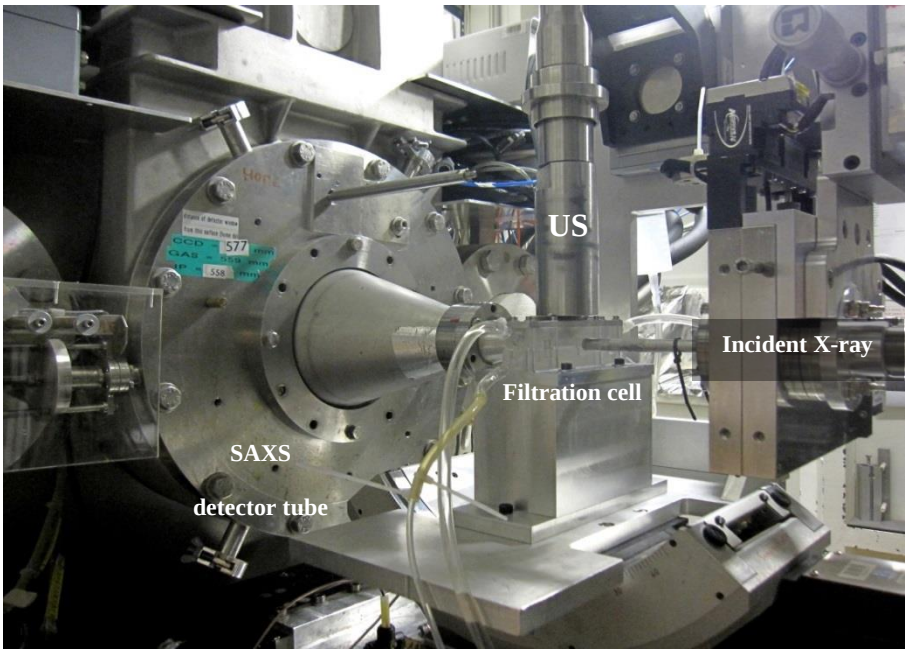

Fig. 2.21 *Combination of SAXS-filtration measurements, photos captured in EH2 at ESRF. a) overview of SAXS-filtration combined setup, b) ''SAXS Cross-Flow US-coupled Filtration Cell''.*

On the basis of this measurement, the membrane position was calibrated for three observation windows. Though the exploitable values were obtained from z = 20 µm, the real SAXS measurements began at z = -100 µm to ensure the gain of intensity values close to the membrane.

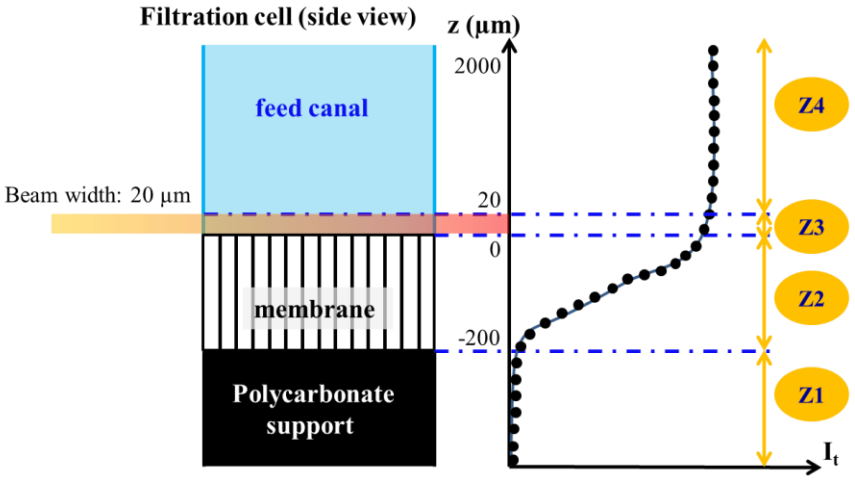

Fig. 2.22 *Evolution of the transmitted X-ray signal with distance z from the membrane surface through the SAXS-filtration cell. Z1 corresponds to the polycarbonate barrier below the membrane, Z2 represents the membrane, Z3 is a zone above the membrane where the SAXS signal is perturbed, and finally Z4 is the SAXS measurement zone.*

5.3 Analysis of SAXS results

2D SAXS patterns of investigated colloidal dispersion samples at a position close to the membrane surface during filtration are presented in Fig. 2.23. The patterns have different features: circle-shape can be observed for Laponite dispersion (with tspp), skim milk and SNC dispersions, whereas the pattern of CNC has an ellipse-shape, and anisotropic patterns with marked diffuse peaks is presented for the natural gel (SWy-2 T3 and NAu-1 T3). Based upon the 2D SAXS pattern, different analyses were performed, which will be discussed below.

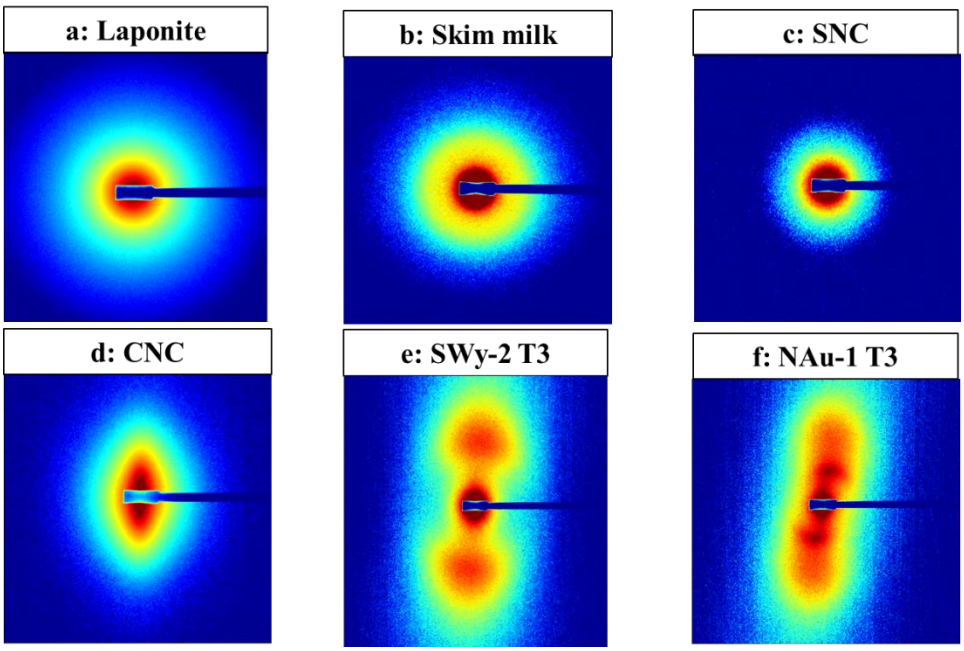

Fig. 2.23 *2D SAXS patterns of investigated colloidal dispersion samples at a position close to the membrane surface during filtration. Sample-detector distance:1 m from a to d; 10 m for e and f.*

5.3.1 Analysis of the anisotropy

Some qualitative information could be directly obtained from the two-dimensional patterns such as the anisotropy and orientation of particles.

To determine the magnitude of anisotropy for SAXS pattern, the scattering along the vertical (I_V) and horizontal (I_H) axes was calculated by integrating the scattered intensity along a sector of 30º around the vertical and horizontal direction, respectively. For comparison, the anisotropic level was represented by the intensity value of I_V and I_H at a fixed scattering vector (q = 0.5 nm^{-1}). The anisotropy magnitude is then defined by the ratio of these two values (I_V/I_H), as shown in Fig. 2.24.

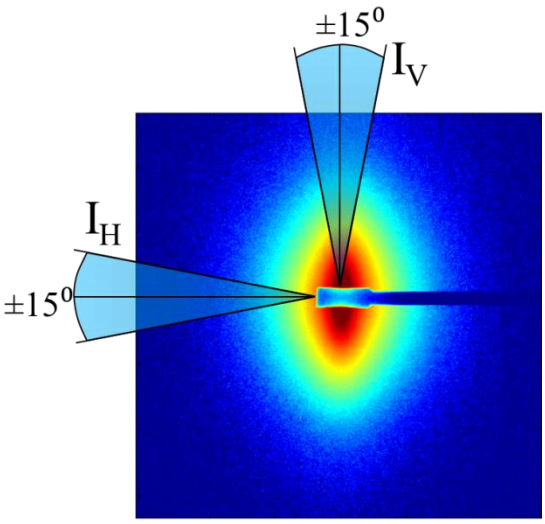

Fig. 2.24 *Demonstration of the anisotropy magnitude calculation*

5.3.2 Determination of colloidal concentration from 1D I(*q*) profiles

As mentioned above, a 2D SAXS pattern and 1D intensity profile denoted as I(*q*) were obtained. Quantitative modeling of I(*q*) provides the mean particle size, shape and their structural arrangement (David *et al*., 2008). It should bear in mind that the scattered intensity originates from the contrast that represents the electron density difference between the particle and the medium in liquid sample. Therefore, for a defined particle-solvent system at high *q*-values range where S(*q*) =1, the scattered intensity is proportional to the number of particles per unit volume. In other word, the concentration of solution can be determined from the scattered intensity at high *q*-values range.

To reach such goal, SAXS measurements on several colloidal dispersions of known concentrations were first performed in a temperature controlled (25±1 °C) flow-through capillary cell (diameter ~ 2 mm). This allowed establishing a relationship between the scattering intensities and the concentrations, leading to a calibration curve. With the obtained calibration curves, the concentration of concerned colloidal dispersions samples could be determined by introducing the corresponding absolute scattered intensity at a given scattering vector. It should be noted that the normalized background scattering was systematically subtracted. Despite the parasitic background from the optical device and windows, this background includes the sample container

Tab. 2.6 *Background solvent and chosen q-values, as well as the intensity-concentration relationship of investigated colloidal dispersions*

Colloidal dispersion	Background solvent	Chosen *q*-value (nm^{-1})	Intensity-Concentration relationship
Laponite	Deionized water	1.2	$I(q = 1.2\ nm^{-1}) = 0.0497\ \Phi_v$
Skim milk	Ultrafiltrate[1]	0.7	$I(q = 0.7\ nm^{-1}) = 0.0338\ C/C_o$
SNC	Deionized water	0.2	$I(q = 0.2\ nm^{-1}) = 0.485\ \Phi_m$
CNC	Deionized water	0.5	$I(q = 0.5\ nm^{-1}) = 0.0838\ \Phi_m$

and the solvent which depends on colloidal dispersions. Tab. 2.6 summarizes the background solvents and the chosen scattering vectors as well as the intensity-concentration relationship for the investigated colloidal dispersions in this study. The related calibration curves are presented in Fig. 2.25. These equations have been established in the flat level in the Kratky plot (q^{-2} power law decay) corresponding to the form factor P(q) of the particles which is not affected by the change in inter-particle interactions (described by the structure factor S(q)) and therefore valid even at higher concentrations.

This method has already been used (David *et al*., 2008; Jin *et al*., 2014; Pignon *et al*., 2012, 2004, 2003) to determine the evolution of the dispersions concentration as a function of the distance z from the membrane during filtration. In other words, the concentration profiles in the accumulated layers during filtration are determined by this method. It can provide a high accuracy of concentration analysis (standard deviation between 0.5 % and 1 % for different samples). Again, at the chosen q-values range, the scattering intensity of sample is not affected by neither the structure factor nor the possible anisotropy of the SAXS pattern, as already discussed before.

[1] Permeate of skim milk after ultrafiltration, which contains lactose and some minerals.

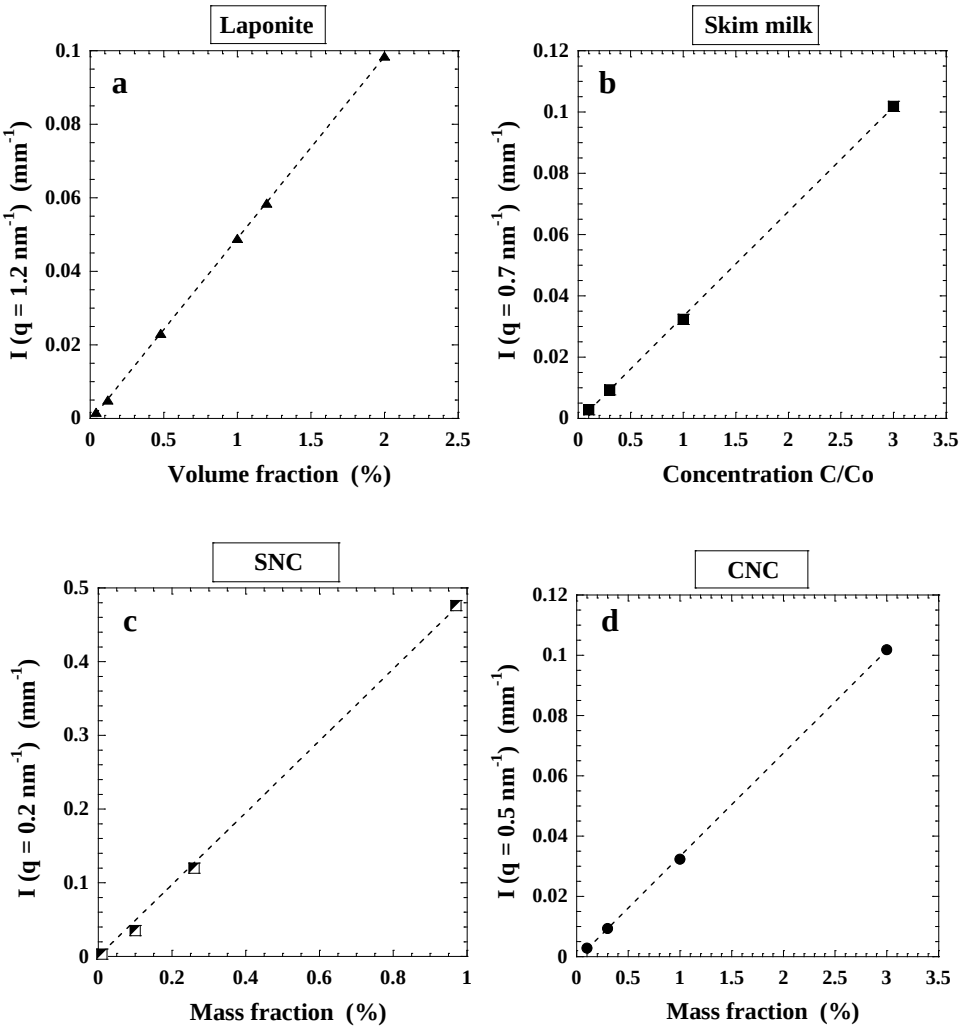

Fig. 2.25 *Calibration curves of investigated colloidal dispersions. Scattered intensities are normalized by thickness of sample container (mm^{-1}). Dotted curves correspond to the linear curve fitting (R>0.99).*

5.3.3 Determination of colloidal concentration from structure factor

The 2D SAXS patterns of natural clay suspensions are anisotropic, as shown in Fig. 2.23. These anisotropic patterns are due to the mutual alignment of the particles. From structure factor curve (q^2*I(q) as a function of q) it can exhibit a marked diffuse peak which correspond to the short-range positional order of the platelets (Fig. 2.26a). An estimate of the experimental average interparticle distance can be deduced from the position of the maximum in the oscillations of the scattering intensity as $d = 2\pi/q_{pic}$, and allowed to deduce the swelling law $d(\Phi_V)$ which relate

the interparticle distance to the volume fraction (Fig. 2.26b). Depending on the volume fraction domain (sol or gel) and of the fraction size of the SWy-2 T3 or NAu-1 T3 suspensions, the swelling laws followed different power law of the volume fraction, being demonstrated in Tab. 2.7. As already being shown (Paineau *et al.*, 2011), in the sol phase the average interparticle distance d tends to scale as $\Phi_v{}^{-1/3}$, corresponding to a 3D swelling of freely rotating object. In the gel domain d scales as $\Phi_v{}^{-1}$, pertaining to the unidimensional regime related to the local order of the platelets.

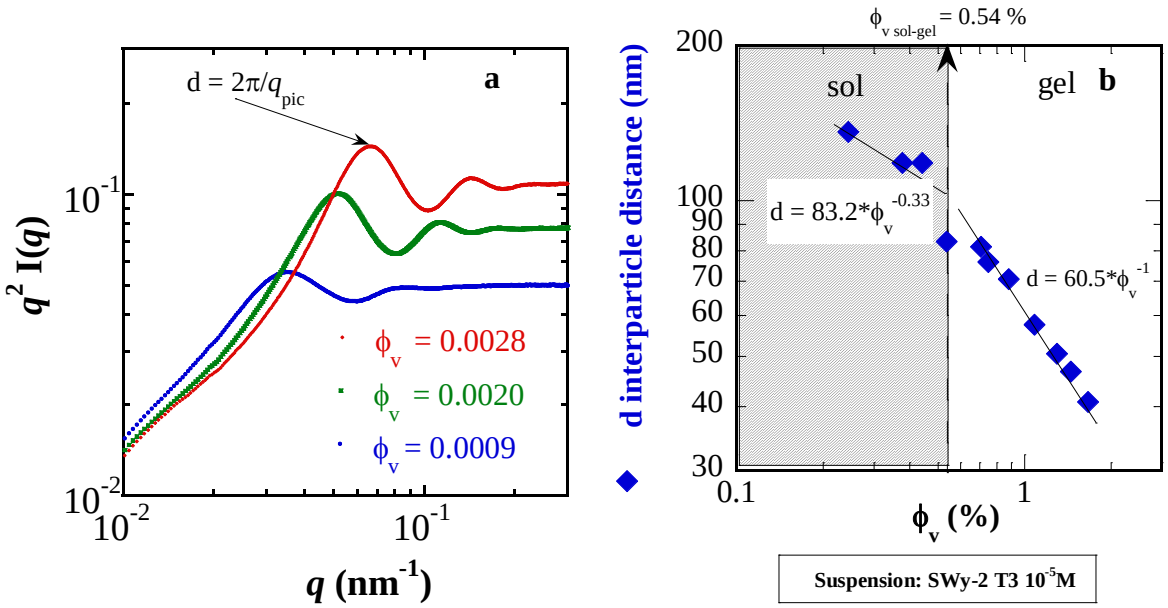

Fig. 2.26 Determination of volume fraction of the swelling clay suspensions. a: structure factor of SWy-2 T3 with different volume fraction; b: swelling law of SWy-2 T3.

Tab. 2.7 *Swelling laws of SWy-2 T3 and NAu-1 T3 suspensions: interparticle distance as a function of volume fraction (data from (Paineau et al., 2011) and (Michot et al., 2013)) and power law adjustment pertaining to the sol or gel phase domain.*

Suspensions	Swelling law: $d(\Phi_v) = a.\Phi_v{}^{-b}$		volume fraction at the sol/gel transition ($\Phi_{v,SG}$)
	Sol phase	Gel phase	
SWy-2 T3	a = 83.2; b = 0.33	a = 60.5; b = 1	0.0054
NAu-1 T3	a = 89.6; b = 0.33	a = 63.6; b = 0.94	0.0083

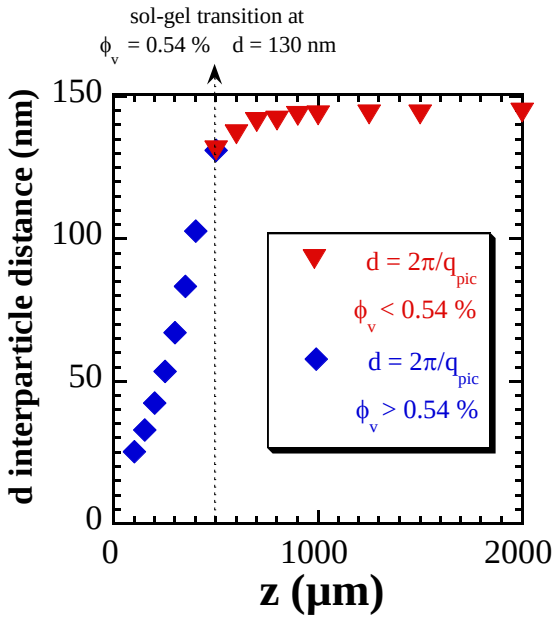

Fig. 2.27 *Example of d(z) curve: Interparticle distance as a function of distance from the membrane z during filtration of SWy-2 T3*

In order to access to the volume fraction in the concentrated layers during filtration, the Kratky plot of the scattered intensity corresponding to the patterns registered in the "SAXS Cross-flow US-coupled Filtration Cell" is plotted for each z position. From the first peak maximum of these curves the corresponding inter-particle distance $d(z) = 2\pi/q_{pic}$ is extracted at each z position in the concentrated layers (Fig. 2.27). The concentration profile $\phi_v(z)$ can be deduce reliably by introducing the swelling law $d(\phi_v)$.

6. Analytical methods

This section will present all the analytical methods involved in this study. Collaborated with several laboratories, some of them were performed by collaborators. They will be indicated in the concerned parts.

6.1 Rheological measurements

The rheological behavior of the colloidal dispersions was studied with shear rate controlled rheometers (HAAKE MARS; ARG2 and DHR3, TA Instrument). Cone and plate geometries were employed (diameter 60 mm and angle 1° for MARS; diameter 49 mm, angle 4°21’ for ARG2 and DHR3), as presented in Fig. 2.28. In order to avoid interfacial effects, the surfaces of the apparatus were covered with sand-paper with a roughness of 200 µm for ARG2 and DHR3. Measurements were carried out at a temperature of 25±1°C. The atmosphere around the sample was saturated with water to prevent evaporation during the measurement (Magnin and Piau, 1990).

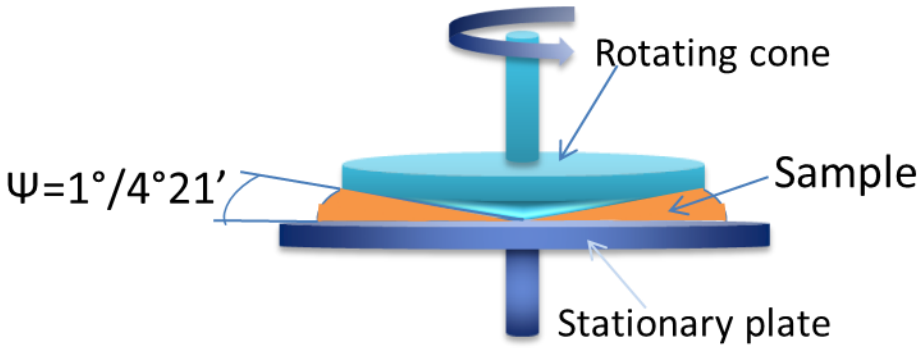

Fig. 2.28 *Schematic representation of used rheometers with cone-plate geometries*

6.2 Gravimetric analysis

This analysis was used to determine the concentration of colloidal samples, which can serve to determine the rejection rate (TR) of membrane. It is also known as dry weight

measurements, by weighing the samples before and after the evaporation of water. Taking a dispersion sample of 10 mL, the analysis was carried out by moisture analyzer (Sartorius MA40) and drying proceeded at 105 °C.

6.3 Microscopic analysis

Nanocrystals morphology was investigated by two microscopic measurements: Atomic Force Microscopy (AFM) and Field-emission Gun Scanning electron microscope (FEG-SEM). The samples from our experiments were sent to Laboratoire Génie des Procédés Papetiers (LGP2) where involved analyses were performed by Ahlem Roudhane.

AFM measurements were performed on a multimodal AFM (DI, Veeco, Intrumentation group, USA) using a mica substrate on which a drop of a diluted nanocrystals suspension was deposited and left to dry at room temperature over night before analysis. Each sample was characterized in tapping mode with a silicon cantilever (OTESPA®, Bruker, USA) at four different locations and a 3x3µm² scanning area. Topographical images were captured and subjected to 1st order polynomial flattening to reduce the effects of bowing and tilt. Image J software was then used to extract particle diameter and size distribution.

FEG-SEM was also used to observe the nanostructure of SNC suspensions (Ultra 55®, Zeiss, Germany). A thin Au-Pd conductive coating (around 1 nm) was deposited on top of the sample to reduce charge effect. The images obtained at 3 kV accelerating voltage (EHT) and working distance of 6 mm lead to the best compromise in terms of SNC contrast and residual charge effect.

6.4 COD analysis

For starch nanocrystals samples, chemical oxygen demand (COD) analysis was also carried out at LGP2 with the help of Ahlem Roudhane using COD cell tests purchased from WTW Company (COD Cell Test Model 14895 and C4/25). Several suspensions at different concentrations between 0.002 % and 0.1 % (w/w) were prepared and their COD value was

measured as recommended by the WTW procedure. A linear relationship, with a very good regression coefficient (R^2=0.9995), was obtained between COD values and SNC suspension concentrations. The calibration curve allowed estimation of the mass concentration of SNC in permeates with an accuracy of 5%.

6.5 Mean particle size analysis

Mean particle size and particle size distribution were assessed by Dynamic Light Scattering (DLS), using a particle size analyzer (VASCO, Cordouan Technologies, France). For an accurate measurement, all samples were diluted to minimize multiple scattering. Permeate samples were analyzed without dilution. For each measurement, one milliliter was injected in the measurement cell. Each measurement was done in triplicate. Particle size was expressed as the mean diameter on intensity basis or diameter-intensity distribution. Results showed a good reproducibility with a standard deviation of about 5 % of the measured values.

6.6 Turbidity and pH measurements

For milk samples, the turbidity was measured using a turbidimeter (AL450T-IR, TURBIDIRECT) by transmission of LED light (λ = 860 nm) through a path, with an accuracy of ±0.01 NTU. The pH of milk suspensions was measured at 25 °C using a pH electrode connected to a pH meter (CRISON PH25).

Conclusions

This chapter described the investigated colloidal suspensions, the experimental systems as well as all analytical methods used in this study. Colloidal suspensions of different structures are filtrated, including the synthetic disk-like clay dispersions (Laponite), two types of naturally swelling plate-like clay dispersions (Wyoming Montmorillonite and Australia Nontronite), suspensions of casein micelles (skim milk) and suspensions of polysaccharide nanocrystals (round-shape starch nanocrystals and rod-like cellulose nanocrystals).

A novel ''SAXS Cross-Flow US-coupled Filtration Cell'' has been developed to, on one hand, apply ultrasonic waves close to the flat membrane by embedding in the feed compartment a thin titanium vibrating blade connected to a 20 kHz ultrasonic generator and on the other hand, to monitor in-situ the colloidal organization of the concentrated layer by SAXS.

In addition, the used ultrasonic system has been characterized including the vibration determination, power estimation, etc. Results show that the vibration of the blade embedded in the filtration cell is not homogeneous, and can be distinguished by four blocks. The effective (dissipated) acoustic power increases with input electric power, and the energy yield varies from 35 to 83 %. Power loss seems to be more important at high-level input electric power. The main action zone of cavitation in this study is in the bulk rather than at the membrane surface during filtration, and rather in the zone located straightly below the sonotrode than the two ends.

SAXS measurements and analysis have also been depicted in details: how to determine the membrane position, how to analyze the 2D SAXS patterns and 1D I(q) profiles, and how to determine the colloidal concentration from different approaches.

3

Ultrasonic assisted ultrafiltration of clay suspensions

From this chapter, obtained results of this work will be presented by three parts. Chapter 3 and 4 will present the results at both macro-scales and nano-scales of ultrasonic assisted cross-flow ultrafiltration of 4 different families of colloids: synthetic clay dispersions, natural swelling clay dispersions, skim milk and polysaccharide nanocrystal suspensions (9 suspensions investigated in total). Chapter 5 will give a review of results followed by an integrated analysis, including the calculation of matter accumulation in the filtration channel, plotting of yield stress charts of the channel and modeling of this process in order to predict the permeate flux.

In this chapter, the investigation of three clay suspensions during the process of ultrasonic assisted ultrafiltration at both macro-scales and nano-scales will be presented. Behaviors of Laponite dispersions in this process have been fully studied with different concentrations and different structural properties; their flow properties when submitted to ultrasound or pre-shearing have also been evaluated for better understanding of phenomena as well as further investigations in chapter 5. Two natural clay suspensions were filtrated as well in order to consolidate the understanding of mechanism.

1. Laponite dispersions

1.1 Introduction

As synthetic clay, Laponite suspensions have already been widely studied (see chapter 2 section 1.1). Ultrafiltration of these dispersions have also been explored in our previous work (Pignon *et al*., 2012). In these previous experiments, the dispersions were studied by *in-situ* SAXS during ultrafiltration, but without the ability to apply ultrasound. In this section, 7 samples were investigated whose properties are listed in Tab. 3.1, with ages of 12 days or 26 days. The time tp that elapsed between the end of preparation and the investigations will be indicated in each case. In the discussion, the term ‘‘Lap-tspp0’’ or ‘‘Lap-tspp6’’ will be also used to denote the pure Laponite dispersions or those containing peptizers without regard to the volume fraction, as already defined in chapter 2 section 1.1.

Tab. 3.1 *Investigated samples of Laponite suspensions in this section*

Sample name	Volume fraction Φv	C_{tspp} of Peptizer	Ionic strength	pH
Lap0.48-tspp6	0.48 %	6 %		
Lap1-tspp6	1 %	6 %		
Lap1-tspp0	1 %	0 %		
Lap2-tspp6	2 %	6 %	10^{-3} *M [NaCl]*	10
Lap2-tspp0	2 %	0 %		
Lap3-tspp6	3 %	6 %		
Lap3-tspp0	3 %	0 %		

1.2 Flow properties of Laponite dispersions

In this section, Laponite dispersion samples have been specifically prepared for investigation of their flow properties after different treatments (e.g. pre-shearing and ultrasonic treatment). It provides information to better understand the following results of filtration (section 1.4-1.5). The studied volume fraction (ϕ_v) ranges from 1 % to 3 %. Two series of samples were prepared: one with 6 % of peptizer (tspp) and the other without it.

1.2.1 Steady-state flow properties at different volume fractions

First of all, steady-state flow properties of Laponite dispersions without any treatment were revealed in Fig. 3.1, presenting the measured shear stresses (τ) in steady shear flows. These curves show the influence of volume fraction and addition of peptizers on the shear stresses of the dispersions when a constant shear rate ($\dot{\gamma}$) is applied.

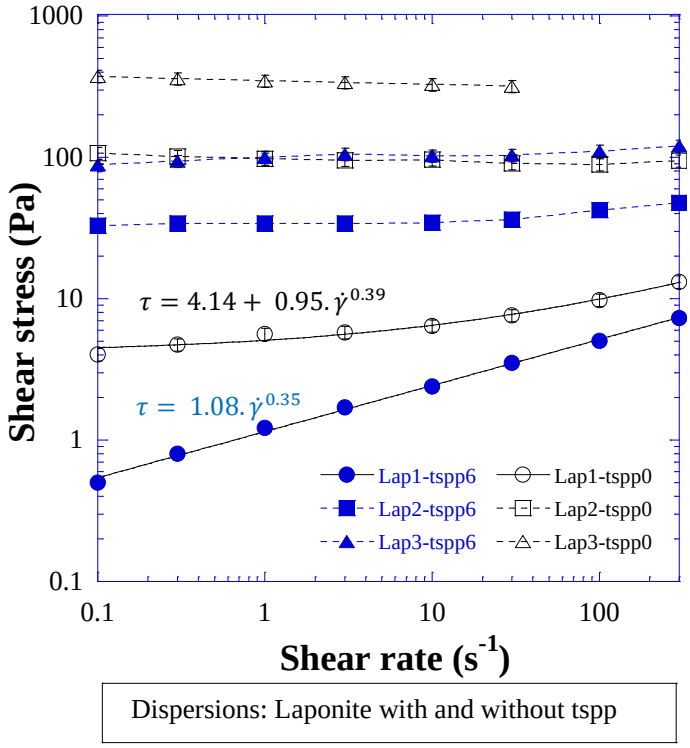

Fig. 3.1 *Steady-state flow curves of Laponite dispersions at different volume fractions and at different peptizer concentrations without treatment. T = 25±1 °C, tp = 12 days. Solid lines represents curve fitting by power law or Herschel-Bulkley law.*

It appears that dispersions which contain no peptizer follow stress curves with a stress plateau (unfilled symbols). As already discussed in literature (Martin et al., 2002), the stress levels at very low shear rates tend towards a yield stress value corresponding to the dynamic yield stress of the gelled dispersions. Addition of peptizers reduces this dynamic yield stress, as shown in Fig. 3.1 (filled symbols). These results indicate that the network of mechanical links of pure Laponite dispersions has been weakened or dissociated by the addition of peptizers.

As mentioned in chapter 1 (section 4.2), non-Newtonian flow behaviors can be described by power law or Herschel-Bulkley law. Two curves of ϕ_v = 1% have been fitted by these laws, presented by the solid lines in Fig. 3.1. Yield stress of Lap1-tspp0 has been revealed while it is vanished for Lap1-tspp6. For this low volume fraction of 1 %, the stain field is homogeneous in the wall gap of the tools and no slip at the wall or localization phenomena have been observed. As volume fraction rises beyond 1 %, the steady stress levels remain quite constant, thus neither

of the two laws is capable to describe such behavior perfectly. This phenomenon is associated with a particular mode of deformation, in which all shear is localized in a thin layer of the sample (Frédéric Pignon et al., 1996). In this case, the values of shear stress at lowest apparent shear rate of this investigation ($\dot{\gamma}$ = 0.1 s^{-1}) were considered as the estimated yield stresses of correspondent samples. It will be further discussed in section 1.2.4.

1.2.2 Effect of sample pre-shearing on flow properties

The dispersion during filtration process is subjected to shear-induced hydrodynamic force. In addition, Laponite dispersions flow over time when shaken, agitated, otherwise stressed, due to their thixotropic behavior (Martin *et al.*, 2002). It has been reported that Laponite dispersions often take several hours to return to their initial higher viscosity, which leaves us enough time to carry out the rheological measurements (Pignon *et al.*, 1998). Therefore, their flow properties have been re-characterized after being sheared at $\dot{\gamma}$ = 300 s^{-1} in order to determine the effect of sample pre-shearing. Duration of pre-shearing was between 5 min to 25 min, depending on samples (until the measured shear stress reach steady-state in constant shear rate $\dot{\gamma}$ = 300 s^{-1}). Fig. 3.2 shows the correspondent steady-state flow curves, the unfilled symbols represent the samples after pre-shearing.

It should be noted that the "steady-state" in the case of pre-shearing refers to a short-term steady state in the order of several minutes, because their flow properties will finally return to the initial state (at rest) after several hours from the pre-shearing, as mentioned before. As the time scale of build-up (several hours) is far from the time scale of measurements (few minutes), we can estimate the rheological behavior of the pre-shearing dispersions and make the assumption that this behavior is not very affected by the slow build-up of the thixotropic structural organization. As shown in Fig. 3.2a, the effect of pre-shearing on flow properties of Laponite dispersions is significant, especially for those with peptizers. When submitted to the pre-shearing stress, the dispersions flow more easily, e.g. at lower apparent shear rates the stress levels are reduced by two orders of magnitude for Lap1-tspp and Lap2-tspp (circles and squares in Fig. 3.2a). A great reduction of stress levels can also be observed for Lap1-tspp0 (Fig. 3.2b). However, effect of pre-shearing on flow properties is limited for the two dispersions without peptizer more concentrated (triangles and squares in Fig. 3.2b).

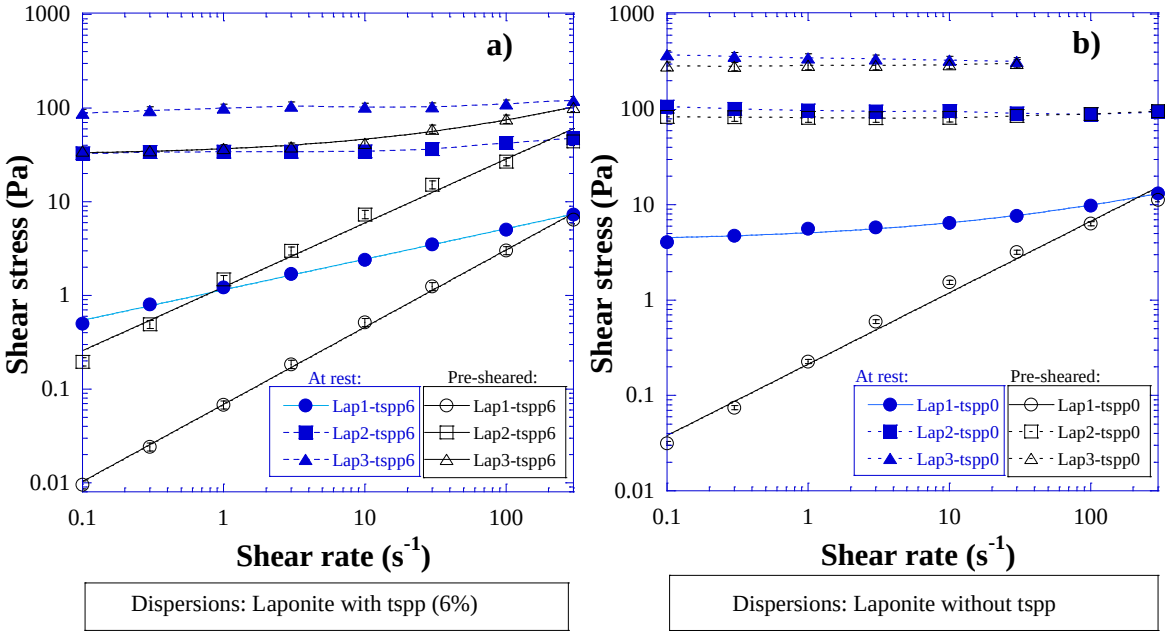

Affiliated table:

Samples	Curves fit values		
	τ_0(Pa)	K(Pa.s^n)	n
Lap1-tspp6-at rest	/	1.08	0.35
Lap1-tspp6-pre-sheared	/	0.068	0.82
Lap2-tspp6-pre-sheared	/	1.25	0.69
Lap3-tspp6-pre-sheared	31.59	5.21	0.46
Lap1-tspp0-at rest	4.14	0.95	0.39
Lap1-tspp0-pre-sheared	/	0.21	0.75

Fig. 3.2 *Steady-state flow curves of Laponite dispersions after pre-shearing. a) Laponite dispersions with peptizers b) Laponite dispersions without peptizer. T = 25±1 °C, tp = 12 days. Solid lines represents curve fitting by power law or Herschel-Bulkley law (corresponded fitting values are presented in affiliated table).*

It was demonstrated that the mechanical interaction of Laponite dispersions evolve with their volume fractions (Pignon *et al*., 1996). They exhibit a mechanically weak fibrous structure at low volume fraction and a denser network of micron-sized aggregates could form which is mechanically more resistant when volume fraction rises. This mechanical links could be

weakened by addition of peptizers, which allows an easier destruction of network by shear. It can explain the main observations of Fig. 3.2. Besides, one stress value is interesting to be noted: 100 Pa. It seems to be the critical stress beyond which the applied pre-shearing can hardly destroy their mechanical network.

These different behaviors at low volume fraction (1%) and high volume fraction would have crucial importance in ultrafiltration process, as shown in the next section that the volume fraction increases near the membrane surface. Under the shear of the cross-flow filtration, the time-dependent properties of these colloidal dispersions and their evolution with volume fraction will affect the way the deposited layer forms during filtration.

1.2.3 Effect of ultrasonic treatment on flow properties

During ultrasonic-assisted filtration process, effect of ultrasound (US) on Laponite dispersions can be determined (and will be presented in the next section), it reveals the current state of dispersions in the process, but it is affected by several parameters, such as the hydrodynamic force, compression force etc. In this section, effect of US on intact Laponite dispersions will be presented. US treatment was exerted using the designed blade for filtration cell (chapter 2, Fig.2.8). 20 ml of prepared Laponite samples were gently laid in a 100 mL rectangle container. US treatment lasted 5 min (the residence time during real filtration) with the commanded amplitude of 80 % (correspond to an input power of 2 $W.cm^{-2}$). Then this sonicated sample was studied on the rheometer around 5 min after the US-treatment. The correspondent steady-state flow curves are presented in Fig. 3.3, the red unfilled symbols represent the samples after US treatment.

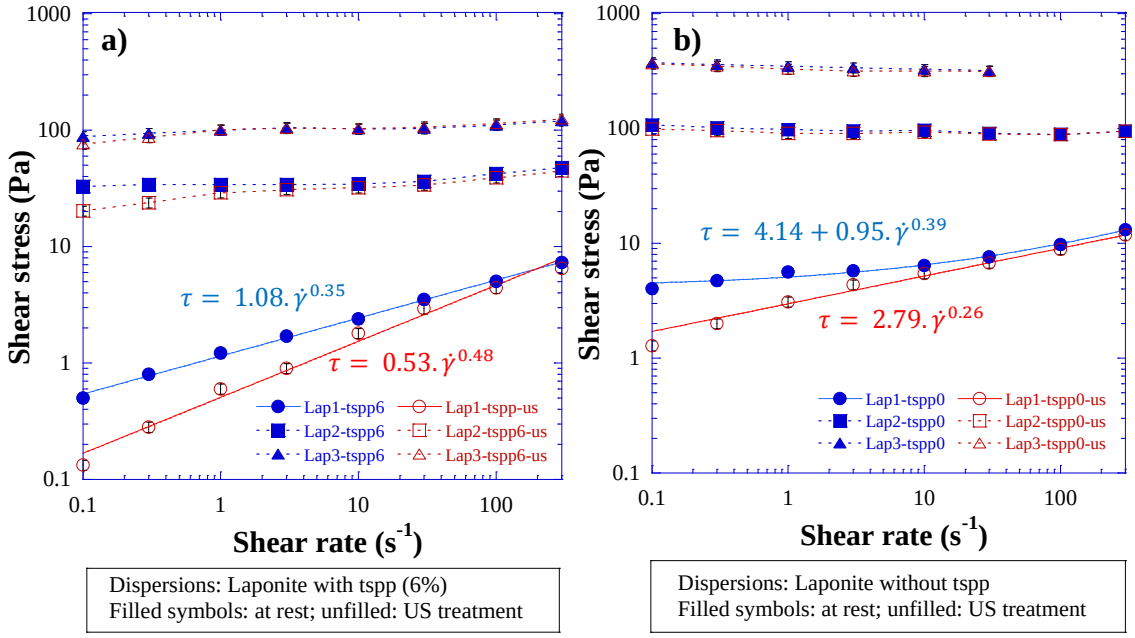

Fig. 3.3 *Steady-state flow curves of Laponite dispersions after US treatment. a) Laponite dispersions with peptizers; b) Laponite dispersions without peptizer. T = 25±1 °C, tp = 12 days. Solid lines represents curve fitting by power law or Herschel-Bulkley law.*

Similar effect as pre-shearing is observed: the samples after US treatment flow more easily (increase of shear-thinning index n or decrease even removal of yield stress), though the effect is less significant than the applied pre-shearing. This comparable effect implies that US can also weaken the mechanical links of Laponite dispersions like shearing force does. Again, the samples concentrated (ϕ_v = 2 % and 3 %) without peptizer whose yield stresses are above 100 Pa were barely affected by the applied US treatment.

1.2.4 Summary

Flow properties of Laponite dispersions under different conditions have been discussed from section 1.2.1 to 1.2.3. Yield stresses (τ_o) of concerned samples in different circumstances have been estimated either by the curve fitting or intercept at $\dot{\gamma}$ = 0.1 s^{-1}. The curves of yield stress/volume fraction dependence for the two series of Laponite dispersions are plotted in Fig. 3.4.

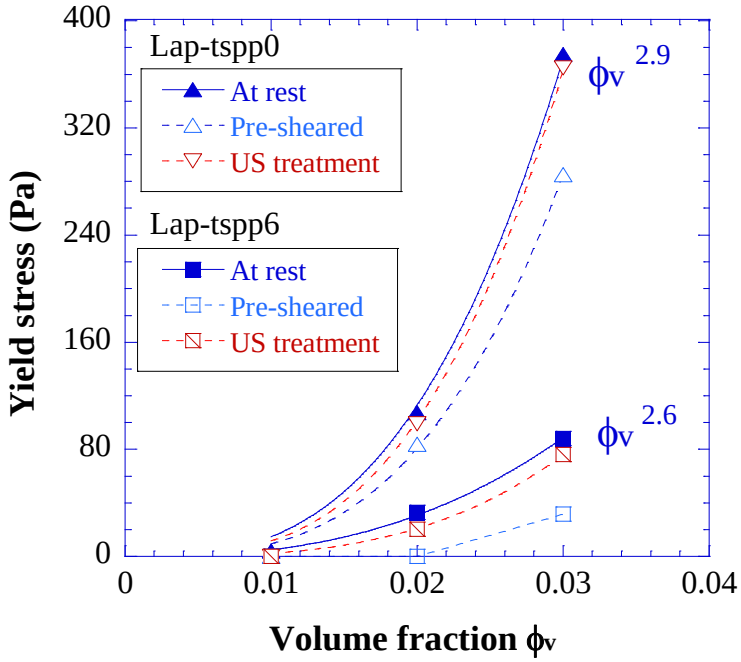

Affiliated table of curve fitting values:

Dispersion	Law of yield stress (τ_o)/volume fraction (Φ_v) dependence	
Lap-tspp0	$\tau_o = 1.12.10^7.{\Phi_v}^{2.94}$	***Eq. 3.1***
Lap-tspp6	$\tau_o = 8.50.10^5.{\Phi_v}^{2.61}$	***Eq. 3.2***

Fig. 3.4 *Yield stress/volume fraction dependence of Laponite dispersions. T = 25±1 °C, tp = 12 days. Solid lines represents curve fitting by appropriate law, correspond fitting values are presented in affiliated table.*

It is reported that the yield stress/volume fraction dependence of Laponite dispersions is governed by power law. In the volume fraction range of 0.6-2 %, the dependence follows $\tau_o \propto {\Phi_v}^{3\pm0.3}$ for those without peptizer (Pignon *et al.*, 1996). Based on this knowledge, curves in Fig. 3.4 are fitted by power law; a good agreement is then found between the reported dependence relation and the fitting value of this study.

Otherwise, effect of pre-shearing and US treatment on yield stress of Laponite sample is revealed. Both treatments reduce their yield stress levels. The reduction is more important for Laponites with peptizers whose yield stresses are much lower than those without peptizer. It

suggests that Laponite dispersions with peptizers (6%) are more susceptible to shearing force or ultrasonic force than those without peptizer, resulting from the reduction in attractive forces between the particles, as discussed in chapter 2. This difference in behavior will have some consequences on the particle accumulation near the membrane surface during the ultrafiltration process.

1.3 Effect of US on Laponite dispersion properties during filtration

In this section, properties of processed Laponite dispersions in the filtration will be presented. They were characterized by two approaches: rheometric and *in-situ* SAXS measurements.

1.3.1 Flow properties (in the filtration)

In Fig. 3.5 the steady state flow curves of Lap1-tspp6 are plotted. For each suspension, four samples were analyzed: one at rest and three others were taken from bulk dispersions during cross-flow filtration with/without ultrasound. In fact, a sampling valve has been added in the filtration cycle which allows us picking up a sample of filtrated suspensions at any of filtration. Then the rheological behaviors of this sample were determined 5 minutes after sampling. For the dispersions at rest, which are not subjected to the shear stress of pump in the filtration setup, a shear thinning fluid behavior can be observed and the stress levels at all shear rates are relatively high. When submitted to a strong shear stress resulting from the pump, the dispersion flows more easily, especially at lower shear rates where the stress levels are reduced by two orders of magnitude, as demonstrated by the curve of filled circles in Fig. 3.5. These results indicate that the network of mechanical links of Lap1-tspp6 has been weakened or dissociated by the additional shear stress due to the pump. After 40 min of conventional filtration, ultrasonic waves were applied simultaneously for another 40 min. We noticed that a 40 min ultrasonication did not have a marked influence on the dispersions already sheared by the pump, but additional break-up could still be observed. Indeed, without any change in the shear-thinning behavior, the shear stresses decrease at given shear rates; when ultrasound was switched off, the shear stresses then

increased slightly as shown by the curve with triangles. Without any quantitative analysis, there is a good agreement between these results and those of section 1.2: US can make certain Laponite dispersions flow more easily as a shearing force does.

Another interesting point is that the stress level after shearing by pump is lower than that after a pre-shearing of 300 s^{-1}. At $\dot{\gamma}$ = 1 s^{-1}, the stress level after shearing by pump is 0.01 Pa (circles in Fig. 3.5) while the one after a pre-shearing of 300 s^{-1} is 0.07 Pa. It shows the important effect of shear due to the pump on this thixotropic system. It has to be, therefore, considered as an important factor of this process, as demonstrated by (Pignon *et al*., 2012).

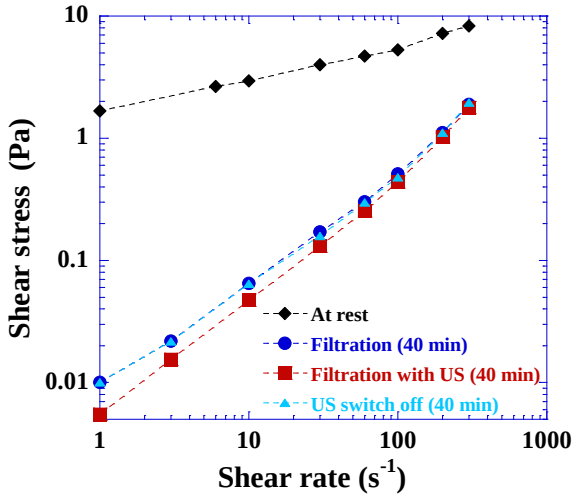

Fig. 3.5 *Steady state flow curve at different times of cross-flow filtration. Laponite suspensions: Lap1-tspp6, tp = 12 days; Filtration conditions: T = 25±1 °C, transmembrane pressure TMP = 1.1×10^5 Pa, cross-flow rate Q_v = 0.6 L.min^{-1}, ultrasound: 20 kHz, 2 W.cm^{-2}.*

1.3.2 SAXS profiles

Fig. 3.6 presents the SAXS intensities of Laponite dispersions as a function of scattering vector q. Two types of dispersions were investigated: with and without peptizer. All the profiles come from the *in-situ* SAXS measurements being carried out at ESRF, Grenoble. They are then used for further investigations such as determination of concentration profiles presented in section 1.5.

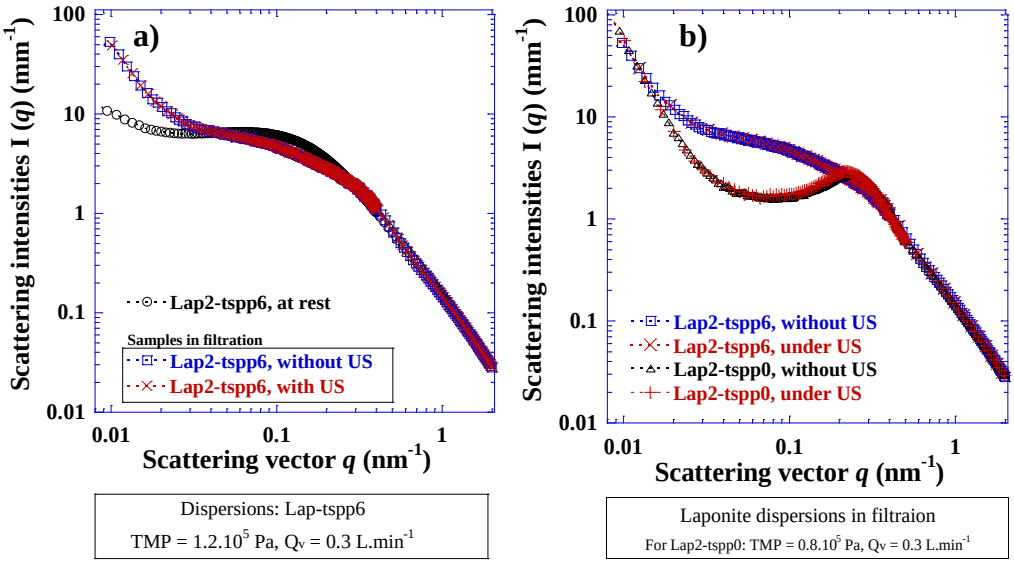

Fig. 3.6 *Comparison of scattering intensities of Laponite suspensions of 2 vol% (tp = 12 days) at different conditions. a) Lap2-tspp6; b) Lap2-tspp0. T = 25±1 °C. Ultrasound: 20 kHz, 2 W.cm^{-2}.*

SAXS profiles of Lap-tspp6 are shown in Fig. 3.6a. In order to reveal the ultrasonic effect on their structure during filtration, the scattering intensities of two dispersions at 2 vol% with and without US during filtration and one at rest, were compared. The sample at rest was analyzed in the capillary flow-through cell (see chapter 2 section5.3.2). It is obvious that the structure has been modified by shear stress at the length scales of interparticles (0.01 nm^{-1} ≤ q ≤ 0.4 nm^{-1}, corresponding to length scales between 600 nm and 15 nm). Such shape change of scattering intensities curve (between the circles and the others) at short range of q vectors (below 0.4 nm^{-1}) could be explained by the fact that the mutual interaction between the particles has decreased, noting that the mechanical properties of Laponite dispersions are controlled by a network of aggregates (Pignon *et al.*, 1997). However, no effective influence of US on Laponite structure is observed on the scattering intensity in this q range (Fig. 3.6a). This is probably due to the fact that both samples were already subjected to US before (the samples were picked up at step 7 and 8, as described in section 1.5.1) and the dispersions were then already disaggregated. Another possible reason: difference could take place at shorter range of q vector (e.g. <0.01 nm^{-1}) which was not revealed by our measurements. Otherwise, no modification of the size and shape of the particles caused by US can observed since the scattering intensities of all three samples are exactly the same at the length scales of particles (above 0.4 nm^{-1}, corresponding to a length of 15 nm, within the range of the average diameter of Laponite discs).

In Fig. 3.6b, SAXS profiles of Lap-tspp0 are added and compared with that of Lap-tspp6. Each profile represents an instantaneous state that $\phi_v \approx 2$ % of Laponite sample within the concentrated layer during filtration. At high q range (q>0.4 nm^{-1}), no difference is observed between them indicating that they share the same Form Factor (which is reasonable since addition of tspp should not change their nature). At short q range (0.01<q<0.4 nm^{-1}), SAXS profiles of these two dispersions are distinct, arising from the different interparticular organization related to their different edge-to-face interactions due to the addition of tspp, as discussed in chapter 2 section 1. Again, as the case of Lap2-tspp6, no effective influence of US on SAXS profiles of Lap2-tspp0 is observed at this q range (0.01<q<2 nm^{-1}), corresponding to length scales between 600 and 3 nm.

1.4 Effect of US on ultrafiltration at macro-scales

An alternating increase-decrease transmembrane pressure filtration procedure, proposed by Espinasse et *al.*(2002), was used to identify concentration polarization phenomena and membrane fouling during filtration. Using such a procedure, reversible fouling can be distinguished from deposit at the range of applied pressure. It also illustrates critical flux and limiting flux, which reveals the filtration performance of a given dispersion. In this section, the filtration characteristics of Lap0.48-tspp6 with and without US at three cross-flow ratees will be compared. Results are given using the parameter J_v/L_p (the ratio between the permeate flux and the permeability of membrane, Pa) in order to minimize the deviation of the permeate flux arising from variations in membrane permeability (variable from 74×10^{-5} $L.h^{-1}.m^{-2}.Pa^{-1}$ to 95×10^{-5} $L.h^{-1}.m^{-2}.Pa^{-1}$).

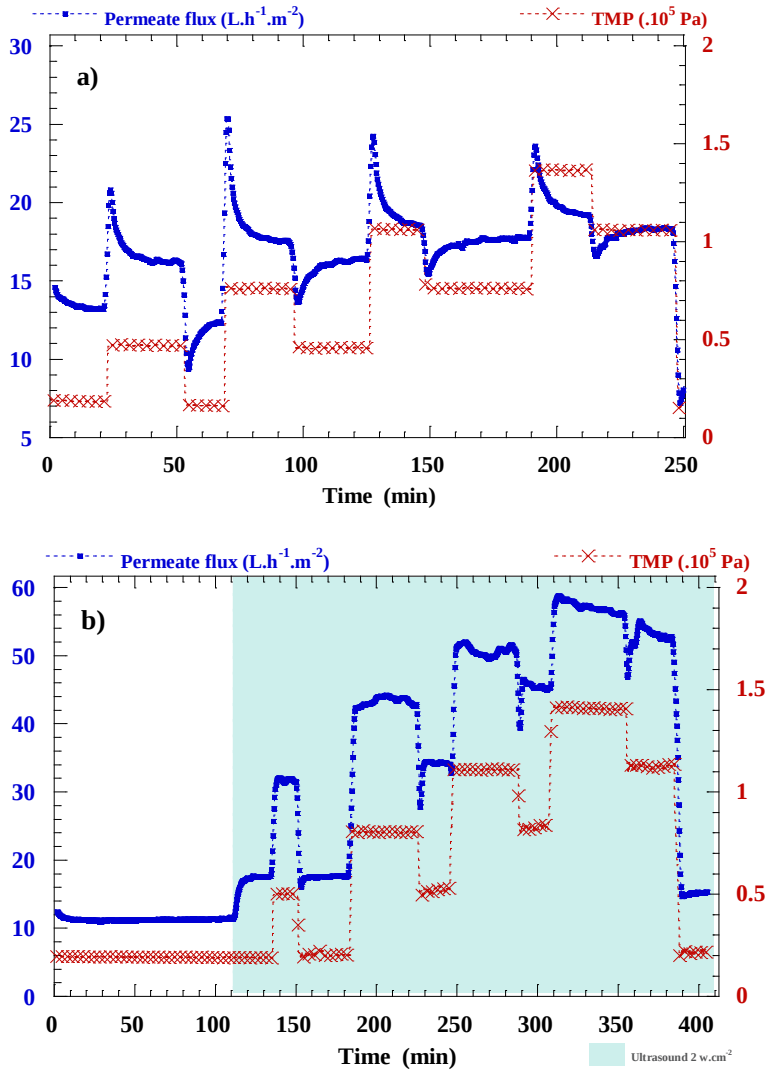

Fig. 3.7 *Cross-flow filtration curve by method of Espinasse: evolutions of permeate flux J_v, applied transmembrane pressure TMP over time at Q_v = 0.6 L.min^{-1} without (a) and with (b) US, the permeability of membrane (L_p) is 83 × 10^{-5} L.h^{-1}.m^{-2}.Pa^{-1}, 95 × 10^{-5} L.h^{-1}.m^{-2}.Pa^{-1}, respectively. Laponite dispersions: Lap0.48-tspp6, tp = 26 days. T = 25±1 °C, Ultrasound: 20 kHz, 2 W.cm^{-2}. Increase of permeate flux obvious; formation of reversible deposit could be avoided under US.*

During the filtration of Laponite dispersions (Lap0.48-tspp6), the evolution of permeate flux J_v, inlet (P_{inlet}) and outlet (P_{out}) pressures of filtration cell and cross-flow rate Q_v over time were monitored, and essential ones among them are displayed in Fig. 3.7. Filtrations at three Q_v (0.2 L.min^{-1}, 0.45 L.min^{-1} and 0.6 L.min^{-1}) were performed both with and without US. Taking an

average dispersion viscosity at high shear rates, η_{Lap} = 0.003 Pa.s, Reynolds numbers (Re) without US can be calculated at 184, 414 and 552 for Q_v = 0.2, 0.45 and 0.6 L.min^{-1} respectively, which shows that these dispersions are in the laminar flow regime.

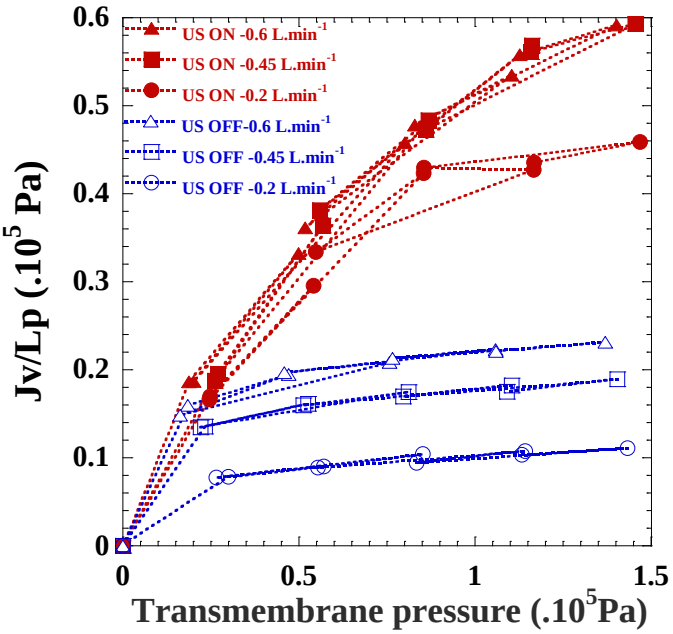

Fig. 3.8 *Steady-state curves of J_v/L_p as a function of transmembrane pressure TMP for different Qv with/without US during ultrafiltration of Lap0.48-tspp6, tp = 26 days. T = 25±1 °C, Ultrasound: 20 kHz, 2 W.cm^{-2}. No more limiting flux under US; competitive/combined effect of US and Q_v.*

The steady-state curves of J_v/L_p versus applied TMP (average of P_{inlet} and P_{out}) were then drawn according to the permeate flux at steady states of every filtration step (Fig. 3.8). At the beginning, a low transmembrane pressure TMP = 0.2 ×10^5 Pa is applied which yields a certain permeate flux J_{v1}. TMP is then increased to 0.5 ×10^5 Pa, once the steady state is reached, it is decreased again to 0.2 ×10^5 Pa so that the new permeate flux J'_{v1} could be compared with J_{v1} for the purpose of differentiating possible deposit formation from a reversible concentration polarization layer. These coupled permeate fluxes at every TMP are denoted J_{v2}-J'_{v2}…J_{v5}-J'_{v5}. As shown in Fig. 3.7a and Fig. 3.8, J'_{vn} is mostly equal to J_{vn} during the three filtrations without US, which indicates that reversible concentration polarization is the dominant phenomenon rather than irreversible deposit formation in this state of filtration. Interestingly, the permeate flux

increases steadily from a very low level every time the pressure is lowered, and it decreases from a very high level once the pressure goes up (Fig. 3.7a). According to Pignon *et al.* (2012), this could be explained by a reversible deposit that is formed as the rise of TMP and which is then eroded by shear-induced hydrodynamic forces when the pressure is released. In addition, a so-called limiting flux is reached very quickly at the very beginning of filtration, since the permeate flux hardly raises whatever TMP increases until 1.4×10^5 Pa. The limiting fluxes are 19 $L.h^{-1}.m^{-2}$ at Q_v = 0.6 $L.min^{-1}$ (Fig. 3.7a) and 14 $L.h^{-1}.m^{-2}$, 8 $L.h^{-1}.m^{-2}$ at Q_v = 0.45, and 0.2 $L.min^{-1}$, respectively. The appearance of limiting flux implies that the concentrated particles layer is dense even though it is reversible.

Fig. 3.7b demonstrates that the application of ultrasound leads to an immediate increase of permeates flux, and that steady states can be reached almost immediately after every operation below 1.1×10^5 Pa. As discussed before, the arc-like shapes in Fig. 3.7a are related to formation/erosion of a reversible deposit, which implies that no such deposit could be formed under US since the evolution of permeate flux follows a constant-deviation regime at these TMP (from 0.2×10^5 Pa to 1.1×10^5 Pa). When TMP further increases to 1.4×10^5 Pa, a slight-depleting curve of permeate flux is observed, indicating a formation of a accumulated particles layer, but a much more thinner one than without US. In addition, those coupled permeate fluxes J_{vn}-J'_{vn} are equal to each other owing to the non-existence of irreversible deposit.

In order to better assess the effect of US on filtration performance of Lap0.48-tspp6, two additional cross-flow ratees (0.2 $L.min^{-1}$, 0.45 $L.min^{-1}$) were applied. Though the filtration curves of these two experiments are not presented here, steady-state curves have all been assembled in Fig. 3.8. In general, the application of US leads to a significant increase of permeate flux, from 3 to 5 times. Moreover, different filtration behaviors have been observed: instead of being limited, the permeate flux continues to increase with TMP up to 1.4×10^5 Pa for all three filtrations under US. Since this limiting flux strongly depends on a dense accumulated particles layer, we infer that the applied ultrasonic waves allow reducing this dense concentrated layer.

It also seems that there is a competition/combination between the effect of ultrasonication and that of cross-flow rate Q_v, since the observed permeate flux are mostly the same at 0.45 $L.min^{-1}$ and 0.6 $L.min^{-1}$ under US. In fact, during conventional filtration, an increase of permeate

flux is currently observed with the increase of Q_v. It should be noted that the formation of concentrated particles layer during cross-flow filtration results from a balance between the transmembrane pressure TMP and the shear-induced hydrodynamic force in the filtration channel, which is determined by the cross-flow rate. The applied ultrasonic waves in this study provoke only mechanical effects because of their low frequency. We assume, therefore, that the ultrasonication enhances the hydrodynamic force and a maximum in the filtration channel has been reached at certain Q_v (between 0.2 $L.min^{-1}$ and 0.45 $L.min^{-1}$) so that a successive increase of Q_v does not affect it any more.

This assumption can also explain the evolution of permeate flux curves in Fig. 3.7b. In this figure we notice that the permeate flux evolution with time reaches an almost constant value for TMP < 1.4×10^5 Pa (for example at time t = 180 min), while the permeate flux slightly decreases over time for TMP = 1.4×10^5 Pa (at time t = 310 min).

We can interpret these evolutions as follows: at TMP < 1.4×10^5 Pa, no additional accumulation of particles occurred in these steps. (Nevertheless the permeation flux was lower than the one for clean water, indicating a possible irreversible fouling layer at the membrane surface.) The filtration channel had a certain level of hydrodynamic force with a constant Q_v and stable ultrasonication, the increase of TMP would result in a reinforcement of convection flux towards the membrane leading to an instantaneous concentrated particles layer, which could be then fluidized by shear-induced hydrodynamic diffusion. Once the convection flux towards the membrane was so important that the instantaneously formed concentrated layer could not be totally fluidized by the hydrodynamic force, a steady concentrated particles layer would appear while the permeate flux decreased over time, as the case here at TMP = 1.4×10^5 Pa (at time t = 310 min).

To sum up, macroscopical effect of US on cross-flow filtration has been revealed in this section. A high efficiency of US to increase the filtration performance of Laponite dispersions has been shown, in the case that it is applied directly to the dispersions on the feed side of the membrane. In addition, no membrane damage was observed since membrane permeability remains stable after every ultrasonic-assisted filtration. No heating effect was observed due to the application of ultrasound neither, since the average temperatures at both inlet and outlet of

filtration cell were around 25 °C, as presented in Tab. 3.2. By measuring dry weight percentage of feed and permeate, the rejection rate of membrane has also been determined and the results are listed in Tab. 3.2. According to these results, application of ultrasound did not change the rejection rate of the used PES membrane.

Tab. 3.2 *Average temperatures at inlet and outlet of filtration cell and rejection rates during 250 min's ultrafiltration of Lap0.48-tspp6, tp = 26 days. Ultrasound: 20 kHz, 2 W.cm^{-2}*

Filtrations	Average temperatures		Rejection rate (±3%)
	Inlet	Outlet	
US ON 0.6 L.min^{-1}	24.97	25.10	94.2%
US ON 0.45 L.min^{-1}	24.92	24.94	95.1%
US ON 0.2 L.min^{-1}	24.88	25.09	93.6%
US OFF 0.6 L.min^{-1}	24.91	24.93	96.6%
US OFF 0.45 L.min^{-1}	25.04	25.31	96.3%
US OFF 0.2 L.min^{-1}	25.11	25.11	97.8%

1.5 Effect of US on ultrafiltration at nano-scales

In this section, filtration behaviors of Laponite dispersions will be discussed at the nanometric length scales. Three dispersions, of different volume fractions and content of peptizer, are concerned: Lap1-tspp6, Lap0.48-tspp6 and Lap1-tspp0. All the filtrations presented in this section were carried out at ESRF, with real-time *in-situ* SAXS measurements. Concentration profiles and structural organization of Laponite dispersions near the membrane surface during filtration have been revealed thanks to this powerful technique.

1.5.1 Ultrafiltration of Lap1-tspp6

1.5.1.1 US effect at steady state

After the introduction of Lap1-tspp6 in the ultrafiltration vessel, several hydrodynamic parameters were explored and US was applied during certain steps of filtration. At TMP = 1.1

$\times 10^5$ Pa, two successive cross-flow rates were explored as presented in Fig. 3.9. When Q_v = 0.2 L.min^{-1}, the permeate flux at steady state is always around 5.5 L.h^{-1}.m^{-2}; it then increases to around 8.5 L.h^{-1}.m^{-2} at Q_v = 0.3 L.min^{-1}, no difference of permeate flux is observed among the filtration steps without US (steps 1, 3 and steps 5, 7, 9).

Once the ultrasonic waves are applied, the permeate flux is reinforced immediately (Fig. 3.9). The first ultrasonic application (step 2) leads to an increasing of permeate flux from 5.5 L.h^{-1}.m^{-2} to 29 L.h^{-1}.m^{-2} progressively. The second one (step 4) then brings the flux up to 45 L.h^{-1}.m^{-2} also progressively but the equilibrium state is reached more quickly. As for the next filtration steps with US, the permeate flux increases instantaneously when US is applied, and they are then brought to 75 L.h^{-1}.m^{-2} and 90 L.h^{-1}.m^{-2} (average) for step 6 and 8 respectively at Q_v = 0.3 L.min^{-1}.

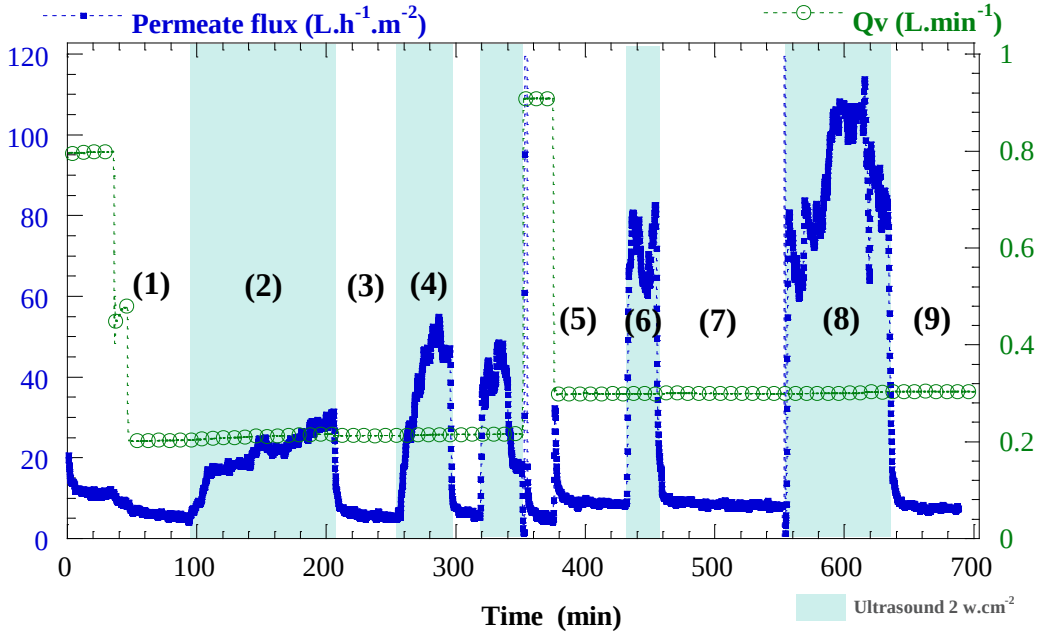

Fig. 3.9 *Cross-flow filtration curve: evolution of permeate flux J_v and cross-flow rate Q_v over time when the transmembrane pressure TMP = 1.1×10^5 Pa, T = 25±1°C. Laponite dispersions: Lap1-tspp6, tp = 12 days. Ultrasound: 20 kHz, 2 W.cm^{-2}. L_p = 139 × 10^{-5} L.h^{-1}.m^{-2}.Pa^{-1}. Increase of permeate flux significant; scenarios of permeate flux are different for each step under US.*

It should be noted that there are both effects of US and increase of Q_v for steps 6 and 8. In order to clarify the relative effects of each of them, another filtration run following the same

procedure from step 1 to step 4 was carried out with Q_v = 0.3 L.min^{-1} using a fresh sample (Fig. 3.10). The results obtained at step 2' in Fig. 3.10 are very similar to those obtained for step 2 in Fig. 3.9 with a progressive increase in flux. Furthermore, the obtained increases in permeate flux (J_v/L_p) are very comparable for different Q_v, as revealed by the data displayed in Tab. 3.3. This clearly shows that, in such a situation, the effect of US dominates over that related to changes in Q_v for steps 6 and 8.

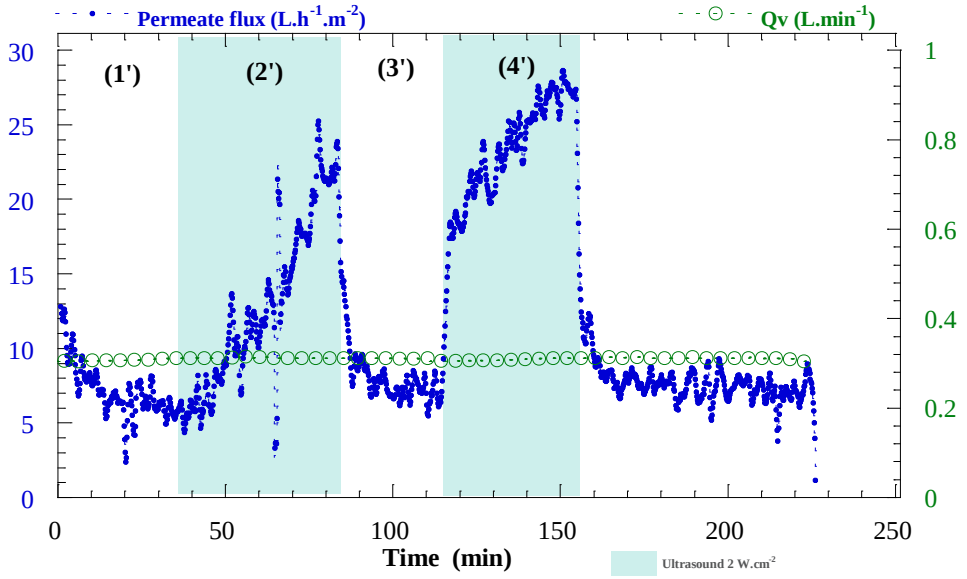

Fig. 3.10 *Cross-flow filtration curve: evolution of permeate flux J_v and Q_v over time when TMP = 1.1 ×10^5 Pa, T = 25±1°C. Laponite dispersions: Lap1-tspp6, tp = 12 days. Ultrasound: 20 kHz, 2 W.cm^{-2}. Membrane permeability: 76 L.h^{-1}.m^{-2}.Pa^{-1}.*

Tab. 3.3 *Comparison of permeate flux between the filtration runs in Fig. 3.9 and Fig. 3.10.*

	Step	US (W.cm^{-2})	J_v (L.h^{-1}.m^{-2}.Pa^{-1})	J_v/L_p (.10^5 Pa)
Filtration run in Fig. 3.9	1	0	8.5	0.06
	2	2	29	0.21
	4	2	45	0.32
	6	2	75	0.54
Filtration run in Fig. 3.10	1'	0	6	0.08
	2'	2	22	0.29
	4'	2	28	0.37

Fig. 3.11 presents the corresponding concentration profiles at steady state for every concerned filtration steps (measured simultaneously with permeate flux).

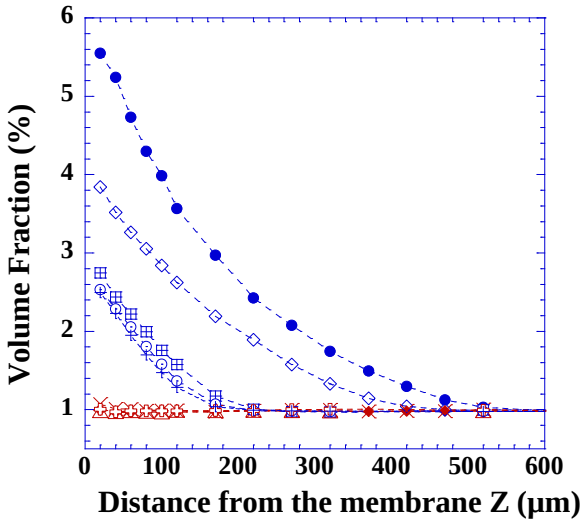

Time (min)	US (W.cm^{-2})	Qv (L.min^{-1})	Step
100	OFF	0.2	(1)
210	2	0.2	(2)
250	OFF	0.2	(3)
300	2	0.2	(4)
430	OFF	0.3	(5)
450	2	0.3	(6)
500	OFF	0.3	(7)
620	2	0.3	(8)
690	OFF	0.3	(9)

Fig. 3.11 *Concentration profiles at steady state within the concentrated layer deduced from in-situ SAXS during ultrafiltration of Laponite dispersions (Lap1-tspp6, tp = 12 days) under US. T = 25±1°C, TMP = 1.1×10^5 Pa. Ultrasound: 20 kHz. Concentrated particles layer removal under US; Concentration profiles evolve over time under the same conditions.*

In accordance to the increase of permeate flux, no more concentrated layer has been found at the end of the steps with US (Step 2, 4, 6, 8): the volume fractions equal 1 %, i.e. the volume fraction of feed Laponite dispersions, from z = 20 µm to the bulk dispersions. Interestingly, at the end of the steps without US (Step 1, 3, 5, 7, 9), lower concentrations for all the distances z are exhibited at the following step than the precedent ones: the concentrated particles layer is thinner and less concentrated at step 3 compared to step 1 although the experimental parameters (Q_v =

0.2 $L.min^{-1}$, TMP = 1.2×10^5 Pa) are the same; similar observations can be made for steps 5 and 7. Furthermore, this decrease in concentration seems to be slowing over time since almost equal concentration profiles have been observed for step 7 and 9.

It should be reminded that the Laponite dispersion has an attractive network that consists of sub-units of particles, micron-sized aggregates formed from a dense stack of sub-units and a fractal mass consisting of a loose mass of micron-sized aggregates (Martin et al., 2002; Pignon et al., 2000, 1997). During filtration, a denser aggregates and more connected gel forms the concentrated particles layer which limits the permeate flux (Pignon et al., 2000). On the basis of the knowledge of this global structural organization, we can speculate the effect of US on the structural modification of these dispersions. It seems that the applied ultrasonication is able to disaggregate this dense network like an additional force but it takes time to complete such a disaggregation. This could explain why different scenarios for increasing permeate flux are observed: at step 2, the ultrasonic waves began to break up the dense aggregates and the connection among them (mass fractal) formed since step 1. There should be however, always some dense and highly connected aggregates in the accumulated particles layer so that the mechanical effect of US was restricted, hence, the permeate flux increased slowly. During step 3 when ultrasonication was stopped, the fragments of aggregates, the aggregates not yet disassembled could re-accumulate on the membrane surface; they could be further disaggregated by ultrasonic waves at step 4. Since the accumulated particles layer became looser due to the partial disassembling of aggregates, the ultrasonic waves could find a pathway more easily to disrupt the concentrated layer more quickly. Consequently, the permeate flux of this step increased much faster than step 2. Presumably, all the dense aggregates have been completely disassembled at the end of this step since the permeate flux increased instantaneously at the next ultrasonication step, suggesting that there was no more restriction of the remaining dense aggregates to prevent ultrasonic action within the concentration layer.

1.5.1.2 Temporal effect of US: break-up of concentrated layer

The application of US appears to lead to a disruption of concentrated particles layer resulting in an increase of permeate flux. It is then particularly important to try to know how this

concentrated layer has been disrupted. With this purpose, the evolution of concentration profiles over time has been investigated for every filtration step. Evolutions of concentration profiles at steps 2, 4 and 6 (with US) are presented in Fig. 3.12. As shown in Fig. 3.12a, at Q_v = 0.2 L.min^{-1}, it takes 100 min for the first ultrasonication (step 2) to completely remove the accumulated particles layer. As described in the former section, the dense structural organization of particles should be disrupted by ultrasonic waves at step 2 so that the second ultrasonication (step 4) takes only 20 min to remove this reformed concentrated layer. For the same Q_v, the layer at step 4 is looser and less concentrated (but with the same thickness) than the one of step 2, shown in Fig. 3.12b. When the cross-flow rate increases to 0.3 L.min^{-1} (step 6), it takes 13 min to remove the whole concentrated particles layer, resulting from both continuous disaggregation by ultrasound and reinforcement of shear-induced hydrodynamic force by the increase of Q_v (Fig. 3.12c).

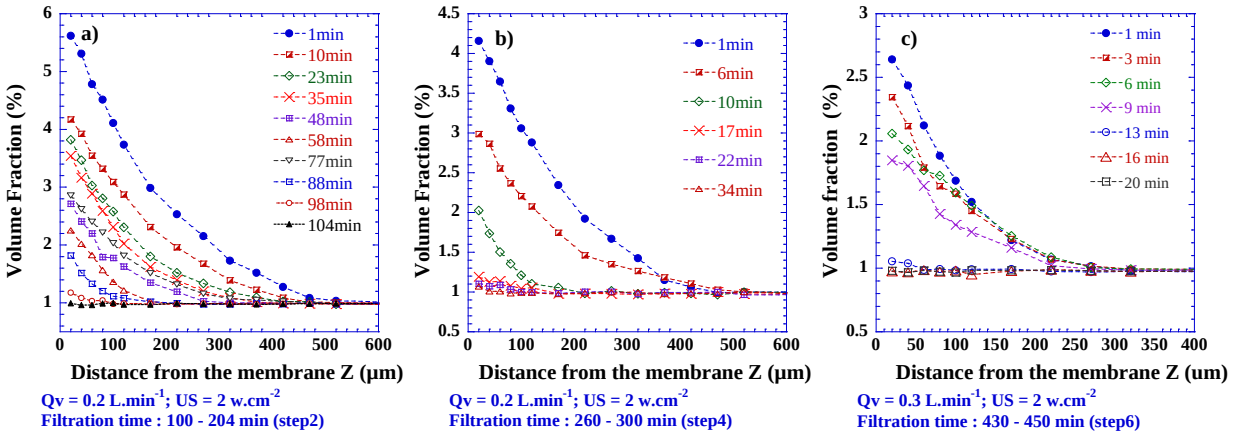

Fig. 3.12 *Evolution of concentration profiles within the accumulated particles layer over time during ultrafiltration of Laponite dispersions (Lap1-tspp6, tp = 12 days) under US. T = 25±1°C, TMP = 1.1×10^5 Pa. Ultrasound: 20 kHz. Break-up time differs from one step to another.*

One explanation for these different break-up times could be, that during the first ultrasonication step (step 2), the ultrasonic action was restricted within the concentrated particles layer arising from the viscous, highly-aggregated dispersions. For instance, the formation and implosion of cavitation bubbles were difficult (high threshold of cavitation owing to high viscous medium) and it was also difficult to find a pathway to create acoustic streaming. At the following ultrasonication steps (step 4 and 6), the dispersions were more disaggregated so that the threshold

of cavitation drops off and acoustic streaming was strengthened thanks to the decrease of viscosity. As a consequence, the break-up time significantly decreases.

Kinetic data on concentrated particles layer break-up by US are presented in Fig. 3.13. Different distances in this layer, 20 µm, 60 µm, 100 µm, 220 µm and 320 µm from the membrane surface were selected. For the three concentration profiles (Fig. 3.12) and for each distance, the evolutions of volume fractions with time were determined. At the first ultrasonication step (step2, Fig. 3.13a), the volume fractions decrease at a similar rate below 100 µm, and they drop off more rapidly than those at higher distance. This indicates that the bottom of the concentrated particles layer (close to the membrane) is the target zone of disruption under US. The same conclusion can be drawn for the second ultrasonication step (step 4, Fig. 3.13b).

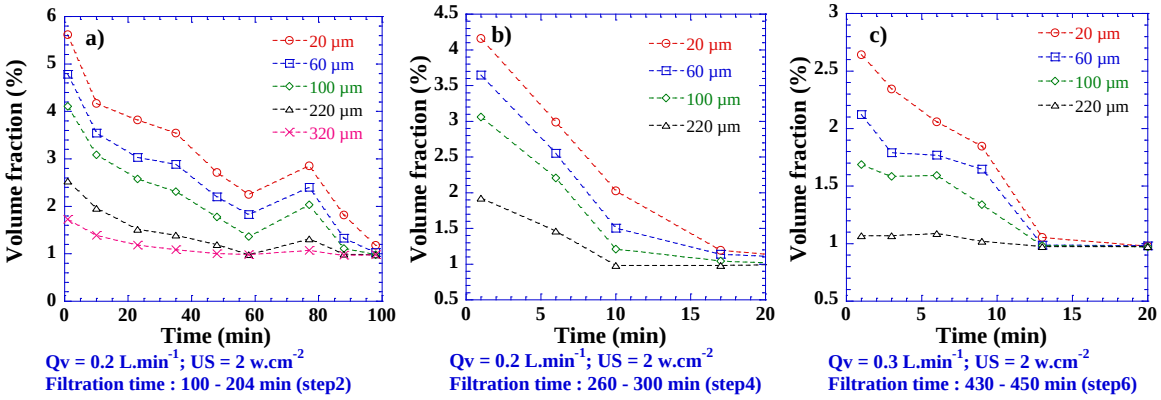

Fig. 3.13 *Time evolution of volume fractions at given distance z within the accumulated particles layer during ultrafiltration of Laponite dispersions (Lap1-tspp6, tp = 12 days) under US. T = 25±1°C, TMP = 1.1×10^5 Pa. Ultrasound: 20 kHz. Bottom of the concentrated layer is the target zone of disruption under US.*

It also appears that the break-up regime is not regular with time at step 2: volume fractions drop with variable velocities, they even start to increase at 77 min for all distances z within the concentrated particles layer, probably owing to the re-balance between the detached gel from others parts of the channel and the remaining concentrated layer of concerned section. Since the measurements were carried out in the middle of the filtration cell (x = 50 mm), it is possible that at 77 min, detached gel from other parts was brought by ultrasound-induced turbulence and added rapidly into the remaining layer driven by pressure gradient.

Otherwise, the concentration profiles at step 2 and 4 (Fig. 3.12a and Fig. 3.12b) are of regular form without sign of disruption. In fact, they follow an exponential shape like those without US, as described in section 1.5.1.3. These observations could be explained by the effective range of ultrasonication: the actions induced by US should be on the order of micrometers even smaller so that the disruption of concentration profile is invisible for measurements performed every 20 µm. However, when the cross-flow rate increases to 0.3 $L.min^{-1}$, the concentration profiles are not regular any more, it seems that the concentrated layer has been subjected to a force of agitation (Fig. 3.12c). For example at time t = 9 min, the evolution of Φv (z) does not follow a continuous decrease. Evidences can also be found in Fig. 3.13c: the volume fraction drop is irregular and very rapid. Firstly, we should note that at step 6 the dispersions have already been subjected to the ultrasonication for quite a while so the disaggregation should be more complete, which made the ultrasound more effective in this medium, for example with more pronounced action of acoustic streaming. Furthermore, the hydrodynamic force was enhanced by increasing the cross-flow rate. Therefore, it should be the combined action of these two factors as the origin of the rapid break-up with the irregular distribution of the concentration as a function of z.

1.5.1.3 Growth of concentrated particles layer after US

Fig. 3.14 presents the growth of polarization layers after ultrasonication at Q_v = 0.2 $L.min^{-1}$ and 0.3 $L.min^{-1}$ (Step 3 and 5, respectively). At the transient state, colloidal matter accumulates to the membrane progressively. Even though the two concentration layers at steady state are different, a complete growth takes 45 min for both of them. This indicates that the effect of US on filtration is almost instantaneous: the accumulation of matter at membrane surface can not be attenuated when US is switched off. In addition, the accumulated layers follow an exponential shape over distance z at any given time during filtration: $\boldsymbol{\Phi v}$ (z) = α.exp (-β**z**), where α is the volume fraction at z = 0 µm, and β defines the curve steepness. The higher the value of β is, the steeper the curve. Similar behavior is also observed for colloidal dispersions in drying process (Boulogne *et al*., 2013). It appears that the concentration profiles at Q_v = 0.3 $L.min^{-1}$ are steeper and the accumulated layers are thinner than those at 0.2 $L.min^{-1}$ (thickness of the accumulated

layer varies from 220 µm at 0.3 L.min^{-1} to 420 µm at 0.2 L.min^{-1}). The reinforcement of Q_v thins the accumulated layers but it seems that it has a reduced influence on the layers closer to the membrane.

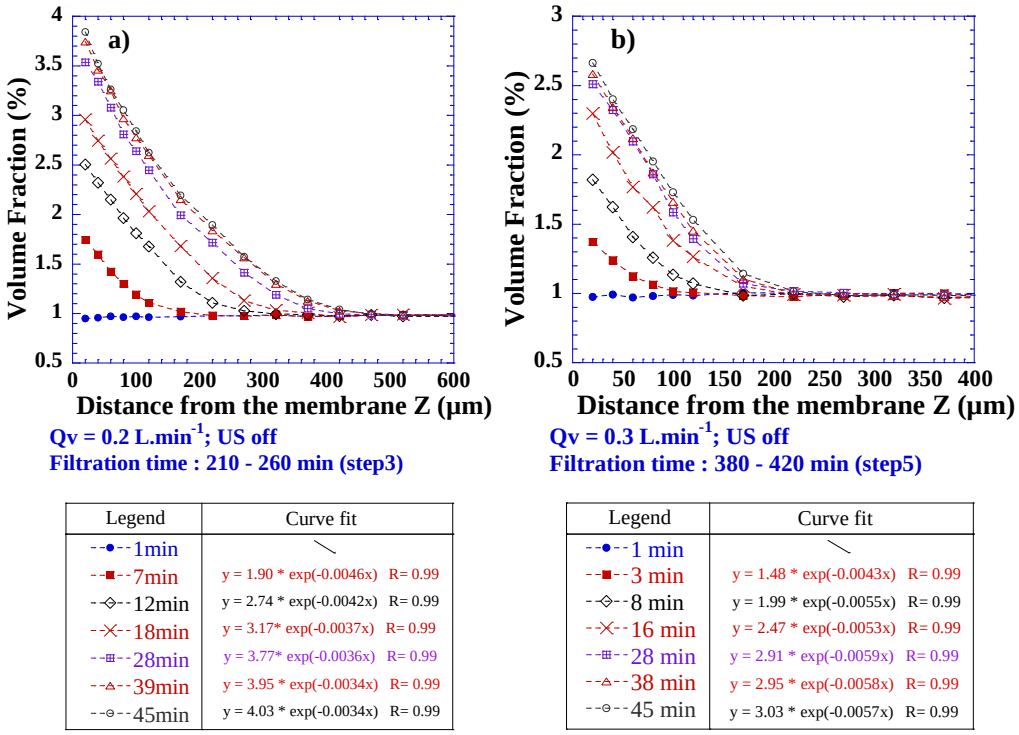

Legend	Curve fit
1min	
7min	y = 1.90 * exp(-0.0046x) R= 0.99
12min	y = 2.74 * exp(-0.0042x) R= 0.99
18min	y = 3.17* exp(-0.0037x) R= 0.99
28min	y = 3.77* exp(-0.0036x) R= 0.99
39min	y = 3.95 * exp(-0.0034x) R= 0.99
45min	y = 4.03 * exp(-0.0034x) R= 0.99

Legend	Curve fit
1 min	
3 min	y = 1.48 * exp(-0.0043x) R= 0.99
8 min	y = 1.99 * exp(-0.0055x) R= 0.99
16 min	y = 2.47 * exp(-0.0053x) R= 0.99
28 min	y = 2.91 * exp(-0.0059x) R= 0.99
38 min	y = 2.95 * exp(-0.0058x) R= 0.99
45 min	y = 3.03 * exp(-0.0057x) R= 0.99

Fig. 3.14 *Evolution of concentration profiles within the concentrated particles layer over time during ultrafiltration of Laponite dispersions (Lap1-tspp6, tp = 12 days) when US is switched off. T = 25±1°C, TMP = 1.1×10^5 Pa. Concentration profiles follow an exponential shape.*

The growth kinetics of concerned accumulated particles layers are presented in Fig. 3.15. For the position nearest from the membrane surface, growth kinetics can be modeled by the following exponential relationship: $\mathbf{\Phi v}$ (t) = m_1+m_2.(1-exp(-m_3**t**)), where m_1 is the initial volume fraction at t = 0 min, m_2 defines the amplitude and m_3 describes the growth rate of the volume fraction Φ_v over time. Curve fittings were performed only for the concentrated particles layers at z = 20 µm, 60 µm and 100 µm, and the parameters illustrate the growth behaviors at different Q_v. For both applied Q_v, the accumulated particles layers close to the membrane (ex. z = 20 µm) grow faster than those far from the membrane (ex. z = 100 µm). However, the growth rates m_3 of accumulated layers are distinct at different Q_v. At Q_v = 0.2 L.min^{-1}, the layers within 100 µm

develop with a slightly changed growth rate, m_3 varies from 0.060 to 0.045. At Q_v = 0.3 L.min^{-1}, the layer close to the membrane (z = 20 µm) grows 3 times faster than that far from the membrane (z = 100 µm), which grows even faster than the layer of the same position at Q_v = 0.2 L.min^{-1} (m_3 value: 0.100 VS 0.060).

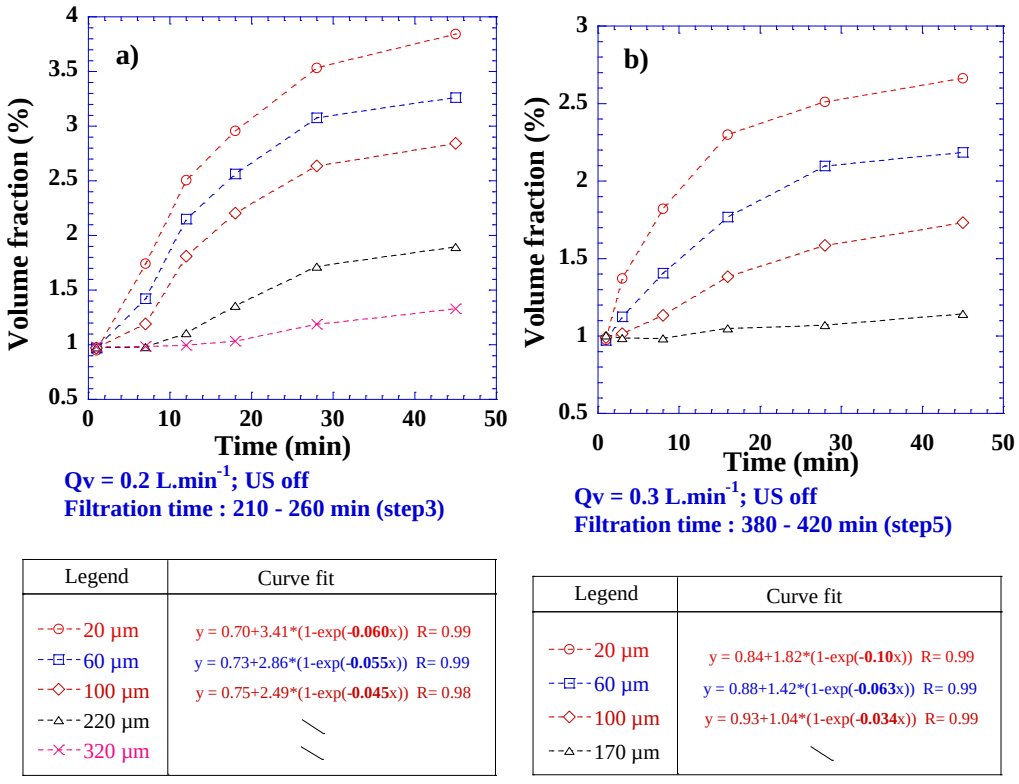

Fig. 3.15 *Time evolution of volume fractions at given distance z within the accumulated particles layer during ultrafiltration of Laponite dispersions (Lap1-tspp6, tp = 12 days) when US is switched off. T = 25±1°C, TMP = 1.1×10^5 Pa.*

As mentioned in previous section, the balance between transmembrane pressure and shear-induced hydrodynamic force determines the formation of polarization layer during cross-flow filtration. The increase of cross-flow rate from Q_v = 0.2 L.min^{-1} to 0.3 L.min^{-1} enhanced the hydrodynamic force so that the growth of concentrated particles layer far from the membrane surface (z = 100 µm) was slowed down (m_3 varies from 0.045 to 0.034). However, it seems not to slow down but speed up the accumulated layer growth near the membrane since the growth rate at 20 µm increases with the applied cross-flow rate. This could be interpreted by the fact that

more particles have been brought during the same time interval by the enhanced cross-flow rate. Consequently, in taking account the observations in Fig. 3.14, it seems not to be the best efficient way to increase cross-flow rate Q_v for removing the polarization layer from the membrane surface.

1.5.1.4 Spatial effect of US along the membrane surface

Three windows of measurements were available, located at 7 mm, 50 mm and 93 mm from the filtration cell entrance, as illustrated in Fig.2.8 in chapter 2. To obtain concentration profiles, we then started with a matrix of 3 columns (x axis, distance from the filtration cell inlet) and 20 rows (z axis, distance from the membrane) with concentration data points. The graphing software ORIGIN was then used to sketch this contour by a four step process: creating Thiessen (Delaunay) triangles in the XY plane; linear interpolation; drawing of contour lines and smoothing.

Fig. 3.16 presents the contour charts of filtration channel during cross-flow ultrafiltration of Lap1-tspp6 with and without US considering a continuous and linear evolution between the three measurements points. SAXS measurements were carried out every 20 µm from the membrane (first point of measurement: z = 20 µm). As depicted in Fig. 3.16a, at steady state of filtration without ultrasonication, the thickness of the concentrated particles layer increases along the filter surface (x axis): no layer is observed at x = 7 mm and a layer of 200 µm is formed at x = 50 mm, this layer then accumulates to 300 µm at x = 93 mm. In addition, local particle volume fraction increases at every distance z within the accumulated layer along x. For instance, at 20 µm from the membrane surface (z = 20 µm), it is 1 vol%, 2.5 vol% and 2.7 vol% at 7 mm, 50 mm and 93 mm, respectively. These observations by *in-situ* SAXS measurements have allowed for the first time, to highlight the existence of concentration distribution along the membrane in accordance to theoretical cross-flow filtration models. Researchers (Bhattacharjee *et al*., 1999; Davis and Leighton, 1987; Elimelech and Bhattacharjee, 1998; Romero and Davis, 1988) have predicted such an axial dependence of particle layer. According to them, a polarized layer could attain a thickness that is constant in time but increases with distance from the filter entrance, which gives rise to a stable permeate flux at steady state. This steady state is maintained by

convective motion of permeate through the membrane and shear-induced hydrodynamic diffusion along the membrane. Romero and Davis also pointed out that a stagnant, concentrated layer beneath the flowing layer could form from certain position and the local permeate velocity decreases along the filter surface (Romero and Davis, 1988).

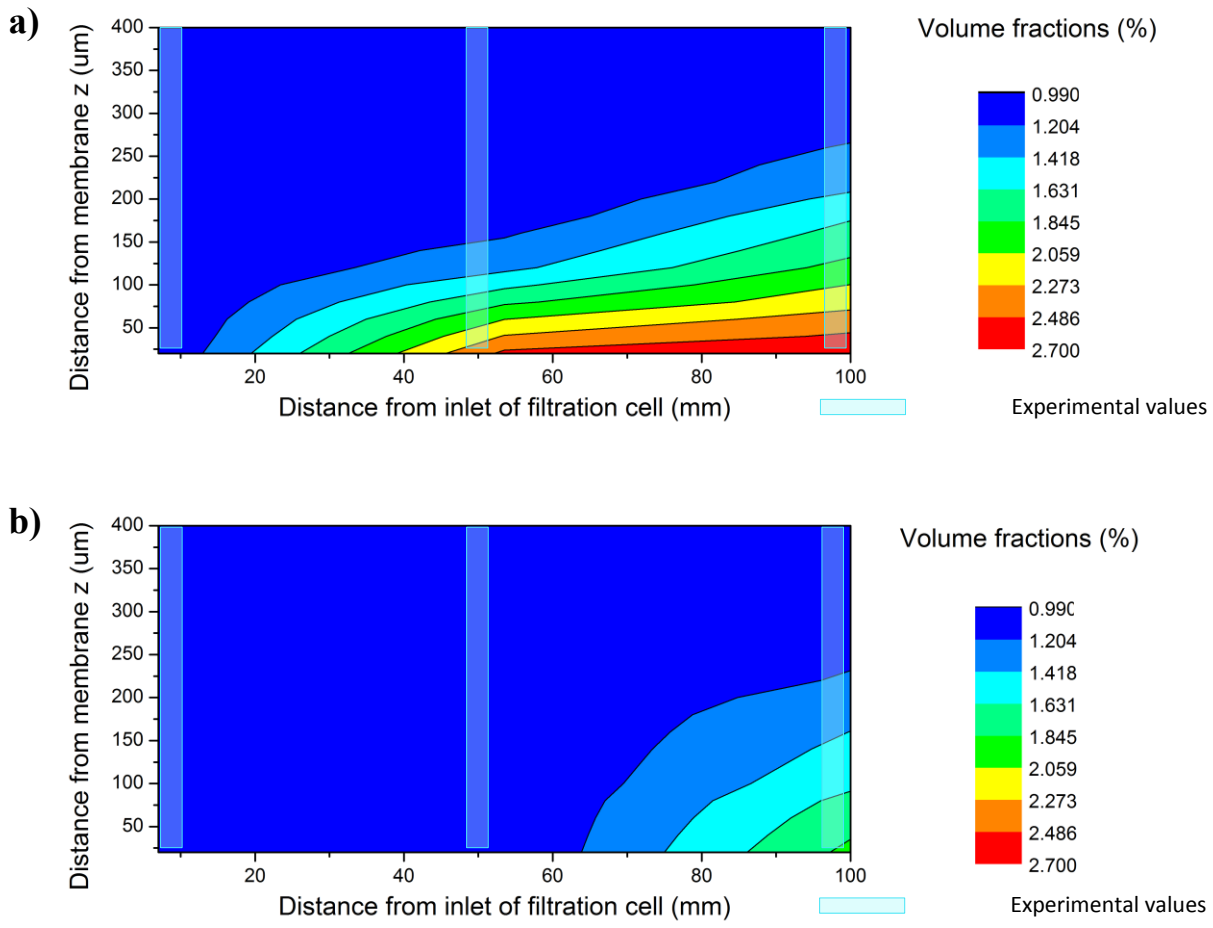

Fig. 3.16 *Contour chart of concentrated layer in the filtration channel at a given moment during ultrafiltration of Laponite dispersions (Lap1-tspp6, tp = 12 days) with/without US. T = 25±1°C, TMP = 1.1×10^5 Pa, Q_v = 0.3 L.min^{-1}. Ultrasound: 20 kHz, 2 W.cm^{-2}.*

An ultrasonication of 20 kHz and 2 W.cm^{-2} was then applied. In Fig. 3.16b, the contour chart after ultrasonication of 1 hour shows a significant disruption of this concentrated layer. Concentration profiles are homogeneous for all distances z at x = 7 mm as well as 50 mm, with the feed concentration (1 vol%). At x = 93 mm, the volume fractions of Laponite decrease 30%

when close to the membrane and 1.9 vol% is attained at z = 20 µm. It is also worth mentioning that, at this x position, ultrasonication does not significantly reduce the thickness of the polarization layer. Similar trends were already noticeable in Fig. 3.12. It then appears that in the transient state, the volume fractions of the whole accumulated layer decreases while maintaining a constant layer thickness. Erosion of this layer only starts once a sufficiently low critical volume fraction is reached. Therefore, it could reasonably be inferred that this disrupted layer in Fig. 3.16b will be thinned over time. We could also ask if this critical volume fraction corresponds to one threshold state of dispersions (with certain yield stress and structural organization) for which the combined effect of shear flow and US is sufficiently high to disrupt the layer by mechanical erosion (thickness reduction).

1.5.2 Ultrafiltration of Lap0.48-tspp6

1.5.2.1 Steady state of filtration

Filtration performance at macro-scale of Lap0.48-tspp6 has been fully investigated in section 1.4. This present section provides supplementary information which is the concentration profiles during filtration and when filtration stops. To ensure significant accumulation of particles as well as to enable comparison between different dispersions, TMP of filtration run was fixed at $1.1.10^5$ Pa. Corresponding filtration curve with the evolution of J_v, TMP and Q_v over time is presented in Fig. 3.17a. Four operating steps are concerned and indicated in this figure. The related concentration profiles at steady state are presented in Fig. 3.17b.

At step1, no US was applied, the permeate flux at steady state is around 11 $L.h^{-1}.m^{-2}$. An immediate increase of J_v was then produced by US at step 2, which continues to increase J_v until around 140 $L.h^{-1}.m^{-2}$. It indicates that the applied ultrasonic force alleviated strongly the permeate flux decline, from 95 % to 35 %. Permeate flux decline in filtration process links directly to the formation of concentrated layer at the membrane surface which limits mass transfer of this process. As shown in Fig. 3.17b, this layer is detected having a thickness of 170 µm with a volume fraction of 2.4 % adjacent to the membrane (at z = 20 µm). Application of US seems to

be efficient to remove this concentrated layer since a nearly homogeneous concentration profile is detected under US at the end of step 2, which is consistent with the results of previous section.

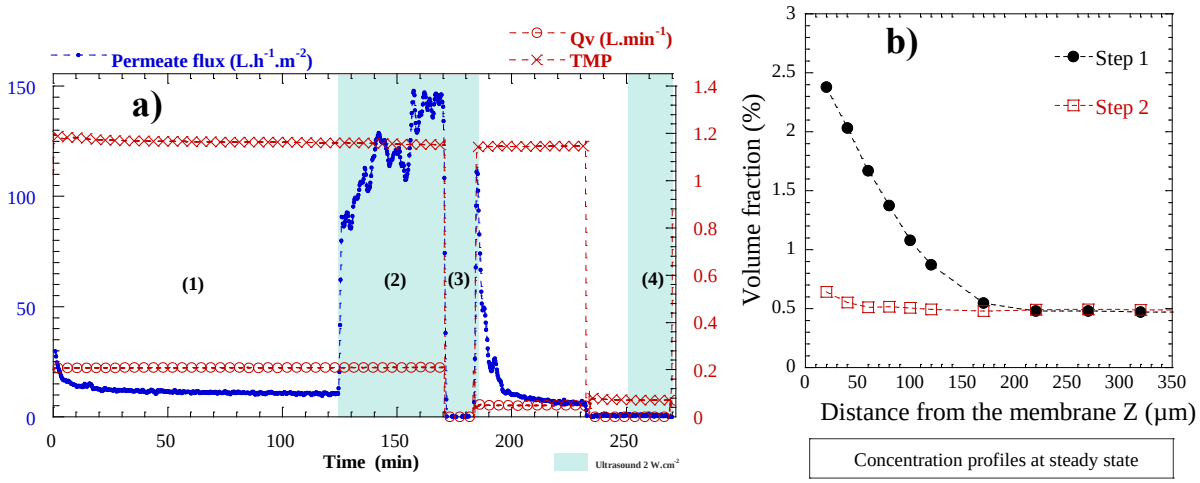

Fig. 3.17 *Combination of macro-scale results and nano-scale detections during ultratfiltration of Lap0.48-tspp6 (tp = 12 days). T = 25±1°C. Ultrasound: 20 kHz, 2 W.cm^{-2}. L_p = 196 × 10^{-5} L.h^{-1}.m^{-2}.Pa^{-1} a) Cross-flow filtration curve: evolution of permeate flux J_v, transmembrane pressure TMP of filtration cell and cross-flow rate Q_v over time. b) Related concentration profiles at steady state from the membrane surface to the bulk, deduced from in-situ SAXS measurements. Increase of permeate flux significant and immediate when US is on; no permeate flux without TMP under US.*

1.5.2.2 Evolution of concentration profiles

Further investigation focuses on the transient state of step 1 and 2. As shown in Fig. 3.18a, at step 1, accumulation of particles occurred at the membrane surface and the concentration profile follows the exponential-shape form as revealed before. At step 2, US was on, this accumulated layer was disrupted immediately. Interestingly, disruption regime seems different from what have been revealed in section 1.5.1.2 (Lap1-tspp6). Comparison between the profile at 1 min and 4 min (Fig. 3.18b) indicates that the top, less concentrated part of the accumulated layer was firstly disrupted at this step and the thickness of accumulated layer reduces since the first moment of US application. It should be noted that the feed dispersion has a sol-gel transition concentration (ϕ_v = [0.35, 0.48] %) corresponding to a mechanically weak fibrous structure, these

fibers would then be entangled to form a denser network of micron-sized aggregates which is mechanically more resistant when concentration increases (Pignon *et al.*, 1996). It could be therefore explained by the fact that the mechanical links between particles within the concentrated layer are so weak at the range of ϕ_v = [0.48, 1.00] % that the applied ultrasonic force can easily break it up, even immediately. New balance between accumulation-induced forces (including the convective force towards the membrane and the interacted force of Laponite particles) and anti-accumulative forces (including the applied ultrasonic force and hydrodynamic force) was established at 4 min and resulted in a thinner accumulated layer. After 4 min, the bottom part is also disrupted until the removal of the entire layer, as what have been revealed in the case of Lap1-tspp6.

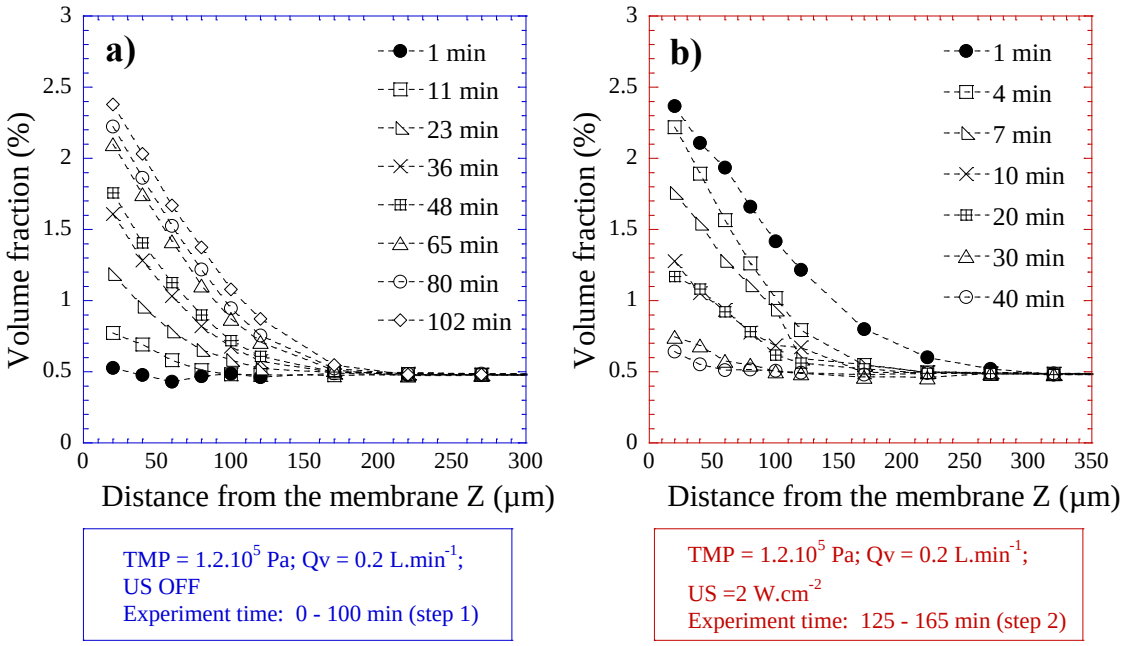

Fig. 3.18 *Evolution of concentration profiles within the accumulated particles layer over time during ultrafiltration of Laponite dispersions (Lap0.48-tspp6, tp = 12 days) without and with US. T = 25±1°C, TMP = 1.1×10^5 Pa. Ultrasound: 20 kHz, 2 W.cm^-2. The top, less concentrated part of the accumulated layer is firstly disrupted at step 2 and the thickness of accumulated layer reduces since the first moment of US application.*

1.5.2.3 US effect on system at rest

At step 3, the concentrated layer was removed by US during step 2, TMP and Q_v were then stopped in order to determine the effect of US on system at rest. As shown in Fig. 3.17a, no permeate flux was produced without TMP under US, suggesting that US cannot bring about a convective flux through the membrane (at least not as strong as that of TMP). In addition, the correspondent concentration profile stays unchanged: always no concentrated layer is detected at the membrane surface, as revealed in Fig. 3.19a. Before step 4, a concentrated layer was pre-formed, then TMP and Q_v were stopped. Step 4 aims at determining the effect of US on formed concentrated layer at rest. Apparently, as shown in Fig. 3.19b, the concentrated layer becomes less compact in this case than under filtration since its thickness grows into 1000 µm. The applied US then led to a disruption of this concentrated layer: its bottom part becomes less and less concentrated over time. However, unlike what happened at step 2 (during filtration), US did not remove this concentrated layer since after 10 min the trend of deconcentration steps down and it starts to follow a constant-fluctuation regime. It suggests that the applied US cannot remove the concentrated layer by itself and the removal at step 2 is a result of the combined action of US and hydrodynamic force (anti-accumulation forces).

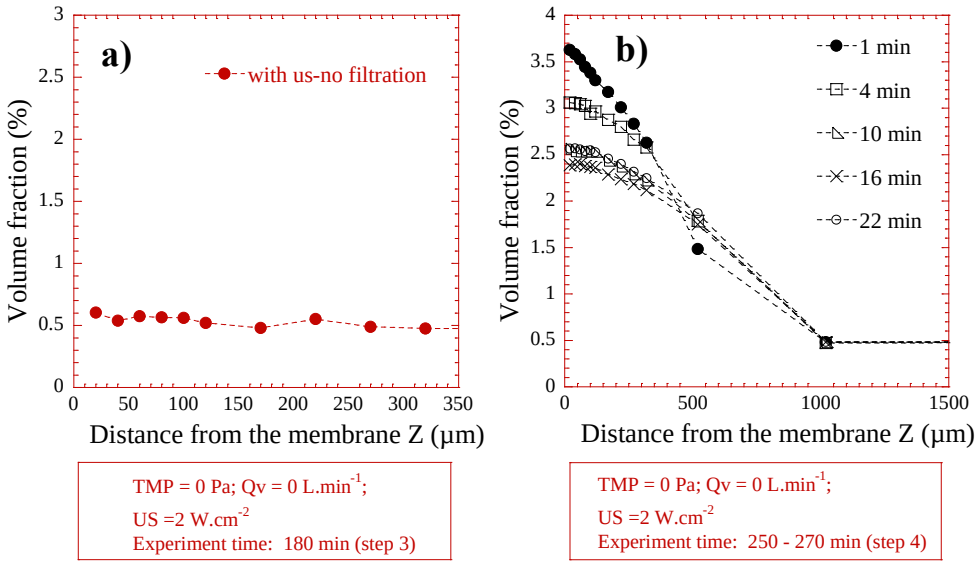

Fig. 3.19 *Concentration profiles under US when TMP and Q_v were stopped (system at rest). Laponite dispersions: Lap0.48-tspp6, tp = 12 days. T = 25±1°C. Ultrasound: 20 kHz, 2 W.cm^{-2}. The applied US disrupts the formed concentrated layer at rest without removing it.*

1.5.3 Ultrafiltration of Lap1-tspp0

Laponite dispersions without peptizer consist of very attractive network that eases the formation of aggregation. As already widely discussed in literature (Martin *et al*., 2006; Pignon *et al*., 1998, 1997), micrometer-sized aggregates consisted from nanometer-sized sub-units could be present in the dispersion and are rearranged to form a continuous three-dimensional isotropic structure that has a fractal behavior, giving the gel its three-dimensional structure that is responsible for the occurrence of a yield stress, which is not detected for the dispersions with peptizers (Pignon *et al*., 2012). This great change of structure gives interests to investigate their filtration performance and effect of US on it.

Fig. 3.20 presents the filtration curve of Lap1-tspp0 ultrafiltration run, different operating steps are distinguished and indicated in it. Step 1 serves as a layer-forming stage where J_v of steady state remains 5 $L.h^{-1}.m^{-2}$. Ultrasonic force of usual parameters (20 kHz, 2 $W.cm^{-2}$) was applied at step 2, an immediate increase of J_v (from 5 to 25 $L.h^{-1}.m^{-2}$) was detected. From step 3 to 6, different TMP were applied with or without US aiming at determining change of the nanometer-sized structure of Laponite sample under different operating conditions. In terms of J_v, application of US didn't bring about a secondary effect rather than an instantaneous one since J_v at step 5 is the same as that of step 1: 5 $L.h^{-1}.m^{-2}$ after two steps of ultrasonication. At step 4, with a TMP of the limiting-flux regime (as shown in Fig. 3.8), J_v remains at the same level of step 2: 25 $L.h^{-1}.m^{-2}$. It suggests that effect of the applied US on Lap1-tspp0 is not time-dependent, contrary to the case of Lap1-tspp6 (section 1.5.1).

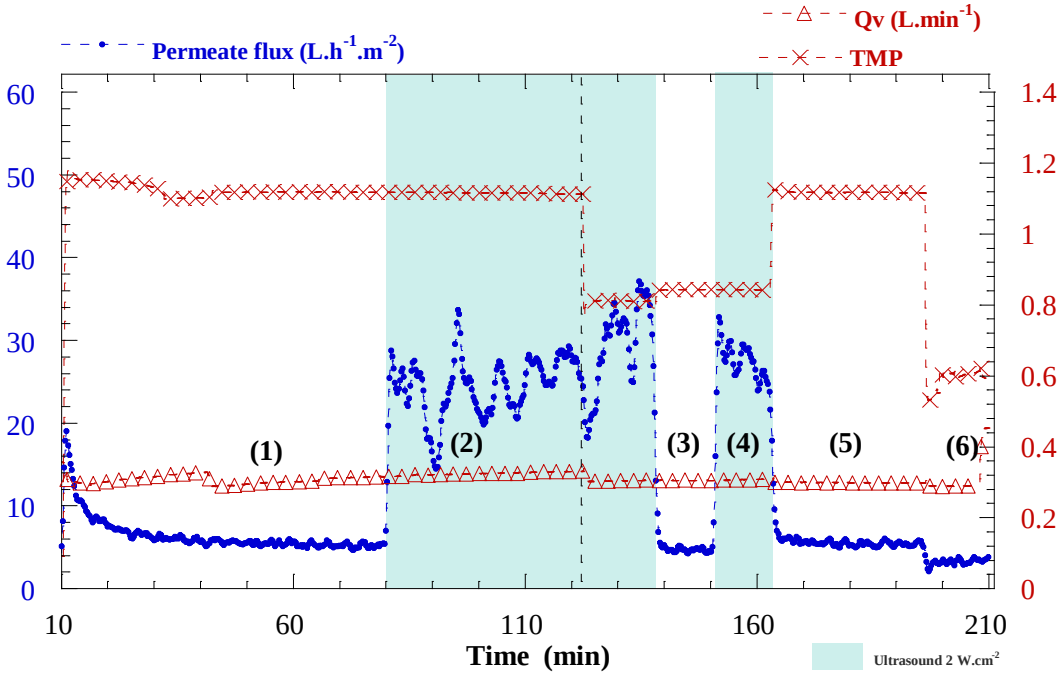

Fig. 3.20 *Cross-flow filtration curve: evolution of permeate flux Jv, TMP and Q_v over time. Laponite dispersions: Lap1-tspp0, tp = 12 days. T = 25±1°C. Ultrasound: 20 kHz, 2 W.cm^{-2}. L_p = 142 × 10^{-5} L.h^{-1}.m^{-2}.Pa^{-1}.*

1.5.3.1 Evolution of concentration profiles

Fig. 3.21 shows the evolution of concentration profiles at step 1 and step 2. At step 1, a progressive accumulation of particles at the membrane surface took place and finally led to a concentrated layer with a thickness of 720 µm and an adjacent-to-membrane concentration of 5.7 vol% (z =20 µm). Surprisingly, concentration profile remains unchanged during step 2 under US as shown in Fig. 3.21b, contrary to what have been revealed before. The concentrated layer was not at all disrupted by the applied US according to SAXS measurement, nevertheless, increase of J_v was important with a factor of 5.

Fig. 3.22 presents the SAXS profiles of Lap-tspp0. Each profile represents an instantaneous state of Laponite sample within the concentrated layer (at z = 80 µm, $\phi_v \approx 5$ %) during filtration (at step 3-6, as described in section 1.5.3). Three different transmembrane pressures (TMP) were applied with or without US. No matter under which operating conditions,

their SAXS profiles are almost fully superposed, at the length scales of both interparticles and particles. This result suggests that neither the compression force induced by TMP nor the applied ultrasonic force influenced the structure of formed deposit of Lap-tspp0 in this specific situation.

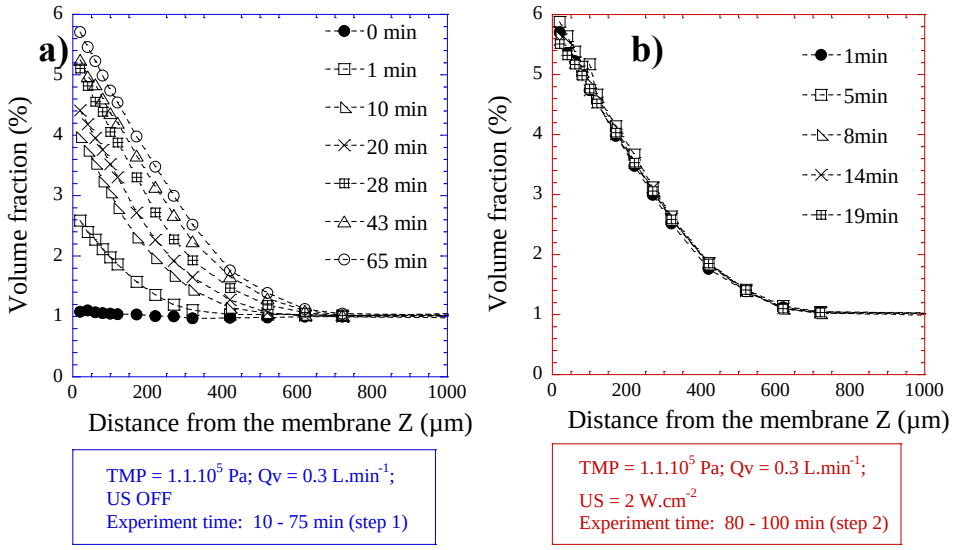

Fig. 3.21 *Evolution of concentration profiles within the accumulated particles layer over time during ultrafiltration of Laponite dispersions (Lap1-tspp0, tp = 12 days) without (a) and with (b) US. T = 25±1°C. Ultrasound: 20 kHz, 2 W.cm^{-2}.''0 min'' represents the initial state before filtration.*

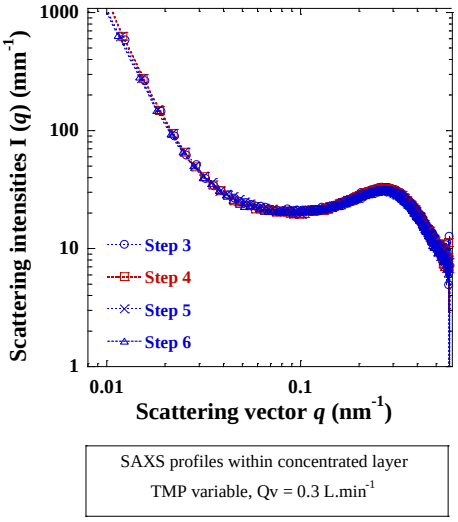

Fig. 3.22 *SAXS profiles of Laponite dispersions (Lap1-tspp0, tp = 12 days) within the concentrated layer during ultrafiltration with or without US. T = 25±1°C. Ultrasound: 20 kHz, 2 W.cm^{-2}.*

1.5.3.2 Particle orientation

Specific particles orientation is found during ultrafiltration of Lap1-tspp0. Fig. 3.23 shows the SAXS scattering patterns of this dispersion at step 1 and 2: each pattern represents one measurement point at different distances from the membrane surface of different filtration time. For step 1 (Fig. 3.23a), under only shear flow, instead of, the X-ray scattering patterns show an isotropic ring-shape (at t = 0 min). Since the first minute of filtration the three patterns closest to the membrane exhibit anisotropic interference peaks along the lateral arcs. As time goes on, more and more patterns appear pronounced anisotropic within the same profile: at t = 65 min, all the patterns below 420 µm are anisotropic. Considering the related concentration profile (Fig. 3.21a), one can find that only the bottom of the concentrated layer (thickness of 720 µm) exhibits anisotropic feature. Similar phenomenon has already reported in the case of dead-end filtration of Laponite dispersions (Pignon *et al*., 2000). It was proposed that upon filtration, the packed Laponite particles within the concentrated layer could exhibit a preferential orientation which is parallel to the membrane. This ordered arrangement was not changed by the applied US at step 2 since almost the same SAXS patterns can be observed at step 2 for all the measured moments.

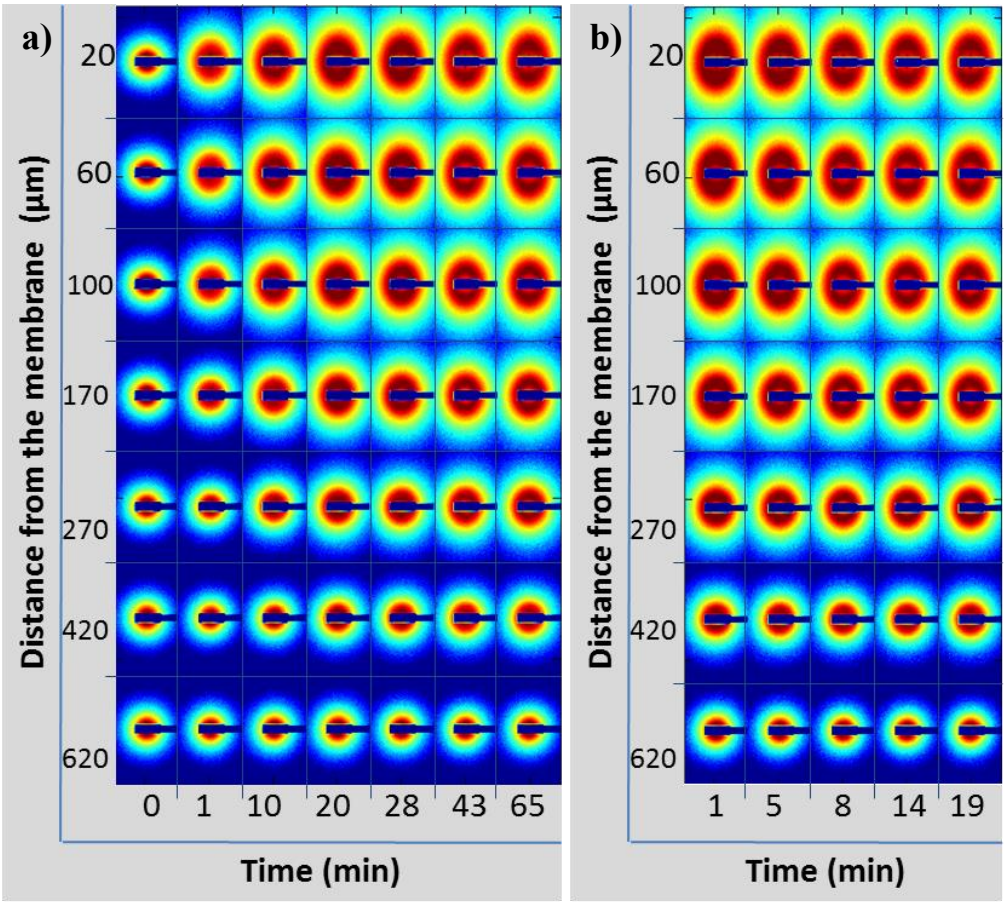

Fig. 3.23 *SAXS patterns of Lap1-tspp0 (tp = 12 days) of different positions z from the membrane surface at step 1 (a) and step 2 (b) during ultrafiltration. T = 25±1 °C, Ultrasound: 20 kHz, 2 W.cm^{-2}.*

1.5.5 Discussions

In this section, different US disruption regimes have been revealed for Laponite dispersions of different properties. Concentration and addition of peptizers are two main parameters to be considered. Feed dispersion with a sol-gel transition concentration corresponds to a mechanically weak fibrous structure with unconnected particles, these fibers would then be entangled to form a denser network of micron-sized aggregates which is mechanically more resistant when concentration increases (Pignon *et al*., 1996; Pignon *et al*., 2000). As discussed in chapter 2, the addition of peptizers in Laponite dispersions makes them flow more easily with a

vanishing of yield stress. The network of mechanical links that produces the solidlike behavior of pure Laponite dispersions could be weakened or dissociated by the addition of peptizers.

In the case of Lap1-tspp6 and Lap0.48-tspp6, the applied US removed the concentrated layer. It could be explained by the fact that the shear stress induced by anti-accumulation forces (including ultrasonic force and hydrodynamic forces) were sufficient to break up their weakened particle interaction. Consequently, the concerned Laponite dispersions were disaggregated over time and the concentrated layers were removed. The fact of disaggregation can also explain the time-dependent feature of US disruption regime (increasing J_v and deceasing duration to reach a concentrated layer removal over time under US).

However, in the case of Lap1-tspp0, neither change of the concentration profile nor modification of nano-sized inter-particle structure of Lap-tspp0 was revealed by SAXS measurement during application of US, then what leads to the increase of J_v?

To answer this question, ultrasonic actions should be reminded. As mentioned before, propagation of ultrasonic waves within liquid generates several phenomena. The most considered phenomena in membrane process intensification are acoustic streaming, microstreaming, and cavitation (Lamminen *et al*., 2004). Which one (ones) dominate(s) this process intensification? Firstly, cavitation activities have been characterized by erosion test of aluminum foil (chapter 2, section 4.3), which suggests that at the zones close to the membrane surface the cavitation activity is very limited, at least not apparent in erosion test. Therefore, on the basis of our results, microstreaming could be considered to play the major role. It occurs often near small obstacles (gas bubble or solid surface) placed within a sound field arising from the frictional forces between the boundary and the medium (Leighton, 1994). Within a fluid medium, a localized circulatory flow (of water in this case) could be generated with particularly large velocity gradients near the boundaries, while strain fields can be produced in non-fluid media. This phenomenon leads to localized actions as cavitation, which is consistent with our results of Lap-tspp6: the bottom, the more concentrated part and farther part from the ultrasonic transducer, of the accumulated layer is more responsive for the applied US rather than the top (Fig. 3.12 and Fig. 3.19b), it should be inverse, that is to say, the looser and closer-to-transducer part is disrupted first if acoustic streaming dominates.

Returning to the question, first of all, gel consistency of concentrated Lap-tspp0 in this case should be so high that the shear stress induced by the applied US was incapable to break up its network, thus removal of the concentrated layer was not detected. Nevertheless, micrometer-sized structure change of this concentrated layer is speculated to occur under US during filtration. As proposed by Pignon *et al.* (1998), consisting of micrometer-sized aggregates bundles, the network of Laponite dispersion is heterogeneous when concentrated, with zones of dense and less dense particle concentrations. These heterogeneous boundaries facilitate the action of microstreaming which generates localized circulatory flow (of water) between the bundles. It consequently speeds up mass transfer and increases J_v when convective force (TMP) is applied.

1.6 Summary

In section 1, effect of US on Laponite dispersions has been investigated, including their flow properties change under US, filtration performance improvement under US at macro-scales as well as nano-scales.

Firstly, this research has shown that a simultaneous transmembrane pressure and ultrasonication of 20 kHz could be an efficient way to improve cross-flow filtration of Laponite dispersions: it has led to a significant increase of permeate flux, which can be explained by a modification of concentrated particles layer at the membrane surface, as evidenced by *in-situ* SAXS measurements.

Secondly, the mechanism of ultrasonication has also been discussed. It could be considered as an additional force of an effective range on the order of micrometers or smaller, which is capable to disaggregate connected Laponite dispersions containing peptizers without modifying their initial particle properties. This progressive disaggregation determines the filtration performance to some extent. In addition, it strengthens the hydrodynamic force of cross-flow ultrafiltration leading to a complete removal of concentrated particles layer. For the pure Laponite dispersions, no change of concentration profile or nanometer-sized inter-particle structure was detected by SAXS measurement. In this case, the increase of J_v could result from

localized high-velocity circulatory flow between the aggregates bundles generated by ultrasonic force, probably by the action of microstreaming.

2. Natural clay suspensions

2.1 Introduction

To reveal the mechanism of ultrasonic action during filtration, more colloidal suspensions were investigated. This section concerns two types of natural clay suspensions: SWy-2 T3 and NAu-1 T3. Different from Laponite dispersions, their plate-like particles with bigger size than Laponite, interact repulsively due to double-layer electrostatic forces, as discussed in chapter 2. Due to the mutual alignment of the particles, their 2D-SAXS patterns exhibit anisotropic feature. From the structure factor curve (q^2*I(q) as a function of q) it can exhibit a marked diffuse peak which correspond to the short-range positional order of the platelets. These characteristics are then used to determine their concentration profiles, as described in chapter 2.

2.2 Ultrafiltration of SWy-2 T3

A filtration run of SWy-2 T3 was carried out at ESRF, whose operating curve is presented in Fig. 3.24. During this filtration run, operating conditions were changed in order to determine effect of different parameters (US and shear flow). Discussions will be given step by step distinguished by operating conditions. Related concentration profiles close to the membrane surface of each step are presented in the following figures.

During the first 230 min a concentrated layer must form since J_v stays around 4 $L.h^{-1}.m^{-2}$. The application of US then leads to an increase of J_v to around 10 $L.h^{-1}.m^{-2}$, it does not occur immediately but with a delay of around 10min. This phenomenon will be discussed with the related concentration profile in the following section. Information of further steps displayed in Fig. 3.24 will be discussed from section 2.2.1 to 2.2.3 as well.

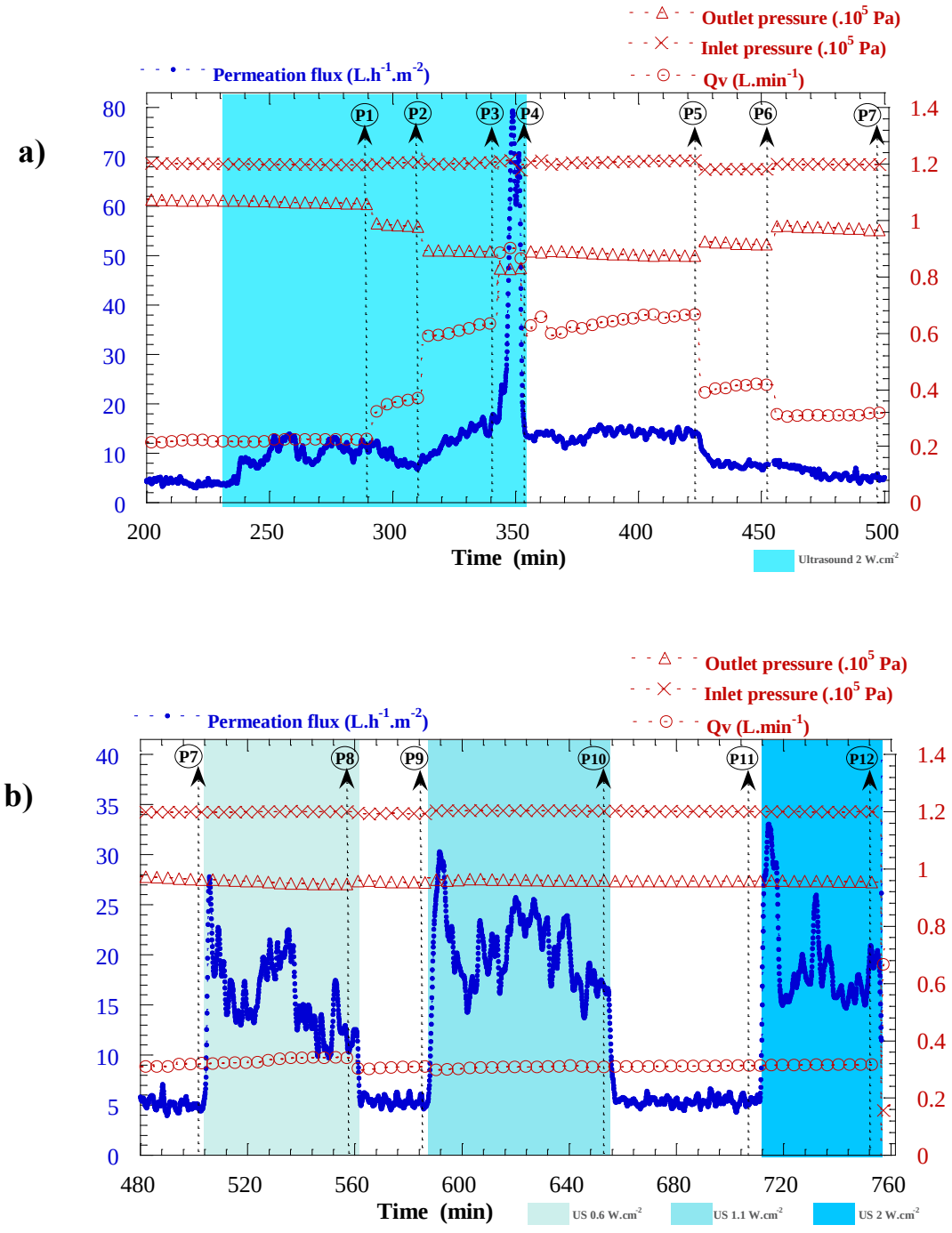

Fig. 3.24 *Cross-flow filtration curve: evolution of permeate flux J_v, inlet and outlet pressure of filtration cell P_{in}/P_{out} and Q_v over time. Feed suspension: SWy-2 T3 (ϕ_v = 0.47 %). T = 25±1°C. Ultrasound: 20 kHz, 2 W.cm^{-2}. L_p = 169 × 10^{-5} L.h^{-1}.m^{-2}.Pa^{-1}.''P1''-''P12'' represent the SAXS measured point of each operating step.*

2.2.1 Effect of US under different magnitudes of shear flow

US was applied at t = 230 min (Fig. 3.24a), no immediate J_v increase was detected, and the related concentration profile remained unchanged until the end of step 1, whose concentration profile is displayed in Fig. 3.25 by P1. This profile confirms a concentrated layer of around 1000 µm with the adjacent-to membrane concentration of 1.8 vol%. Afterwards, Q_v was raised from 0.2 to 0.9 $L.min^{-1}$ expecting a disruption of the concentrated layer. As shown in Fig. 3.25, the expected disruption indeed took place: the concentrated layer became thinner and thinner with rise of Q_v under US, and it was nearly removed at Q_v = 0.9 $L.min^{-1}$. The rise of Q_v from 0.2 to 0.3 $L.min^{-1}$ brought about a slight reduction of layer thickness and the concentrated part (from z = 80 to 400 µm) was barely changed thus this operation did not lead to an increase of J_v (Fig. 3.24). J_v began to increase when Q_v was raised to 0.6 $L.min^{-1}$, which can be explained by the disruption of concentrated part of the accumulated layer. At Q_v = 0.9 $L.min^{-1}$, this concentrated part was greatly disrupted resulting in an important J_v, of 70 $L.h^{-1}.m^{-2}$ (Fig. 3.24).

It is also worth noting that the deduced concentration profiles at the membrane surface are very different from those of Laponite dispersions. It seems that they are consisted of two independent layers: a loose one close to the bulk and a dense one at the membrane surface. It is reported that the sol-gel transition of SWy-2 T3 is around 0.54 vol% (Michot *et al*., 2004), which is slightly higher than the concentration of the feed suspension (0.47 vol%) for this filtration. It implies that the filtrate concentration must pass through the sol-gel transition during particle accumulation under filtration. Interestingly, this sol-gel transition is absent in the deduced concentration profiles: as shown in Fig. 3.25, the concentration range of 0.54 vol% to 1 vol% can not be found in all the displayed profiles. It seems that a gel deposit is formed without any transient phase once the suspension reaches certain critical state during filtration. One possible explanation could be that this suspension is well stabilized by its repulsive interaction between particles when concentration is low, so that the particles can not approach closely, thus no significant increase of concentration occurs in this regime. However, when this repulsive force between particles is overcome, structural change of suspension could be abrupt: the double-layered plate-like particles could be compressed, flattened or overlapped which leads to a formation of gel deposit.

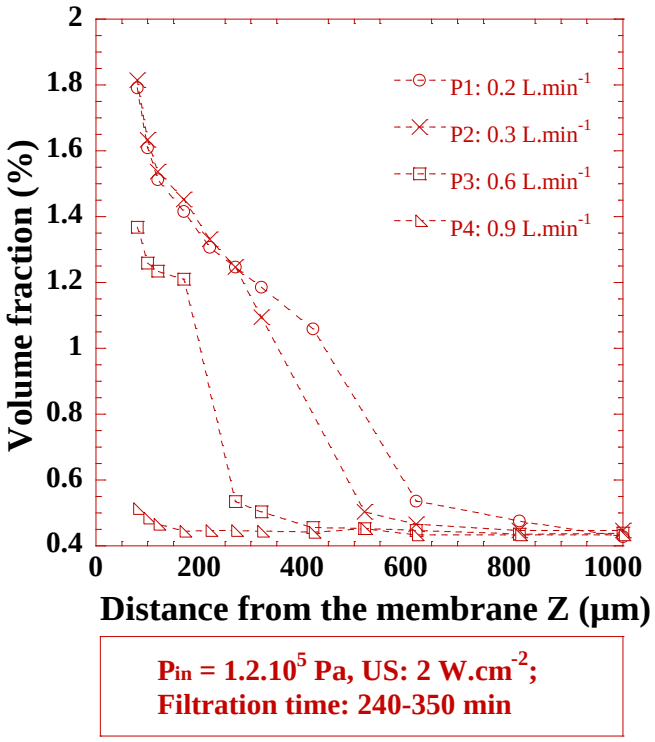

Fig. 3.25 *Concentration profiles within the accumulated layer at different Q_v during ultrafiltration of SWy-2 T3 (feed suspension: ϕ_v = 0.47 %) under US. T = 25±1°C. Ultrasound: 20 kHz, 2 W.cm^{-2}. Disruption of concentrated layer at high Q_v.*

2.2.2 Effect of shear flow without US

In this section, different Q_v was applied without US. Lowering the shear flow indeed promotes the formation of concentrated layer, as shown in Fig. 3.26. In addition, almost the same profile can be found at the same Q_v no matter US is turned on or not (0.3 L.min^{-1}: P2 versus P7; 0.6 L.min^{-1}: P3 versus P5). These results indicate that the disruption of concentrated layer occurred in section 2.2.1 could mainly result from the rise of Q_v and the contribution of US could be very limited. Nevertheless, US increased J_v as usual: as displayed in Fig. 3.24a, at Q_v = 0.3 L.min^{-1}, J_v is around 10 L.h^{-1}.m^{-2} with US (P2) while only 5 L.h^{-1}.m^{-2} without US (P7).

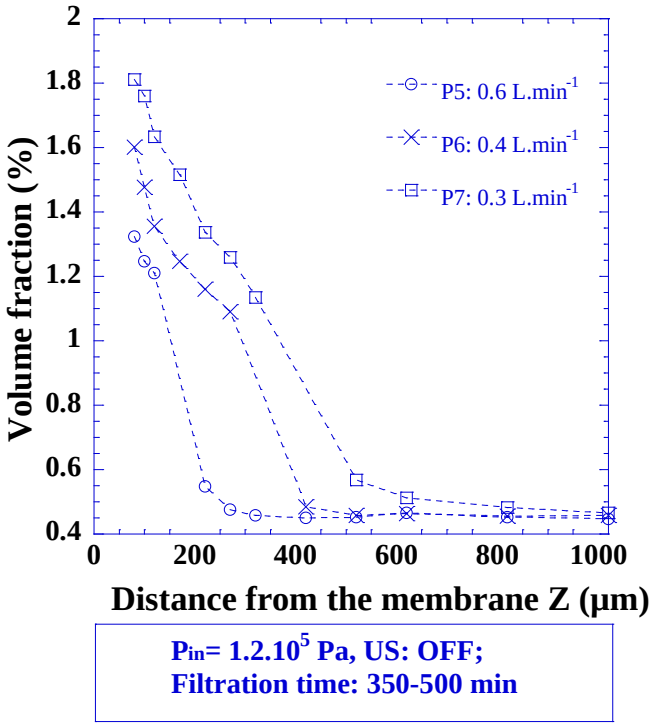

Fig. 3.26 *Concentration profiles within the accumulated layer at different Q_v during ultrafiltration of SWy-2 T3 (feed suspension: ϕ_v = 0.47 %) without US. T = 25±1°C. Lowering the shear rate promotes the formation of concentrated layer.*

2.2.3 Effect of ultrasonic intensity

When a concentrated layer was re-formed during step 7 (P7), US was applied again. Three ultrasonic intensities were applied at steps 8-12. Correspondent concentration profiles are presented in Fig. 3.27a. Whichever the applied ultrasonic intensity, the concentration profile remains always unchanged as what have been revealed in the case of Lap1-tspp0 (section 1.5.3). In terms of J_v, US brought about significant increase, with a factor of at least 3, as shown in Fig. 3.24b. The similarity between this case and the case of Lap1-tspp0 suggests the same scenario could take place during filtration of SWy-2 T3 under US. The interacted force of SWy-2 T3 particles could be stronger than which was induced by US so that the network of the concentrated layer was not broken up.

The 2D-SAXS patterns of SWy-2 T3 of different positions z from the membrane surface during ultrafiltration are presented in Fig. 3.27b at two filtration states: a state without US (P7) and the other under US (P8). No significant difference of patterns can be observed between these two states, confirming the results of concentration profiles. In addition, it can be seen that the diffuse peaks of the SAXS patterns flip regularly at increasing distance from the membrane surface denoting a change in the inter-particles distance in the concentrated layers.

As a natural swelling clay mineral, this suspension is highly polydisperse in terms of size, shape and charge (Michot et al., 2004). Therefore heterogeneous boundaries within the concentrated layer could be found and localized circulatory flows are then produced under ultrasonic force. However, this localized circulation might not lead to an increase of J_v immediately, as mentioned in section 2.2.1, a delay of 10 min occurred when the ultrasonication was applied for the first time (Fig. 3.24a). Considering the morphological feature of SWy-2 T3, it is possible that these plate-like particles were highly overlapped so that the ‘‘pathway’’ of the additional circulation was blocked at the beginning, then a disaggregation of weak mechanical links (probably at the micrometer-sized scales) enabled the connection of localized circulation and a ‘‘pathway’’ of water formed finally. Consequently, increase of J_v was detected with a delay of 10 min. This possible micrometer-sized disaggregation could be permanent (at least in the short term) so that increase of J_v occurred immediately while US was applied for the following steps (step 8, 10 and 12). It is consistent with the results of Lap1-tspp6 (section 1.5.1).

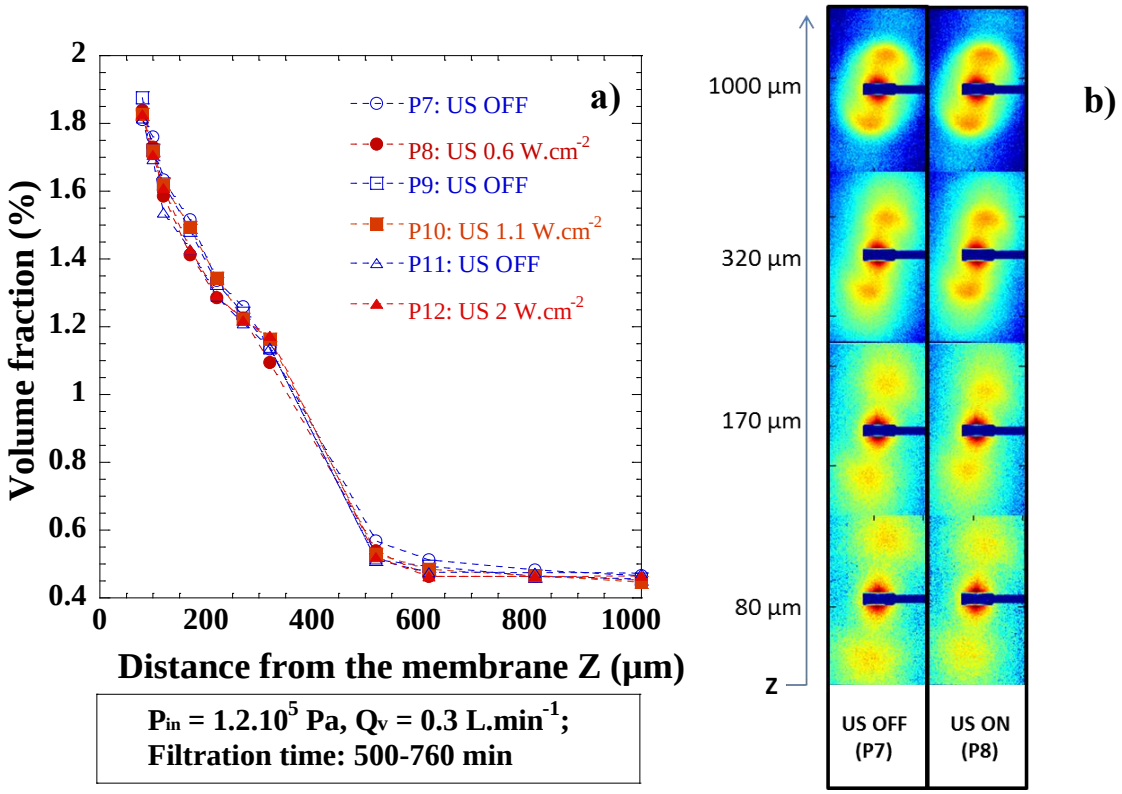

Fig. 3.27 a) *Concentration profiles within the accumulated layer for different ultrasonic intensity during ultrafiltration of SWy-2 T3 (feed suspension: ϕ_v = 0.47 %). T = 25±1°C. b) SAXS patterns of this dispersion of different positions z from the membrane surface during ultrafiltration. No change of concentration profile occurs under US of different intensities.*

2.3 Ultrafiltration of NAu-1 T3

As a type of natural swelling clay, NAu-1 T3 suspension is consisted of dioctahedral particles of bigger size than that of SWy-2 T3 (see chapter 2 section 1.4). Their behavior in the process of ultrasonic-assisted filtration were also investigated. Fig. 3.28 presents the filtration curve of the performed run as well as correspondent concentration profiles of concerned moments. J_v of steady state is around 11 $L.h^{-1}.m^{-2}$ without US (P1 and P3) while increasing to 30 $L.h^{-1}.m^{-2}$ at P2 and 75 $L.h^{-1}.m^{-2}$ at P5. Concentration profiles at the five measured points (P1-P5) are displayed in Fig. 3.28b. As the case of SWy-2 T3, the accumulated layer also exhibits a two-independent-layer feature with a gap zone where the suspension should hold the sol-gel transition concentration (ϕ_v = 0.83 %). Moreover, little change is detected during all this process even

under US of two different intensities. At P5 the concentrated layer was slightly thinned, which could probably explain the fact that J_v takes a new rise from t = 240 min. It should be noted that NAu-1 T3 could be more susceptible to US since their average particle sizes are bigger than the other gels in this study. A particle rupture could occur, which then leads to a disruption of particle network. Therefore, at the beginning, the shear stress induced by the applied US was not able to break up the mechanical links of NAu-1 T3 network, but their yield stress decreased over time with the particle rupture thus US could finally disrupt this concentrated layer, as shown in P5 of Fig. 3.28b.

By gravimetric analysis, the rejection rate was determined for this filtration run, which is 42 %. It suggests that a great amount of particles passed through the membrane. This low rejection rate could explain the J_v decline under US from t = 80 to 140 min and from t =180 to 240 min. it is possible that an inner membrane fouling occurred when particles passed and some were detained.

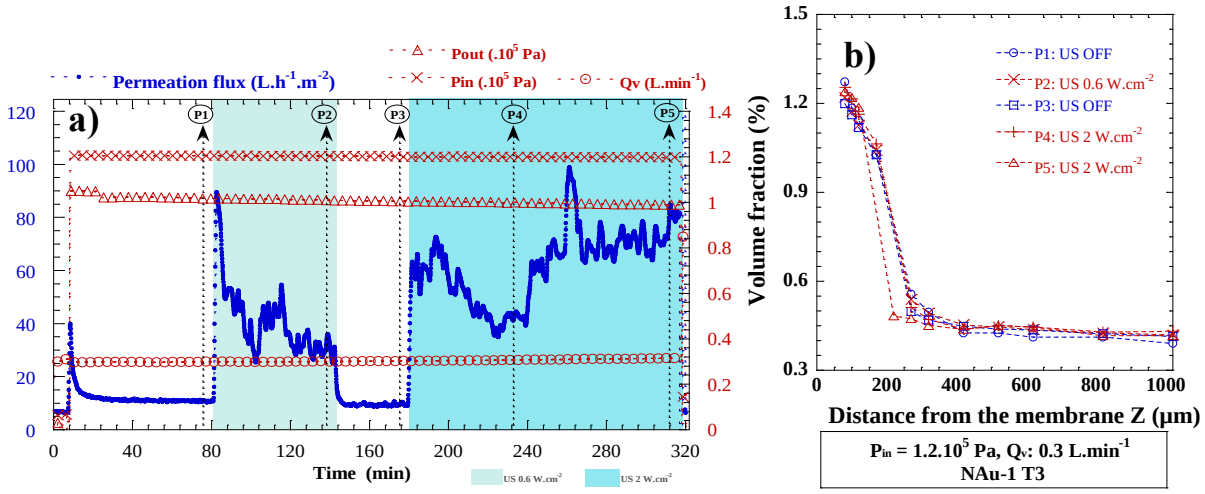

Fig. 3.28 *Combination of macro-scale results and nano-scale detections during ultratfiltration of NAu-1 T3 (feed suspension: ϕ_v = 0.40 %). T = 25±1°C. Ultrasound: 20 kHz, 2 W.cm^{-2}. L_p = 187 × 10^{-5} L.h^{-1}.m^{-2}.Pa^{-1} a) Cross-flow filtration curve: evolution of J_v, inlet and outlet pressure of filtration cell P_{in}/P_{out} and Q_v over time. b) Related concentration profiles from the membrane surface to the bulk, deduced from in-situ SAXS measurements. Increase of permeate flux significant and immediate when US is on; a slight thinning of concentrated layer at the end of step 5 under US.*

2.4 Summary

In section 2, two natural swelling clay suspensions were investigated in the ultrasonic-assisted ultrafiltration. In both cases, the concentrated layers were identified as a combination of two independent layers. The applied US barely disrupted the concentrated layer but it always brought about significant J_v increase, exactly as the case of Lap1-tspp0. Increase of applied shear flow reduced the concentrated layer, combing with US then led to a great increase of filtration performance.

Conclusions

In this chapter, mechanisms of ultrasonic assisted ultrafiltration of three clay suspensions were revealed.

Firstly, flow properties of Laponite dispersions under different conditions have been discussed. Their yield stress/volume fraction dependence was established and effects of pre-shearing and US treatment on yield stress of Laponite sample were revealed. It shows that both treatments reduce their yield stress levels and Laponite dispersions with peptizers (6%) are more susceptible to shearing force or ultrasonic force than those without peptizer.

Secondly, a simultaneous ultrasonication of 20 kHz has been proven efficient to improve cross-flow filtration of clay suspensions: it has led to a significant increase of permeate flux, which can be explained by a modification of concentrated particles layer at the membrane surface, as evidenced by in-situ SAXS measurements.

Finally, taking into account the results of these three clay suspensions, the mechanism of ultrasonication during filtration can be proposed. Ultrasonic force induces shear stress by the means of localized high-velocity circulatory flow within the network of accumulated clay particles, if this shear stress is higher than the yield stress of suspension, disaggregation occurs which leads to a progressive removal of accumulated layer. Otherwise, the (nanometer-sized) structure of particle network remains unchanged and the additional localized water circulation itself is responsible for the increase of J_v.

4

Ultrasonic assisted ultrafiltration of colloids of industrial interest

In this chapter, two types of colloidal suspensions of great interest in industry were investigated: skim milk and nanocrytals. The related results will be presented successively. In section 1, effect of ultrasonication on structural organization of skim milk will be discussed under different circumstances. The second section involves US enhanced ultrafiltration of starch nanocrystals and cellulose nanocrystals; it will focus on the structural properties of nanocrystals under the multi-forces field. Some supplementary characterizations will also be contained in this chapter such as rheological behaviors and microscopic observation of milk and/or nanocrystals samples.

1. Skim milk

1.1 Introduction

In dairy industry concentration and fractionation processes of milk components are largely performed with membrane operations. Ultrafiltration (UF) is used to standardize the protein content of milk prior to the cheese manufacture. The bottleneck of skim milk ultrafiltration is the fouling phenomenon that affects the performance of the process and thus limits its productivity.

Since fouling is the major problem during milk filtration, ultrasonic assisted fouling control presents a great potential in this application. Several successful examples have already been found in literature. In immersing the cross-flow filtration cell in an ultrasonic water bath where the dissipated power is 20 $W.L^{-1}$, Muthukumaran *et al.* (2005, 2007) reported that ultrasound of low frequency (50 kHz) can be effective in enhancing both the production and cleaning cycles of whey ultrafiltration. Their results suggested that the application of ultrasound can lower the compressibility of protein deposit and increase the mass transfer coefficient within the concentration polarization layer. More recently, Mirzaie *et al.* studied effects of various ultrasonic related parameters on flux enhancement in dead-end microfiltration of milk and obtained a flux enhancement factor of 490% by applying ultrasonic waves of 20 kHz and 31.57 $W.cm^{-2}$ (Mirzaie and Mohammadi, 2012). In addition, effect of ultrasound (20 kHz, 20 and 41 W) on the physical and functional properties of skim milk has been reported by Shanmugam *et al*.

(2012). They found a slight denaturation of whey proteins (followed by their self-aggregation and aggregation with free caseins), but no change of milk viscosity caused by ultrasonication and no influence of acoustic cavitation on casein micelle structure. They suggested that the minor change to the milk imparted by US foresees its potential for optimizing this technique for industrial applications.

Using the designed 'SAXS Cross-Flow US-coupled Filtration Cell', this study is devoted to enhance skim milk cross-flow ultrafiltration by applying *in-situ* ultrasonication and to characterize effects of ultrasound at multi-scales. Macroscopic results, presented by the permeate flux, will be combined with simultaneous observations of structure at nanometer length scale (mainly concentration profiles of casein micelles), revealed by real-time *in-situ* small-angle X-ray scattering (SAXS) measurements by synchrotron radiation.

1.2 Flow properties of casein micelle suspensions

Summarizing some precedent data from the work of Christophe David and Mouhammad Abyan, flow properties of casein micelle suspensions were investigated by rheometric measurements in order to better understand their filtration behavior. The studied concentration ranged from 27 to 216 $g.L^{-1}$ (from C_o to $8.00*C_o$). The approximate volume fraction (Φ_V) was calculated by taking a specific volume of casein of 4 $mL.g^{-1}$ (David *et al.*, 2008). The steady state flow curves are presented in Fig. 4.1, which shows an evolution of rheological behavior with the increase of casein micelle concentration. The suspensions exhibit a Newtonian behavior below $4.00*C_o$ (108 $g.L^{-1}$, the blue part) and a shear thinning behavior from $4.00*C_o$ to $6.80*C_o$ (183.6 $g.L^{-1}$, the green part). For the suspensions with higher concentrations, from $7.00*C_o$ to $8.00*C_o$ (from 189 $g.L^{-1}$ to 216 $g.L^{-1}$), a yield stress is revealed (the red part). For the sample at the highest concentration (8.00*Co, 216 $g.L^{-1}$, Φ_V = 0.9), the rheological measurements were carried out only at low shear rates so that only the yield stress was detected. Although rheological behavior of casein micelle suspensions has been investigated by several groups (Bouchoux *et al.*, 2009; Dahbi *et al.*, 2010; David *et al.*, 2008; Kromkamp *et al.*, 2007), it is the first time that the yield stress behavior is reported.

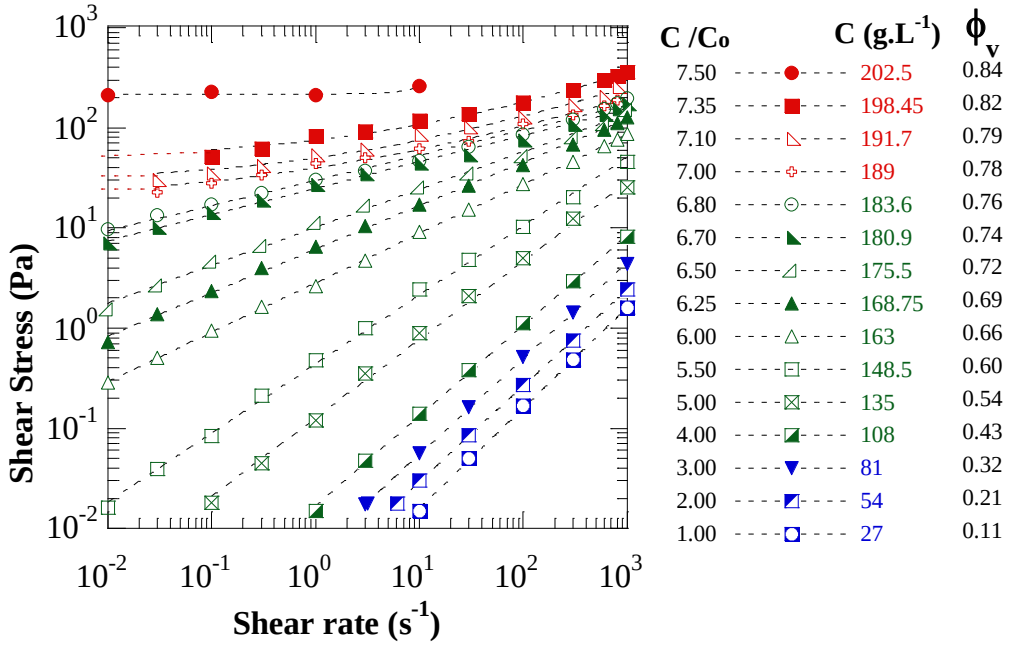

Fig. 4.1 *Steady state flow curves of casein micelle suspensions in deionized water as a function of concentration. Dashed curves correspond to power law or Herschel-Bulkley law fitting. T = 25±1°C.*

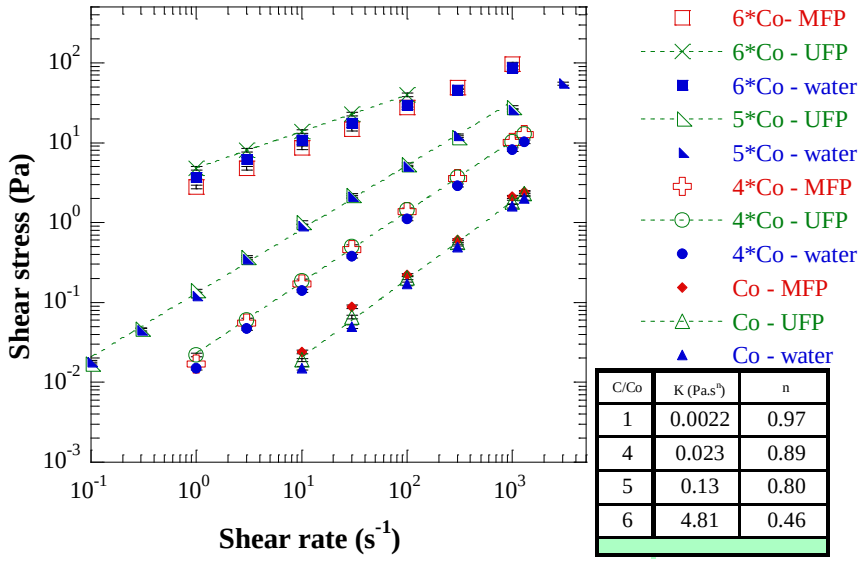

C/Co	K (Pa.s^n)	n
1	0.0022	0.97
4	0.023	0.89
5	0.13	0.80
6	4.81	0.46

Fig. 4.2 *Steady state flow curves of casein micelle suspensions dispersed in different aqueous phases (in deionized water, in ultrafiltrate (UFP) or in microfiltrate (MFP)) as a function of concentration. Dashed curves correspond to Power law fitting. T = 25±1°C. The suffixes of legend indicate the aqueous phases, e.g. ''-water'', ''-UFP'' means that the casein micelle suspension was dispersed in deionized water, in ultrafiltrate, respectively.*

Effect of aqueous phase on flow properties of casein micelle suspensions has also been evaluated. The results presented in Fig. 4.2 suggest that the evolution of rheological behavior from Newtonian to shear-thinning with the increase of concentration is not dependent on the nature of aqueous phase (deionized water, ultrafiltrate and microfiltrate) for the suspensions at $C_o<C<6*C_o$. The measured shear stresses vary within the error bars (±5%) of the rheometric measurements. These results signify that the flow properties of casein micelle suspensions in low concentration regime obtained in Fig. 4.1 can be used for further discussions concerning skim milk.

A Newtonian or shear-thinning behavior without any yield stress (sample concentration C<189 g.L^{-1}, less than 7.00*C_o) is well depicted by a power law: $\tau = K\dot{\gamma}^n$, where τ represents the shear stress (Pa), K is the consistency (Pa.s^n), $\dot{\gamma}$ is the shear rate (s^{-1}) and n is the shear-thinning index. Therefore, the experimental points were fitted by this model and presented by the dashed curves in Fig. 4.1 and Fig. 4.2. Evolution of K (filled squares) and n (filled circles) as a function of concentration C and volume fraction Φ_V of casein micelle was plotted in Fig. 4.3a. The values of K and n stay stable (n close to 1 and K stays at the range of 10^{-3}) until 135 g.L^{-1} (Φ_V = 0.55). Beyond this critical concentration, the consistency K increases strongly and the shear-thinning index drops significantly with the increase of concentration.

When the concentration of casein micelle suspension samples becomes higher than 189 g.L^{-1} (more than 7.00*C_o), the suspensions exhibit a gel consistency and yield stresses emerge on the flow curves (Fig. 4.1). In this case, a Herschel-Bulkley viscoplastic model was used for curve fitting (Macosko, 1994): $\tau = \tau_o + K\dot{\gamma}^n$, where τ_0 is the yield stress (Pa). In Fig. 4.3b, evolution of their yield stresses as a function of concentration or volume fraction of casein micelle is plotted. A percolation law (Piau, 2007) was adopted to fit the experimental data: $\tau_o \propto (C - C^*)^a$. This model allows to estimate the concentration of sol-gel transition of casein micelle C* (g.L^{-1}), which equals to 185 g.L^{-1} (Φ_V = 0.76). This estimated value is close to the reported value (178 g.L^{-1}) by Bouchoux *et al.* (2009). By studying the evolution of elastic modulus as a function of concentration, the authors concluded that beyond this critical value, the suspension behaves as an elastic gel. This value corresponds to random-close packing concentration for a 40 % polydisperse hard-spheres suspension.

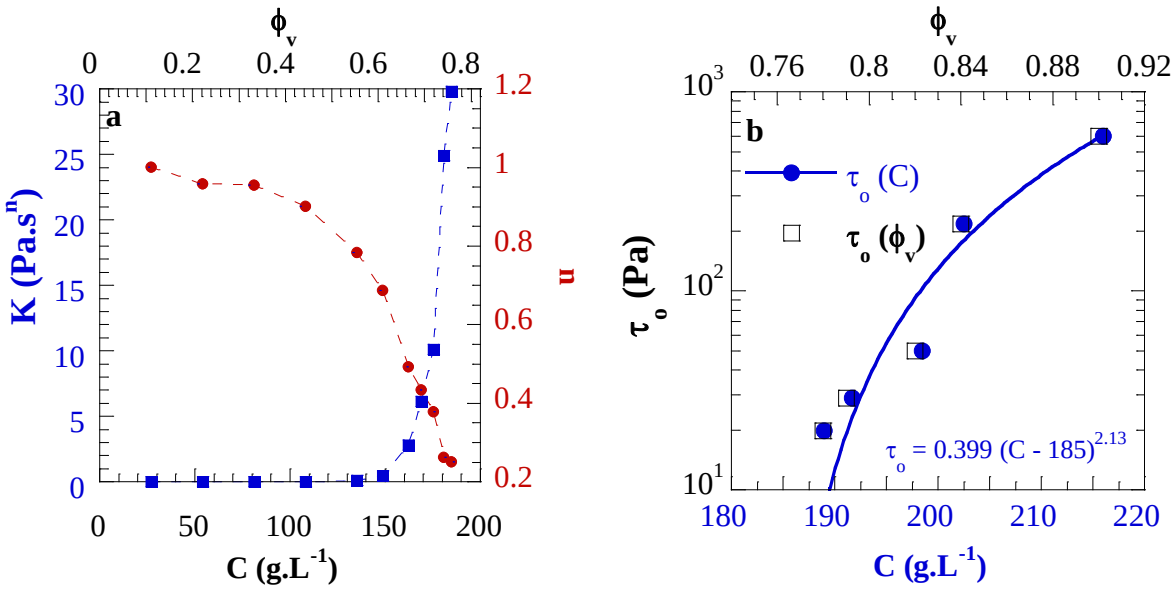

Fig. 4.3 *a) Evolution of the consistency K and the shear-thinning index n as a function of concentration C or volume fraction* $\boldsymbol{\Phi_v}$ *of casein micelle in deionized water. These parameters were deduced from power law based on Fig. 4.1. b) Evolution of yield stress* $\boldsymbol{\tau_0}$ *as a function of concentration C or volume fraction* $\boldsymbol{\Phi_v}$ *of casein micelle in deionized water.* $\boldsymbol{\tau_0}$ *were deduced from Herschel-Bulkley law based on Fig. 4.1. T = 25±1°C.*

Some explanations can be found in literature for this evolution of flow properties of casein micelle as their concentration increase. Bouchoux *et al.* (2010, 2009) point out that in a concentration regime of 25-150 $g.L^{-1}$, the dispersions are liquid and turbid, and the micelles interact as repelling spheres with free volume between them. There are no changes of internal structure of casein micelles but only their relative positions are changed by compression. David *et al.* (2008) suggest that the evolution of rheological behavior from Newtonian to shear-thinning (critical concentration: 108 $g.L^{-1}$, as shown in Fig. 4.1) was attributed to the apparition of excluded volume interaction as well as weak electrostatic interactions between the casein micelles. Dalgleish *et al.* summarize the related studies (Alexander *et al.*, 2002; Bouchoux *et al.*, 2010, 2009; Dahbi *et al.*, 2010; de Kruif, 1999; Ferrer *et al.*, 2011; Sandra *et al.*, 2011) in literature and suggest that in low concentration regime (C<178 $g.L^{-1}$) the micelles cannot approach closely and behave as hard spheres in a liquid because of the stabilizing layer of κ-casein (Dalgleish and Corredig, 2012). Further concentration (C>178 $g.L^{-1}$) leads to overlap,

compression of the hairy layers, and distortion of the micellar structure, thus the concentrated milk forms a soft solid (which explains the emergence of yield stress in Fig. 4.1).

1.3 US effect on properties of feed suspensions for filtration

From this section, only skim milk suspensions prepared from "low heat" powder were investigated. In order to reveal the effect of ultrasound on feed suspensions of skim milk, rheological behavior and SAXS profiles have been investigated. Ultrasonic effect (20 kHz, 20 and 41 W, 60 min) on skim milk at C_o has already been investigated by Shanmugam *et al.* (2012) and no viscosity change was observed at this concentration. A more concentrated one was used in this study. Fig. 4.4a presents the steady state flow curves of skim milk suspension at $4*C_o$. Three samples were analyzed: one at rest and two others were taken from bulk suspensions during cross-flow filtration with/without ultrasound (20 kHz, 2 $W.cm^{-2}$, 90 min). The rheological behaviors were determined 5 minutes after sampling. For the suspension at rest, which is not subjected to the shear stress of the pump in the filtration setup, a shear thinning fluid behavior can be observed which confirms the observation in Fig. 4.1. When submitted to the shear stress resulting from the pump, the suspension flows more easily seeing the decrease of viscosity at each applied shear rate, as demonstrated by the curve of unfilled squares in Fig. 4.4a. These results indicate that the network of mechanical links of milk suspensions has been weakened or dissociated by the additional shear stress (the pump). One can also notice that two curves without and with ultrasonication are superposed (unfilled squares and unfilled triangles), indicating that ultrasound applied in our experiment did not have any effect on the viscosity of this concentrated skim milk.

In Fig. 4.4b, the SAXS profiles of casein micelles are displayed. All the profiles come from the *in-situ* SAXS measurements being carried out in the filtration cell; they are then used for the concentration profiles presented in section 1.5. For the suspension at $C = C_o$, three SAXS intensity curves were drawn under three different conditions: one at rest and the two others under filtration with or without US. Two profiles of milk suspension at $C = 2*C_o$ during filtration with and without US are also compared in the same figure. The two profiles involve two measured points within the concentrated layer during filtration of feed skim milk suspension at $C = C_o$.

Except different scattering intensities between two groups resulting from different concentrations, all the curves are superposed. Since the range of scattering vector q (from 1^{-1} nm to 0.1 nm^{-1}) corresponds to the internal structure of casein micelles (Marchin *et al*., 2007; Pignon *et al*., 2004; Shukla *et al*., 2009), it indicates that their internal structure was not affected by US.

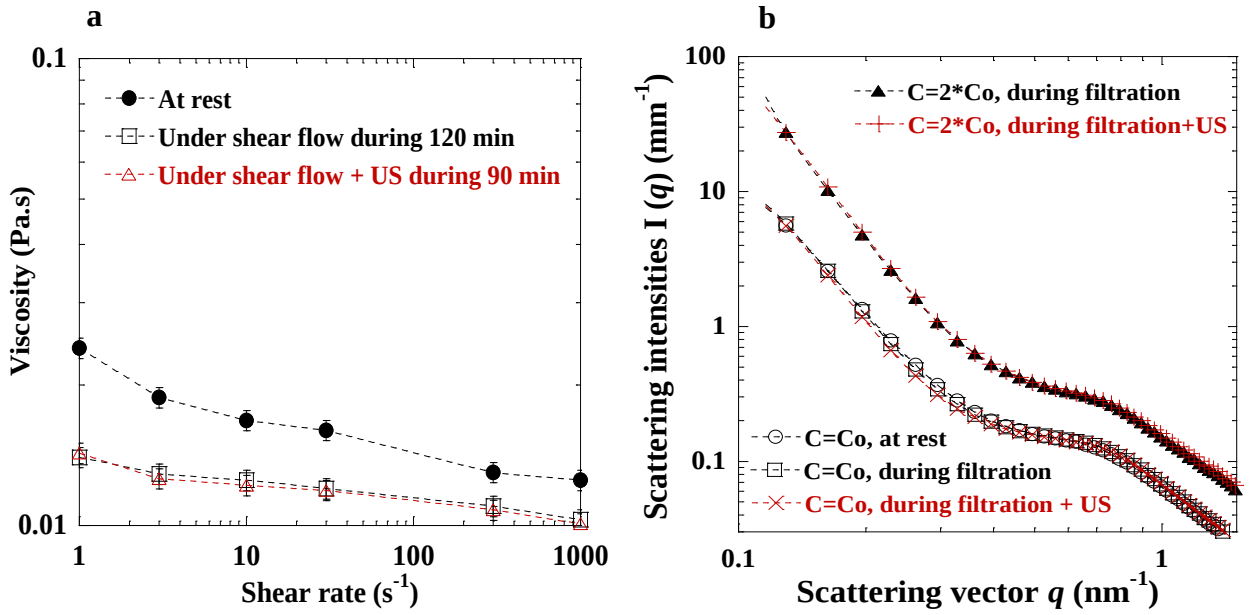

Fig. 4.4 *Ultrasonic effect on milk suspensions during filtration (T = 25±1 °C, transmembrane pressure TMP = 1.1×10^5 Pa, ultrasound: 20 kHz, 2 W.cm^{-2}): a) Steady state flow curve at different times of cross-flow filtration (C = 4*C$_o$, pH = 6.5; cross-flow rate Q$_v$=0.3 L.min^{-1}); b) Comparison of scattering intensities at different conditions (C = C$_o$, pH = 6.8; Q$_v$ =0.1 L.min^{-1}).*

1.4 US effect on ultrafiltration at macro-scales

1.4.1 US effect under different magnitudes of shear flow

Cross-flow ultrafiltrations were carried out at three different cross-flow rates Q_v. A step-up transmembrane pressure (TMP) procedure was used: filtration during 30 min at each TMP step with a gap of 5 min between steps. In order to keep the same membrane for comparison, two filtration runs (without and with US) were carried out in series at the same Q_v. Between the two experiments a 60 min interval was applied at a high shear flow (Q_v = 0.9 L.min^{-1}, $\dot{\gamma} \approx 352\ s^{-1}$) to detach the accumulated layer. Although this operation did not remove the overall irreversible

deposit, it makes the comparison of the two experiments possible: additional filtration runs actually demonstrated that permeate flux was similar before and after the interruption of filtration: the permeate flux was slightly lower for the run after the filtration interruption but the slight variation was negligible (±2.5 %) for the main interpretations of this paper.

Filtrations without US were run at first and ended by the filtrations with US. In this section, all the filtration runs with US were carried out by preventive US application mode, denoting that US was applied before the application of TMP. During the filtration of skim milk suspensions (C_o), evolution of permeate flux J_v, inlet and outlet pressures at feed side of filtration cell and cross-flow Q_v over time were monitored, the most relevant of which are displayed in Fig. 4.5, showing two filtration runs with and without US at Q_v = 0.3 L.min^{-1}.

At each TMP step during the filtration run without US (Fig. 4.5a), permeate flux curve exhibits an arc-like shape with a forepart decline phase. It is a classic filtration curve shape related to the formation of a reversible layer or deposit on the membrane surface. It is worth noting that no such shape is observed when US is on (Fig. 4.5b): permeate flux is quite constant until 0.8×10^5 Pa, indicating no formation of such reversible layer. At TMP = 1.1 ×10^5 Pa and 1.4 ×10^5 Pa, the permeate curves start with a brief decline followed by a progressive climb. In these conditions one can assume that due to reinforced pressure gradient, the reversible layer or deposit was formed at the beginning of the filtration, it was then disrupted progressively by US. This explanation could be confirmed by a second observation: the first (e.g. t=170 min) and last values (e.g. t=205 min) of permeate flux J_v for each step of pressure (TMP=1.1 ×10^5 Pa and 1.4 ×10^5 Pa) were similar. Additional filtration runs have been carried out with longer ultrasonication duration under the same conditions (Q_v = 0.3 L.min^{-1} and TMP = 1.1 ×10^5 Pa, results not shown). After 30 min, the permeate flux stayed constant.

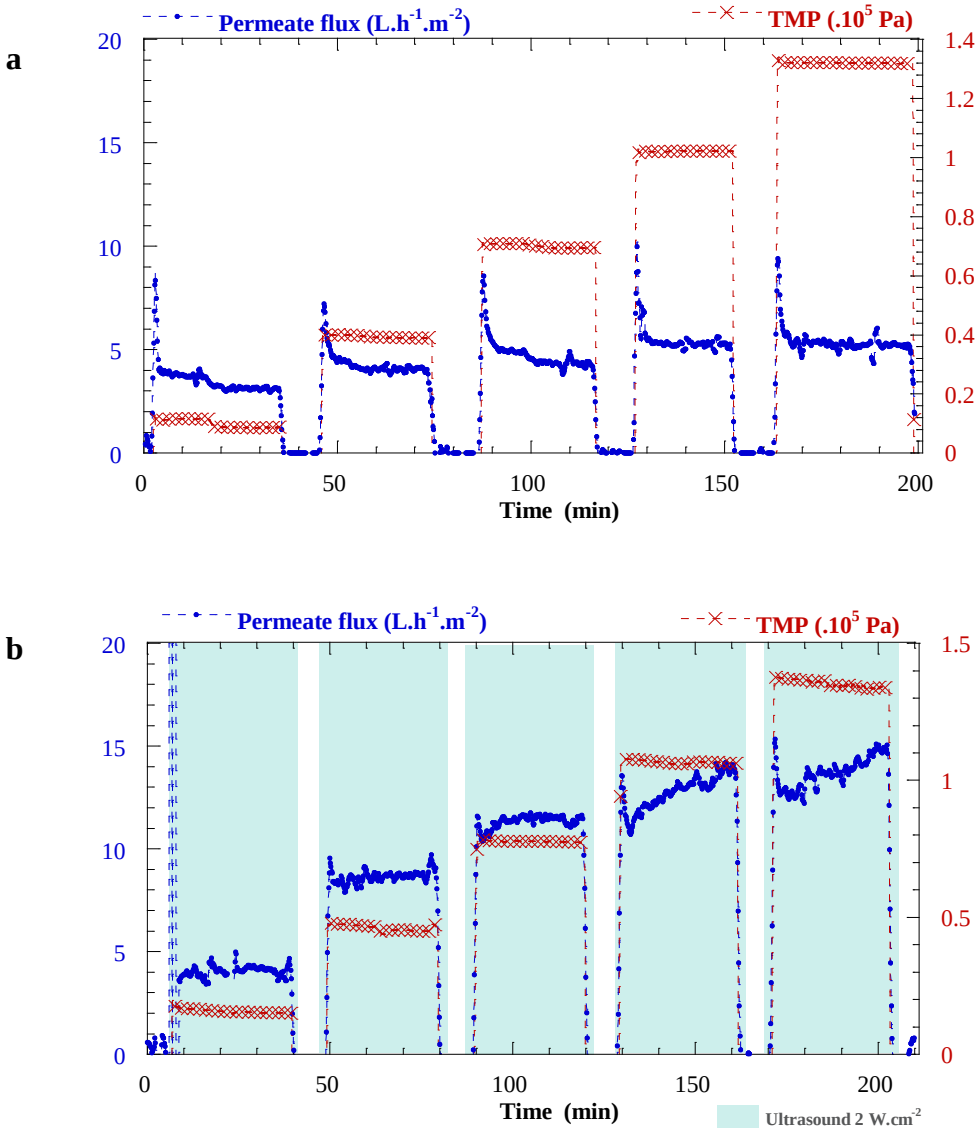

Fig. 4.5 *Cross-flow filtration curve: evolutions of permeate flux J_v, transmembrane pressure TMP over time at Q_v = 0.3 L.min^{-1} without (a) and with (b) US. Used milk suspensions: C = C_o, pH = 6.7. T = 25±1 °C, Ultrasound: 20 kHz, 2 W.cm^{-2}. Increase of permeate flux obvious; formation of reversible deposit could be avoided under US.*

Four other filtration runs using the same procedure were also performed at Q_v = 0.1 and 0.6 L.min^{-1} with and without US (filtration curves not shown). As well as the two runs at Q_v = 0.3 L.min^{-1}, six curves of permeate flux (J_v) versus applied TMP are assembled in Fig. 4.6. All the

permeate flux values in this figure were picked up at the end of each step (t = 30 min). In general, a so-called limiting flux was observed without US and the filtration performance was indeed improved by rising shear flow seeing that the limiting flux increases from 1.8 to 8.2 $L.h^{-1}.m^{-2}$ when Q_v varies from 0.1 to 0.6 $L.min^{-1}$. The application of US then leads to a significant increase of permeate flux. In order to quantify the US effect, an enhancement factor (E_{US}) was used in this study (Hengl *et al.*, 2014). It is defined by the ratio between the permeate flux obtained in the presence of US (J_{us}) and the one obtained without US (J_v) under the same operating conditions:

$$E_{US} = \frac{J_{US}}{J_V} \qquad \textbf{\textit{Eq. 4.1}}$$

In this case, E_{us} at TMP = 1.4×10^5 Pa vary from 2.0 (Q_v = 0.6 $L.min^{-1}$) to 4.7 (Q_v = 0.1 $L.min^{-1}$) under present operating conditions. Moreover, different filtration behaviors have been observed: instead of being limited, the permeate flux continues to increase with TMP up to 1.4×10^5 Pa for all three filtrations under US. Since this limiting flux strongly depends on a dense accumulated particles layer, we infer that the applied ultrasonic waves allow reducing or at least disrupt this accumulated protein layer. This hypothesis will be confirmed in the section 1.5 by the observations of *in-situ* SAXS measurements near the membrane surface during filtration.

Taking an average viscosity η_{milk} = 1.9 mPa.s, and density ρ_{milk} = 1035 $kg.m^{-3}$ of standard skim milk (C_o) at 25 °C, Reynolds numbers (Re) without US were estimated for three applied Q_v: $\mathrm{Re} = (\rho u D_H)/\eta$, with u the mean velocity of fluid ($m.s^{-1}$) and D_H the hydraulic diameter of the filtration channel (m). As presented in Tab. 4.1, it indicates that these suspensions were in the inertial laminar flow regime. Effective Reynolds numbers with US were not estimated but they should be higher than that without US, since US is considered to be able to enhance the hydrodynamic force of fluid (Jin *et al.*, 2014). Simon *et al.* (2000) suggest that low-frequency US effect is similar to that brought about by a classical mechanical stirrer. They defined a pseudo ‘‘ultrasonic stirring’’ speed to predict mass transfer coefficients under ultrasonic conditions and reported a good agreement between experimental and predicted values. Bearing this in the mind, an interesting finding could be explained. It is shown in Fig. 4.6 that the filtration run at Q_v = 0.1 $L.min^{-1}$ with US and that at Q_v = 0.6 $L.min^{-1}$ without US have the same-level J_v at high TMP ($1.1.10^5$ Pa and $1.4.10^5$ Pa). It indicates that the application of US (2 $W.cm^{-2}$) had equal effect on filtration performance as an enhancement of hydrodynamic force by 5 times in this circumstance.

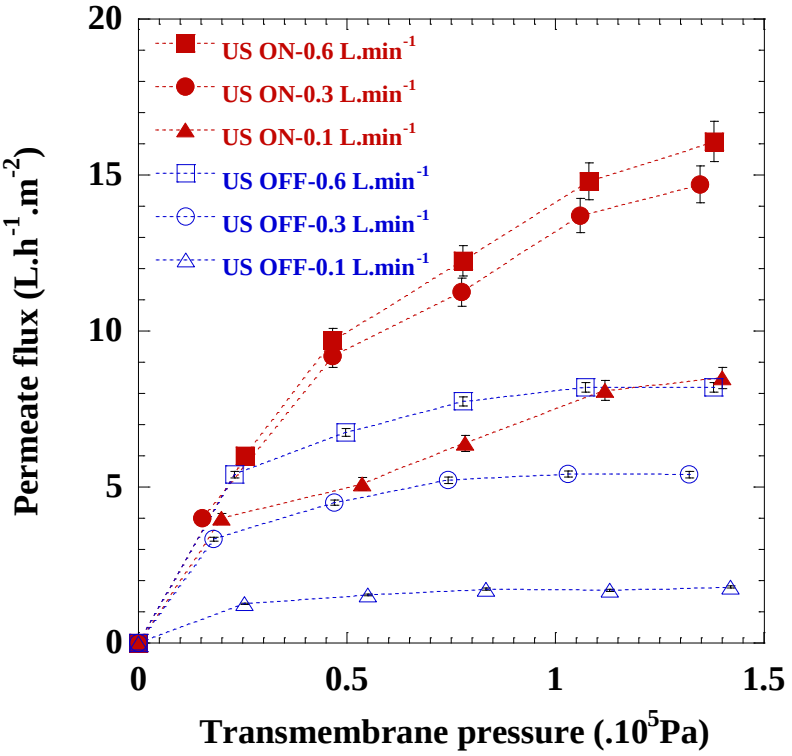

Fig. 4.6 *Steady-state curves of J_v as a function of TMP for different Q_v with/without US during ultrafiltration of milk suspensions ($C = C_o$, mean pH = 6.6). T = 25±1 °C, Ultrasound: 20 kHz, 2 W.cm^{-2}. No more limiting flux under US.*

Otherwise, no significant fluid heating was observed during all filtration runs in this study when US was applied. Since temperature difference between inlet and outlet of filtration cell has already been shown previously in chapter 3 (Jin *et al.*, 2014), which can also describe the case of skim milk, it will be no longer narrated here. Compared to the initial state, membrane permeability decreases by about 20% after the cleaning procedure at the end of each series (Tab. 4.1), which is in accordance with the cleaning results in literature (Rabiller-Baudry *et al.*, 2008). Turbidity of feed (NTU_{feed}) and permeate ($NTU_{permeate}$) was measured for each filtration run and the rejection rate of casein proteins ($TR_{caseins}$) can be calculated by:

$$TR_{caseins} = 1 - \frac{NTU_{permeate}}{NTU_{feed}} \times 100\% \qquad \textit{Eq. 4.2}$$

Tab. 4.1 *Reynolds numbers, mean velocities of fluid, membrane permeability and rejection rate of filtration runs of milk suspensions (C = C_o, mean pH = 6.6). Ultrasound: 20 kHz, 2 W.cm^{-2}*

Filtrations	u **(m.s^{-1})**	**Re**	**Membrane permeability (×10^{-5} L.h^{-1}.m^{-2}.Pa^{-1})**		**TR$_{caseins}$**
			Before UF	After UF	
US ON 0.6 L.min^{-1}	0.31	/	92.6	81.5	99.9%
US OFF 0.6 L.min^{-1}		902			99.7%
US ON 0.3 L.min^{-1}	0.16	/	75.5	62.7	99.2%
US OFF 0.3 L.min^{-1}		451			99.8%
US ON 0.1 L.min^{-1}	0.05	/	99.7	85.2	99.8%
US OFF 0.1 L.min^{-1}		150			99.0%

As shown in Tab. 4.1, the turbidities of permeate are very low (below 5 NTU) compared to that of feed (500 NTU on average), hence the rejection rates are above 99 % for all the six filtration runs. In addition, no difference can be observed between the runs with US and those without US. These results suggest that application of US did not change the rejection rate of casein micelle, implying that no membrane structure modification was induced by ultrasonication.

1.4.2 US effect with different casein micelle concentrations

For a better understanding of US effect on skim milk filtration performance, another suspension more concentrated (4*C_o, corresponding to a casein micelle concentration of 108 g.L^{-1}) has also been assessed using the same step-up TMP procedure. Fig. 4.7 presents four filtration

runs of two different feed concentrations of milk with/without US at Q_v = 0.3 L.min^{-1}. As mentioned before, at C = C_o, US brings about a significant increase of J_v at high TMP: no longer being limited at 5 L.h^{-1}.m^{-2}, J_v has risen to 15 L.h^{-1}.m^{-2} at TMP = 1.4.10^5 Pa. When the feed milk suspension is concentrated to 4*C_o, J_v becomes quite low and nearly nil for low TMPs, even with US.

In order to explain this observation, skim milk structure should be reminded. Skim milk contains colloidal particles that are composed of a complex association of protein and calcium phosphate. These heterogeneous association colloids are named casein micelles, which are made of four distinct caseins (α_{s1}, α_{s2}, β and κ). Casein micelles make up to 80 % of the protein content of bovine milk. It has been reported (Brans *et al*., 2004; Holt *et al*., 2003; Pignon *et al*., 2004; Shukla *et al*., 2009) that the interior of the micelle consists of entangled hydrophobic casein and calcium phosphate, while the exterior of the micelle is mainly hydrophilic κ-casein. This negatively-charged outer layer is called the ‘‘hairy layer’’ that provides both steric and electrostatic stability to the casein micelle hence prevents aggregation of the casein micelles in milk. The other proteins found in milk are whey proteins. The major whey proteins in bovine milk are β-lactoglobulin (β-LG) and α-lactalbumin (α-LG). During skim milk filtration, accumulation of these deformable colloids occurs on the membrane surface, as already emphasized in precedent work in dead-end mode (Pignon *et al*., 2004). More recently, this issue has been discussed by Gebhardt (2014; 2012) and Bouchoux *et al.* (2013). In fact, the colloids are deformed and in contact with each other at the membrane surface during filtration, which corresponds to the formation of a gel or irreversible deposit. Within this deposit, casein micelles structure is reported to transform from an originally spherical shape to an ellipsoidal-deformed shape. Above this layer, a polarized layer exists where the objects are still more concentrated than in the bulk but where phase transition has not yet occurred. Works also propose that a multi-layer fouling is often formed during skim milk filtration. Moving from the bulk to the membrane surface, Wemsy *et al*. (2013) summarize the related studies (Delaunay *et al*., 2008; Rabiller-Baudry *et al*., 2008) and describe it as (i) a reversible deposit among which is a gel part fully reversible, then (ii) a cohesive fouling layer strongly adherent to the membrane, made of proteins such as β-LG. They also stated that the strongly attached layer is probably not a mono-layer of proteins adsorbed on the membrane.

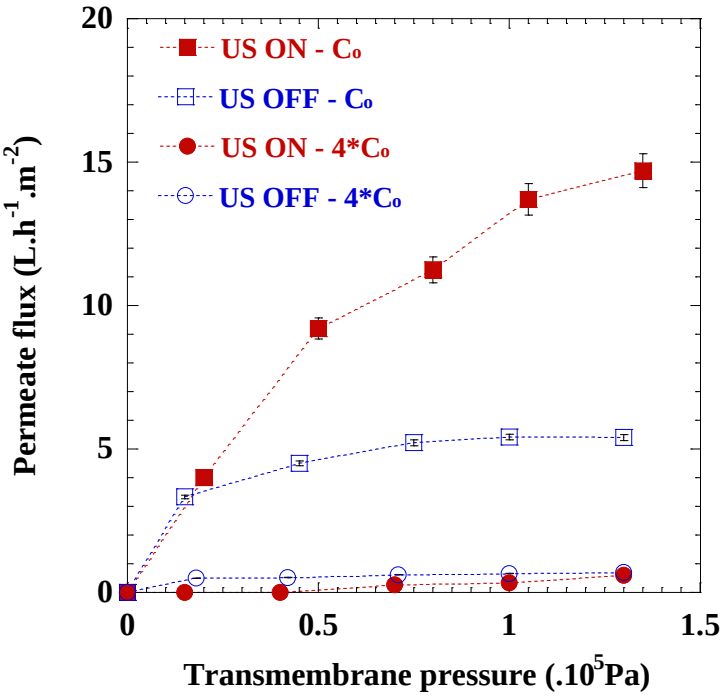

Fig. 4.7 *Steady-state curves of J_v as a function of TMP for different milk concentration (pH = 6.5) with/without US at Q_v = 0.3 L.min^{-1}. T = 25±1 °C, Ultrasound: 20 kHz, 2 W.cm^{-2}. Filtrations are completely obstructed with 4*C_o, even with US.*

In this case, a suspension of 4*C_o (108 g.L^{-1}) was filtrated. As discussed in section 1.2, it is the first critical concentration where the rheological behavior of suspension changes from Newtonian to shear-thinning, indicating stronger interactions among casein micelles than standard skim milk. Therefore, considering the multi-layer fouling concept, we speculate that a highly cohesive fouling layer could form as soon as the filtration begins thus the membrane was totally fouled. The concentration of casein micelle within this highly cohesive fouling layer could exceed the sol-gel transition (random-close packing concentration) which is estimated at around 6.85*C_o (185 g.L^{-1}) in this study (178 g.L^{-1} in the study of Bouchoux *et al.* (2009)). In addition, US did not bring any change of filtration behavior, indicating that the applied ultrasonic waves did not disrupt this cohesive fouling layer at all. A higher ultrasonic intensity could be needed to generate the expected disruption of fouling layer.

The ultrasonic system in this study is designed to transmit low intensity ultrasound in order to avoid any possible membrane damage, and the highest intensity it can transmit is 2.9 $W.cm^{-2}$. During filtration, combined action of the applied ultrasonic force and hydrodynamic force (anti-accumulative forces) is in competition with that of the convective force towards the membrane and the interacted force of casein micelles (accumulation-induced forces). Increase of concentration of feed suspension strengthens the interacted force of casein micelles. In this specific circumstance, the accumulation-induced forces could be so important that the anti-accumulative forces were not strong enough to counteract them.

1.4.3 US effect under different ultrasonic intensities

Four different ultrasonic intensities were applied during two filtration runs of skim milk suspension at C_o. After introducing milk into the cleaned filtration cell, conventional filtration (without US) was carried out first (TMP = 1.1×10^5 Pa; Q_v = 0.3 $L.min^{-1}$). US was applied when J_v stabilized, and then switched off when J_v reached the steady state. This US application mode will be denoted as curative mode in the following part of this study.

Fig. 4.8 presents the averaged enhancement factor for these four applied ultrasonic intensities: 0.6, 1.1, 2.0 and 2.9 $W.cm^{-2}$. The enhancement factors are around 2 for all the applied US intensities, indicating that US intensity in the chosen operating conditions hardly affects the process enhancement factor. It is even better for the future industrial development since the same filtration performance can be achieved in consuming less energy at lower ultrasonic intensity.

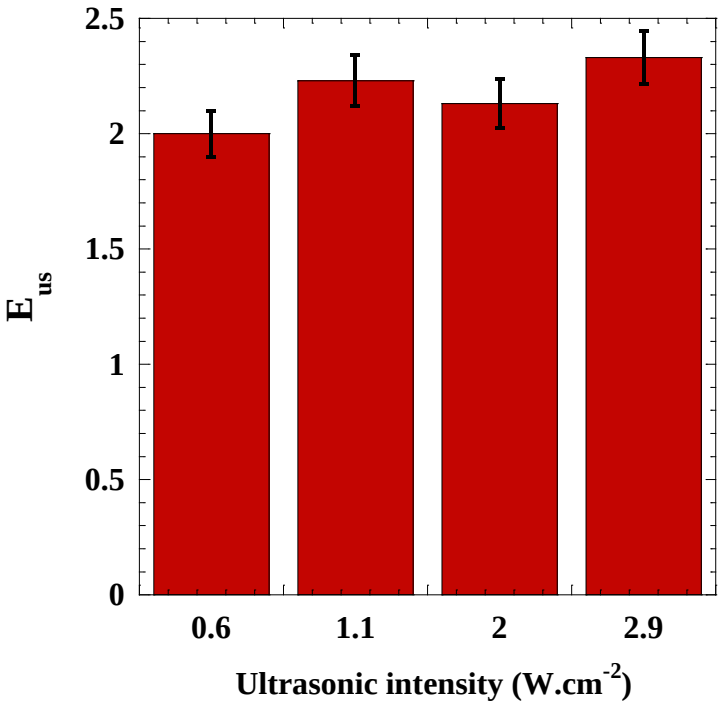

Fig. 4.8 *US enhancement factors at different ultrasonic intensities during milk ultrafiltration at T = 25±1 °C, TMP = 1.1×10^5 Pa, Q_v = 0.3 L.min^{-1}. Milk suspensions: C = C_o, mean pH = 6.7. Ultrasound: 20 kHz.*

1.5 US effect on ultrafiltration at nano-scales

In order to better understand the US effect on ultrafiltration of skim milk, concentration profiles of casein micelle near the membrane surface has been investigated by *in-situ* SAXS measurements. They were carried out simultaneously during cross-flow filtration, as shown in chapter 3 (Jin et al., 2014). In this section two concentrations of skim milk suspensions are involved: a standard skim milk (C = C_o) and a more concentrated one: C = 2*C_o, which is often treated in dairy industry. Except the contour chart of concentrated layer (Fig. 4.9c-d), all the presented results in this section are the concentration profiles of the middle window of the filtration cell (see Fig.2.8 in chapter 2).

1.5.1 Ultrafiltration of C_o milk suspension

1.5.1.1 US effect at steady state

During filtration, two cross-flow rates (Q_v = 0.3 and 0.1 L.min^{-1}) were applied and US was added for a given duration after steady state was reached (curative mode). These different conditions divided the filtration run into 4 steps, as presented in Fig. 4.9a, displaying the evolution of permeate flux J_v, inlet and outlet pressures of filtration cell and cross-flow rate Q_v over time. The related concentration profiles at steady state of each step are presented in Fig. 4.9b. Applied cross-flow rate was changed from 0.3 to 0.1 L.min^{-1} between step 1 and step 2, which induced a decline of permeate flux from 5.2 to 2.1 L.h^{-1}.m^{-2} (Fig. 4.9a), as well as a growth of concentrated layer (Fig. 4.9b). US was then applied at step 3 and a progressive increase of permeate flux followed, from 2.1 to 4.5 L.h^{-1}.m^{-2}, which can be explained by a partial removal of concentrated layer. When US was switched off at step 4, the permeate flux got down back to 2.2 L.h^{-1}.m^{-2} and exactly the same concentrated layer as step 2 is obtained at steady state, indicating that the US effect on filtration is almost instantaneous: no further change takes place during filtration when US is switched off.

Thanks to three windows located at 7 mm, 50 mm and 93 mm from inlet of filtration cell, concentration profiles along the membrane (x axis) can also be obtained. Fig. 4.9c-d presents the contour charts of the steady-state concentrated layer in the filtration channel at step 2 (without US, Fig. 4.9c) and step 3 (with US, Fig. 4.9d). Details of the graphing procedure can be found in chapter 3 (Jin *et al.*, 2014).

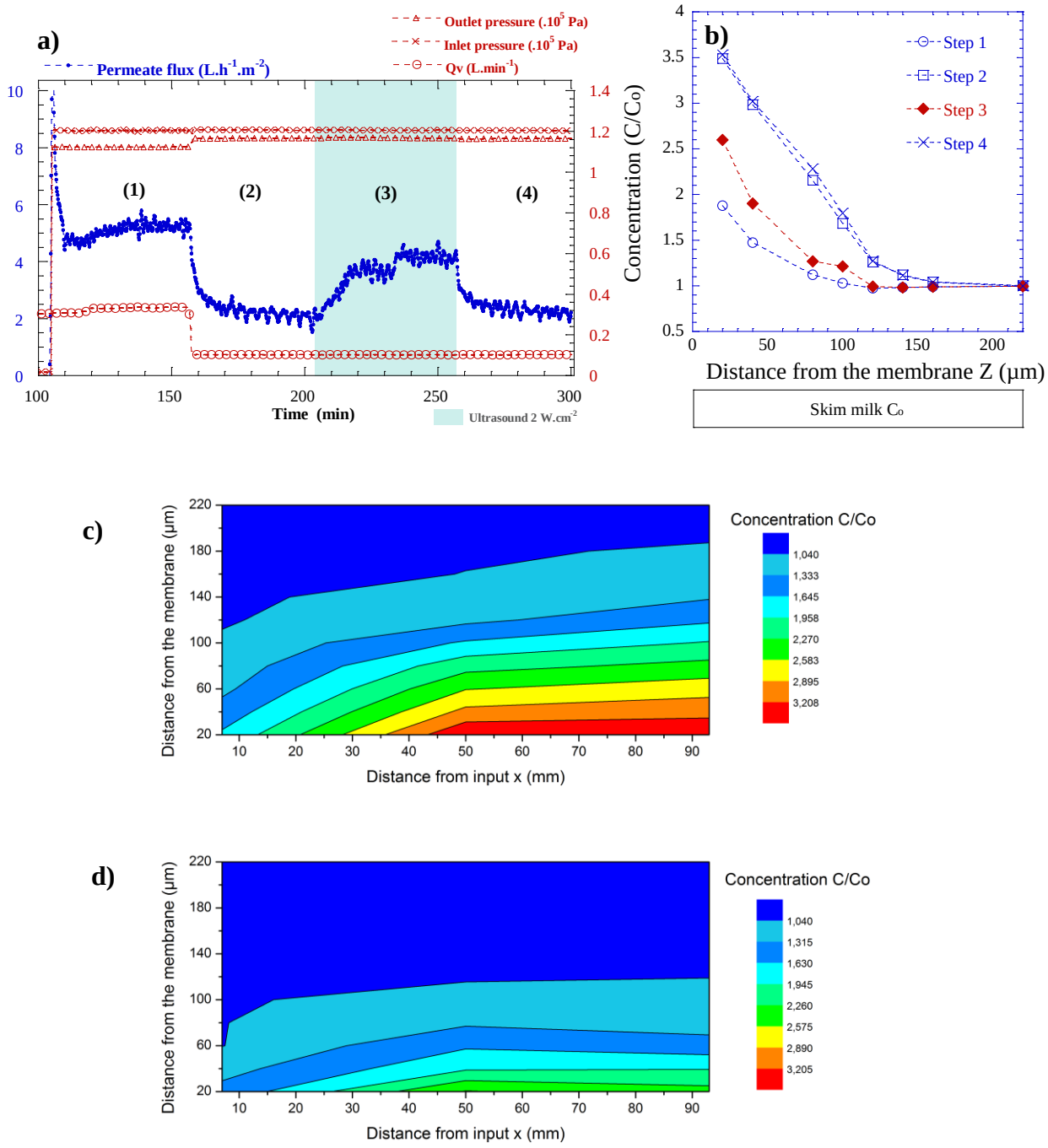

Fig. 4.9 *Combination of macro-scale results and nano-scale detections during milk ultrafiltration ($C = C_o$, pH = 6.8). T = 25±1°C. Ultrasound: 20 kHz, 2 W.cm^{-2}. a) Cross-flow filtration curve: evolution of J_v, inlet and outlet pressure of filtration cell and cross-flow rate Q_v over time. b) Related concentration profiles at steady state from the membrane surface to the bulk, deduced from in-situ SAXS measurements. c-d) Contour chart of concentrated layer in the filtration channel at steady state of step 2 (c) and step 3 (d). Permeate flux value corresponds to the concentrated layer; a partial disruption of concentration profile by US is observed.*

At the end of step 2 (Fig. 4.9c), the concentration profile along the filter surface (x axis) shows an increase of the concentrated thickness ranging from 120 µm at inlet to 160 µm at outlet of filtration cell. In addition, local particle concentration at inlet is lower than the other two positions at every distance z. Such profile accords with the expectation that the concentrated layer grows along the membrane, which results in an inhomogeneous flux along the membrane. When US were applied, the accumulated layer was disrupted, as shown in Fig. 4.9d: the layer thickness is reduced to around 100 µm and the concentrations decrease within the whole layer. The concentrated layer is not removed and still covers the whole membrane surface, which explains in some extents the limited enhancement factor (around 2), contrary to our previous results on Laponite dispersions (chapter 3 section 1.5.1, Lap1-tspp6) where about 60% of membrane surface was swept by US application resulting in a great increase of J_v.

1.5.1.2 US effect at transient state

Further investigation focuses on the transient state of step 1, 2 (without US) and step 3 (with US). As shown in Fig. 4.10a, at step 1, the casein micelles accumulated immediately when TMP was applied, seeing a formation of concentrated layer with a thickness of 40 µm at t = 1 min. This layer then took a quick growth until 100 µm (see the profile at t = 5 min) and stayed stable afterwards. At step 2, when Q_v was decreased to 0.1 $L.min^{-1}$, filtration equilibrium was broken with the weakening of shear-induced hydrodynamic force, hence, the concentrated layer re-grew. Progressively, this layer reached a final thickness of 160 µm with the concentration of $3.5*C_o$ at z = 20 µm from the membrane surface.

US was then applied (step 3, Fig. 4.10b). 1 min later, one piece of the concentrated layer seems to be "bit off" by US in view of the layer thinning (from 160 µm to 120 µm) and the concentration decrease exclusively at the part close to the bulk. 3min later, the rest of the concentrated layer was also disrupted and the concentration adjacent to the membrane (at z = 20 µm) fell to $3*C_o$. Then the concentration continued to drop slightly within the whole layer until the steady state whose first point concentration (z = 20 µm) was $2.7*C_o$; the layer thickness did not change any more. Finally, the total concentration decline at z = 20 µm is about 23% ((3.5 –

2.7)/3.5 × 100%). In one word, the accumulated protein layer was disrupted but not completely removed by US. Nevertheless, the permeate flux was increased by a factor of 2.

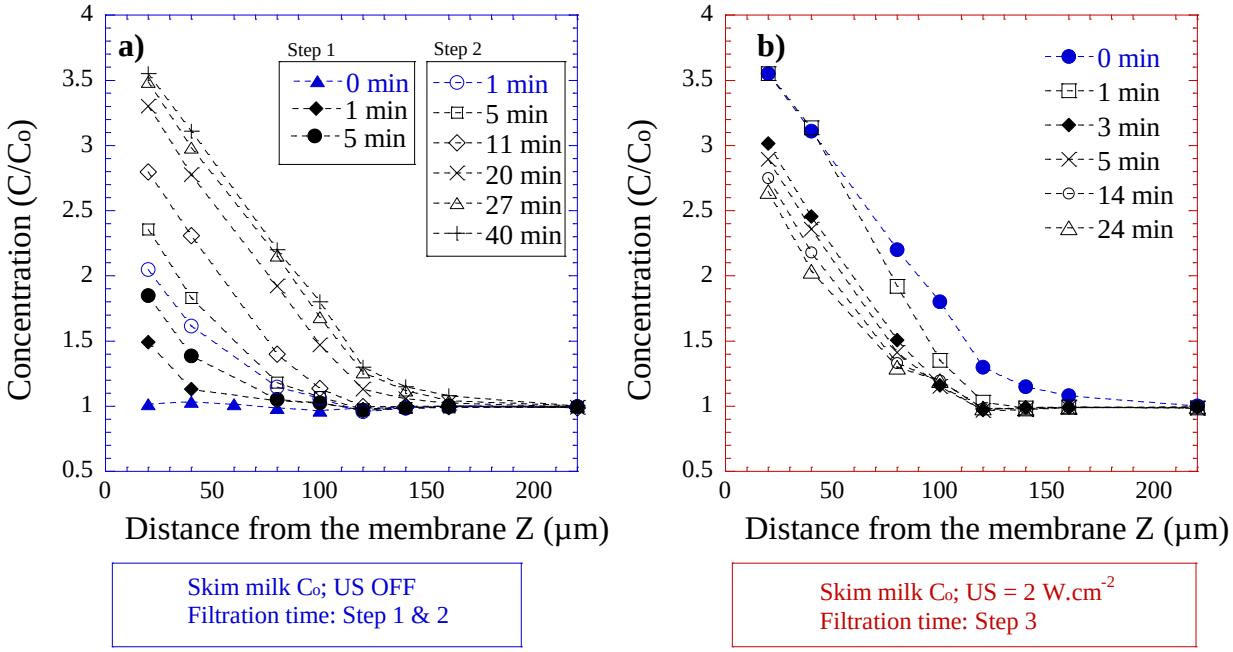

Fig. 4.10 *Evolution of concentration profiles within the accumulated layer over time during milk ultrafiltration (C = Co, pH = 6.8). ‘‘0 min’’ represents the initial state before operation, e.g. the profile before filtration in (a) and the profile just before the application of US in (b).Concentration polarization layer is ‘bit off’ immediately by US while the reversible deposit is disrupted progressively from the bottom of layer.*

The described concentration profile evolution could be explained through a multi-layer fouling composed both of a reversible layer and a strongly-attached one. Thanks to the ‘‘hairy layer’’ of casein micelle, the first part of the concentrated layer was fragile, which was, therefore, “bit off” immediately by US; it then continued to disrupt the remaining concentrated layer. Similar phenomenon is then observed just like the break-up regime by US during filtration of Lap1-tspp6 (chapter 3 section 1.5.1 or Jin *et al.*, 2014): casein micelle concentration decreases progressively within the whole accumulated layer and principally at the bottom part (close to the membrane), instead of being eroded from the top one (close to the bulk). As discussed before, ultrasonication can be considered as an additional force field of an effective range on the order of micrometers or smaller, and the interacted or accumulated particles within this force field could

be broken up or dispersed. Hence, in this case, the interacted casein micelles within the reversible layer could be disrupted by US and then a new balance built up progressively between the transmembrane pressure, the shear-induced hydrodynamic force and ultrasonic force. The new balance finally resulted in a less concentrated layer, which was not completely removed, indicating that the additional ultrasonic force was not strong enough to totally counteract the convective force towards the membrane for this specific protein suspension (accumulation-induced forces).

1.5.2 Ultrafiltration of 2*Co milk suspensions

Concentration effect on ultrafiltration of skim milk suspension has already been shown in section 1.4.2. However, permeation was completely stopped in the case of filtration of highly concentrated feed suspension ($4*C_o$). In this section, the concentration profiles during filtration will be discussed with a moderately concentrated feed suspension: $C = 2*C_o$. Two US application modes, preventive and curative modes, were adopted for comparison. The preventive mode is particularly interesting since it may be very promising for future industrial production to control fouling.

1.5.2.1 US effect at steady state

Filtration run was carried out at $Q_v = 0.3$ L.min^{-1} and TMP = 1.1×10^5 Pa. Three steps could be distinguished by whether US was applied, as shown in Fig. 4.11a. At step 1, US was applied from the beginning of the filtration run, with the aim of preventing the accumulated protein layer formation (preventive mode). A stable permeate flux of 8.3 L.h^{-1}.m^{-2} was obtained since the beginning of this step. In addition, a very thin and little concentrated layer was observed at the end of step (thickness of 60 µm and $C = 2.3*C_o$ at z = 20 µm), as shown in Fig. 4.11b. US was then switched off at step 2. Permeate flux dropped off to 3.3 L.h^{-1}.m^{-2} and the accumulated protein layer grew in both concentration and thickness: $C = 3.1*C_o$ instead of $2.3*C_o$ at z = 20 µm and thickness grew to 120 µm. Therefore, the US enhancement factor between step 1 and step 2 is 2.5. US was applied again at step 3. Permeate flux then increased progressively to 6.7

$L.h^{-1}.m^{-2}$ at the end of step. The accumulated protein layer was indeed disrupted compared to that of step 2, but it was not totally removed by US, same as previous observation in section 1.5.1.

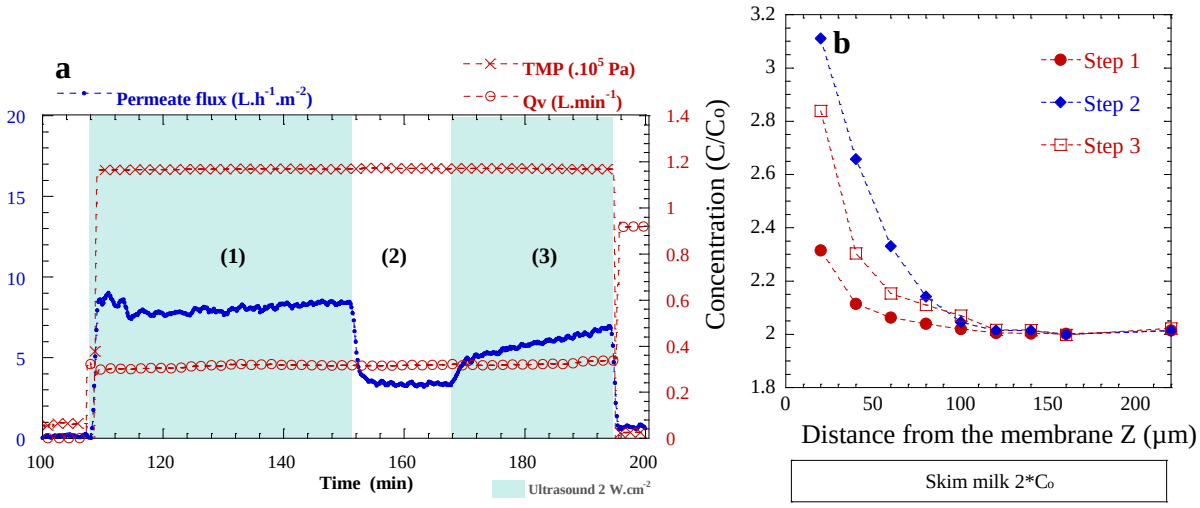

Fig. 4.11 *Combination of macro-scale results and nano-scale detections during milk ultrafiltration (C = 2*C_o, pH = 6.7). T = 25±1°C. Ultrasound: 20 kHz, 2 W.cm^{-2}. a) Cross-flow filtration curve: evolution of J_v, TMP and Q_v over time. b) Related concentration profiles at steady state from the membrane surface to the bulk, deduced from in-situ SAXS measurements. At preventive mode, growth of concentrated layer is limited.*

1.5.2.2 US effect at transient state

Evolution of concentration profiles at each step over time is presented in Fig. 4.12. At step 1 (Fig. 4.12a), even on preventive mode, an accumulated protein layer has been formed since the first minute. Although thin, this layer became a barrier for mass transfer so that the related permeate flux could not be reinforced further than 8.3 $L.h^{-1}.m^{-2}$. In fact, the permeability of membrane was 96×10^{-5} $L.h^{-1}.m^{-2}.Pa^{-1}$, implying that the permeate flux when filtrating water at this TMP will be 105 $L.h^{-1}.m^{-2}$. This dramatic difference might be due to the formation of cohesive fouling layer which is probably very thin (under 20 µm) but very concentrated near the membrane surface. It also indicates the limitation of the applied US in dealing with this specific layer.

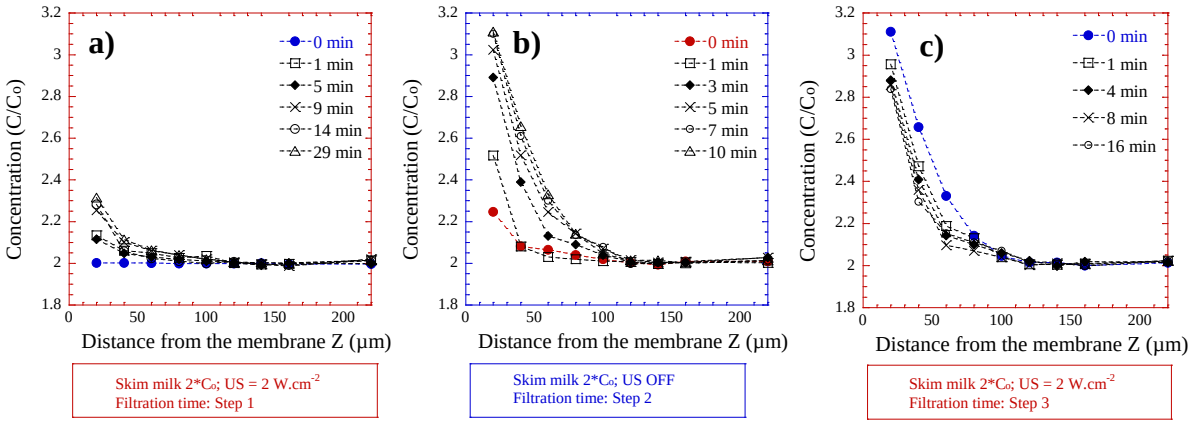

Fig. 4.12 *Evolution of concentration profiles within the accumulated layer over time during milk ultrafiltration (C = 2*C_o, pH = 6.7). 0 min represents the initial state before operation. Preventive mode holds back the growth of concentrated layer, while formed fouling layer can not be thouroughfully disrupted by US. Presence of the cohesive fouling layer is more pronounced with increase of feed protein concentration from C_o to 2*C_o.*

At step 2 (Fig. 4.12b), US was switched off, we can see clearly an immediate increase of concentration at z = 20 µm, referring to the bottom of the accumulated layer. Besides, steady state was reached very quickly since 10 min later no more evolution of concentration profile could be observed. It seems that the ultrasonic force "suspended" the casein micelles; they were then "dragged" towards the membrane once US was off. By comparing step 1 and step 2, we can state the success of preventive mode: though US could not stop the formation of cohesive layer, it did attenuate significantly the accumulation of casein micelles during filtration.

During step 3, the formed concentrated layer did not evolve significantly under US, especially for the bottom part of layer since the casein micelle concentration only decreases from 3.1*C_o to 2.9*C_o at z = 20 µm (corresponding to 6% of concentration decline). The middle part of accumulated layer is the most disrupted part: at z = 40 µm, the concentration decreases progressively from 2.7*C_o to 2.3*C_o (corresponding to 15% of concentration decline). In fact, the evolution of concentration profile can be divided into two regimes: at the bottom of layer, little change took place; above this part, a similar regime as step 3 of C_o filtration (Fig. 4.10b) can be observed. As mentioned in section 1.4.2, a highly cohesive fouling layer might form with a concentrated feed milk suspension during filtration. Therefore, we assume that at feed

concentration of 2*C_o, the cohesive fouling layer was either more concentrated or thicker than that of C_o. Thus, the measured points at z = 20 µm were either more affected by this cohesive layer or closer to it. Beyond the cohesive layer, the casein micelles were accumulated mainly by increase of interactions, thus the combination of ultrasonic force and shear-induced hydrodynamic force was strong enough to counteract the convective force, resulting in a new accumulated layer with lower concentration, as shown in Fig. 4.12c.

The observation at step 3 confirms again that the applied US was not strong enough to disrupt the cohesive fouling layer under the present experiment conditions. It could also confirm the observation in section 1.4.2 that the feed concentration of skim milk plays an important role in ultrasonic assisted filtration: the bottom of the accumulated protein layer was indeed more disrupted with a less concentrated feed suspension (at z = 20 µm, concentration decline is 23% at C_o versus 6% of 2*C_o, even though at different Q_v.). In all cases, the cohesive fouling layer was so thin that from z = 20 µm to 170 µm corresponded only to the reversible layer. Another technique, grazing incidence SAXS (GISAXS), could be employed in order to characterize this thin cohesive layer within 20 µm from the membrane surface (Gebhardt and Kulozik, 2014; Smilgies *et al.*, 2002).

1.5.2.3 Discussions

It should be noted that all the obtained concentration profiles in this section are below 4*Co, the critical concentration where the rheological behavior of suspension changes from Newtonian to shear-thinning. It indicates that the casein micelles are almost randomly dispersed within the concentrated layer except the cohesive one (below 20 µm, not detected by SAXS experiments). Meanwhile, the decline of J_v is significant, of more than 90% (compared to the permeate flux of water filtration in the same conditions) even with US, suggesting that the membrane fouling is quite severe during skim milk filtration. What cause this dramatic decline? First of all, the presence of soluble proteins and minerals in skim milk indeed exacerbates the J_v decline. Jimenez-Lopez *et al.* (2008) shown that during filtration, soluble proteins participate in the irreversible fouling by adsorption phenomena and/or by accumulation of the proteins in the micelle deposit. The mineral aqueous phase of milk plays also an important role in critical

hydrodynamic conditions and in irreversible fouling. In addition, calcium is supposed to increase micelle deposit cohesion by establishing bonds between the micelles themselves. The filtration performance depends also on ionic strength of treated milk suspension (Jimenez-Lopez *et al*., 2011). Therefore, we speculate that the network of casein micelles becomes more strongly bonded with the presence of soluble proteins and minerals close to the membrane surface during filtration.

It should be noted that the overall performance of the process is governed by the accumulation of casein micelles at the membrane surface, as suggested by Jimenez-Lopez *et al.* (2011) This statement is consistent with our previous work (Pignon *et al*., 2004) where the filtration performances of "low heat" skim milk and a purified casein micelle suspensions (named PPCN) were compared, the J_v declines were shown to be dramatic in both cases, confirming that casein micelles dominate the filtration performance of skim milk. Nevertheless, in order to answer the question "What cause this dramatic decline?", two points should still be clarified: (i) what is the casein micelle concentration on the membrane surface (from 0 to 20 µm)? (ii) Do the flow properties of casein micelle suspensions change by applying a pressure higher than the atmospheric one? Firstly, whether the suspension within the cohesive layer exhibits a "gel" behavior (concentration close to $7*C_o$) is crucial for understanding the fouling mechanism. Though it is reasonable to state that the cohesive fouling layer which might be very thin but highly concentrated dominates the filtration performance, it needs to be confirmed. Secondly, according to the rheological measurements at atmospheric pressure, the concentrations reached within the concentrated layer correspond to the Newtonian fluid regime; nevertheless, this low concentrated layer is resistant against the ultrasonic force (as shown in Fig. 4.12c). Thus we assume that casein micelles become more interacted when the applied pressure is higher than the atmospheric one so that the rheological critical concentrations ($4*C_o$ and $7*C_o$, from Newtonian to shear-thinning until the emergence of yield stress) shift towards lower values. Therefore, it will be interesting to characterize the flow properties of casein micelle suspensions in applying a pressure higher than standard atmosphere (corresponding to the transmembrane pressures ranges during ultrafiltration) in future investigation.

1.6 Summary

In the first part of this section, flow properties of casein micelle suspensions have been investigated. It shows an evolution of their rheological behavior from Newtonian to shear-thinning (critical concentration C= 108 $g.L^{-1}$) until the emergence of yield stress with the increase of concentration (sample concentration from 189 $g.L^{-1}$ to 216 $g.L^{-1}$). The nature of aqueous phase (deionized water, UF and MF) does not affect their rheological behavior at low concentration regime ($C_o<C<6*C_o$).

In the main part of this section, ultrasonic effects on cross-flow ultrafiltration of skim milk have been characterized from macro-scale to nano-scale.

Firstly, the applied ultrasound (20 kHz, 2 $W.cm^{-2}$) did not affect the viscosity of feed milk suspensions as well as the internal structure of casein micelles, revealed by real-time *in-situ* SAXS profiles. Meanwhile, the filtration performance was significantly improved by this simultaneously applied US: the permeate flux was increased and the limiting-flux filtration scenario was replaced by a consistent-rising one. All these occurred without any change of membrane selectivity since $TR_{caseins}$ were always above 99%.

Secondly, the *in-situ* SAXS measurements have revealed for the first time the evolution of the concentration profiles on the membrane surface over time during skim milk cross-flow ultrafiltration process. The steady-state thickness of the skim milk concentrated layers is from 120 to 160 µm under our operating conditions. In addition, the effect of US induced a partial disruption of concentrated layer which led to an increase of permeate flux by a factor from 2.0 to 4.7. When the feed concentration increases, the effect of the applied US on concentrated layer weakened. This effect could be governed by the balance between the internal interactions within casein micelles suspensions and the ultrasonic force.

Finally, US power varying from 0.6 to 2.9 $W.cm^{-2}$ does not influent the US enhancement factor. More importantly, the preventive US application mode is proven promising since it did attenuate significantly the accumulation of casein micelles during filtration: formation of the reversible fouling layer was strongly limited in this mode, inducing higher permeate flux.

2. Suspensions of polysaccharide nanocrystals

2.1 Introduction

With increasing demand for renewability and sustainability, use of biomass as starch and cellulose represents a highly potential option in many different applications due to their abundance, biodegradability and non-toxic nature. In particular, considerable effort has been devoted in recent years to the research of their derivatives: starch nanocrystals (SNC) and cellulose nanocrystals (CNC). For example, SNC are of great interest in packaging applications due to their crystallinity and platelet-like structure that enhance barrier properties (Angellier-Coussy *et al*., 2009; Chen *et al*., 2008; Kristo and Biliaderis, 2007; Le Corre *et al*., 2010); and CNC are promising as a reinforcing component in high performance nanocomposites and numerous other applications thanks to their extraordinary mechanical properties such as high Young's modulus and tensile strength specific strength and modulus, high surface area, etc. (Bras *et al*., 2010; Marcovich *et al*., 2006; Peng *et al*., 2011; Siqueira *et al*., 2010; Šturcová *et al*., 2005).

However, there is one big challenge for their development and large-scale application: production. SNC production is limited by a very low reaction yield (10-15%) even if the production time is long (5 days) by current processes (Angellier *et al*., 2004). A recent study shows that SNC are produced at a very early stage during the hydrolysis process. It indicates that the formed nanocrystals and other microparticles are firstly mixed together in the suspension and some nanocrystals might turn to sugar later by the degradation of hydrolyzing agent, which explains the low yields (LeCorre *et al*., 2011a). As for CNC, acid hydrolysis of cellulose is a well-known process for their production, but the production is often limited to amounts only sufficient for lab scale usage. However, the application as a nanoreinforcement in biopolymers requires a compounding process that consumes larger quantities of cellulose whiskers (Bondeson *et al*., 2006). Hence, the preparation procedure has been widely discussed to find the optimized one for better production, it has also been mentioned that a degradation of crystalline cellulose could occur during hydrolysis (Beck-Candanedo *et al*., 2005; Bondeson *et al*., 2006; Filson and Dawson-Andoh, 2009).

Therefore, a timely separation of nanocrystals from the hydrolyzing agent is crucial in the production. LeCorre *et al.* (2011b) proposed a continuous process to produce SNC: a cross-flow membrane filtration was integrated in order to extract SNC from the hydrolyzed suspension as soon as they were produced. This innovative solution was proved to be an efficient operation for separating SNC from the bulk suspension, which could improve not only the production yield of SNC but also the quality and homogeneity of SNC suspensions. Their investigation concerns only the production of SNC, but it represents a high potential for applying in the CNC production with appropriate modifications since similar challenges present in both production processes. Besides, it is rarely reported in literature concerning cross-flow filtration performance of nanocrystals of both starch and cellulose, which encourages us to carry out this investigation. At first time, ultrafiltration was selected since no report could be found yet in literature.

In this study, SNC and CNC suspensions are simultaneously subjected to pressure, shear flow and ultrasound (US) during specific cross-flow filtration. The filtration performance has been investigated at both macro-scale (permeate flux) and nano-scale, referring to the structural organization of nanocrystals during filtration at nanometer length scale, revealed by real-time *in-situ* small-angle X-ray scattering (SAXS) measurements of synchrotron radiation. To the best of our knowledge, it is the first time that SNC and CNC suspensions are characterized by *in-situ* measurements in such complex environment.

2.2 Sample suspension characterization

SNC sample suspensions were characterized by different approaches: DLS, AFM, FEG-SEM, SAXS and rheological measurements. The CNC suspensions used for filtration were also characterized by DLS, AFM and SAXS measurements. In this section, results will be presented by technique.

2.2.1 DLS and microscopic characterizations

DLS measurement gives a global description of the particle size distribution in the suspension. For SNC suspensions, a high polydispersity was revealed with particles in the analyzed sample ranging from hundreds of nanometers to some micrometers. Measured mean diameter of this used suspensions are 1600±80 nm (Tab. 4.2).

Tab. 4.2 *DLS and AFM measurements*

Dispersions	Techniques	properties	Values
SNC	DLS	Mean diameter (nm)	1600±80
CNC	DLS	Mean diameter (nm)	125±12
CNC	AFM	Length (nm)	270±90
CNC	AFM	Thickness (nm)	10±3
CNC	AFM	Aspect ratio	30

In Fig. 4.13a-1, AFM image of SNC sample reveals the presence of round shape isolated particles with diameters ranging from 20 to 120 nm. There are also some aggregates not shown in this figure with a size up to 1µm. In fact, we can assume that large particles present in the samples are mainly aggregates of small particles formed during centrifugation step. The presence of such particles even in small amounts makes the calculated mean diameter switch to high values.

In addition, samples of SNC suspensions during filtration were characterized by FEG-SEM (Fig. 4.13b), principally for detecting the presence of SNC particles in the permeates, which will be discussed in section 2.3. Generally, the same observation is revealed as AFM image: polyhedron-shaped particles of 100-200 nm with some micron-size aggregates in feed and retentate, and small similar particles are also observed in the permeates.

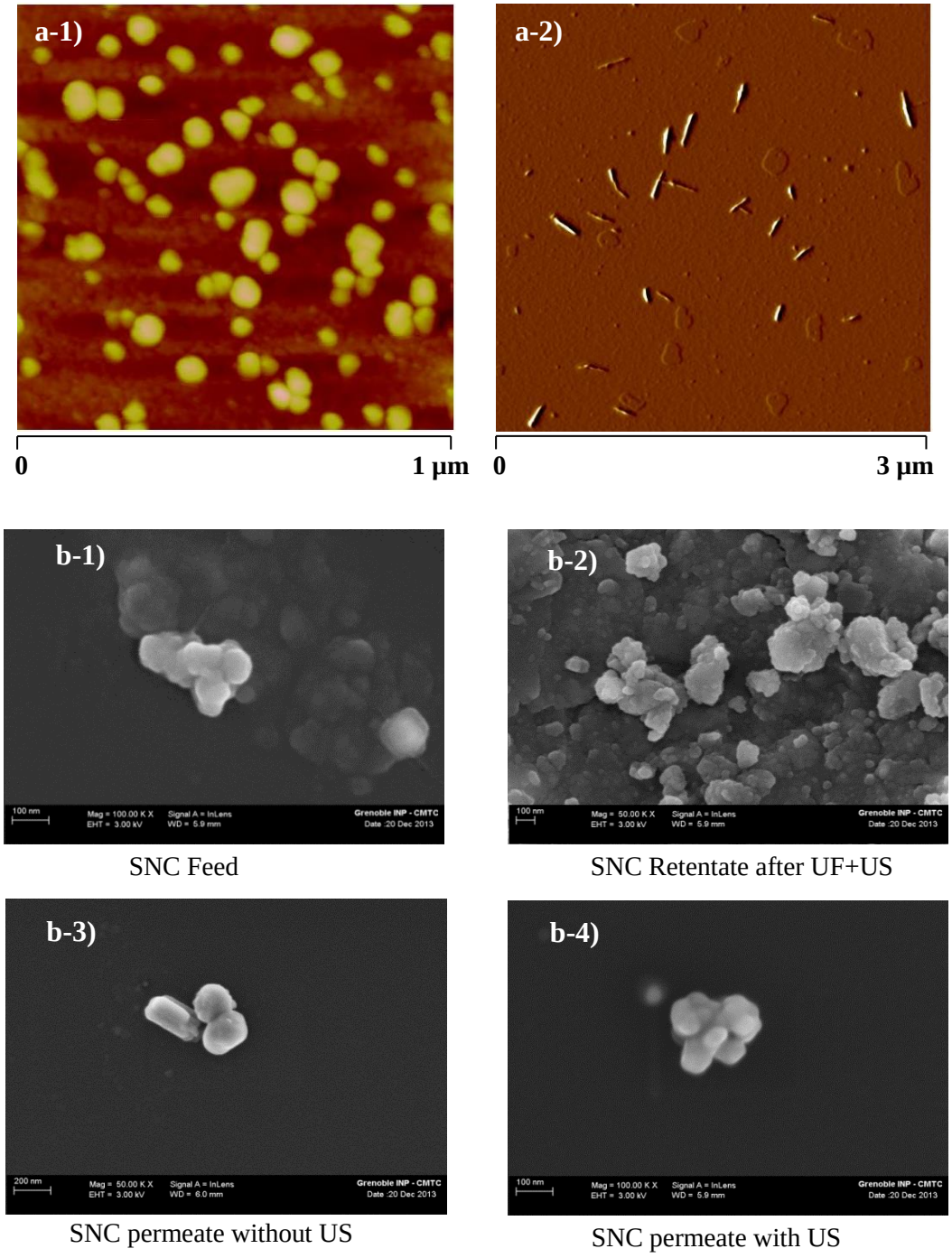

Fig. 4.13 *a) AFM images: a-1) feed SNC suspension and a-2) individualized nanocrysllaine cellulose. b) FEG-SEM images: b-1) SNC feed suspensions; b-2) SNC retentate after ultrafiltration under ultrasound (US); b-3) SNC permeate of ultrafiltration without US; b-4) SNC permeate of ultrafiltration with US.*

As for the CNC suspensions used for filtration, combined characterization of DLS and AFM reveals the rod-like particles of around 125 nm with aspect ratio of 30. The thickness of these particles is 10±3 nm while length varies around 270 (±90) nm, as shown in Tab. 4.2 and Fig. 4.13a-2.

2.2.2 SAXS profiles

SAXS measurement is usually employed to probe the microstructure and non-equilibrium of soft matter and related systems, exhibited by the SAXS profiles. Fig. 4.14 presents the azimuthally averaged scattered intensities I of SNC and CNC suspensions samples as a function of scattering vector modulus q (nm^{-1}) in log-log scale. Scattering vector modulus q describes the sample's structure in reciprocal space, the correspondent length scale in real space can be calculated by $l = 2\pi/q$. The length scale of Fig. 4.14 thus ranges from 6 nm to 60 nm. All the profiles come from the *in-situ* SAXS measurements being carried out in the filtration cell; they are then used for the concentration profiles presented in section 2.3.2 and 2.4.

For the SNC suspensions (Fig. 4.14a), SAXS profiles of four different samples were plotted: the feed suspension and three others under filtration with or without US measured at z = 60 µm from the membrane surface. All the profiles follow a $q^{-2.5}$ power law, indicating that no structure change occurred in this length scale range (from 10 nm to 60 nm) under filtration. In addition, an increase of scattered intensity can be observed at z = 60 µm after 40 minutes' filtration (the squares), suggesting that SNC concentration rose at this position from the membrane (Φ_m =1.0 %). US did not affect the SNC structure, but it led to a decrease of scattered intensity resulting from a concentration drop (the triangles), this phenomenon will be discussed in detail in section 2.3.2.

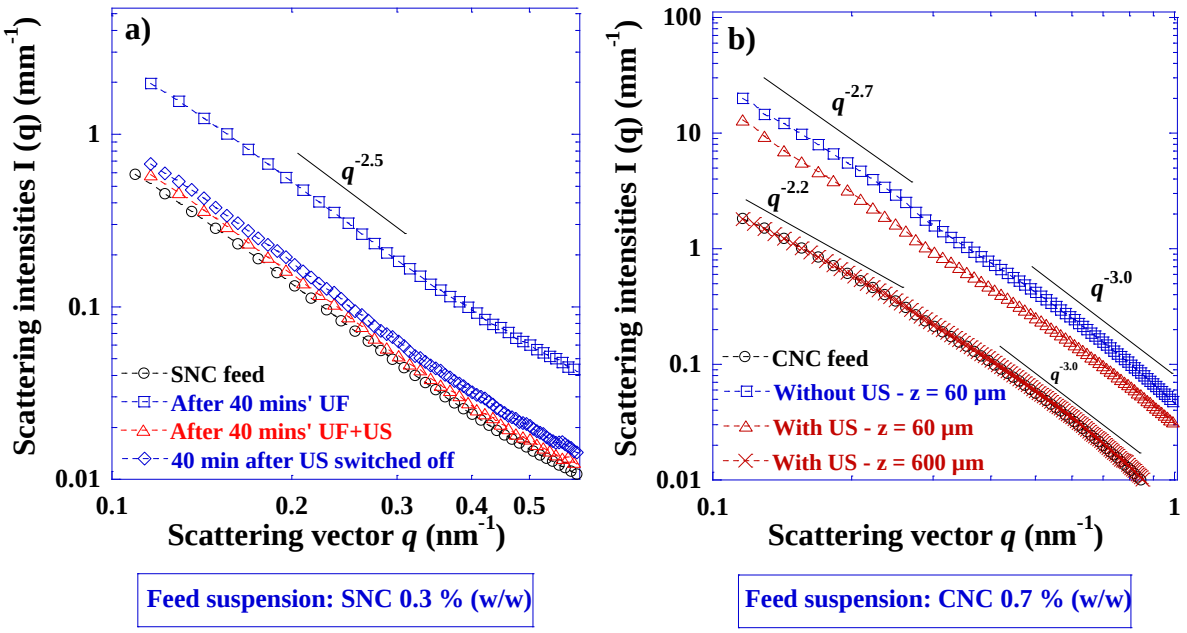

Fig. 4.14 *SAXS profiles of nanocrystal suspensions during filtration. a) SNC suspension (TMP = 1.1×10^5 Pa, Q_v = 0.45 L.min^{-1}; measured points: z = 60 µm from the membrane surface.); b) CNC suspension (TMP = 1.1×10^5 Pa, Q_v = 0.3 L.min^{-1}). T = 25±1 °C, ultrasound: 20 kHz, 2 W.cm^{-2}. No internal structure change of both SNC and CNC suspensions occurs under ultrasonication.*

Fig. 4.14b presents the SAXS profiles of four CNC suspensions samples under different conditions during filtration. Two profiles are superimposed: the feed suspension (the circles) and the sample being measured at z = 600 µm from the membrane surface during filtration after 90 minutes' ultrasonication (the crosses). It suggests that the CNC suspension at this position from membrane has the same structure and concentration properties as the feed, otherwise, "bulk" of the filtrate is identified. It also implies that the applied US did not influent the CNC internal structure since no SAXS profile change occurs between the circles and the crosses. Scattered intensities increase for two samples closed to the membrane surface (z = 60 µm), denoting that a concentration rise occurred during filtration (without US: Φ_m =4.8 %, represented by squares symbols; with US: Φ_m =2.6 %, triangles. More results of concentration information will be presented in section 3.3). Moreover, slight structure change can be observed due to this particle concentration: at relative low scattering vector range (q < 0.3 nm^{-1}), the SAXS profiles follow a different power law when the samples are more concentrated (the squares and the triangles). This

can be explained by the change of interaction, e.g. the change of particle orientation from a randomly arrangement to an ordered arrangement. In fact, this change of particle orientation was indeed observed which will be presented in section 2.4. At relative high scattering vector range (q > 0.3 nm^{-1}), the SAXS profiles shift parallelly with the increase of concentration in following $q^{-3.0}$ power law. In this range, for a given substance with defined "form factor", scattered intensity depends only on the number of particles, otherwise, the sample concentration. It implies that the interpretation of concentration from q = 0.5 nm^{-1} (which will be presented in section 2.4) should not be affected by this change of particle arrangement.

2.2.3 Flow properties

Flow properties of SNC suspensions have been investigated. The steady state flow curves of SNC samples are plotted in Fig. 4.15. Effects of concentration (filled, in black) and temperature (unfilled, in blue) on rheological properties are demonstrated as well as the effect of ultrafiltration and ultrasonication (in red) in this figure. Samples of different concentrations from 0.3% (w/w) to 16.8% (w/w) were prepared by dilution or evaporation at ambient temperature.

Generally, all the samples exhibit a shear thinning fluid behavior. For the samples whose concentrations are below 9.6 % (w/w), rheological behavior is well depicted by a power law: $\tau = K\dot{\gamma}^n$, where τ represents the shear stress (Pa), K is the consistency (Pa.s^n), $\dot{\gamma}$ is the shear rate (s^{-1}) and n is the shear-thinning index. Therefore, the experimental points were fitted by this model and presented by the dotted curves in Fig. 4.15, the fitted values are given in the affiliated table in Fig. 4.15. The feed suspension for filtration (mass fraction Φ_m = 0.3 %) have a near-Newtonian-behavior since the shear-thinning index n is close to 1 (for Newtonian fluid, n = 1). With the increase of sample concentration, a gradual decrease of shear-thinning index n and increase of consistency K can be observed, indicating a shear-thinning behavior more and more pronounced.

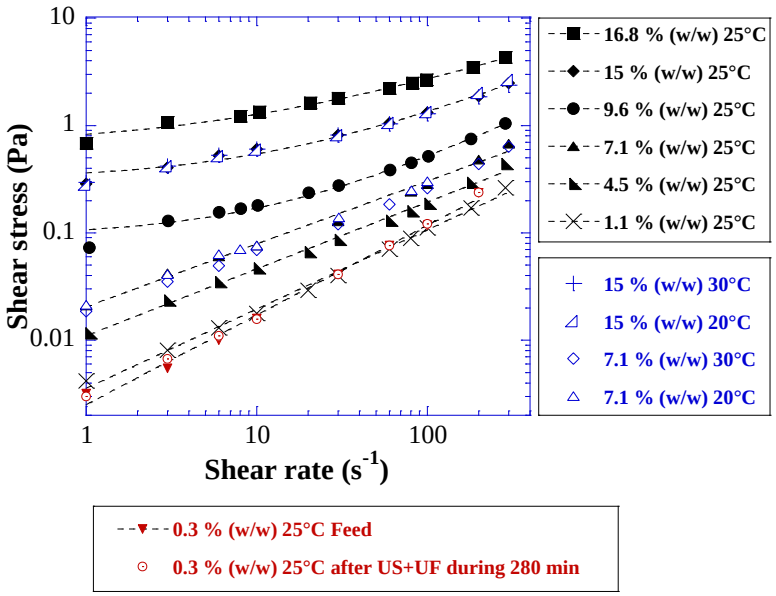

Affiliated table of Fig. 4.15: curves fit values

Samples	Curves fit values		
	τ_0(Pa)	K(Pa.s^n)	n
16.8% (w/w) 25°C	0.63	0.196	0.51
15% (w/w) 25°C	0.31	0.054	0.64
9.6% (w/w) 25°C	0.093	0.014	0.75
7.1% (w/w) 25°C	/	0.020	0.59
4.5% (w/w) 25°C	/	0.011	0.62
1.1% (w/w) 25°C	/	0.004	0.74
0.3% (w/w) 25°C Feed	/	0.003	0.83

Fig. 4.15 *Steady state flow curves of SNC suspensions revealing (i) the effect of concentration and temperature on flow behavior of SNC samples, and (ii) the effect of ultrasonication and ultrafiltration on flow behavior of feed suspension: US+UF during 280 min. SNC: Φ_m =0.3 % (mass fraction), TMP = 1.1×10^5 Pa, Q_v = 0.45 L.min^{-1}, Ultrasound: 20 kHz, 2 W.cm^{-2}. Curves of different concentrations are fitted by power law ($\boldsymbol{\tau = K\dot{\gamma}^n}$) or Herschel-bulkley viscoplastic model ($\boldsymbol{\tau = \tau_o + K\dot{\gamma}^n}$), as the dotted ones, corresponded values are presented in affiliated table. Shear-thinning behavior of SNC suspensions is revealed and yield stress emerges from 9.6 % (w/w).*

When the SNC concentration becomes higher than 9.6 % (w/w), the suspensions exhibit a gel consistency and yield stresses emerge on the flow curves (Fig. 4.15). In this case, a Herschel-Bulkley viscoplastic model was used for curve fitting (Macosko, 1994): $\tau = \tau_o + K\dot{\gamma}^n$, with τ_0 the yield stress (Pa). The estimated yield stress values are provided in the affiliated table inFig. 4.15, e.g. for the sample of 16.8% (w/w), a yield stress of 0.63 Pa is present.

According to Angellier *et al*. (2005), above a given volume fraction (6.7 vol %, i.e. 10 w/w %), SNC clusters could connect to form a continuous infinite and open network by hydrogen bonding between nanocrystals. It could explain the evolution of rheological behavior. The increasing shear-thinning character with the increase of SNC concentration until the emergence of yield stress from 9.6% (w/w) could be due to a more and more pronounced interaction between starch nanocrystals until the formation of a rigid network.

In addition, effect of temperature on rheological behavior has been explored for all samples in varying it from 20°C to 30°C, two samples are shown in Fig. 4.15 since the same phenomenon was observed for the other samples. Steady state flow curves are all superimposed at three concerned temperatures for the sample of 15% (w/w) and 7.1% (w/w), indicating that temperature did not affect the rheological behavior at the range from 20°C to 30°C.

The steady state flow curves of SNC suspensions (Φ_m = 0.3 %) after ultrasonic assisted ultrafiltration are also plotted in Fig. 4.15 (in red). Two samples were analyzed: one before feeding into the filtration cell and the other picked up from bulk suspensions during cross-flow filtration with US, the rheological properties being determined 5 minutes after sampling. No change of suspension viscosity occurred during filtration even though under US for 280 min.

2.3 Filtration performance of SNC

2.3.1 Filtration performance of SNC at macro-scale

Cross-flow ultrafiltration runs were carried out at two different cross-flow rates Q_v. In order to characterize the filtration performance of SNC suspensions, a step-up transmembrane pressure (TMP) procedure was used: filtration during 30 min at each TMP step with a gap of 5

min between steps. During the filtration of SNC suspensions (Φ_m = 0.3%), the evolution of permeate flux J_v, TMP and Q_v over time were monitored, essential ones among them are displayed in Fig. 4.16, showing two filtration runs with and without US at Q_v = 0.3 L.min^{-1}.

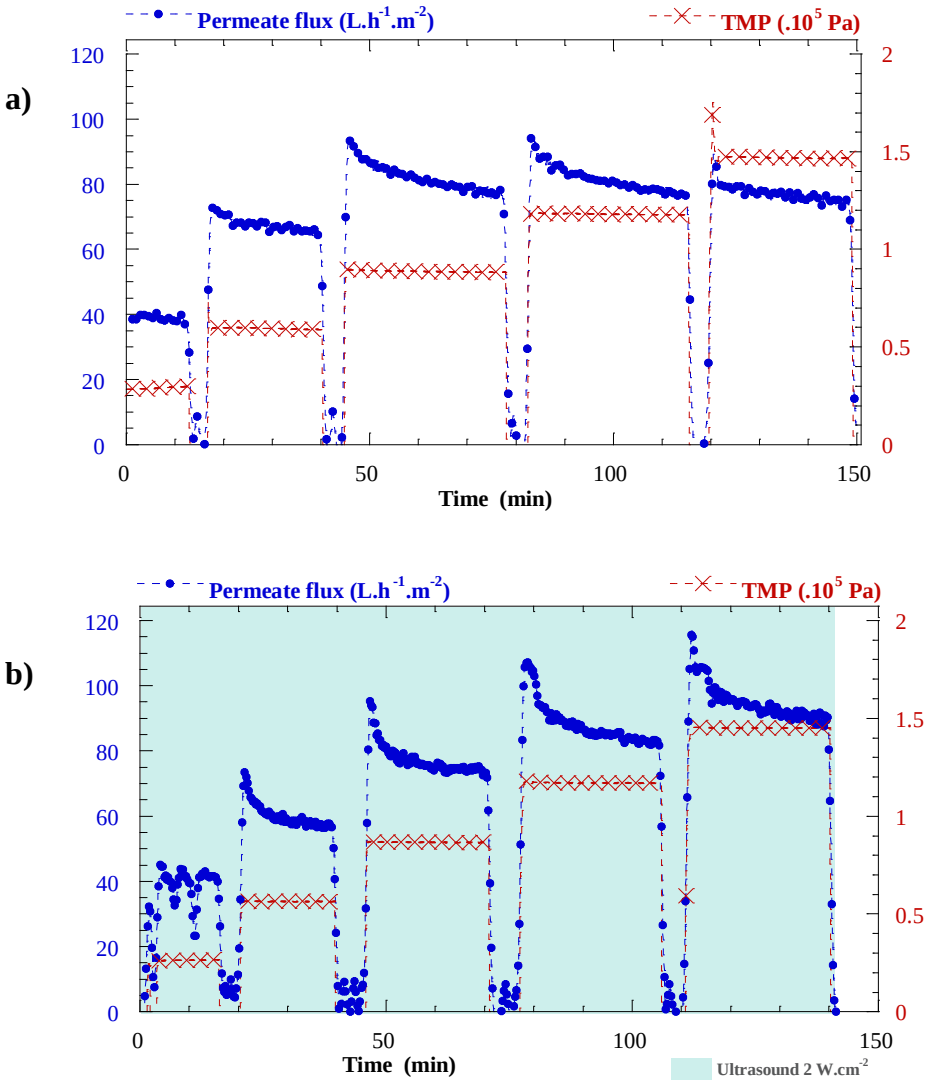

Fig. 4.16 *Filtration curves of SNC suspensions without (a) and with (b) US: evolutions of TMP and permeate flux J_v over time. Φ_m = 0.3%, Q_v = 0.3 L.min^{-1}. T = 25±1 °C, Ultrasound: 20 kHz, 2 W.cm^{-2}. Filtration curves follow different scenarios with or without US.*

Two other filtration runs were performed at Q_v = 0.45 L.min^{-1} with and without US (filtration curves not shown), Fig. 4.17 assembles these four steady-state curves of J_v/L_p (the ratio

between the permeate flux and the permeability of membrane, Pa) versus TMP for both applied Q_v. No difference can be seen among these four filtration runs when TMP is below 0.6×10^5 Pa: the filtration performance of SNC suspensions is independent of Q_v and US under these conditions. The filtration curves diverge beyond 0.6×10^5 Pa. Two blue curves with unfilled symbols, standing for the filtration runs without US, present clearly the so-called limiting fluxes, despite of different flux values because of different Q_v. Represented by the two red curves with filled symbols, the application of US leads to an improvement of filtration performance: instead of being limited, the permeate fluxes continue to increase with TMP up to 1.4×10^5 Pa.

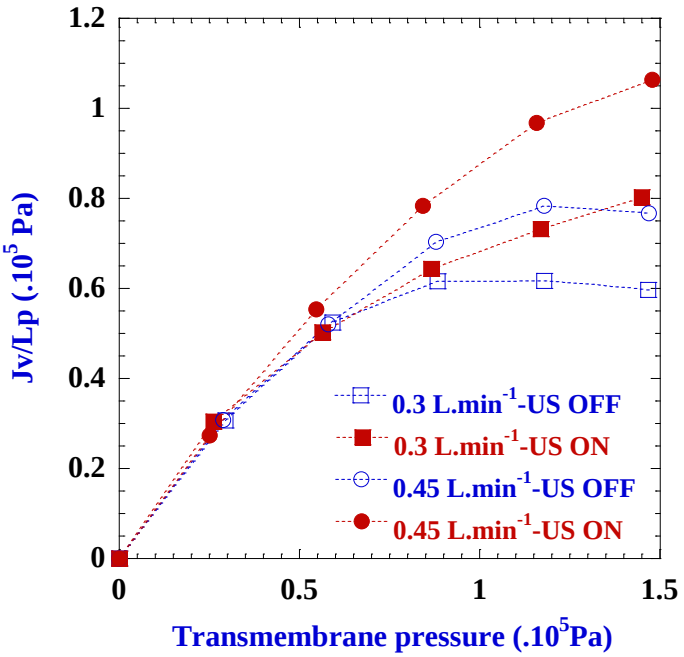

Fig. 4.17 *Steady-state curves of J_v/L_p as a function of TMP for different Q_v with/without US during ultrafiltration of SNC dispersions (Φ_m = 0.3 %). T = 25±1 °C, Ultrasound: 20 kHz, 2 W.cm^{-2}. No more limiting flux under US.*

This general observation needs more details carried by the filtration curves presented in Fig. 4.16. Putting the permeate flux values aside, different filtration curve shapes are observed between Fig. 4.16a and Fig. 4.16b. At each TMP step, the permeate flux declines slightly without US (Fig. 4.16a) while dramatically with US (Fig. 4.16b). Some first trials have already been carried out (results not shown), indicating that irreversible fouling could occur during filtration of

SNC suspensions without US. We assume, therefore, that under US, this fouling layer was disrupted when TMP was released (between two steps) and it would reform when TMP was again applied. Consequently, a thinner fouling layer gave rise to the instantaneous permeate flux increase relatively important, a rapid reformation of concentrated layer then led to the following pronounced decline. Compared to the run with US, the irreversible fouling layer stayed on the membrane surface even when TMP was released without US, and the newly-formed layer was superimposed on the elder one. In brief, the membrane was all the time covered by a fouling layer without US and the additional concentrated layer formed at each step led to the slightly decline of permeate flux. Returning to Fig. 4.17, the favorable increase of permeation capacity induced by US could be, therefore, explained by this disruption of concentrated layer, considering that the limiting flux strongly depends on a resistant concentrated layer.

Tab. 4.3 *Reynolds numbers and rejection rate of SNC filtration at four different conditions (further information of Fig.6).* Φ_m *= 0.3 %, T = 25±1 °C, Ultrasound: 20 kHz, 2 W.cm*$^{-2}$.

Filtrations	u (m.s^{-1})	Re	Rejection rate TR (%)	
			dry weight (±3%)	COD(±5%)
US OFF 0.3 L.min^{-1}	0.16	828	95	90
US OFF 0.45 L.min^{-1}	0.23	1242	89	93
US ON 0.3 L.min^{-1}	0.16	828	82	85
US ON 0.45 L.min^{-1}	0.23	1242	76	92

Tab. 4.3 reports mean velocities of fluid (u), Reynolds numbers (Re) and rejection rate (TR) of these four filtration runs. As studied in section 2.2.3 concerning the flow behaviors of SNC suspensions, an average suspension viscosity at high shear rates, η_{SNC} = 0.001 Pa.s, is taken to calculate Reynolds numbers, which are 828 and 1242 for Q_v = 0.3 and 0.45 L.min^{-1} respectively. The calculation of Reynolds numbers did not yet take into account the US effect. The effective Reynolds number should be more important under US, as discussed before.

As all the previously investigated suspensions, no significant fluid heating was observed during filtration of SNC (as well as CNC). By dry weight measurements and COD analysis of

feed and permeate suspensions, the rejection rate of membrane (TR) has also been determined. TRs of these four runs are presented in Tab. 4.3. In order to reveal the real chemical oxygen demand of SNC samples, COD of some blank samples were also analyzed, including the deionized water used for sample preparation and the recovered water passed through the membrane before each filtration run. All of them present a negligible COD compared to the permeate samples. Generally, high membrane rejection can be seen for all the four runs. Though not many, there were indeed some SNC particles that passed through the membrane, since they were re-found in the permeate suspensions, revealed by COD analysis and FEG-SEM microscopic analysis (Fig. 4.13b). Another interesting point is that the TRs are slightly lower with US, indicating that more SNC have passed through the membrane in this case. This observation will be further discussed in the following section.

2.3.2 Filtration performance of SNC at nano-scale

In order to better understand the SNC filtration behaviors, structural organization, referring to the concentration profiles, of SNC suspensions on the membrane surface at nanometer scale has been investigated by real-time *in-situ* SAXS measurements, which were carried out simultaneously during cross-flow filtration.

2.3.2.1 Temporal evolution of concentration profiles

The SNC suspensions with the same concentration as previous section were used: Φ_m = 0.3%. Three different filtration steps can be distinguished by the application of US. The evolution of permeate flux and the related concentration profiles (in the middle of the filtration cell) over time are displayed in Fig. 4.18. TMP was applied immediately once the SNC suspensions were introduced to the filtration cell, as shown in Fig. 4.18a.

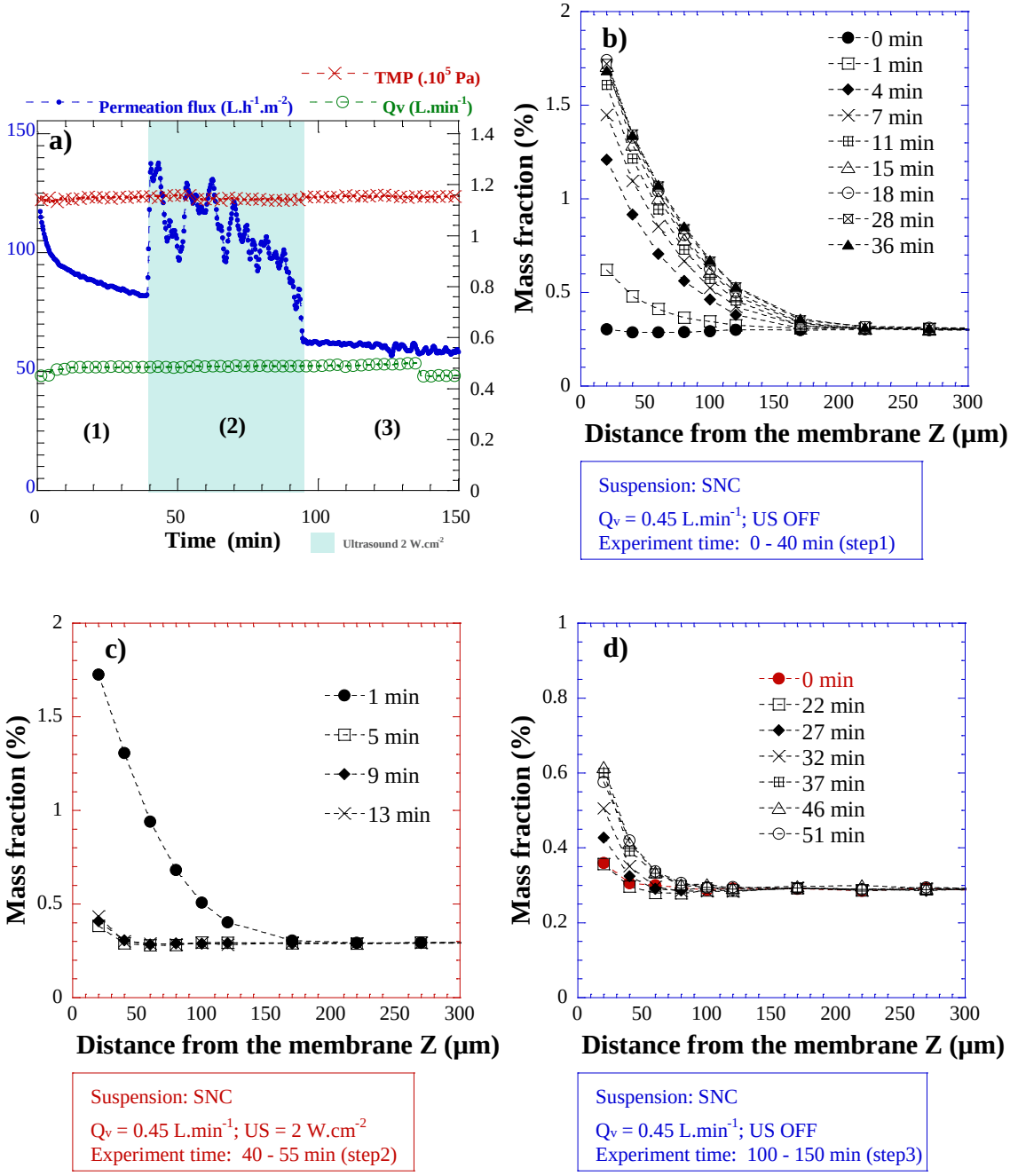

Fig. 4.18 *Combination of macro-scale results and nano-scale observations during SNC ultrafiltration. Φ_m = 0.3 %, T = 25±1 °C, Ultrasound: 20 kHz, 2 W.cm^{-2}. a) Cross-flow filtration curve: evolution of J_v, TMP and cross-flow rate Q_v over time. b-d) Related concentration profiles from the membrane surface to the bulk, deduced from in-situ SAXS measurements, for step 1,step 2, and step 3, respectively. ''0 min'' represents the initial state before operation, e.g. the profile before filtration in (b) and the profile before US was switched off in (d).Concentrated layer is broken up very quickly by US; reformation of concentrated layer is very slow at step 3.*

At step 1, the permeate flux declines from 120 $L.h^{-1}.m^{-2}$ to 80 $L.h^{-1}.m^{-2}$, which relates to a progressive formation of accumulated particles layer on the membrane surface, presented in Fig. 4.18b. US were then applied at step 2 when no more evolution of this concentration profile was observed (final state: thickness of 170 µm and Φ_m = 1.7 % at 20 µm from the membrane surface). The permeate flux is reinforced immediately once US is applied, from 80 to 130 $L.h^{-1}.m^{-2}$. We should note that the destabilization of concentrated layer was so rapid that almost the whole layer was removed after 5 min under US, since the mass fractions equal 0.3% from z = 40 µm to the bulk suspensions (Fig. 4.18c). It indicates that this accumulated SNC particles layer was fragile. In fact, the investigation of the rheological behavior has provided us the evidence (Fig. 4.15): similar steady-state flow curve can be observed for the SNC suspension of 0.3 % (w/w) and 1.1 % (w/w), suggesting that no great structure change could happen when concentration varies in this range. Hence, we assume that the whole concentrated layer in step 1 (Fig. 4.18b) had a non-connected structure so that the ultrasonic waves were efficient to break it up.

Otherwise, the concentrated layer removal by US could explain the lower TR with US. In fact, the concentrated particle layer is often considered as the second barrier in membrane process which can retain certain substances in the feed. Since this barrier is weaken by US, more particles that smaller than membrane pores would pass through the membrane. However, though polydispersed the SNC feed, majority of them were bigger than the membrane pores. Hence, TR did not decrease significantly with US.

However, the permeate flux declines over time until 85 $L.h^{-1}.m^{-2}$ at step 2 even under US. As mentioned before, the rejection rate is lower with US, suggesting that more SNC particles may pass through the membrane. Membrane resistances were also determined in two circumstances: with US and without US, and the first results (not shown) hint that an more severe inner membrane fouling could occur with US. Consequently, the observed permeate flux decline could probably relate to an inner membrane fouling. This phenomenon is particularly related to the used membrane (MWCO is 100 kDa), which can be avoided by choosing another membrane with different MWCO.

At step 3, US were switched off. The permeate flux decreases from 85 $L.h^{-1}.m^{-2}$ to 62 $L.h^{-1}.m^{-2}$ immediately then begins a slow decline until 58 $L.h^{-1}.m^{-2}$. At nano-scale (Fig. 4.18d), the

SNC particles re-accumulated slowly on the membrane surface but only a thin layer is formed with lower concentration, compared with step1 (Fig. 4.18b). The origin of this phenomenon could be the decline of convection flux from bulk towards the membrane since it was fouled during the previous step. Due to this reduced convection flux, the rate of particles accumulation towards the membrane slowed down. Therefore, the decline of permeate flux at this step was very slow and such concentrated layer at step1 could not be reformed even after 51 min.

2.3.2.2 Concentration profiles along the membrane

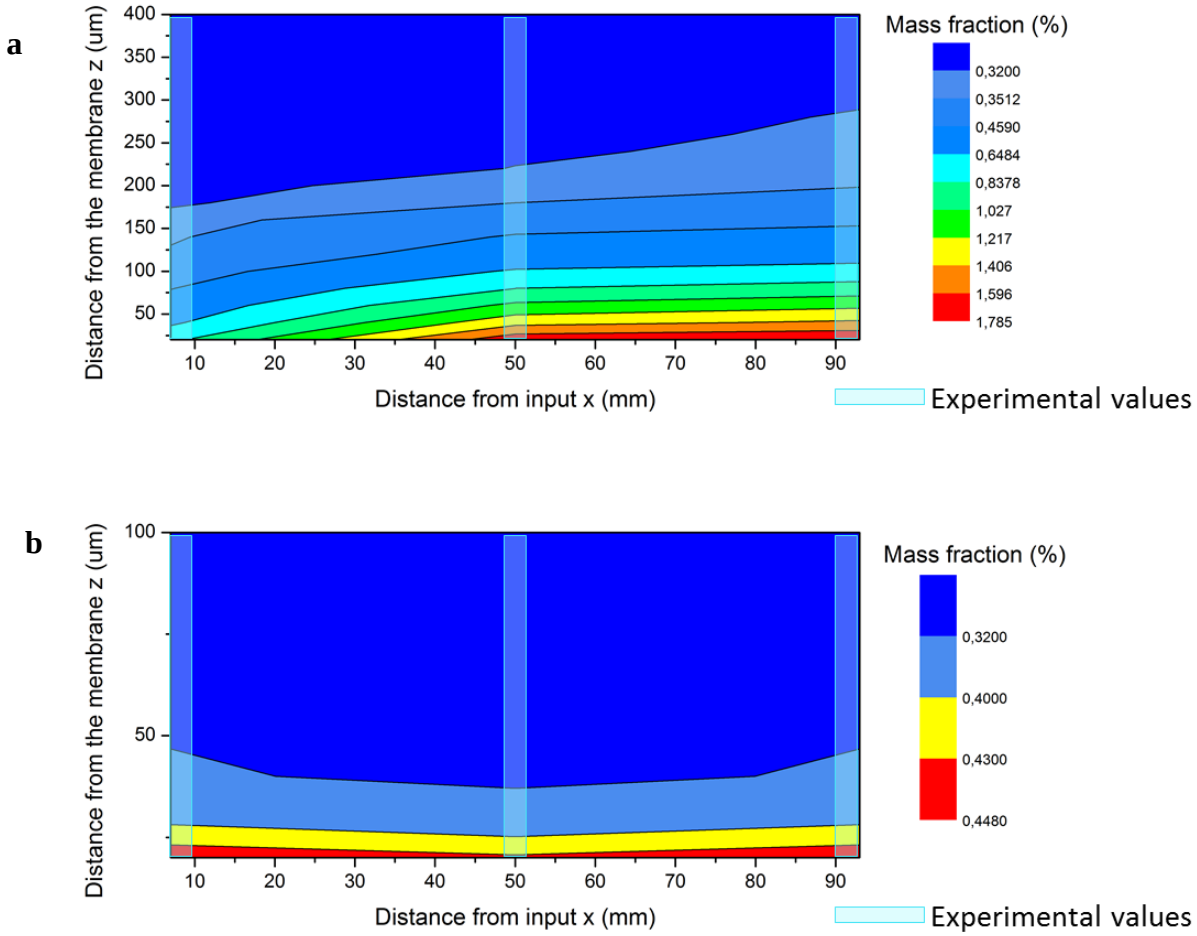

Fig. 4.19 *Contour chart of accumulated particles layer in the filtration channel at step 1 (without US) and step 2 (with US) during ultrafiltration of SNC dispersions (Φ_m = 0.3 %). T = 25±1°C, TMP = 1.1×10^5 Pa, Q_v = 0.45 L.min^{-1}. Ultrasound: 20 kHz, 2 W.cm^{-2}. The break-up of the concentrated SNC particles layer is more pronounced in the middle of the filtration cell.*

Deduced from the results of three windows located at 7 mm, 50 mm and 93 mm from inlet of filtration cell, Fig. 4.19 presents the contour charts of filtration channel at step 1 (without US) and step 2 (with US). At the end of step 1 (Fig. 4.19a), a concentration profile with an increasing thickness along the filter surface (x axis) is observed: from 160 µm at inlet to 280 µm at outlet of filtration cell. In addition, local particle concentration at inlet is lower than the other two positions at every distance z. Such profile accords with our previous results. When US were applied, the accumulated layer was disrupted, as shown in Fig. 4.19b: the layer thickness is reduced to 40 µm for the inlet and outlet parts and 20 µm for the middle part of filtration cell. Interestingly, US seem to be more efficient in removing the concentrated layer in the middle of the filtration cell than the two other positions. This could be explained by inhomogeneity of ultrasonic activity within the filtration channel. As shown in chapter 2 section 4, the ultrasonic power is relatively higher in the middle of the channel than the two ends where amplitude loss is more pronounced. Stronger ultrasonic activity then results in the disruption of the concentrated SNC particles layer more marked in the middle of the filtration cell.

2.4. Filtration performance of CNC

A filtration run has been carried out at ESRF for the SAXS measurements. Interesting phenomena were revealed by this filtration run which provides us guiding information for future investigation. They are enlightening in the aspect of both filtration of CNC and US effect on CNC/filtration. In this section, results will be firstly presented and discussed in combination of macro-scale and nano-scale detections. A specific phenomenon-particle orientation-occurred during filtration of CNC will then be emphasized and discussed in the second part.

2.4.1 Filtration performance and concentration profiles

For this run, US were applied before filtration (preventive mode), TMP was then set at 1.1×10^5 Pa. Fig. 4.20 presents the evolution of permeate flux over time and the related concentration profile (in the middle of the filtration cell) meanwhile. A sharp decline of permeate flux produces once TMP is applied (Fig. 4.20a), which could be associated with the formation of a highly concentrated layer shown by SAXS measurements only after 1 min's filtration,

presented in Fig. 4.20b. Afterwards, particles accumulation continues within this concentrated layer resulting in a further concentration increase as well as a slight layer thickness growth. 10 min is the time it takes to reach the steady state of concentration profile since no more evolution is observed after 10 min at nano-scale. Returning to the macro-scale curve, one can find that the decline phase of permeate flux takes also 10 min to reach the plateau of 35 $L.h^{-1}.m^{-2}$. Interestingly, the permeate flux then increases to 55 $L.h^{-1}.m^{-2}$ at the end of this step, after about 30 min, which relates to a slight disruption of concentration profile (unfilled triangle in Fig. 4.20b).

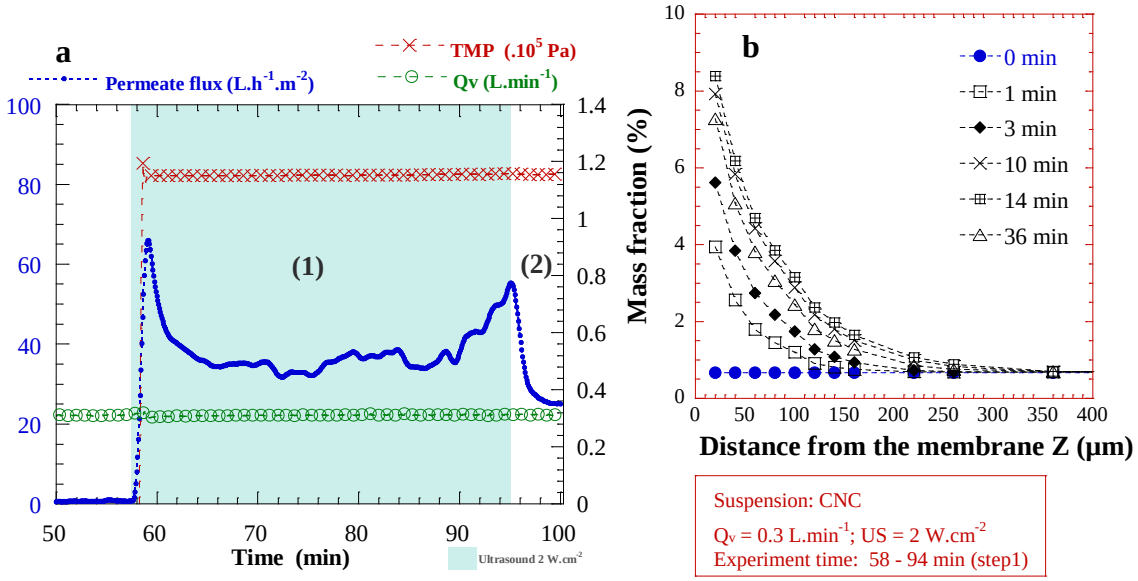

Fig. 4.20 *Combination of macro-scale results and nano-scale observations at step 1 during CNC ultrafiltration. Φ_m = 0.7 %, T = 25±1 °C, Ultrasound: 20 kHz, 2 $W.cm^{-2}$. a) Cross-flow filtration curve: evolution of Jv, TMP and Q_v over time. b) Related concentration profiles from the membrane surface to the bulk, deduced from in-situ SAXS measurements. Concentrated layer grows over time but seems to be disrupted at t = 36 min.*

It should be noted that CNC are very polar and attract each other by hydrogen bonding thus they have tendency to form bundles or aggregates (Lu and Hsieh, 2010; Marcovich *et al.*, 2006). During drying, the abundant hydrogen bonds of cellulose draw the cellulose nanocrystals together to pose significant problems in their re-dispersion for effective processing (Tingaut *et al.*, 2010). Therefore, ultrasonication is often integrated in the CNC production to disperse the

particles (Bondeson *et al*., 2006; Dong *et al*., 1998). Colloidal aqueous suspensions of CNC are known to form chiral nematic ordered structure above a critical concentration (Beck-Candanedo *et al*., 2005; Revol *et al*., 1994, 1992) and birefringent gel-like material at even higher concentrations (Liu *et al.*, 2011; Ureña-Benavides *et al*., 2011). X. M. Dong *et al.* (1998) studied the effect of ultrasonic treatment (20 kHz, around 350 W) on the properties of CNC suspension. They reported a decrease of CNC particle size as well as an influence of ordered phase of suspension with US treatment, which suggested that US could break the microcrystallites and hence lower the mean axial ratio of rods in the suspension. Shafiei-Sabet *et al*. (2012) evaluated the effect of ultrasound energy (20 kHz, 130 W) on the microstructure and rheological properties of CNC aqueous suspensions (5 wt % and 7 wt %). They also observed a reduction of the hydrodynamic size of CNC attributed to breakage of aggregates. In addition, they found that the viscosity dropped significantly with US and their profiles changed from a shear-thinning behavior to a three-region behavior, typical of liquid crystals. They suggested that sonication break up the gel structure of high concentration samples and dispersed the individual CNC nanorods.

On the basis of this reported results, we could explain what happened at step 1: driven by the transmembrane pressure, CNC were concentrated and aggregates were formed at the beginning. The applied US in the experiment were not strong enough to disrupt this course immediately due to their low power feature. They needed time: effect of US then emerged at the end of step 1, revealed by the slight disruption of concentrated layer, suggesting that US began to break up the aggregates and disperse CNC particles.

Another noticeable point is the fact that US is not efficient to prevent the accumulated layer formation during CNC filtration under our operation conditions. Nevertheless, the filtration performance was indeed improved under US since the permeate flux decreased dramatically from 55 $L.h^{-1}.m^{-2}$ to 25 $L.h^{-1}.m^{-2}$ when US was switched off, as shown in Fig. 4.20a. Moreover, no significant change of the concentration profile was detected after US was switched off, while the permeate flux stayed constant at this step (step 2, shown in Fig. 4.20a as well as in Fig. 4.21a).There is, therefore, no interest to show the concentration profiles evolution of this step.

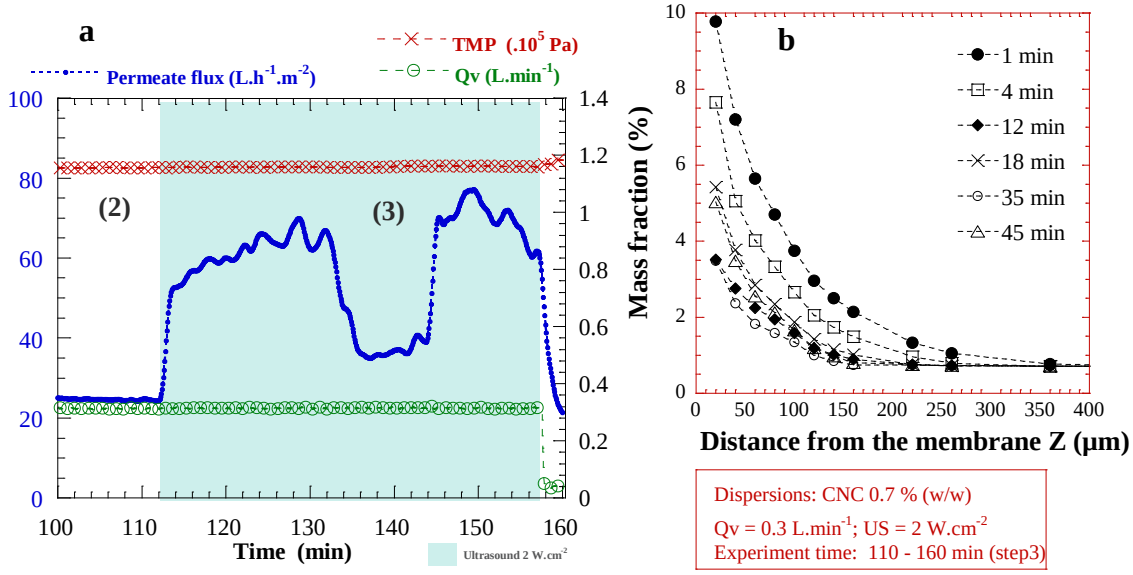

Fig. 4.21 *Combination of macro-scale results and nano-scale observations at step 3 during CNC ultrafiltration. Φ_m = 0.7 %, T = 25±1 °C, Ultrasound: 20 kHz, 2 W.cm^{-2}. a) Cross-flow filtration curve: evolution of J_v, TMP and Q_v over time. b) Related concentration profiles from the membrane surface to the bulk, deduced from in-situ SAXS measurements. The accumulated CNC particles layer is disrupted by US, but an oscillation of concentration profile is observed.*

When steady state reached, US were again applied. As shown in Fig. 4.21a, the permeate flux increases immediately from 25 L.h^{-1}.m^{-2} to 55 L.h^{-1}.m^{-2}, it then continues to increase gradually until 65 L.h^{-1}.m^{-2}. A following decline occurred but it went back to the high level at the end of step. The key to this strange feature could be found in Fig. 4.21b. For the first minutes, the accumulated layer is disrupted by US: the layer thickness reduces with a decrease of particles concentration, which, with no doubt, gives rise to the permeate flux increase. However, this layer break-up regime is not permanent seeing that layer reforms at 18 min (the crosses), leading to the decline of permeate flux. This layer reformation lasted for several minutes since the same phenomenon was also observed in the concentration profile at 21 min (not shown for a better figure legibility). "The battle" is far from over between layer break-up and reformation since the concentration profiles "oscillates" between two concentration levels at 35 min (the unfilled circles) and 45 min (the unfilled triangles).

It should bear in mind that formation of concentrated layer during cross-flow filtration results from the balance between accumulation-induced forces (transmembrane pressure, interaction force among particles, etc.) and anti-accumulative forces (shear-induced hydrodynamic force and ultrasonic force). In this circumstance, accumulated CNC particles could be disaggregated by US and the former balance was broken by the additional ultrasonic force. A new balance should build up but it took time to reach it. Hence, the observed "battle" of layer break-up and reformation in step 3 could be a presentation of a transient state at which anti-accumulative forces were counteracting accumulative forces.

2.4.2 Particle orientation

Specific particles orientation is also found during ultrafiltration of CNC suspension. Fig. 4.22 shows the SAXS scattering patterns of CNC suspensions at filtration step 1 and 3: each pattern represents one measurement point at different distances from the membrane surface of different filtration time. For step 1 (Fig. 4.22a), under only shear flow, instead of an isotropic ring-shape, the X-ray scattering patterns indicate already a preferential orientation (at t = 0 min). Since the first minute of filtration the three patterns closest to the membrane exhibit pronounced anisotropic interference peaks along the lateral arcs. As time goes on, more and more patterns appear highly anisotropic within the same profile: at t = 14 min, all the patterns below 160 µm are highly anisotropic while it is 80 µm at t = 1 min. Considering the related concentration profile (Fig. 4.20b), one can find that all the patterns within the concentrated layers are highly anisotropic. More concentrated the concerned position, more anisotropic the scattered pattern is. Such evidence can be found in Fig. 4.22b as well: the anisotropy magnitude oscillates from 12 min to 45 min, corresponding to the oscillation of related concentration profiles in Fig. 4.21b.

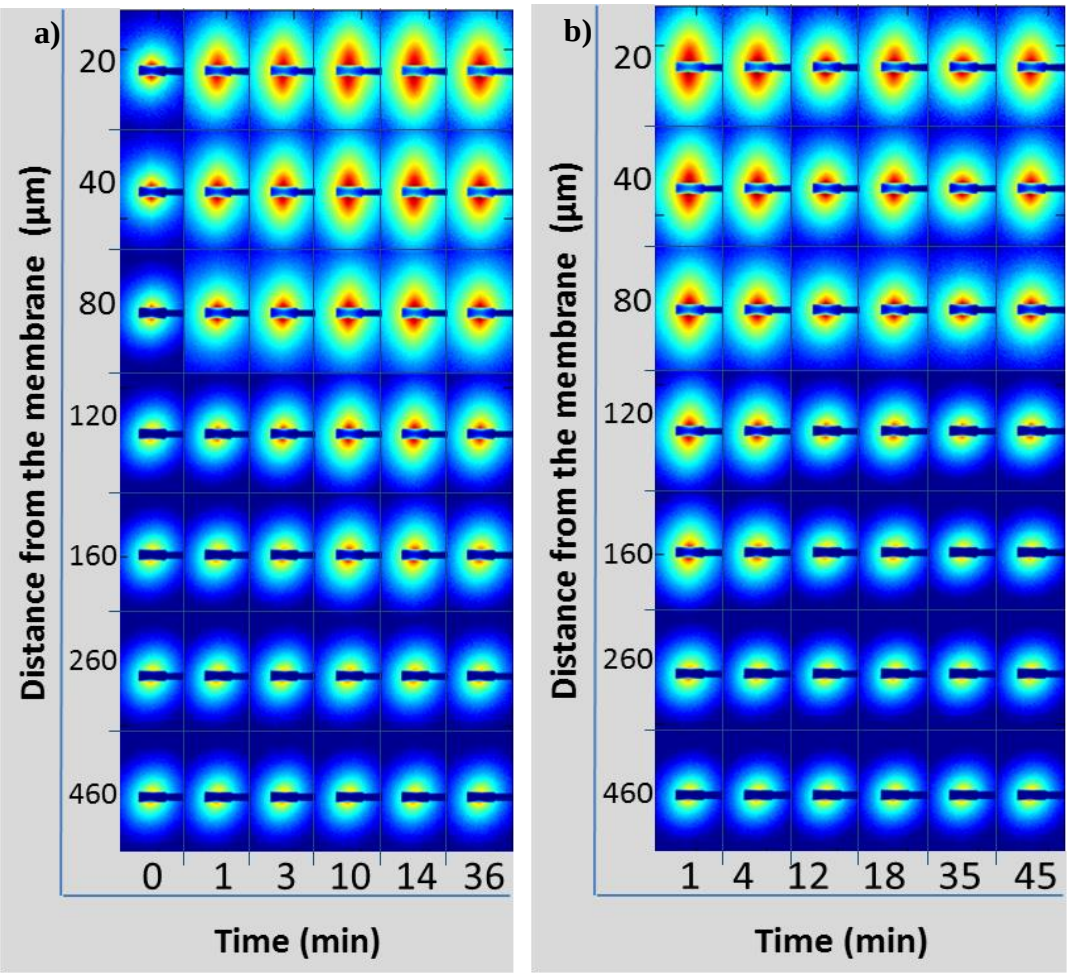

Fig. 4.22 *SAXS patterns of CNC samples of different positions z from the membrane surface at step 1 (a) and step 3 (b) during CNC ultrafiltration.* Φ_m *= 0.7 %, T = 25±1 °C, Ultrasound: 20 kHz, 2 W.cm*$^{-2}$*. The scattered patterns are anisotropic during filtration and this anisotropy evolves over time.*

T.Ebeling *et al.* (1999) have already observed this anisotropic feature of cellulose microcrystals. They reported that the microcrystals were aligned horizontally along the shear direction at shear rates of 5 s^{-1} and higher, which could explain the preferential orientation at t = 0 min and all the points at suspension bulk (for example, at 460 µm from the membrane surface). As mentioned before, it has been proposed in literature that some chiral nematic phases could form above a critical concentration (Revol *et al.*, 1992). Called chiral nematic liquid crystals, they contain rodlike particles arranged in pseudolayers with their long axes parallel to the plane of the layers (Beck *et al.*, 2010). According to these reports, we speculate that driving by the convective flux during filtration, those CNC particles accumulated in a nematic manner, or at

least an ordered manner adjacent to the membrane, which gave rise to the highly anisotropic X-ray scattering patterns.

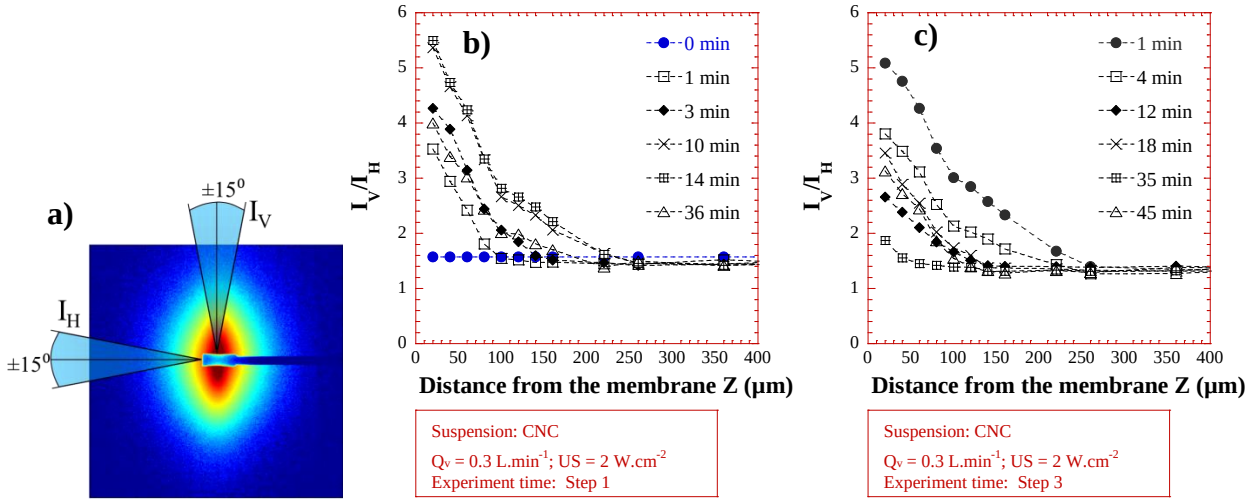

Fig. 4.23 *Demonstration of the anisotropy magnitude calculation (a); and the anisotropy magnitude (I_V/I_H) profiles of CNC samples as a function of distance z from the membrane surface at step 1 (b) and step 3 (c) during CNC ultrafiltration. Φ_m = 0.7 %, T = 25±1 °C, Ultrasound: 20 kHz, 2 W.cm^{-2}. These profiles follow similar evolutions as the related concentration profiles, but the two types of profiles are not perfectly correlated.*

Fig. 4.23b and Fig. 4.23c show the anisotropy magnitude at different time as a function of distance z from the membrane surface for step 1 and step 3, respectively. At step 1, the anisotropy magnitude is equal to 1.6 before filtration under shear flow (t = 0 min in Fig. 4.23b), which emphasizes the fact that the shear flow has already oriented the particles of initial filtrate dispersion. The anisotropy magnitude then increases along with the filtration, reaching a value of 5.5 at t = 10 or 14 min at z = 20 µm. However, the anisotropy magnitude remains all the time the same level above z = 260 µm, being equal to 1.5, which is close to the initial value before filtration (t = 0 min). If one compares the anisotropy magnitude profile with the related concentration profile (Fig. 4.20b), the distances above z = 260 µm correspond to the bulk dispersion with the feed CNC concentration. It suggests that even during filtration, the CNC particles were freely dispersed as initial state at bulk. The anisotropy magnitude starts to increase once the concentrated particle layer is reached. The same profile evolution over time can be observed between the concentration profiles and anisotropy magnitude profiles: both the two

types of profile follow a growth phase from 1 min to 14 min and a slight decline at t = 36min. This phenomenon also appears at step 3: as the concentration profile (Fig. 4.21b), the anisotropy magnitude profile oscillates from t = 12 min to t = 45 min as well (Fig. 4.23c).

Though they have similar evolution, perfect correlation can hardly be found to quantify the relation between the particles concentration and their anisotropy magnitude in this circumstance, probably due to the intervention of US. Taking step 3 as example, the concentration profiles are very comparable at t = 12 min and t = 35 min (Fig. 4.21b), but the related anisotropy magnitude is much lower within the whole profile at t = 35 min than that at t = 12 min (Fig. 4.23c). Similar phenomenon can be observed in step 1 involving the profiles at t = 3 min and t = 36 min (Fig. 4.20b and Fig. 4.23b). In one word, these profiles (t = 35 min for step3 and t = 36 min for step 1) have the same level of concentrations as some earlier ones of the same step but lower anisotropy magnitude than expected. It is reported that US treatment could influence the structure of ordered chiral nematic phase of CNC suspensions (Dong *et al*., 1998; Shafiei-Sabet *et al*., 2012). Beck et al. (2010) suggested that ultrasound energy could liberate excess ions trapped in bound layer of CNC particles leading to expansion of electrical double layer which resulted in weaker chiral interaction between the particles. This led to uncoiling the chiral nematic domains and increase in the pitch size. On the basis of the reported results, we assume, therefore, that in addition to the action of disaggregation, the applied ultrasonic force could also disrupt the ordered arrangement of CNC particles within the concentrated layer during filtration. Combined with hydrodynamic force, it may convert the expanded weak-interacted chiral nematic phase into isotropic phase. Consequently, the anisotropy magnitudes of their SAXS patterns decreased at the end of each ultrasonication step.

It is also interesting to notice that the ultrasonic force has the ability to act in the ordering and structural organization in the entire thickness of the deposit (from the first layers near the membrane surface towards the center of the ultrafiltration cell), suggesting that the applied ultrasound is well propagated within the whole concentrated structured layers, as already shown in other clay systems.

2.5 Summary

In this section, starch and cellulose nanocrystals are characterized at multi-scales under multi-forces environment during ultrasonic assisted cross-flow filtration. It is especially the first time that their concentration profiles and structural organizations have been revealed by real-time *in-situ* SAXS measurements during this process.

Several conclusions could by summarized from this study:

- Rheological behaviors of SNC suspensions have been investigated. Increase of sample concentration led to a shear-thinning character more and more pronounced until the emergence of yield stress from 9.6% (w/w). No effect of temperature on rheological behaviors of tested SNC samples was observed when it varied from 20º C to 30º C.
- No structure change of SNC suspensions occurred at the length scales ranging from 10 nm to 60 nm during ultrasonic assisted cross-flow ultrafiltration, revealed by *in-situ* SAXS measurements; while CNC particles shown an ordered arrangement within the concentrated layer close to membrane surface during the same process.
- During ultrafiltration, SNC particles accumulation could lead to a fouling layer which results in a limiting flux. In our experiments, the accumulated SNC particle layer was not really concentrated and “fragile”, hence, the applied US removed it very quickly and brought about an improvement of filtration performance: an increase of permeate flux. Besides, for the used membrane, the SNC particles were re-found in the permeates for both filtration runs with and without US. In addition, the rejection rate with US was slightly lower than that without US.
- Contrary to SNC, CNC particles accumulation close to the membrane was really severe during ultrafiltration: the concentration of CNC particles adjacent to the membrane can increase 10 times more than the feed suspension with an increase of the anisotropy magnitude 5 times than the feed suspension. The anisotropic structural organization of the CNC particles has induced a denser structure during filtration which is less destabilized by US, compared to the ‘‘fragile’’ and open structure formed by SNC particles. Nevertheless, the applied US led to a decrease in anisotropy and concentration within the whole layer thickness from the membrane surface to the bulk, resulting in an increase of permeate flux by a factor of 3.

Conclusions

In this chapter, two colloidal suspensions of industrial interest have been filtrated using the ''SAXS Cross-Flow US-coupled Filtration Cell''. Their filtration behaviors at both macro-scale and nano-scale have been discussed respectively.

Firstly, the applied ultrasound did not affect the internal structure of the concerned suspensions, as revealed by the SAXS profiles. Meanwhile, the filtration performance was significantly improved by this simultaneously applied US: the permeate flux was increased and the limiting-flux filtration scenario was replaced by a consistent-rising one. All these occurred without significant change of membrane selectivity.

Secondly, additional ultrasonic force has led to different phenomena within the accumulated particle for different types of suspensions. During skim milk filtration, a partial disruption of concentrated protein layer was observed. This US-disrupted fouling layer corresponds probably only to the reversible deposit but not the cohesive one, with the applied US of 2 $W.cm^{-2}$. During SNC filtration, the removal of the accumulated particles was very quickly because of a non-connected structure due to low concentration even within the accumulated layer. During CNC filtration, the particles accumulation close to the membrane was really severe: the concentration of CNC particles adjacent to the membrane can increase 10 times more than the feed dispersion. The applied US led to a destabilization of this concentrated layer resulting in an increase of permeate flux.

Finally, US intensity varying from 0.6 $W.cm^{-2}$ to 2.9 $W.cm^{-2}$ seems not to influent the US enhancement factor during skim milk filtration. Two filtration modes have been employed: preventive mode and curative mode. The preventive US application mode is proven promising in milk filtration since it did attenuate significantly the accumulation of proteins during milk filtration: formation of the reversible fouling layer was strongly reduced in this mode. However, it was not quite efficient for CNC filtration under investigated conditions (also within the given filtration duration) since the formation of accumulated layer was still severe. This difference originates from the structure properties (e.g. interaction among particles) of concerned colloidal suspensions, which needs more investigations in the future.

5

Analysis of concentration profiles and modeling approach

This chapter will firstly review the obtained results of this study. A brief comparison between different colloidal suspensions will be given. Then some chosen results will be analyzed in an integrated way: matter accumulation and yield stress chart of concentrated layer in the filtration channel will be calculated with the help of Matlab. At the end, a new approach of modeling has been conducted thanks to the obtainment of concentration profiles of the accumulated particle layers. It takes into account two key factors: permeability and osmotic pressure of concentrated layer. Permeate flux has been predicted and compared with the experimental one to assess the validity of modeling.

1. Review of results in this study

This study focuses on ultrasonic assisted cross-flow ultrafiltration of colloidal suspensions. In order to widen the investigation range and provide an understanding of process and interaction colloid/process as complete as possible, four types of colloids have been used:

- Laponite diserpsions: synthetic clay consisting of disc-shape particles of 1 nm × 30 nm, which form an attractive network containing some micro-sized aggregates. Three dispersions have been studied with different feed concentration with or without tspp. They are denoted as: Lap1-tspp6, Lap0.48-tspp6 and Lap1-tspp0.
- Natural swelling gels: which consist of diocthaedral platelets, organized by repulsive interactions in suspensions. They can exhibit liquid-crystal feature with strong oriental order in suspensions. Two of them have been investigated: SWy-2 T3 and NAu-1 T3.
- Skim milk: a classic colloid consisting of spherical deformable particles with broad size distribution (1 nm-20 µm, the casein micelles with a mean size of 200 nm in diameter), organized by repelling interaction with interparticle free volume. Two feed concentrations have been explored: a standard one (C_o) and a concentrated one ($2*C_o$).
- Nanocrystal suspensions: two types of them have been investigated: 1) starch nanocrystals (SNC), consisting of round-shape crystals, a polydisperse system with unconnected clusters; 2) cellulose nanocrystals (CNC), consisting of rod-like crystals

of 10 nm (thickness) × 270 nm (length), organized by attractive network which can also exhibit liquid-crystal feature.

Tab. 5.1 assembles all of them and demonstrates the key consequence of US application for each suspension.

As defined in chapter 4 Eq.4.1, E_{us} refers to the enhancement factor which is the ratio between the permeate flux obtained in the presence of US and the one obtained without US under the same operating conditions. The common operating conditions are: T = 25±1°C; TMP = $1.1.10^5$ Pa; US: 20 kHz, 2 $W.cm^{-2}$; Qv = 0.2-0.3 $L.min^{-1}$ (0.11-0.16 $m.s^{-1}$). It should be noted that E_{us} depends on ample factors even the operating conditions are fixed:

- US application mode can affect it: for instance, in the case of skim milk, preventive mode gives a E_{us} of 2.5 while that of curative mode is 2.0.
- Operating procedure can also affect it strongly: in the case of Lap0.48-tspp6, E_{us} extracted from Espinasse procedure is only 4.4 while that from TMP-constant procedure (by the way, curative mode) is as 13.5 as high.
- Filtration history also plays its role in performance enhancement by US: in the case of Lap1-tspp6, E_{us} extracted from beginning of filtration is 3.7 while it reaches 10 later. It can be explained by the consequence of particle disaggregation induced by US.

Therefore, in Tab. 5.1, both minimum and maximum of E_{us} are presented to determine the general range of US enhancement factor. The maximums of E_{us} for all the investigated suspensions are displayed in Fig. 5.1 for comparison.

Tab. 5.1 *US effects on investigated suspensions during cross-flow ultrafiltration in this study*

Feed suspension	Structural property		Operating conditions	Eus		US effects at nano-scales
	Morphology	Interaction		Min	Max	
Lap1- tspp6	Disc-like particles of 1 nm × 30 nm	Attractive network, present of micro-sized aggregations	T = 25±1°C; TMP = 1.1.10^5 Pa; US: 20 kHz, 2 W.cm^{-2}; Q_v = 0.2 L.min^{-1} (0.11 m.s^{-1}) for Lap0.48-tspp6 and 0.3 L.min^{-1}(0.16 m.s^{-1}) for the others	3.7	10	Bottom part-targeted layer removal
Lap0.48-tspp6				4.4	13.5	Quick removal of top layer
Lap1- tspp0		Strongly-attractive Network		5.7		No layer change
SWy-2 T3 0.47 % v/v	Diocthaedral platelets of 0.75 nm × 100 nm	Oriented repulsive Network		2	4.2	No layer change
NAu-1 T3 0.40 % v/v	Diocthaedral platelets of 0.76 nm × 350 nm (length) × 54 nm (width)			2.7	6.8	No layer change
SNC 0.3% w/w	Round-shape crystals, mean diameter of 1600 nm, polydisperse	Unconnected clusters		1.2	1.6	Quick layer removal
CNC 0.7% w/w	Rod-like crystals of 10 nm (thickness) × 270 nm (length)	Oriented attractive network		1.5	2.8	Layer disruption, oscillation between layer break-up and reformation
Skim milk Co	Spherical deformable particles with broad size distribution (1 nm-20 µm)	Repelling interaction with interparticle free volume		2.1	2.7	Layer disruption
Skim milk 2*Co				2	2.5	

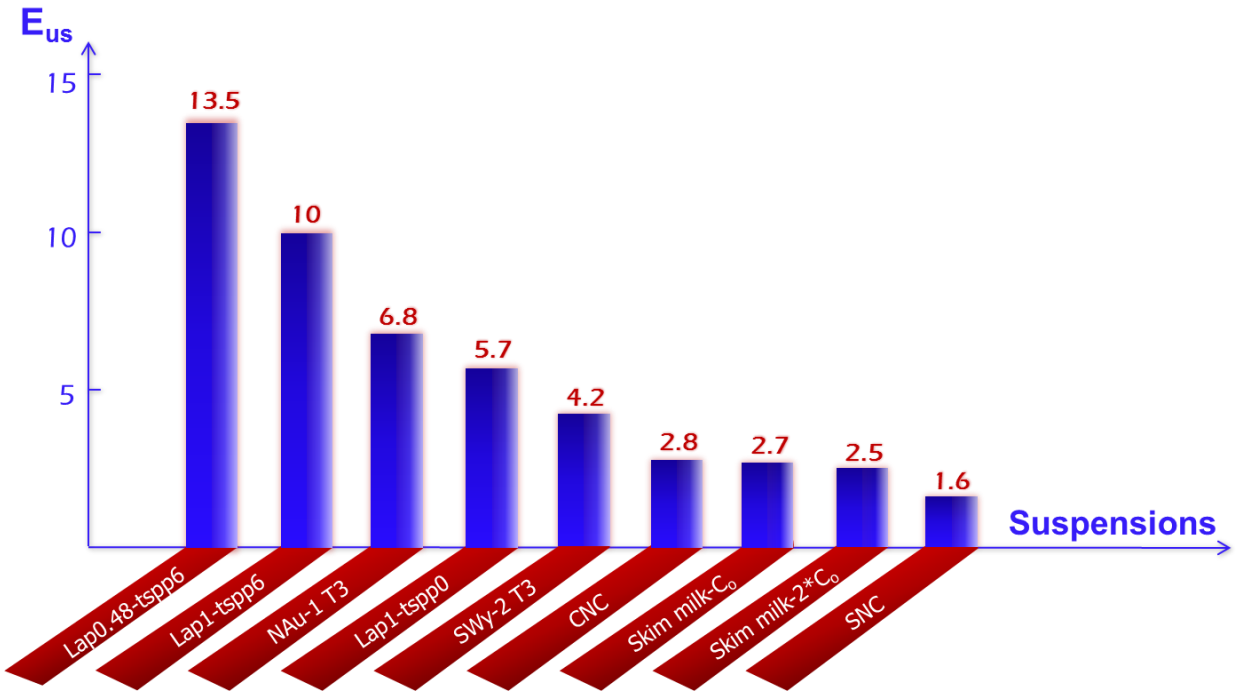

Fig. 5.1 *US enhancement factor E_{US} for all the investigated suspensions in this study*

Depending on different suspensions, E_{US} varies from 1.6 to 13.5, suggesting a great difference of US enhancement. US enhancement factor for SNC is relatively low since the permeate flux decline is not severe for this suspension as discussed in chapter 4 section 2.3. E_{US} of Laponite dispersions without tspp are the highest among them, between 10 and 13.5. This great difference of E_{US} for different suspensions could be explained by different mechanisms related to this concentrated layer. Generally, they can be classified by three groups, as shown in Fig. 5.2. The applied US induced a removal of accumulated particle layer, as in the case of Lap-tspp6 (both Lap1-tspp6 and Lap0.48-tspp6) and SNC; it led to a partial disruption of concentrated layer, as in the case of skim milk and CNC; or no change of concentrated layer was detected by the employed SAXS measurement but a great increase of permeate flux J_v as usual in the case of Lap1-tspp0, SWy-2 T3 and NAu-1 T3.

Based on these results, we speculate two principal phenomena induced by ultrasonication during filtration: *i)* Ultrasonic force induces shear stress by the means of localized high-velocity circulatory flow within the network of accumulated particles, if this shear stress is higher than the yield stress of suspension, disaggregation occurs which leads to a progressive removal of

accumulated layer. This phenomenon is principally observed in the case of an open structural organization of the particles (aggregation of particles due to dominant attractive colloidal forces and/or fractal organization). Otherwise, *ii)* in the case of a denser network of particles pertaining to an accumulation of repulsive particles and/or assembled in an anisotropic way close to membrane, the denser (nanometer-sized) structure of particle network remains unchanged under ultrasonic force which can still induce an additional localized water circulation inside this denser network and will be responsible for the increase of permeate flux.

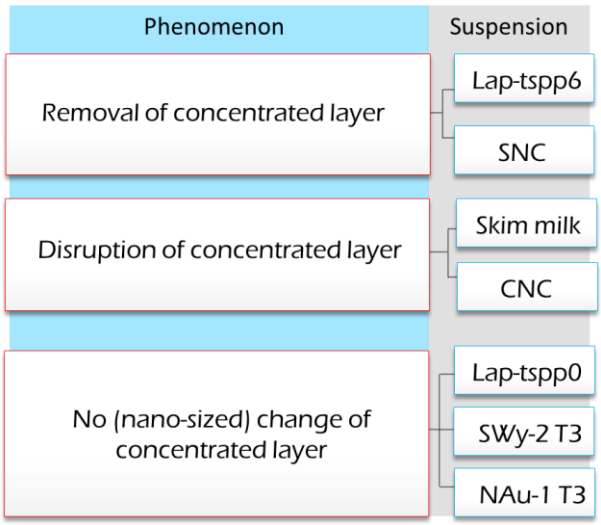

Fig. 5.2 *Key phenomena related to concentrated layer during US assisted cross-flow ultrafiltration for different colloidal suspensions.*

Therefore, representative of each group was chosen devoting to further investigation which will be presented in section 2. The three representatives are: Lap1-tspp6, skim milk and Lap1-tspp0.

2. Global analysis of results

This study involves several suspensions whose physico-chemical properties are different. Concentration profiles of filtrated suspensions at steady state and at transition have been deeply discussed in previous chapters. Interesting results have been obtained, but most of them present the scenarios of middle window (x = 50 mm). In order to provide a global version of process performance so as to reveal the general mechanism of concerned process, results obtained by SAXS measurements have been further analyzed by integrated calculations. Matlab was used to carry out the calculations. We are interested in matter accumulation as well as the yield stresses of different positions of concentrated particle layer. Some theoretical models have then been taken into account to predict the local permeate flux along the membrane surface. In this section, Laponite dispersions and skim milk are chosen since they represent different colloidal families which exhibit disparate filtration performance in ultrasonic-assisted cross-flow ultrafiltration, as mentioned before.

SAXS measurements provide the concentration information of suspension at three positions (vectors) along the membrane (x axis): at inlet (x = 7 mm), at the middle (x = 50 mm) and at outlet (x = 93 mm) of the filtration cell. The minimum distance above the membrane surface for obtaining exploitable SAXS data is 20 µm. Since exponential law of concentration profiles have been expected (as interpreted in chapter 3 section 1.5), an extrapolation by exponential law was firstly executed to complete the concentration profiles, as shown in Fig. 5.3. It appears that concentration at membrane surface stays the same at the downstream section (from x = 50 to 93 mm), while layer thickness increases along x axis. This phenomenon can be better visualized in Fig. 5.4a.

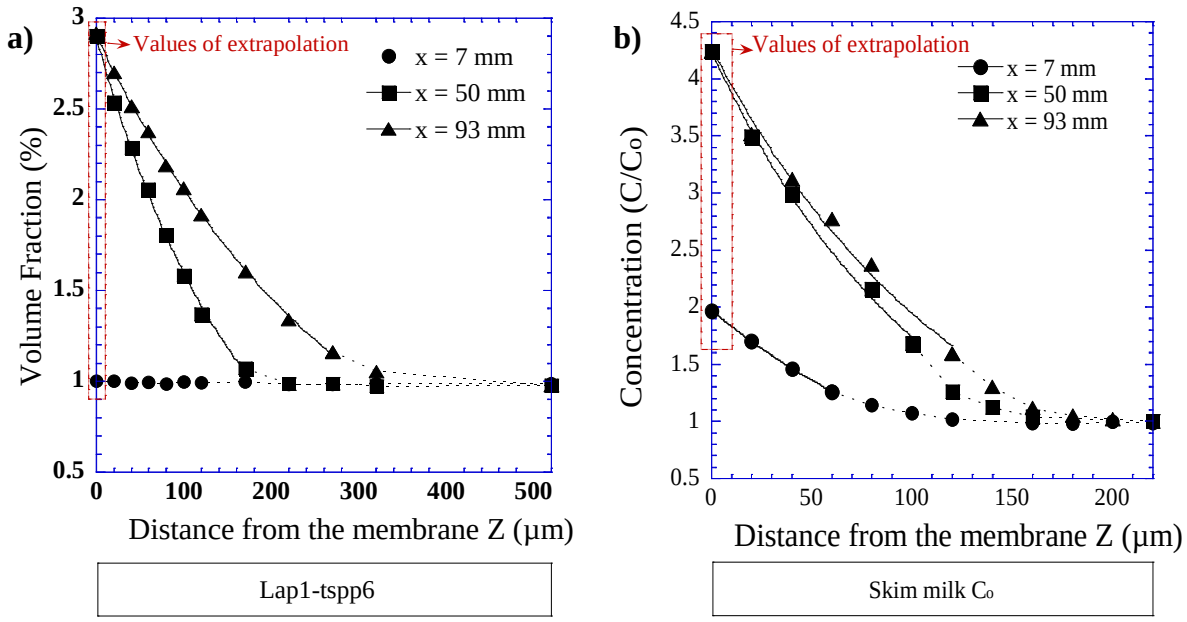

Fig. 5.3 *Examples of data extrapolation by exponential law for the concentration profiles upstream, in the middle and downstream of filtration channel. a)Lap1-tsp6, data extracted from Fig.3.16 of chapter 3: T = 25±1°C, TMP = 1.1×10^5 Pa, Q_v = 0.3 L.min^{-1}, without US; b) Skim milk (C = C_o), data extracted from Fig.4.9 of chapter 4 (step 2): T = 25±1°C, TMP = 1.1×10^5 Pa, Q_v = 0.3 L.min^{-1}, without US. Solid lines correspond to exponential fits.*

In order to execute the desired analysis, an appropriate interpolation is required. In this study, a linear interpolation was applied and a matrix of 51×86 was constituted with the help of Matlab. Fig. 5.4a shows an example of the obtained chart of filtration channel (beyond z = 1000 µm) after these operations. Every single mesh of this figure corresponds to an infinitesimal box arising from the discretization of concentration profile. Then, for certain calculations such as matter accumulation or prediction of permeate flux, only concentrated layer was taken into account, bulk part was thus excluded. As shown in Fig. 5.4b, instead of feed concentration (ϕ = 1% in this case), a value of zero was given to the bulk part. This operation allows not only excluding the effect of bulk part in the concerned calculations but also defining the thickness of concentrated layer and boundary layer of integrations presented later in this chapter. These two charts are plotted for all the investigated situations , they are the bases of calculations in this section.

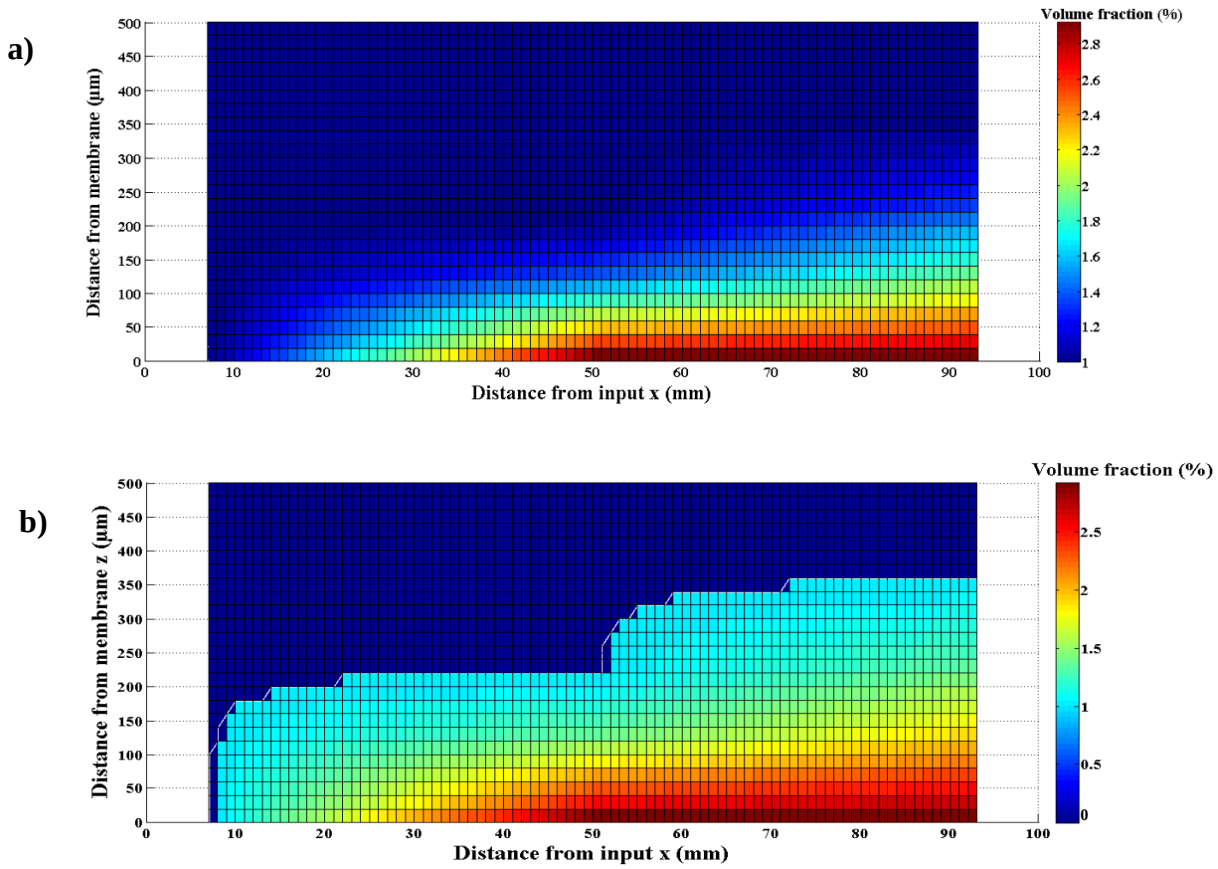

Fig. 5.4 *Example of filtration channel charts. a) after data extrapolation and interpolation; b) after a further exclusion of bulk part. Data source: Lap1-tspp6, extracted from Fig.3.16 of chapter 3: T = 25±1°C, TMP = 1.1×10^5 Pa, Q_v = 0.3 L.min^{-1}, without US.*

2.1 Matter accumulation of concentrated layer

It is well known and it has already been illustrated in previous chapters that particles accumulate on the membrane surface during filtration. We are interested in therefore what is the quantity of matter accumulation for different suspensions. Concentration evolution and thickness of accumulated layer have been fully discussed before. They provide us information about porosity of the concentrated layer. In the simplest case (e.g. Laponite dispersions), volume fraction profiles reflect directly porosity profiles of the same layer. However, they can not

provide a global version of how severe the matter accumulation is especially when different suspensions are filtrated or feed concentration changes.

In section 2.1, mass of the accumulated layer will be calculated from the concentration profiles in order to illustrate the coherence between matter accumulation and filtration performance.

2.1.1 Method of calculation

As described before, a matrix was established providing the concentration information of mapping points (particle density of infinitesimal boxes) within the filtration cell as function of x (along the membrane) and z (above the membrane). A triple integral of these infinitesimal boxes of concentration ($g.m^{-3}$) over a three-dimensional region in xyz-space arises in the computation of mass, as denoted:

$$\text{mass} = \iiint C(x,y,z)\,dx\,dy\,dz \qquad \textit{Eq. 5.1}$$

Where C(x,y,z) is suspension concentration which is as function of spatial vectors (x, y, z), as illustrated in Fig. 5.5.

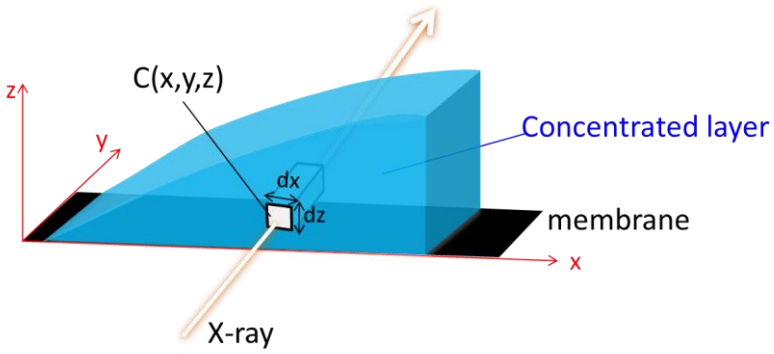

Fig. 5.5 *Schematic of concentrated layer on the membrane surface*

This integral was achieved step by step. Firstly, a numerical integral by trapezoidal rule of C(x,y,z) in the concentration-z plane was carried out, as exampled by Fig. 5.6a. The integration region is bounded by the curve C(z) at given x (x = 50 mm in Fig. 5.6a), the z-axis and two vertical lines z = 20 µm (the closest positon from the membrane) and the first position where the concentration begins to be higher than feed suspension (z = 220 µm in Fig. 5.6a). The second vertical boundary line (z = 220 µm in Fig. 5.6a) is also considered as the beginning of the concentrated layer, which defines its thickness. Accumulated mass of each infinitesimal column was then calculated by multiplying $\int_0^{\delta} c(x,y,z)dz$ with dx and Δy, with an assumption that there is no evolution of concentration along the y-axis. So far, matter accumulation can be plotted along x-axis. The mass of each infinitesimal column was then summed up to obtain the total mass of investigating concentrated layer.

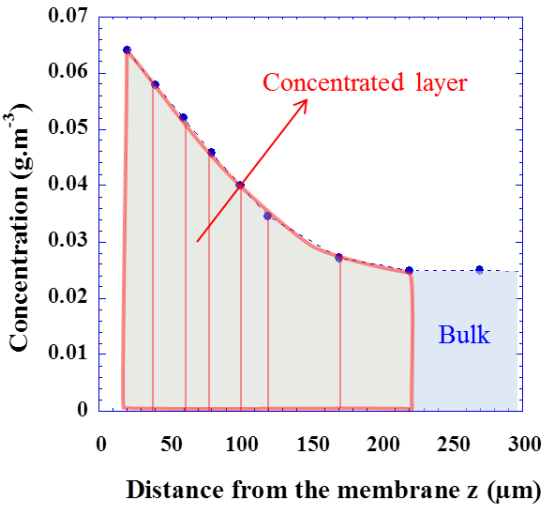

$$\int_0^{\delta=220\ \mu m} C(x,y,z)dz,\ at\ x = 50\ mm$$

Fig. 5.6 *Example of numerical integrals executed in this chapter in order to compute matter accumulation of concentrated layer.*

2.1.2 Results

All the results presented in this section are sourced from chapter 3 (Laponite) and 4 (skim milk) where their concentration profiles have been fully discussed. Matter accumulation of Laponite dispersions and skim milk will be discussed in the first place followed by a summary of total mass accumulation/permeate flux dependence.

2.1.2.1 Laponite dispersions

Sourced from chapter 3 section 1.5.1.4 (Lap1-tspp6) and section 1.5.3 (Lap1-tspp0), Fig. 5.7 shows the matter accumulation of two Laponite dispersions at steady state during filtration with and without US under the same operating conditions. Figure a and b demonstrate the difference between Lap1-tspp6 and Lap1-tspp0 without US. As expected, matter accumulation is much more severe during filtration of Lap1-tspp0 than Lap1-tspp6. With the same feed concentration, total matter accumulation increases with a factor of 3.7. Moreover, it appears that particles accumulate more severely in the middle of channel rather than downstream, which is not consistent with theoretical prediction. No definitive conclusion can be drawn till it is verified by more measured points between x = 50 and 93 mm.

Under US, accumulated particles were totally swept upstream and were reduced downstream for Lap1-tspp6. US results in a total matter accumulation reduction of more than 50 % for Lap1-tspp6 while it did not alleviate matter accumulation in the case of Lap1-tspp0 at all.

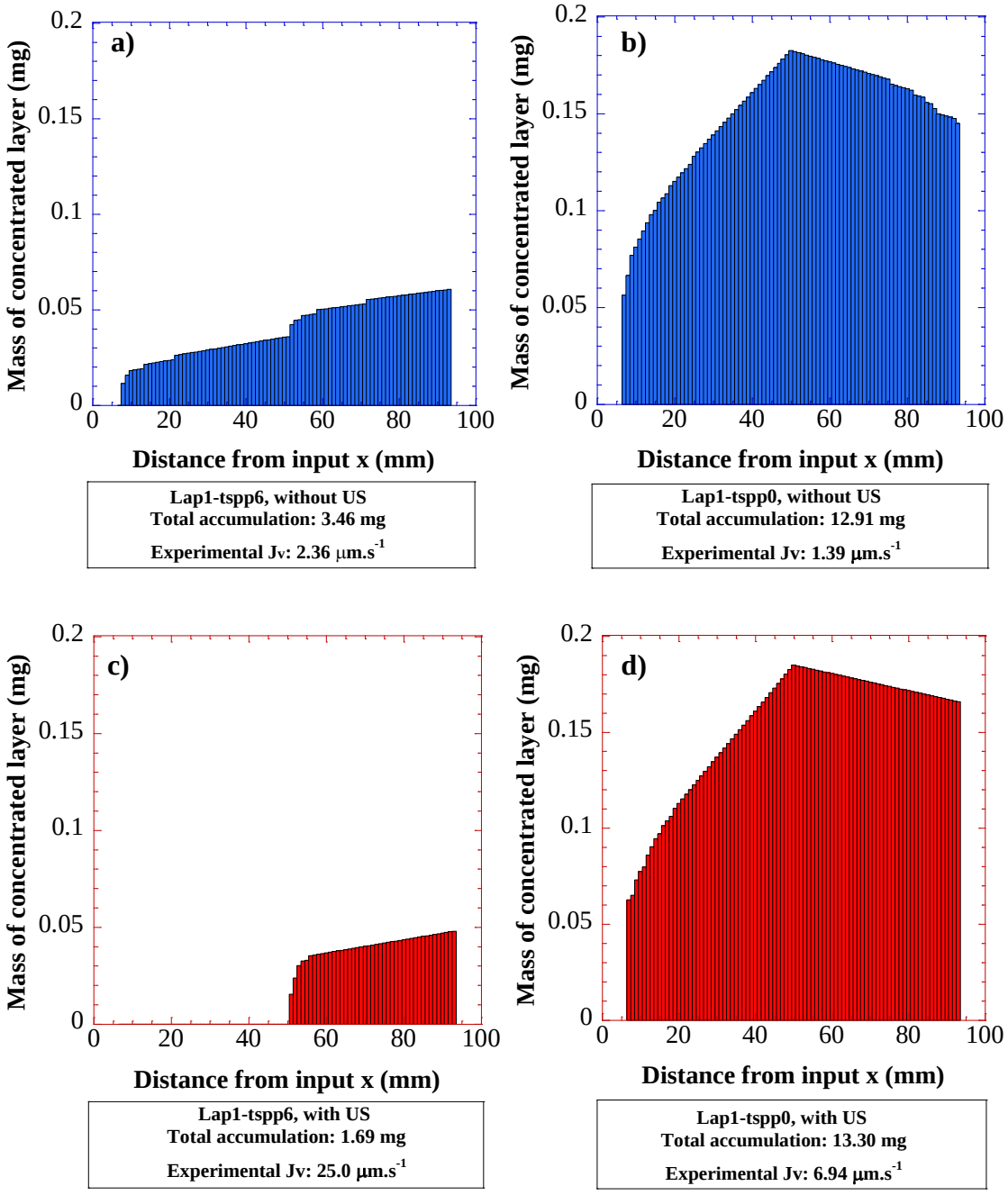

Fig. 5.7 *Matter accumulation of concentrated layer along x axis during filtration of Laponite dispersions. T = 25±1°C, TMP = 1.1×10^5 Pa, Q_v = 0.3 L.min^{-1}. US: 20 kHz, 2 W.cm^{-2}.*

2.1.2.2 Skim milk

Sourced from chapter 4 section 1.5, Fig. 5.8 and Fig. 5.9 demonstrate respectively the mass of concentrated layer along x axis for skim milk suspensions at feed concentration of C_o and $2*C_o$. They are presented the same way as section 1.5 of chapter 4: by operational steps.

During filtration of skim milk at C_o (Fig. 5.8), reduction of cross-flow rate from 0.3 to 0.1 $L.min^{-1}$ resulted in a double mass accumulation, from step 1 to 2 (see Figure a and b). It seems to have a good coherence between mass accumulation and permeate flux J_v since J_v dropped off by 2 times from step 1 to 2. This correlation will be discussed later in this section. Moreover, the additional particles were attributed rather downstream than upstream, which can be observed clearly by comparing these two curves (Figure d). It implies that the axial dependent particle layer was respected all the time during these two steps of filtration. US was applied at step 3, as discussed in chapter 4, it could not remove this concentrated layer but it brought about a reduction of matter accumulation (see Figure b and c). We claim that it is difficult to remove the accumulated layer once it is formed during filtration of skim milk. In addition, total mass accumulation of step 3 is slightly lower than that of step 1 (2.09 VS 1.82 mg), which corresponds to a slightly lower permeate flux J_v (5.2 VS 4.5 $L.h^{-1}.m^{-2}$). Again, this correlation will be discussed later in this section. At step 4, US was switched off, the operating conditions were the same as step 2. As shown in Figure d, mass profile is also the same as step 2, which suggests that effect of US was instantaneous in this situation.

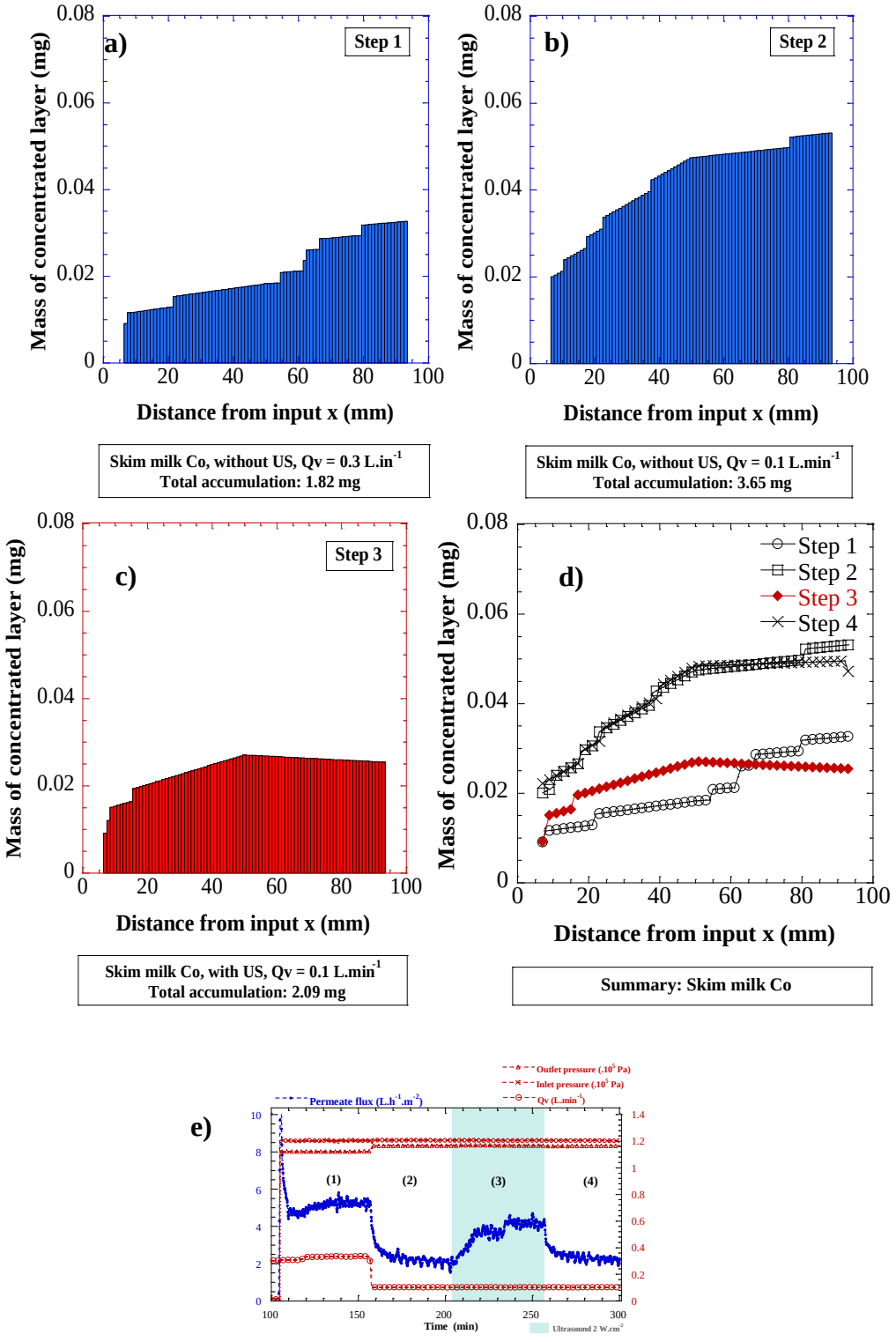

Fig. 5.8 *Matter accumulation of concentrated layer along x axis during filtration of skim milk suspensions (feed: C_o). T = 25±1°C, TMP = 1.1×10^5 Pa. US: 20 kHz, 2 W.cm^{-2}. a-d: mass profiles; e: reminder of permeate flux J_v curve for step 1 to 4.*

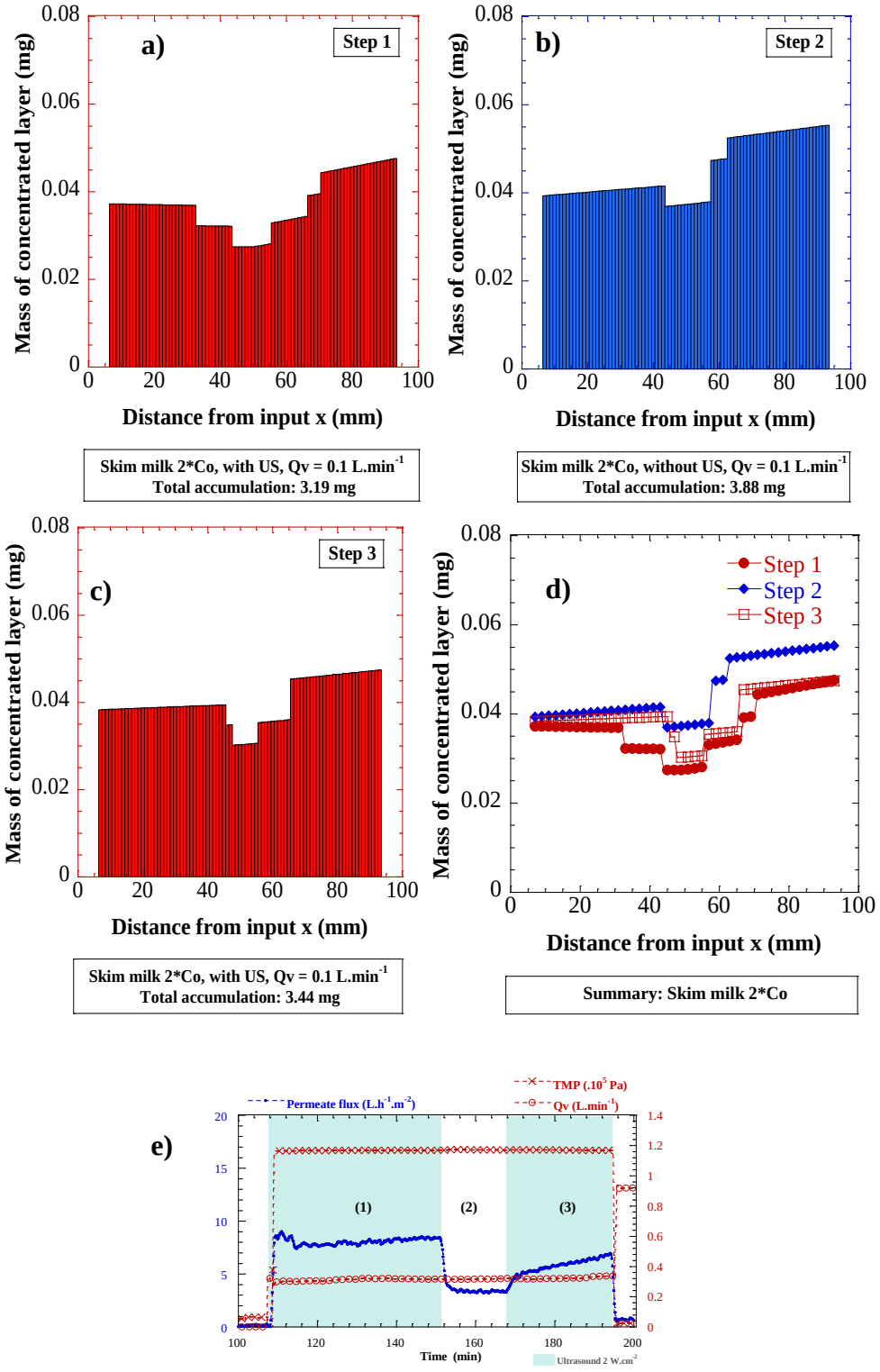

Fig. 5.9 *Matter accumulation of concentrated layer along x axis during filtration of skim milk suspensions (feed: 2*C_o). T = 25±1°C, TMP = 1.1×10^5 Pa. US: 20 kHz, 2 W.cm^{-2}. a-d: mass profiles; e: reminder of permeate flux J_v curve for step 1 to 3.*

As for skim milk at 2*Co (Fig. 5.9), US was applied before filtration (preventive mode). At step 1, the concentrated layer was thin and the concentration did not ‘‘climb’’ high at x = 50 mm, as shown in chapter 4. However, profiles of both upstream (x = 7 mm) and downstream (x = 93 mm) were slightly thicker and more concentrated than midstream. Consequently, a U-shape mass profile is revealed, as illustrated in figure a. Similar form of concentration profile has already been observed during filtration of SNC (chapter 4 section 2.3.2). It could be related to the inhomogeneity of ultrasonic activity within the filtration channel. Moreover, even though the concentration profile didn’t ‘‘climb’’, matter accumulation was relatively severe simply because of a more concentrated feed.

At step 2, US was switched off, matter accumulation was indeed more severe, somehow, less severe than expected (see Fig. 5.9d). From step 1 to 2, J_v declines by 60 % (from 8.3 to 3.3 $L.h^{-1}.m^{-2}$) while accumulated mass increases only by 20 % (from 3.19 to 3.88 mg). Furthermore, mass profile still exhibits U-shape form as step 1 even without US which does not respect the axial dependent particle layer as predicted by several groups (Bhattacharjee *et al.*, 1999; Davis and Leighton, 1987; Elimelech and Bhattacharjee, 1998; Romero and Davis, 1988).

Now considering all the three mass profiles presented in Fig. 5.9, it seems that the U-shape form was a ‘‘solid base’’ formed during step 1. The operation of step 2 filled it with more particles and then that of step 3 dig them out again. This phenomenon implies that one part of the accumulated protein layer is stagnant in this condition. It consolidates the remarks we give in chapter 4 that there is a cohesive layer on the membrane surface and increase of feed concentration may strengthen this layer in an important extent.

2.1.2.3 Correlation between matter accumulation and permeate flux

As announced before, an attempt to find out the correlation between total accumulated mass and permeate flux J_v is presented in Fig. 5.10. In figure a, all the investigated points are presented: two families of suspensions, under different operation conditions. There is no master fit that can correlates all the investigated points, especially, the points of Laponite are dispersed.

Figure b then shows the points excluding those of Laponite under US. It illustrates that there is indeed correlation between these two factors for each suspension. However, a general fit can't be found for skim milk even only feed concentration changes. To sum up, matter accumulation can't solely determine the permeate flux in a cross-flow filtration process for colloidal suspensions. Nevertheless, it is not surprising since more other factors such as permeability k_p and osmotic pressure Π of accumulated layer can also play an important role in this process. It will further be discussed in this chapter.

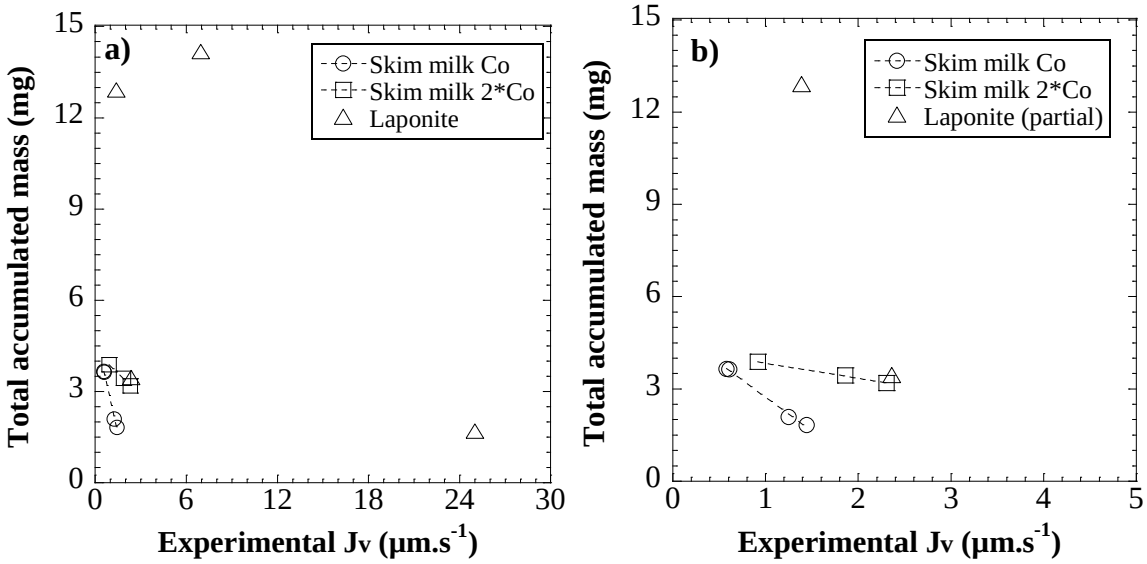

Fig. 5.10 *Correlation between total accumulated mass and averaged permeate flux for different suspensions. Figure a presents all the investigated points and in b the points of Laponite dispersion under US is excluded.*

2.2 Flow property of concentrated layer

In US assisted cross-flow filtration process, colloidal suspensions are constantly subjected to shear stress, thus their flow properties are crucial for understanding their filtration performance. Such examples can be found in previous chapters as in the case of Laponite dispersions with or without tspp.

As discussed in chapter 3, flow properties of Lap-tspp0 and Lap-tspp6 are extremely different arising from the mechanical resistance of particle network. In addition, their yield

stress/volume fraction dependences have been investigated (see chapter 3, Fig.3.4). It is therefore interesting to determine yield stress charts within the filtration channel for both of them to illustrate what happened during this process.

Based upon the concentration profiles along the membrane (shown in Fig. 5.4), yield stress charts were plotted in the light of yield stress/volume fraction dependence (chapter 3, Fig.3.4). Fig. 5.11 shows the yield stress charts of Lap1-tspp6 (a) and Lap1-tspp0 (b) within the filtration channel when US was not applied.

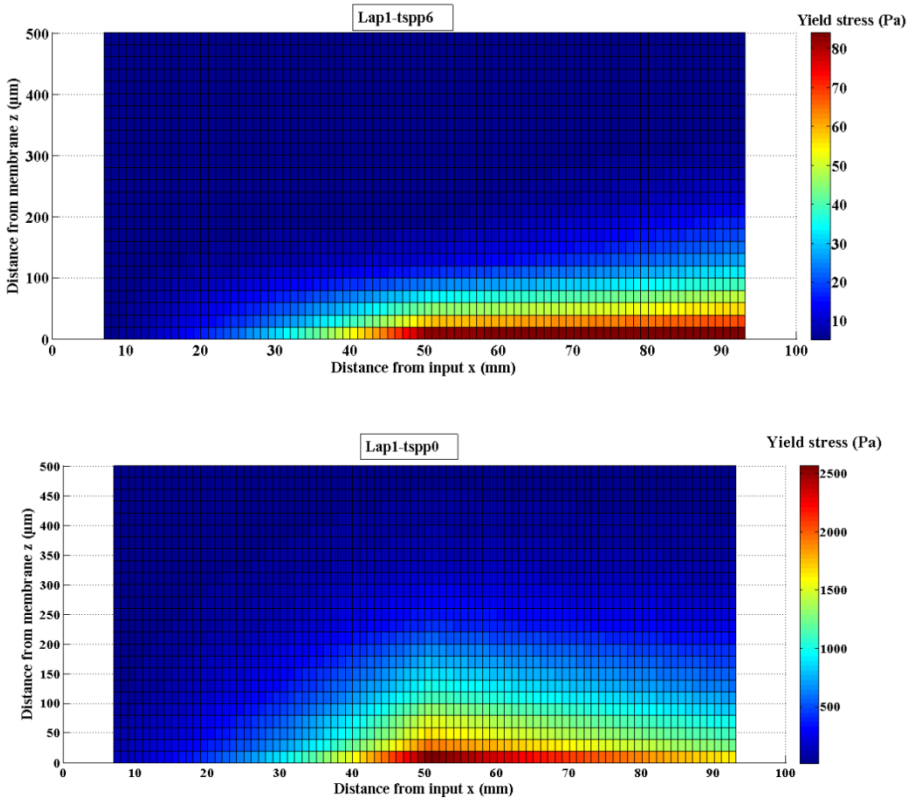

Fig. 5.11 *Charts of yield stress during filtration of Laponite dispersions. a) Lap1-tspp6, b) Lap1-tspp0. Source from chapter 3 section 1.5. T = 25±1°C, TMP = 1.1×10^5 Pa, Q_v = 0.3 L.min^{-1}.*

Yield stress of concentrated layer does not exceed 100 Pa for Lap1-tspp6 while it can reach around 2500 Pa maximum for Lap1-tspp0. Moreover, a yield stress of Laponite dispersion is marked in the investigation of its flow properties (chapter 3, section 1.2): 100 Pa, beyond which the applied US can hardly destroy its mechanical network. These two charts confirm the

speculation given in chapter 3: gel consistency of concentrated Lap1-tspp0 was so high that the shear stress induced by US was incapable to break down its network, while yield stress of concentrated Lap1-tspp6 was within the capacity of the applied US so that its network was broken down.

Flow property may also explain the quick removal of certain part of concentrated layer by US in the case of Lap0.48-tspp6 (chapter 3, section 1.5.2) and SNC (chapter 4, section 2.3.2). Absence of yield stress at the range of ϕ = [0.48, 1.00] %, the top part of concentrated layer of Laponite dispersion can flow easily under additional US field, which results in the quick removal of involved part in the case of Lap0.48-tspp6. Similarly, the whole concentrated layer (at least the measurable one) of SNC was in the shear-thinning fluid range without yield stress, thus the quick removal occurred under US.

However, as discussed in chapter 4 section 1.5, flow property of concentrated layer has difficulty to explain what happened in the case of skim milk based upon present results. Though situated in the shear-thinning fluid range, the concentrated layer resisted against the ultrasonic force. To clarify this situation, it requires more data from *in-situ* measurements, such as the concentration at z = 0 µm (membrane surface) and real flow property of concentrated layer during filtration.

2.3 Prediction of permeate flux along the membrane

On the basis of mass transfer and solvent transfer balances, modeling of filtration process has been studied since two decades. However, for cross-flow filtration, the calculation cycles are often met with numerous hypotheses and iteration are required to obtain desired values such as concentration profiles or local permeate flux along x axis. Our results can greatly facilitate the modeling. In this section, an attempt to predict permeate flux along the membrane will be presented.

2.3.1 Theory

Basic balance of solute transfer between convection and diffusion in a polarized layer is described in Eq.1.5 in chapter 1. For a fully retentive membrane it can be rewritten as

$$J(x)C - D(C)\frac{dC}{dz} = 0 \text{ or } J(x)\phi - D(\phi)\frac{d\phi}{dz} = 0 \qquad \textit{Eq. 5.2}$$

For cross-flow filtration, a second integral mass balance for the polarized layer, relating the axial (along x direction) and transverse (along z direction) convection of the solute can be written as (Elimelech and Bhattacharjee, 1998; Romero and Davis, 1988; Song and Elimelech, 1995):

$$\int_0^{\delta} u(x,z)(\phi - \phi_o)dz = \int_0^{x} J(x)\phi_o dx \qquad \textit{Eq. 5.3}$$

Where u(x,z) is the local axial velocity in the given position of channel ($m.s^{-1}$). δ is the thickness of concentrated layer (m), and ϕ_o is feed volume fraction. This equation states that, at steady state, the volume rate of particles per unit filter width flowing across the plane of given x in the concentrated layer is equal to the total volume of particles which have been deposited onto the layer everywhere upstream of x.

In addition, solvent transfer, described by Darcy's law, is also very important for modelling since it directly relates J to the osmotic pressure Π_m at the membrane surface:

$$J(x) = \frac{TMP(x) - \Pi_m(x)}{\eta R_m} \qquad \textit{Eq. 5.4}$$

Where η is the dynamic viscosity of the solvent. It should be emphasized that the permeate flux J(x) in Eq. 5.2, Eq. 5.3 and Eq. 5.4 is the local permeate flux in the filtration channel and will vary along the axial direction.

Eq. 5.2, Eq. 5.3 and Eq. 5.4 are the keys for modelling cross-flow filtration of colloidal suspensions. Iterations are then required to obtain the predicted values for certain input factors. Here highlights the great advantage of our results: with our obtained concentration profiles, iteration is no longer necessary and we can verify Eq. 5.2, Eq. 5.3 and Eq. 5.4 one by one. To reach such goal, an appropriate estimation of the diffusion coefficient D and axial velocity u(x,z) is necessary.

In literature, stokes-Einstein equation and shear-induced migration model are the major considerations for estimating D. Stokes-Einstein law links the diffusion coefficient to the osmotic pressure $\Pi(\phi)$, and to the hydrodynamic coefficient $K_h(\phi)$. It has been used in the modelling by groups of Bacchin (2002a and b), Bowen (2000; 2007) and Elimelech (1998). Shear-induced migration model is based on experimental observations for suspensions of rigid spheres which links the diffusion coefficient to the local shear rate $\dot{\gamma}$ and particle volume fraction ϕ. It involves the modelling works of groups of Davis (Romero and Davis, 1988) and Kromkamp (2007).

As for u(x,z), assumptions are always taken in modelling. Common assumption that can be found in literature: u stays constant at x axis and $u(z) = \dot{\gamma}z$. Bacchin *et al*. (2002) proposed an estimation with more considerations such as the friction dependence and viscosity dependence of u, it still needs to be verified by real velocity profile in the channel for specific colloidal suspensions (e.g. by Particle Image Velocimetry).

Since there is no convincible assumption of u(x,z) yet in literature, prediction of permeate flux along the membrane will only take into account Eq. 5.2 and Eq. 5.4. Future investigation will integrate Eq. 5.3 once the real velocity profile is measured.

2.3.2 Modeling

In this study, diffusion coefficient D will be estimated by Stokes-Einstein equation:

$$D(\phi) = D_B \frac{K_h(\phi)}{S(\phi)} \qquad \textbf{\textit{Eq. 5.5}}$$

where D_B is the dilute-limit value of the Brownian diffusion coefficient, which may be estimated by

$$D_B = \frac{kT}{6\pi\eta a_p} \qquad \textbf{\textit{Eq. 5.6}}$$

$S(\phi)$ is the thermodynamic coefficient. Eq. 5.5 is valid over the entire range of volume fraction. The thermodynamic coefficient may be determined from the osmotic pressure, $\Pi(\phi)$, which gives us:

$$\frac{1}{S(\phi)} = \left[\frac{4\pi {a_p}^3}{3kT}\frac{d\Pi(\phi)}{d\phi}\right] \qquad \textit{Eq. 5.7}$$

With a_p hydrodynamic particle radius (m), k Bolzmann constant ($J.K^{-1}$), T temperature (K).

Combining Eq. 5.5, Eq. 5.6 and Eq. 5.7, we can obtain:

$$D(\phi) = \frac{2{a_p}^2}{9\eta} K_h(\phi)\frac{d\Pi(\phi)}{d\phi} \qquad \textit{Eq. 5.8}$$

In this equation, $K_h(\phi)$ can be calculated for specific suspensions, e.g. for completely disordered hard spheres, is has been estimated by Batchelor (1972). Recent work of Bouchoux inspires us that like the deposit, it could also exist a permeability k_p for the polarized layer (Bouchoux *et al.*, 2013). Then following relationship between $k_p(\phi)$ and $K_h(\phi)$ can be used (Zick and Homsy, 1982):

$$k_p(\phi) = \frac{2{a_p}^2}{9}\frac{K_h(\phi)}{\phi} \qquad \textit{Eq. 5.9}$$

Using Eq. 5.8 and Eq. 5.9, Eq. 5.2 can be written as:

$$J(x)\phi dz = \frac{k_p(\phi)\phi}{\eta} d\Pi(\phi) \qquad \textit{Eq. 5.10}$$

Integration of this equation on the thickness δ of the concentrated layer then leads to:

$$J(x)\int_0^{\delta} \phi dz = \int_{\Pi_b}^{\Pi_m} \frac{k_p(\phi)\phi}{\eta} d\Pi(\phi) \qquad \textit{Eq. 5.11a}$$

It can also be written as:

$$J(x)\int_0^{\delta} c dz = \int_{\Pi_b}^{\Pi_m} \frac{k_p(c)c}{\eta} d\Pi(c) \qquad \textit{Eq. 5.11b}$$

This equation is similar to that proposed by Bouchoux *et al*. who considered both the polarized layer and deposit deduced by Darcy's law (Bouchoux *et al*., 2013). According to them, the osmotic pressure Π of a colloidal suspension reflects the balance of all interactions in the system. The permeability k_p measures the resistance of the system to the hydraulic flow that passes through it. Their evolutions with concentration of involved colloid during filtration can describe performance of this process. Moreover, $k_p(c \text{ or } \phi)$ and $\Pi(c \text{ or } \phi)$ can both be

determined by experiments for diverse suspensions, avoiding any inappropriate use of theoretical laws or assumptions. It highlights the advantage of this interpretation of mass transfer balance. Eq. 5.11 is therefore the key equation used in the present section to obtain J(x) for any infinitesimal boxes (columns) in Fig. 5.4. All the integral terms are estimated through graphical method.

In the case that no concentrated layer covers the membrane, Eq. 5.4 is used to estimate the locale permeate flux J(x).

2.3.3 Required laws

The laws of $k_p(c \text{ or } \phi)$ and $\Pi(c \text{ or } \phi)$ for investigated suspensions are required to fulfill the modeling. In this section, Laponite dispersions and skim milk are chosen since they represent different colloidal families which exhibit disparate filtration performance in ultrasonic-assisted cross-flow ultrafiltration.

Permeability of Laponite dispersions has been investigated by Lelièvre (2005) with a specific designed device. Ranging from ϕ = 7 to 13 %, he claimed that the permeability of Laponite deposit did not change with the addition of tspp especially for the lower concentration range. Therefore, a common law was considered for the Laponite dispersions both with and without tspp in our modeling:

$$k_p(\phi) = 6.10^{-21}.\phi^{-2.08} \qquad \textit{Eq. 5.12}$$

Osmotic pressure of Laponite dispersions has been previously investigated by our group using the method well described by Martin (2006). Again, for the same range of concentration (ϕ = 2 to 10%), difference between two types of dispersions (with or without tspp) can be neglected considering the experimental error. In fact, osmotic pressure of Laponite dispersions have been deeply investigated by Lelièvre. He claims that Π depends greatly on concentration but the dependence of Π and addition of tspp is low (Lelièvre, 2005). Consequently, a common law for both dispersions was then considered in our modeling:

$$\Pi(\phi) = 1.11.10^{7}.\phi^{2.26} \qquad \textit{Eq. 5.13}$$

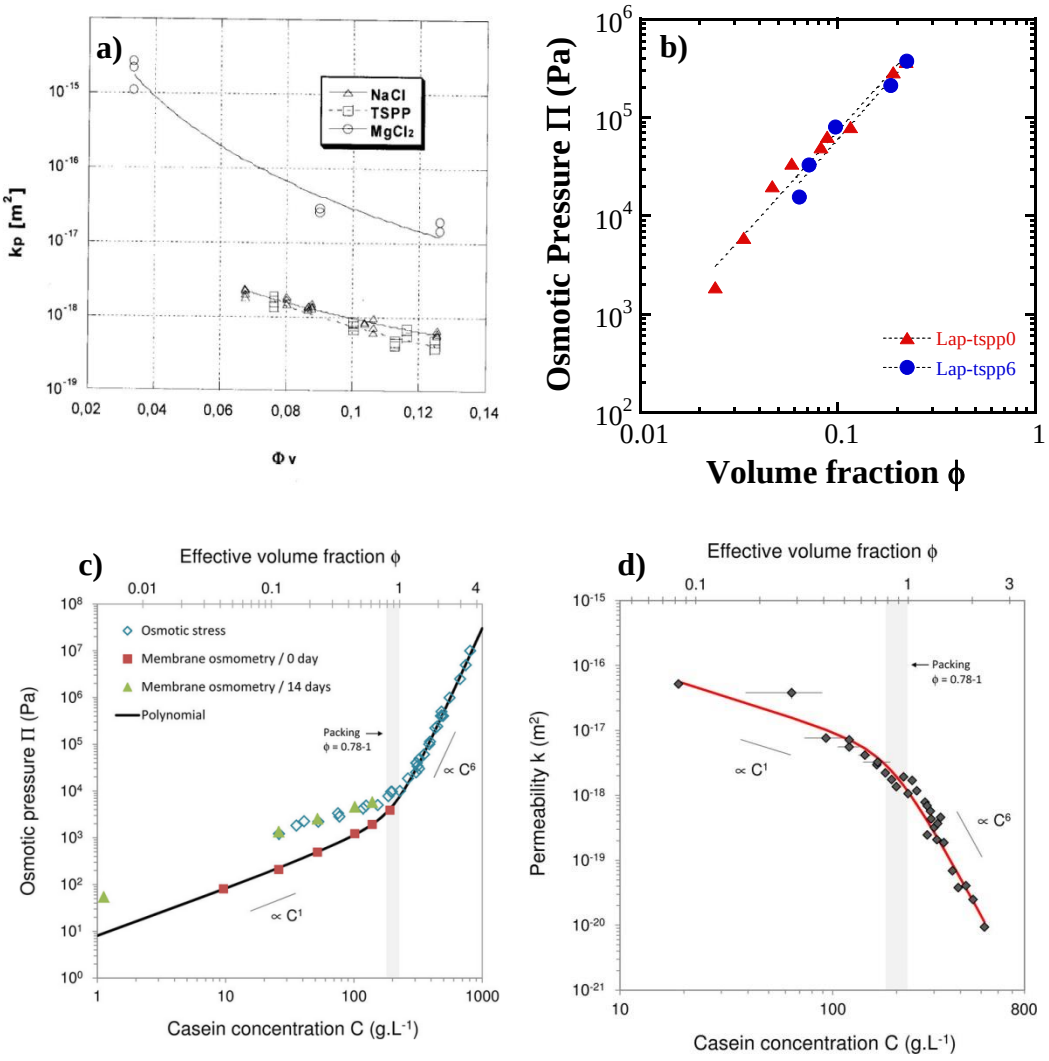

Fig. 5.12 *Laws of permeability and osmotic pressure for Laponite dispersions and casein micelle suspension. a) permeability law of Laponite, captured from (Lelièvre, 2005); b) osmotic pressure law of Laponite; c) permeability law of casein micelle suspension, captured from (Bouchoux et al., 2013); d) osmotic pressure law of casein micelle suspension, captured from (Bouchoux et al., 2013).*

As for skim milk, concentration dependence laws of these two factors are reported in recent work of Bouchoux (2013) for casein micelle suspension (Fig. 5.12 c and d). However, the laws they proposed did not provide us a good prediction of J(x) probably because the empirical laws are dominated by high concentration regime and don't fit well in low concentration regime

where our results are positioned. Therefore, we refit their data in low concentration regime and we obtained:

$$k_p(C) = 5.10^{-14}.C^{-1.47}, C < 200\ g.L^{-1} \quad \textit{Eq. 5.14}$$

$$\Pi(C) = 2.57.C^{1.25}, C < 200\ g.L^{-1} \quad \textit{Eq. 5.15}$$

2.3.4 Results

On the basis of the discretized concentration profiles of each case (example described in Fig. 5.4), model prediction of local permeate flux along x axis J(x) was calculated with Eq. 5.4 and Eq. 5.11 taking into account principally two factors: permeability k_p and osmotic pressure Π of the concentrated layer. This section will present the results from modeling for two types of colloids: Laponite and skim milk. Modeling will be then assessed by comparing the values of modeled permeate flux with experimental ones.

2.3.4.1 Laponite dispersions

1) Without US

Fig. 5.13 presents the permeate flux profiles along the membrane at steady state during filtration of Laponite dispersions without US. Both of them exhibit an x axial dependence: higher permeate flux near the inlet than outlet of the channel. It is consistent with the correspondent concentration profiles and mass profiles illustrated before. Again, difference between Lap1-tspp0 and Lap1-tspp6 is revealed: better performance for Lap1-tspp6 with higher average flux (shown in affiliated table). The average of local permeate flux should match the experimental J_v in ideal situation. This issue will be specifically discussed later in this section.

2) With US

In Fig. 5.14, permeate flux profiles of steady state during filtration under US are demonstrated. For Lap1-tspp6, half of the membrane was not covered with particle layer under US; J(x) is therefore very high. It results in a great increase of average flux (see affiliated table).

For Lap1-tspp0, permeate flux profile does not change, which is not surprising since its concentration and mass profiles are both unchanged under US.

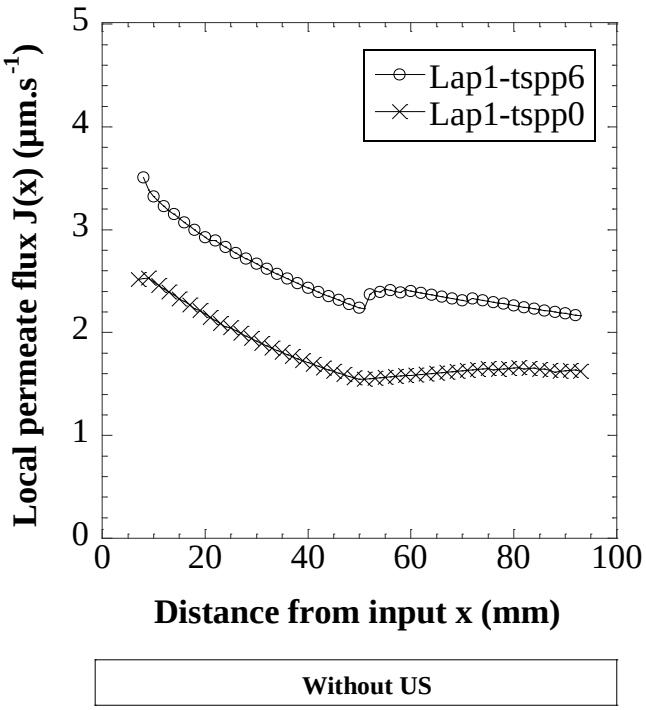

Affiliated table: average flux

Dispersion	US	Modeled average flux J_v (µm.s^{-1})	Experimental average flux J_v (µm.s^{-1})
Lap1-tspp6	OFF	2.97	2.36
Lap1-tspp0		1.81	1.39

Fig. 5.13 *Permeate flux profile along the membrane for Laponite dispersions (without US). Source from chapter 3 section 1.5. T = 25±1°C, TMP = 1.1×10^5 Pa, Q_v = 0.3 L.min^{-1}.*

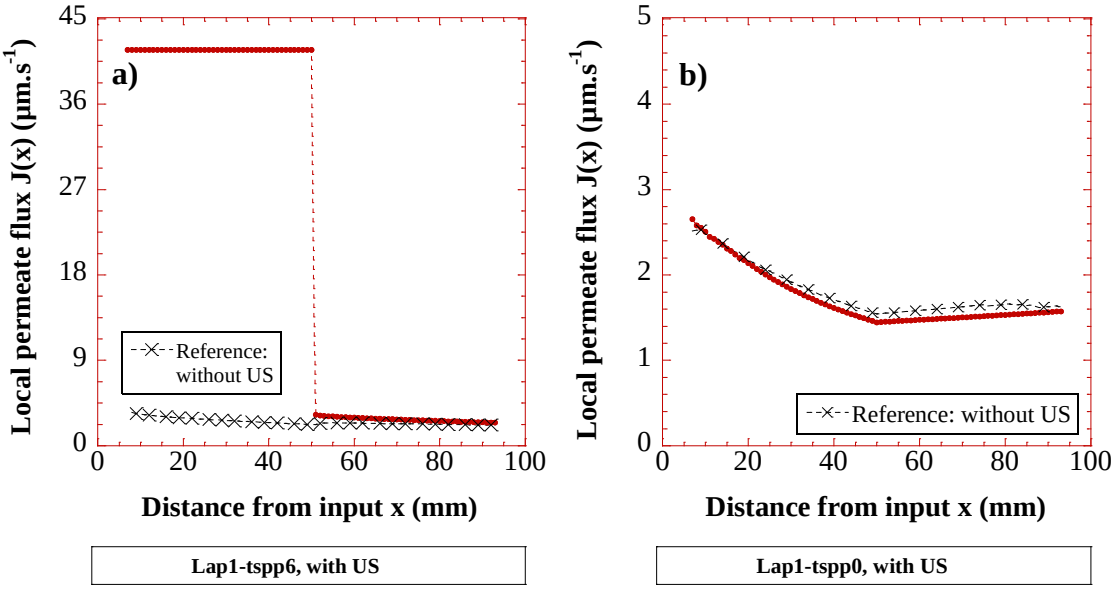

Affiliated table: average flux

Dispersion	US	Modeled average flux J_v (µm.s^{-1})	Experimental average flux J_v (µm.s^{-1})
Lap1-tspp6	ON	22.46	25.00
Lap1-tspp0		1.73	6.94

Fig. 5.14 *Permeate flux profile along the membrane for Laponite dispersions (with US). Source from chapter 3 section 1.5. T = 25±1°C, TMP = 1.1×10^5 Pa, Q_v = 0.3 L.min^{-1}. US: 20 kHz, 2 W.cm^{-2}.*

2.3.4.2 Skim milk

Results of skim milk will be presented by operational steps. Fig. 5.15 assembles all the permeate flux profiles for both suspensions (feed concentration at C_o and 2*C_o). Fig. 5.15a shows three profiles in the case of feed concentration C=C_o. Consistent with previous results (concentration profiles and mass profiles), decrease of Q_v induced a reduction of local permeate flux which was then enhanced by application of US. In Fig. 5.15b, three profiles during filtration of 2*C_o are presented. Just like their mass profiles (section 2.1.2.2), they loss the x axial

dependence feature and the difference between steps are not pronounced. As discussed before, this phenomenon could be explained by the combined effect of US and feed concentration.

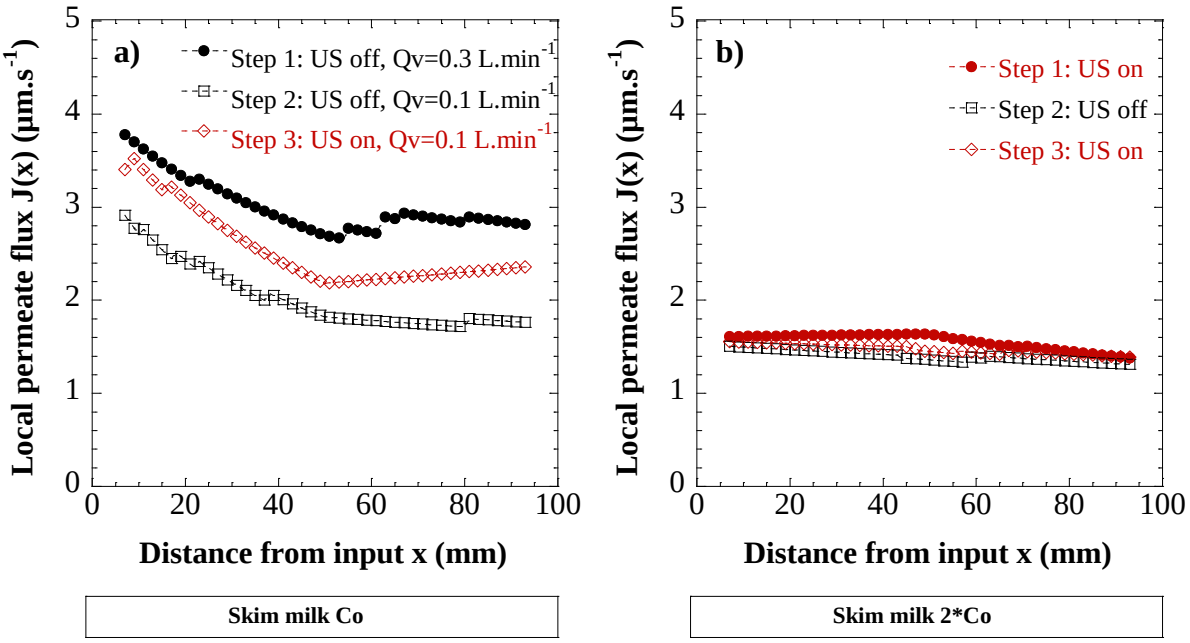

Affiliated table: average flux

Feed concentration	Step	US	Q_v (L.min^{-1})	Modeled average flux J_v (µm.s^{-1})	Experimental average flux J_v (µm.s^{-1})
C_o	1	OFF	0.3	3.00	1.44
C_o	2	OFF	0.1	2.02	0.58
C_o	3	ON	0.1	2.49	1.25
2*C_o	1	ON	0.1	1.56	2.30
2*C_o	2	OFF	0.1	1.40	0.92
2*C_o	3	ON	0.1	1.48	1.86

Fig. 5.15 *Permeate flux profile along the membrane for skim milk. Source from chapter 4 section 1.5. T = 25±1°C, TMP = 1.1×10^5 Pa. US: 20 kHz, 2 W.cm^{-2}.*

2.3.4.3 Assessment of modeling

Gathering all the average flux by modeling of this section, Fig. 5.16 provides a simple mean to assess the modeling by plotting the values from modeling as a function of experimental ones. Diagonals then stand for the perfect matches that split the charts by two zones: overestimated zone and underestimated zone. First of all, we should emphasize that the modeling approach is very satisfactory since all the modeled permeate flux values are in the same order of magnitude of the experimental ones. Then the agreement between modeling and experimental data differs from case to case.

In the case of Laponite dispersions without US, model predictions are slightly overestimated, as shown in Fig. 5.16a. If we plot a fitting curve with the two obtained points (true, more points are required to plot for real), it will be parallel to the perfect match line (diagonal), suggesting that the applied model is capable to predict the process performance.

However, model predictions largely underestimate the cases with US. To explain it, model needs to be reminded. In fact, principal factors of this model are permeability k_p and osmotic pressure Π of concentrated layer. The used laws of both factors in modeling are established without US, which don't take into account, naturally, the effect of US. Does US affect these two factors of Laponite dispersions? Permeability measures the resistance of the system to the hydraulic flow that passes through it. US can enhance local circulation of this measured system, as discussed in chapter 3. As a consequence, the apparent permeability should increase and the used law in modeling is not true anymore. Contrary to permeability, osmotic pressure reflects the property of the medium at equilibrium and it depends principally on concentration (Lelièvre, 2005). It is therefore plausible that for a given concentration profile, no matter with or without US, the corresponding osmotic pressure profile is the same. Returning to Fig. 5.16a, underestimation of J_v could arise from the modification (enhancement) of permeability of concentrated layer by US.

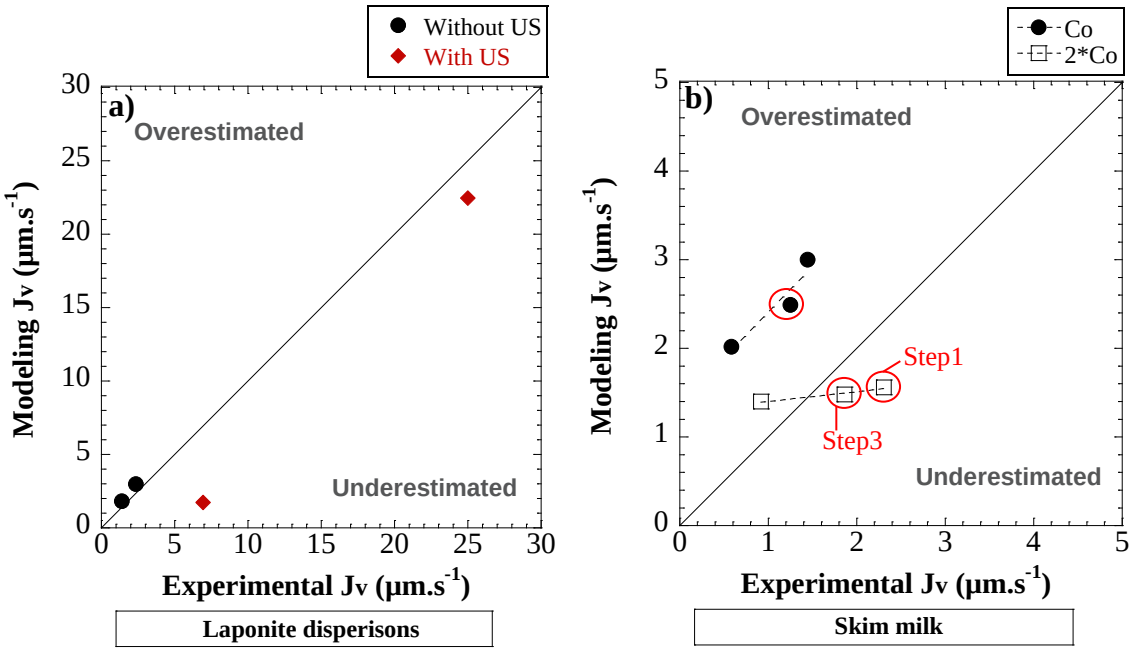

Fig. 5.16 *Comparison of model predictions with experimental results of average flux J_v. Diagonals represent the perfect match lines. Dashed lines represent fitting curve of points. In figure b, circled points correspond to the results with US.*

Deviation is more important in the case of skim milk than Laponite, as shown in Fig. 5.16b. At $C = C_o$, model predictions overestimate J_v to a large extent. Nevertheless, the applied model seems to be still valid since corresponding fitting curve is parallel to the perfect match line. This tremendous deviation could result from the used laws of k_p and Π in modeling. In fact, the used laws are both empirical for native phosphocaseinate (NPC) dispersions which contains principally casein micelles. Content of whey proteins is much lower than skim milk in this dispersion. It implies that the presence of whey protein, which may hamper the permeation of solvent through the network, could affect k_p and Π of concentrated layer resulting in different filtration performance. In addition, concentration at z = 0 µm (membrane surface) was extrapolated by exponential law in the light of obtained concentration information, as shown in Fig. 5.3b. It needs to be verified by experimental data, using technique as GISAXS. It is possible that the concentration at membrane surface is much higher than the estimated one by extrapolation, which results in the overestimation of permeate flux.

In the case of skim milk at 2*Co, model predictions seem to be bad: fitting curve of presented points crosses the perfect match line. The points with US (the circled ones) are underestimated while the point without US is overestimated. How does it happen? The answer to this question could still be the effect of US. Under US, the permeability of concentrated layer is supposed to be underestimated by the employed law, as discussed in the case of Laponite. Especially, US was applied before filtration in step 1 (preventive mode), signifying that the growth of the concentrated layer was all the time companied by US in this situation. Effect of US on permeability of concentrated layer could be therefore more significant. Though this is only a speculation, it is actually illustrated in Fig. 5.16b: deviation is more important for step 1 than step 3, indicated by the distance to the perfect match line. With this speculation, cross-over of the fitting curve and perfect match line can be easily explained. Without taking into account effect of whey protein, the employed model overestimates permeate flux; application of US then counteracts this overestimation since it may enhance the permeability of concentrated layer.

2.3.5 Summary

With our obtained *in-situ* concentration profiles during filtration, model predictions of permeate flux have been carried out on the basis of experimentally-obtainable factors. This approach of modeling demonstrates the correlation between the key factors of model (permeability and osmotic pressure of concentrated layer) and filtration performance (permeate flux). Generally, these two factors can provide an overall description of filtration performance. However, effect of US is not taken into account. Therefore, permeability and osmotic pressure law (or at least permeability law) should be re-determined by experiments for suspensions under US in the future. Model could also be improved by integrating more factors, for instance, diffusion coefficient D could be re-interpreted by taking into account flow property of concentrated layer. Otherwise, velocity profile of filtration channel is envisaged to be measured for further investigation, such as the second mass balance (Eq. 5.3).

Conclusions

In this chapter, all the obtained results involving 4 different families of colloidal suspensions have been reviewed. The applied US has enhanced filtration performance of all the suspensions to different extents. Three typical phenomena have been revealed: it leads to either a total or a partial removal or no nano-sized change of concentrated layer during filtration.

Integrated analysis was then carried out for three representative suspensions to provide a global version of what happened in the filtration channel. Matter accumulation within the concentrated layer was calculated attempting to correlate with permeate flux. No general fit was found between matter accumulation and permeate flux, though correlation indeed exists for each suspension. Then yield stress charts of Laponite dispersions within filtration channel were plotted and flow property of concentrated layer was discussed. This factor can explain most of revealed phenomena in this study except those of skim milk that requires more experimental data. Thanks to the obtained concentration profiles, modeling was executed on the basis of permeability and osmotic pressure. The agreement between modeled values and experimental values of permeate flux is satisfactory. Though more considerations should be taken into account (e.g. to better predict the cases under US), filtration performance can be well described on the basis of permeability and osmotic pressure of accumulated particle layer.

To sum up, in this chapter, factors as matter accumulation, flow property, permeability and osmotic pressure of concentrated layer were examined attempting to find the "master factor(s)" of this process. There is no master factor. Flow property, permeability and osmotic pressure of concentrated layer all play an important role during ultrasonic assisted cross-flow filtration. Therefore, a combination of them could provide a good explanation of most phenomena in this process.

General conclusions

This study has characterized ultrasonic assisted cross-flow ultrafiltration at multi-scales. Thanks to SAXS measurements which provides us non-destructive, real-time, *in-situ* observations of the concentrated particle layers, this work has achieved to combine macroscopic results (the permeate flux) with simultaneous nanometric observations of phenomena during this process. The results obtained can be summarized in three parts:

I - Firstly, flow properties and the changes with ultrasound of different colloidal suspensions have been investigated.

1) In the case of Laponite dispersions. Their yield stress/volume fraction dependence was established and effects of pre-shearing and US treatment on yield stress of Laponite sample were revealed. It shows that both treatments reduce their yield stress levels and Laponite dispersions with peptizers (6%) are more susceptible to shearing force or ultrasonic force than those without peptizer.

2) In the case of skim milk without ultrasound, an evolution from Newtonian to shear-thinning behavior (critical concentration C= 108 $g.L^{-1}$) until the emergence of yield stress with the increase of concentration (sample concentration from 189 $g.L^{-1}$ to 216 $g.L^{-1}$) was revealed. The nature of aqueous phase (deionized water, UF and MF) does not affect their rheological behavior at low concentration regime ($C_o<C<6*C_o$). It has also been emphasis that ultrasound (20 Khz, 2 $W.cm^{-2}$) does not affect the viscosity of standard skim milk (C = 27 g/l) as well as the internal structure of casein micelles.

3) In the case of starch nanocrystal suspensions, increase of sample concentration led to a shear-thinning character more and more pronounced until the emergence of yield stress from 9.6% (w/w). No effect of temperature on rheological behaviors of tested SNC samples was observed when it varied from 20º C to 30º C. Furthermore, no change of feed suspension viscosity occurred during filtration even though under US for 280 minutes.

II - Secondly, the effect of ultrasound on filtration performance has been studied from macro-scale to nano-scale.

In terms of industrial interest (at macro-scales), our results demonstrate that a simultaneous application of ultrasound (US) (20 kHz, 0.6-2.9 $W.cm^{-2}$) can be an efficient way to intensify filtration process. The applied US increased significantly the permeate flux of ultrafiltration: for the 9 investigated suspensions, enhancement factor varies from 1.6 to 13.5. In addition, US intensity varying from 0.6 $W.cm^{-2}$ to 2.9 $W.cm^{-2}$ seems not to influence the US enhancement factor as shown in the case of skim milk filtration.

Revealed by real-time *in-situ* SAXS measurements, at nano-scales, our results illustrate:

1) The applied US under ultrafiltration did not affect the internal structures of all the investigated suspensions.
2) Three major mechanisms related to this concentrated layer:
   i) The applied US induced a removal of accumulated particle layer, as in the case of Lap-tspp6 (both Lap1-tspp6 and Lap0.48-tspp6) and SNC; *ii)* it led to a partial disruption of concentrated layer, as in the case of skim milk and CNC; or *iii)* no change of concentrated layer was detected by the employed SAXS measurement but a great increase of permeate flux J_v as usual in the case of Lap1-tspp0, SWy-2 T3 and NAu-1 T3.
3) Two principal phenomena induced by ultrasonication during filtration can be proposed:
   i) Ultrasonic force induces shear stress by means of localized high-velocity circulatory flow within the network of accumulated particles, if this shear stress is higher than the yield stress of suspension, disaggregation occurs which leads to a progressive removal of accumulated layer. This phenomenon is principally observed in the case of an open structural organization of the particles (aggregation of particles due to dominant attractive colloidal forces and/or fractal organization). Otherwise, *ii)* in the case of a denser network of particles pertaining to an accumulation of repulsive particles and/or assembled in an anisotropic way close to membrane, the denser (nanometer-sized) structure of particle network remains unchanged under ultrasonic force which can still

induce an additional localized water circulation inside this denser network and will be responsible for the increase of permeate flux.

III - Thirdly, an integrated analysis has also been carried out for three representative suspensions to provide a global interpretation of what happened in the filtration channel, thanks to the obtained concentration profiles from real-time *in-situ* SAXS measurements.

1) Matter accumulation within the concentrated layer was calculated attempting to correlate with permeate flux. No general fit was found between matter accumulation and permeate flux, though correlation indeed exists for each suspension.
2) Yield stress charts of Laponite dispersions within filtration channel were deduced from the concentration profiles and flow property of concentrated layer was discussed. This parameter can explain most of revealed phenomena in this study except those of skim milk that requires more experimental data.
3) Modeling was performed thanks to the knowledge of concentration in the polarized layer or deposit and the preceding established permeability and osmotic pressure laws as a function of concentration. Considering only the mass transfer balance in an accumulated particle layer, the permeate flux has been calculated for three different systems: Laponite with/without tspp and casein micelles. The agreement between modeled and experimental values of permeate flux is very satisfactory. Though more considerations should be taken into account (e.g. to better predict the cases under US), filtration performance can be well described on the basis of permeability and osmotic pressure of accumulated particle layer.

Future directions

This work has shown the effectiveness of US application at both macro-scales and nano-scales, suggesting its promising future in industry.

From the point of view of fundamental understanding, the sol/gel transition of colloids under pressure and ultrasound will be further investigated using SAXS measurements in a broader *q* vector range to access to the structure factor S(*q*) of the different systems and to give insight on the structural organization at higher length scales and changes in inter-particles interactions due to pressure and ultrasound forces.

For future work, velocity profile during filtration could be measured to deepen the understanding of such process and introduce this data in the modeling to access to the time dependent evolution of filtration parameters during the cross-flow filtration.

From the perspective of application, optimum US operating configurations could be investigated to provide guiding information for the real application. A scale-up of the existing ultrafiltration-US module has to be developed to reach the industrial scale. The effect of US on several membrane support (polymeric, ceramic) has to be tested and the design of different configurations (spiral wound, plate and frame, etc.) including an ultrasonic probe should also be explored.

Nomenclature

Latin symbols

A	Displacement of ultrasonic wave	m
A_m	Maximum of displacement amplitude of ultrasonic wave	m
a_p	Hydrodynamic particle radius	m
$A_1(q)$	Total scattering amplitude of a single particle	-
c	Propagation speed of ultrasonic wave	$m.s^{-1}$
C_b	Concentration of solute in the feed suspension	$kg.m^{-3}$
C_g	Concentration of gel layer	$kg.m^{-3}$
C_m	Concentration of solute on the membrane surface	$kg.m^{-3}$
C_o	Casein micelle concentration of standard skim milk	$kg.m^{-3}$
C_p	Concentration of solute in the permeate	$kg.m^{-3}$
$C_{p,liq}$	Heat capacity of liquid	$J.kg^{-1}.K^{-1}$
C_{tspp}	Relative concentration of peptizer	%
C*	Concentration of sol-gel transition of casein micelle	$g.L^{-1}$
D	Coefficient of diffusion of solute	$m^2.s^{-1}$
D_B	Dilute limit Brownian diffusion coefficient	$m^2.s^{-1}$
D_H	Hydraulic diameter of the filtration channel	m
Dur.	Duration of cavitation erosion test	Unit of time
D_{sensor}	Distance between the vibrating blade and aluminum foil	mm
e′	Apparent thickness of membrane	m
E_{US}	Ultrasonic enhancement factor	-
f	Wave/vibration frequency	Hz
F_D	Fractal dimension	-
I	Acoustic intensity	$W.m^{-2}$

I_H	Scattering intensity along the horizontal axes of SAXS pattern	mm^{-1}
$I_{in,b}$	Ultrasonic power per unit area of the blade surface	$W.cm^{-2}$
$I_{in,m}$	Ultrasonic power per unit area of the membrane surface	$W.cm^{-2}$
$I_{in,v}$	Ultrasonic power per unit volume of feed suspension	$W.cm^{-3}$
I_i	Incident flux of X-ray beam	-
I_m	Absolute scattering intensity	mm^{-1}
I_V	Scattering intensity along the vertical axis of SAXS pattern	mm^{-1}
$I_1(q)$	Total scattered intensity of single particle	-
J_d	Diffusive flow from the membrane surface to the bulk	$kg.s^{-1}.m^{-2}$
J_{lim}	Limiting flux of filtration	$m^3.m^{-2}.s^{-1}$
J_{us}	Permeate flux obtained in the presence of US	$m^3.m^{-2}.s^{-1}$
J_v	permeate flux of filtration	$m^3.m^{-2}.s^{-1}$
J_w	Specific volumetric flux of pure water	$m^3.m^{-2}.s^{-1}$
J(x)	Local permeate flux along the membrane	$m^3.m^{-2}.s^{-1}$
k	Bolzmann constant	$J.K^{-1}$
K	Consistency for Herschel-Bulkley model	-
K_h	Hydrodynamic coefficient	-
k_p	Permeability of a concentrated milieu	m^2
L_p	Hydraulic permeability of membrane	$m^3.m^{-2}.Pa^{-1}.s^{-1}$
M	Mass transfer coefficient	$m.s^{-1}$
n	Rheological behavior index	-
N_p	Pore number per unit of membrane surface	$pores/m^2$
P	Instantaneous acoustic pressure	Pa
P_{CET}	Applied pressure of cavitation erosion test	Pa
P_{diss}	Dissipated acoustic power	W
P_{in}	Input electric power of ultrasound generator	W
P_m	Maximum of acoustic pressure amplitude	Pa
$P(q)$	Form factor	-
q	Length of scattering vector	nm^{-1}

Q_v	Cross-flow rate	$L.min^{-1}$
r	Pore radius of membrane	m
Re	Reynolds number	-
R_{cp}	Filtration resistance due to concentration polarization	m^{-1}
R_{if}	Filtration resistance due to internal fouling	m^{-1}
R_g	Filtration resistance due to gel formation	m^{-1}
R_m	Hydraulic resistance of clean membrane	m^{-1}
S_m	Effective surface of membrane	m^2
S(q)	Structure factor	-
S(ϕ)	Thermodynamic coefficient (or structure factor)	-
T	Temperature	K/°C
T_{amb}	Environmental temperature	K
T_M	General averaged temperature	°C
T_{m_n}	Averaged temperature of thermocouple No.n	°C
tp	Duration between the end of preparation and the investigation	day
TR	Rejection rate of membrane	%
u	Mean velocity of fluid	$m.s^{-1}$
$\hat{v}$	Velocity amplitude of vibration	$m.s^{-1}$
V_1	Volume of one single particle	-
$\hat{x}$	Displacement amplitude of vibration	m
Z	Acoustic impedance	$N{\cdot}s{\cdot}m^{-3}$

Greek symbols

$\dot{\gamma}$	Shear rate	s^{-1}
δ	Thickness of boundary layer of polarization is	m
η	Viscosity of fluid	Pa.s
η_E	Energy yield of ultrasonic dissipation	%
λ	Wavelength of ultrasound/X-ray	m

Π	Osmotic pressure of solution	Pa
$\Delta\Pi$	Osmotic pressure difference across the membrane	Pa
ρ	Mass density of a medium	$kg.m^{-3}$
ρ_1	Electron density of single particle	-
ρ_m	Electron density of medium	-
$\Delta\rho$	Contrast of electron density	-
τ_o	Yield stress	Pa
τ	Shear stress	Pa
ω	Circular frequency of ultrasonic wave	Hz
Φ, ϕ_V	Volume fraction	-
ϕ_m	Mass fraction	-

Abbreviations

AFM	Atomic Force Microscopy
α/β-LG	α/β-lactalbumin
CCP	Colloidal calcium phosphate clusters
CET	Cavitation erosion test
CNC	Cellulose nanocrystals
COD	Chemical oxygen demand
DLS	Dynamic Light Scattering
FEG-SEM	Field-emission Gun Scanning electron microscope
GISAXS	Grazing incidence SAXS
Lap-tspp0	Pure Laponite dispersions
Lap-tspp6	Laponite dispersions containing peptizers of 6 %
MF	Microfiltration
MFP	Permeate of microfiltration (microfiltrate)
MWCO	Molecular weight cut-off

NAu-1 T3	Australia Nontronite, the third size fraction
NF	Nanofiltration
NPC	Native phosphocaseinate
PES	Polyethersulfone
PPCN	Condensed native phosphocaseinate
RO	Reverse osmosis
SANS	Small Angle Neutron Scattering
SAXS	Small Angle X-ray Scattering
SLS	Static Light Scattering
SNC	Starch nanocrystals
SWy-2 T3	Wyoming Montmorillonite, the third size fraction
TC1/2/3	Calibrated thermocouples No.1/2/3
TEM	Transmission electron microscopy
TMP	Transmembrane pressure
tspp	Tetrasodium diphosphate ($Na_4P_2O_7$, $10H_2O$)
UF	Ultrafiltration
UFP	Permeate of Ultrafiltration (ultrafiltrate)
US	Ultrasound

References

A

Abend, S., Lagaly, G., 2000. Sol–gel transitions of sodium montmorillonite dispersions. Appl. Clay Sci. 16, 201–227.

Agbangla, G.C., Climent, E., Bacchin, P., 2012. Experimental investigation of pore clogging by microparticles: Evidence for a critical flux density of particle yielding arches and deposits. Sep. Purif. Technol.

Agra, R., Trizac, E., Bocquet, L., 2004. The interplay between screening properties and colloid anisotropy: Towards a reliable pair potential for disc-like charged particles. Eur. Phys. J. E 15, 345–357.

Ahmad, A.L., Lah, N.F.C., Ismail, S., Ooi, B.S., 2012. Membrane Antifouling Methods and Alternatives: Ultrasound Approach. Sep. Purif. Rev. 41, 318–346.

Airey, D., Yao, S., Wu, J., Chen, V., Fane, A.G., Pope, J.M., 1998. An investigation of concentration polarization phenomena in membrane filtration of colloidal silica suspensions by NMR micro-imaging. J. Membr. Sci. 145, 145–158.

Al-Akoum, O., Ding, L.H., Jaffrin, M.Y., 2002. Microfiltration and ultrafiltration of UHT skim milk with a vibrating membrane module. Sep. Purif. Technol. 28, 219–234.

Alexander, M., Rojas-Ochoa, L.F., Leser, M., Schurtenberger, P., 2002. Structure, Dynamics, and Optical Properties of Concentrated Milk Suspensions: An Analogy to Hard-Sphere Liquids. J. Colloid Interface Sci. 253, 35–46.

Almécija, M.C., Guadix, A., Martinez-Ferez, A., González-Tello, P., Guadix, E.M., 2009. A flux enhancing pretreatment for the ultrafiltration of acid whey. Desalination 245, 737–742.

Altmann, J., Ripperger, S., 1997. Particle deposition and layer formation at the crossflow microfiltration. J. Membr. Sci. 124, 119–128.

Angellier, H., Choisnard, L., Molina-Boisseau, S., Ozil, P., Dufresne, A., 2004. Optimization of the Preparation of Aqueous Suspensions of Waxy Maize Starch Nanocrystals Using a Response Surface Methodology. Biomacromolecules 5, 1545–1551.

Angellier, H., Molina-Boisseau, S., Lebrun, L., Dufresne, A., 2005. Processing and Structural Properties of Waxy Maize Starch Nanocrystals Reinforced Natural Rubber. Macromolecules 38, 3783–3792.

Angellier-Coussy, H., Putaux, J.-L., Molina-Boisseau, S., Dufresne, A., Bertoft, E., Perez, S., 2009. The molecular structure of waxy maize starch nanocrystals. Carbohydr. Res. 344, 1558–1566.

Avery, R., Ramsay, J.D.., 1986. Colloidal properties of synthetic hectorite clay dispersions: II. Light and small angle neutron scattering. J. Colloid Interface Sci. 109, 448–454.

B

Bacchin, P., Derekx, Q., Veyret, D., Glucina, K., Moulin, P., 2014. Clogging of microporous channels networks: role of connectivity and tortuosity. Microfluid. Nanofluidics 17, 85–96.

Bacchin, P., Meireles, M., Aimar, P., 2002a. Modelling of filtration: from the polarised layer to deposit formation and compaction. Desalination 145, 139–146.

Bacchin, P., Si-Hassen, D., Starov, V., Clifton, M.., Aimar, P., 2002b. A unifying model for concentration polarization, gel-layer formation and particle deposition in cross-flow membrane filtration of colloidal suspensions. Chem. Eng. Sci. 57, 77–91.

Baker, R.W., 2004. Overview of Membrane Science and Technology, Membrane Technology and Application, 2nd ed. John Wiley and Sons, New York.

Baravian, C., Vantelon, D., Thomas, F., 2003. Rheological Determination of Interaction Potential Energy for Aqueous Clay Suspensions. Langmuir 19, 8109–8114. doi:10.1021/la034169c

Barnes, H.A., 1989. Shear‐Thickening (“Dilatancy”) in Suspensions of Nonaggregating Solid Particles Dispersed in Newtonian Liquids. J. Rheol. 1978-Present 33, 329‐366.

Barnes, H.A., 1997. Thixotropy—a review. J. Non-Newton. Fluid Mech. 70, 1–33.

Batchelor, G.K., 1972. Sedimentation in a dilute dispersion of spheres. J. Fluid Mech. 52, 245–268.

Batchelor, G.K., 2000. An Introduction to Fluid Dynamics. Cambridge University Press.

Beck, S., Bouchard, J., Berry, R., 2010. Controlling the Reflection Wavelength of Iridescent Solid Films of Nanocrystalline Cellulose. Biomacromolecules 12, 167–172.

Beck-Candanedo, S., Roman, M., Gray, D.G., 2005. Effect of Reaction Conditions on the Properties and Behavior of Wood Cellulose Nanocrystal Suspensions. Biomacromolecules 6, 1048–1054.

Ben Hassan, I., Lafforgue, C., Ayadi, A., Schmitz, P., 2014a. in situ 3D characterization of bidisperse cakes using confocal laser scanning microscopy. J. Membr. Sci. 466, 103–113.

Ben Hassan, I., Lafforgue, C., Ayadi, A., Schmitz, P., 2014b. In situ 3D characterization of monodispersed spherical particle deposition on microsieve using confocal laser scanning microscopy. J. Membr. Sci. 454, 283–297.

Ben Hassan, I., Lafforgue, C., Ayadi, A., Schmitz, P., 2014c. Study of the separation of yeast by microsieves: In situ 3D characterization of the cake using confocal laser scanning microscopy. Adv. Biosep. Food Bioprocess. 92, 178–191.

Bhattacharjee, S., Kim, A.S., Elimelech, M., 1999. Concentration Polarization of Interacting Solute Particles in Cross-Flow Membrane Filtration. J. Colloid Interface Sci. 212, 81–99.

Blatt, W.F., Dravid, A., Michaels, A.S., Nelsen, L., 1970. Solute Polarization and Cake Formation in Membrane Ultrafiltration: Causes, Consequences, and Control Techniques, in: Flinn, J.E. (Ed.), Membrane Science and Technology. Springer US, pp. 47–97.

Bond, L.J., Greenberg, A.R., Mairal, A.P., Loest, G., Brewster, J.H., Krantz, W.B., 1995. Real-Time Nondestructive Characterization of Membrane Compaction and Fouling, in: Thompson, D., Chimenti, D. (Eds.), Review of Progress in Quantitative Nondestructive Evaluation. Springer US, pp. 1167–1173.

Bondeson, D., Mathew, A., Oksman, K., 2006. Optimization of the isolation of nanocrystals from microcrystalline cellulose by acid hydrolysis. Cellulose 13, 171–180.

Bonggotgetsakul, Y.Y.N., Ashokkumar, M., Cattrall, R.W., Kolev, S.D., 2010. The use of sonication to increase extraction rate in polymer inclusion membranes. An application to the extraction of gold(III). J. Membr. Sci. 365, 242–247.

Bouchoux, A., Debbou, B., Gésan-Guiziou, G., Famelart, M.-H., Doublier, J.-L., Cabane, B., 2009. Rheology and phase behavior of dense casein micelle dispersions. J. Chem. Phys. 131, 165106.

Bouchoux, A., Gésan-Guiziou, G., Pérez, J., Cabane, B., 2010. How to Squeeze a Sponge: Casein Micelles under Osmotic Stress, a SAXS Study. Biophys. J. 99, 3754–3762.

Bouchoux, A., Qu, P., Bacchin, P., Gésan-Guiziou, G., 2013. A General Approach for Predicting the Filtration of Soft and Permeable Colloids: The Milk Example. Langmuir 30, 22–34.

Boulogne, F., Pauchard, L., Giorgiutti-Dauphiné, F., Botet, R., Schweins, R., Sztucki, M., Li, J., Cabane, B., Goehring, L., 2013. Structural anisotropy of directionally dried colloids. ArXiv13091048 Cond-Mat.

Bowen, W.R., Calvo, J.I., Hernández, A., 1995. Steps of membrane blocking in flux decline during protein microfiltration. J. Membr. Sci. 101, 153–165.

Bowen, W.R., Kingdon, R.S., Sabuni, H.A.M., 1989. Electrically enhanced separation processes: the basis of in situ intermittent electrolytic membrane cleaning (IIEMC) and in situ electrolytic membrane restoration (IEMR). J. Membr. Sci. 40, 219–229.

Bowen, W.R., Liang, Y., Williams, P.M., 2000. Gradient diffusion coefficients — theory and experiment. Chem. Eng. Sci. 55, 2359–2377.

Bowen, W.R., Williams, P.M., 2007. Quantitative predictive modelling of ultrafiltration processes: Colloidal science approaches. Surf. Forces Wetting Phenom. Membr. Sep. Rheol. Top. Issue Honour Victor Starov 134–135, 3–14.

Brans, G., Schroën, C.G.P.H., van der Sman, R.G.M., Boom, R.M., 2004. Membrane fractionation of milk: state of the art and challenges. J. Membr. Sci. 243, 263–272.

Bras, J., Hassan, M.L., Bruzesse, C., Hassan, E.A., El-Wakil, N.A., Dufresne, A., 2010. Mechanical, barrier, and biodegradability properties of bagasse cellulose whiskers reinforced natural rubber nanocomposites. Ind. Crops Prod. 32, 627–633.

Brumberger, H., 1994. Modern Aspects of Small-Angle Scattering. Springer.

Bryjak, M., Gancarz, I., Pozniak, G., 2000. Plasma-modified porous membranes. Chem Pap. 54, 496–501.

C

Cai, M., Wang, S., Zheng, Y., Liang, H., 2009. Effects of ultrasound on ultrafiltration of Radix astragalus extract and cleaning of fouled membrane. Sep. Purif. Technol. 68, 351–356.

Callaghan, I.C., Ottewill, R.H., 1974. Interparticle forces in montmorillonite gels. Faraday Discuss. Chem. Soc. 57, 110–118.

Chai, X., Kobayashi, T., Fujii, N., 1999. Ultrasound-associated cleaning of polymeric membranes for water treatment. Sep. Purif. Technol. 15, 139–146.

Cheeke, J.D.N., 2002. Fundamentals and Applications of Ultrasonic Waves. CRC Press.

Chen, J.C., Li, Q., Elimelech, M., 2004. In situ monitoring techniques for concentration polarization and fouling phenomena in membrane filtration. Adv. Colloid Interface Sci. 107, 83–108.

Chen, V., Li, H., Fane, A., 2004. Non-invasive observation of synthetic membrane processes – a review of methods. J. Membr. Sci. 241, 23–44.

Chen, Y., Cao, X., Chang, P.R., Huneault, M.A., 2008. Comparative study on the films of poly(vinyl alcohol)/pea starch nanocrystals and poly(vinyl alcohol)/native pea starch. Carbohydr. Polym. 73, 8–17.

Collis, J., Manasseh, R., Liovic, P., Tho, P., Ooi, A., Petkovic-Duran, K., Zhu, Y., 2010. Cavitation microstreaming and stress fields created by microbubbles. Ultrasonics 50, 273–279.

Crawford, A.E., 1964. The measurement of cavitation. Ultrasonics 2, 120–123.

Cui, Z.F., Chang, S., Fane, A.G., 2003. The use of gas bubbling to enhance membrane processes. J. Membr. Sci. 221, 1–35.

Cui, Z.F., Wright, K.I.T., 1996. Flux enhancements with gas sparging in downwards crossflow ultrafiltration: performance and mechanism. J. Membr. Sci. 117, 109–116.

Curcio, S., Calabrò, V., Iorio, G., 2002. Monitoring and control of TMP and feed flow rate pulsatile operations during ultrafiltration in a membrane module. Desalination 145, 217–222.

D

Dahbi, L., Alexander, M., Trappe, V., Dhont, J.K.G., Schurtenberger, P., 2010. Rheology and structural arrest of casein suspensions. J. Colloid Interface Sci. 342, 564–570.

Dalgleish, D.G., Corredig, M., 2012. The Structure of the Casein Micelle of Milk and Its Changes During Processing. Annu. Rev. Food Sci. Technol. 3, 449–467.

Daufin, G., René, F., Aimar, P., 1998. Séparations par membrane dans les procédés de l'industrie alimentaire, SCIENCES ET TECHNIQUES AGROALIMENTAIRES. ed. TECHNIQUE & DOCUMENTATION.

David, C., 2008. Thèse: Compréhension et maitrise des mécanismes de structuration des dépôts lors de la filtration tangentielle de produits laitiers. Institut Polytechnique de Grenoble.

David, C., Pignon, F., Narayanan, T., Sztucki, M., Gesan-Guiziou, G., Magnin, A., 2008. Spatial and temporal in situ evolution of the concentration profile during casein micelle ultrafiltration probed by small-angle x-ray scattering. Langmuir 24, 4523–4529.

Davis, R.H., Leighton, D.T., 1987. Shear-induced transport of a particle layer along a porous wall. Chem. Eng. Sci. 42, 275–281.

De Barros, S.T.D., Andrade, C.M.G., Mendes, E.S., Peres, L., 2003. Study of fouling mechanism in pineapple juice clarification by ultrafiltration. J. Membr. Sci. 215, 213–224.

De Kruif, C., 1999. Casein micelle interactions. Int. Dairy J. 9, 183–188.

De Kruif, C.G., Huppertz, T., Urban, V.S., Petukhov, A.V., 2012. Casein micelles and their internal structure. Adv. Colloid Interface Sci. 171–172, 36–52.

Delaunay, D., Rabiller-Baudry, M., Gozálvez-Zafrilla, J.M., Balannec, B., Frappart, M., Paugam, L., 2008. Mapping of protein fouling by FTIR-ATR as experimental tool to study membrane fouling and fluid velocity profile in various geometries and validation by CFD simulation. Chem. Eng. Process. Process Intensif. 47, 1106–1117.

Delville, A., 1994. Monte Carlo simulations of the mechanical properties of charged colloids. Langmuir 10, 395–402.

Ding, L., Al-Akoum, O., Abraham, A., Jaffrin, M.Y., 2002. Milk protein concentration by ultrafiltration with rotating disk modules. Desalination 144, 307–311.

Dong, X.M., Revol, J.-F., Gray, D.G., 1998. Effect of microcrystallite preparation conditions on the formation of colloid crystals of. Cellulose 5, 19–32.

Dular, M., Bachert, B., Stoffel, B., Širok, B., 2004. Relationship between cavitation structures and cavitation damage. Wear 257, 1176–1184.

Dular, M., Delgosha, O.C., Petkovšek, M., 2013. Observations of cavitation erosion pit formation. Ultrason. Sonochem. 20, 1113–1120.

E

Ebeling, T., Paillet, M., Borsali, R., Diat, O., Dufresne, A., Cavaillé, J.-Y., Chanzy, H., 1999. Shear-Induced Orientation Phenomena in Suspensions of Cellulose Microcrystals, Revealed by Small Angle X-ray Scattering. Langmuir 15, 6123–6126.

Elazzouzi-Hafraoui, S., Nishiyama, Y., Putaux, J.-L., Heux, L., Dubreuil, F., Rochas, C., 2008. The Shape and Size Distribution of Crystalline Nanoparticles Prepared by Acid Hydrolysis of Native Cellulose. Biomacromolecules 9, 57–65.

Elimelech, M., Bhattacharjee, S., 1998. A novel approach for modeling concentration polarization in crossflow membrane filtration based on the equivalence of osmotic pressure model and filtration theory. J. Membr. Sci. 145, 223–241.

Engler, J., Wiesner, M.R., 2000. Particle fouling of a rotating membrane disk. Water Res. 34, 557–565.

Espinasse, B., Bacchin, P., Aimar, P., 2002. On an experimental method to measure critical flux in ultrafiltration. Desalination 146, 91–96.

Evans, P.J., Bird, M.R., 2006. Solute-Membrane Fouling Interactions During the Ultrafiltration of Black Tea Liquor. Food Bioprod. Process. 84, 292–301.

F

Ferrer, M., Alexander, M., Corredig, M., 2011. Does ultrafiltration have a lasting effect on the physico-chemical properties of the casein micelles? Dairy Sci. Technol. 91, 151–170.

Filson, P.B., Dawson-Andoh, B.E., 2009. Sono-chemical preparation of cellulose nanocrystals from lignocellulose derived materials. Bioresour. Technol. 100, 2259–2264.

Frank, A., Lipscomb, G.G., Dennis, M., 2000. Visualization of concentration fields in hemodialyzers by computed tomography. J. Membr. Sci. 175, 239–251.

G

Gabriel, J.-C.P., Sanchez, C., Davidson, P., 1996. Observation of Nematic Liquid-Crystal Textures in Aqueous Gels of Smectite Clays. J. Phys. Chem. 100, 11139–11143.

Gebhard Schramm, 1998. A Practical Approach to Rheology and Rheometry, second edition. ed. Gebrueder HAAKE GmbH, Karlsruhe, Federal Republic of Germany.

Gebhardt, R., 2014. Effect of filtration forces on the structure of casein micelles. J. Appl. Crystallogr. 47, 29–34.

Gebhardt, R., Kulozik, U., 2014. Simulation of the shape and size of casein micelles in a film state. Food Funct. 5, 780.

Gebhardt, R., Steinhauer, T., Meyer, P., Sterr, J., Perlich, J., Kulozik, U., 2012. Structural changes of deposited casein micelles induced by membrane filtration. Faraday Discuss. 158, 77.

Gésan-Guiziou, G., Daufin, G., Merin, U., Labbé, J.-P., Quémerais, A., 1993. Fouling during constant flux crossflow microfiltration of pretreated whey. Influence of transmembrane pressure gradient. J. Membr. Sci. 80, 131–145.

Glatter, O., Kratky, O., 1982. Small Angle X-ray Scattering. ACADEMIC PRESS.

Gonzalez-Avila, S.R., Prabowo, F., Kumar, A., Ohl, C.-D., 2012. Improved ultrasonic cleaning of membranes with tandem frequency excitation. J. Membr. Sci. 415, 776–783.

Gowman, L.M., Ethier, C.R., 1997. Concentration and concentration gradient measurements in an ultrafiltration concentration polarization layer Part I: A laser-based refractometric experimental technique. J. Membr. Sci. 131, 95–105.

Guerra, A., Jonsson, G., Rasmussen, A., Waagner Nielsen, E., Edelsten, D., 1997. Low cross-flow velocity microfiltration of skim milk for removal of bacterial spores. Int. Dairy J. 7, 849–861.

Guinier, A., Fournet, G., 1955. Small-angle scattering of X-rays. Wiley.

H

Hengl, N., Jin, Y., Pignon, F., Baup, S., Mollard, R., Gondrexon, N., Magnin, A., Michot, L., Paineau, E., 2014. A new way to apply ultrasound in cross-flow ultrafiltration: Application to colloidal suspensions. Ultrason. Sonochem. 21, 1018–1025.

Hermia, J., 1982. Constant Pressure Blocking Filtration Law Application to Powder-Law Non-Newtonian Fluid. Trans Inst Chem Eng 60, 183–187.

Holt, C., de Kruif, C.G., Tuinier, R., Timmins, P.A., 2003. Substructure of bovine casein micelles by small-angle X-ray and neutron scattering. Colloids Surf. Physicochem. Eng. Asp. 213, 275–284.

Horne, D.S., 1998. Casein Interactions: Casting Light on the Black Boxes, the Structure in Dairy Products. Int. Dairy J. 8, 171–177.

Horne, D.S., 2006. Casein micelle structure: Models and muddles. Curr. Opin. Colloid Interface Sci. 11, 148–153.

Huang, H., Schwab, K., Jacangelo, J.G., 2009. Pretreatment for Low Pressure Membranes in Water Treatment: A Review. Environ. Sci. Technol. 43, 3011–3019.

Hubbell, J.H., O/verbo, I., 1979. Relativistic atomic form factors and photon coherent scattering cross sections. J. Phys. Chem. Ref. Data 8, 69–106.

Hubbell, J.H., Veigele, W.J., Briggs, E.A., Brown, R.T., Cromer, D.T., Howerton, R.J., 1975. Atomic form factors, incoherent scattering functions, and photon scattering cross sections. J. Phys. Chem. Ref. Data 4, 471–538.

J

Jaffrin, M.Y., Gupta, B.B., Paullier, P., 1994. Energy saving pulsatile mode cross flow filtration. J. Membr. Sci. 86, 281–290.

Jimenez-Lopez, A.J.E., Leconte, N., Dehainault, O., Geneste, C., Fromont, L., Gésan-Guiziou, G., 2008. Role of milk constituents on critical conditions and deposit structure in skimmilk microfiltration (0.1 μm). Sep. Purif. Technol. 61, 33–43.

Jimenez-Lopez, A.J.E., Leconte, N., Garnier-Lambrouin, F., Bouchoux, A., Rousseau, F., Gésan-Guiziou, G., 2011. Ionic strength dependence of skimmed milk microfiltration: Relations between filtration performance, deposit layer characteristics and colloidal properties of casein micelles. J. Membr. Sci. 369, 404–413.

Jin, Y., Hengl, N., Baup, S., Pignon, F., Gondrexon, N., Magnin, A., Sztucki, M., Narayanan, T., Michot, L., Cabane, B., 2014. Effects of ultrasound on colloidal organization at nanometer length scale during cross-flow ultrafiltration probed by in-situ SAXS. J. Membr. Sci. 453, 624–635.

Jones, S., 2012. Thesis: The application of Enhanced Fluid Dynamic Gauging as a Fouling Sensor for Pressure Driven Membrane Separations in the Food Industry. University of Bath.

Jönsson, B., Labbez, C., Cabane, B., 2008. Interaction of Nanometric Clay Platelets. Langmuir 24, 11406–11413.

Juang, R.-S., Lin, K.-H., 2004. Flux recovery in the ultrafiltration of suspended solutions with ultrasound. J. Membr. Sci. 243, 115–124.

K

Kallioinen, M., Manttari, M., 2011. Influence of Ultrasonic Treatment on Various Membrane Materials: A Review. Sep. Sci. Technol. 46, 1388–1395.

Kang, S.-T., Subramani, A., Hoek, E.M.V., Deshusses, M.A., Matsumoto, M.R., 2004. Direct observation of biofouling in cross-flow microfiltration: mechanisms of deposition and release. J. Membr. Sci. 244, 151–165.

Khulbe, K.C., Feng, C.Y., Matsuura, T., 2008. Synthetic polymeric membranes: characterization by atomic force microscopy. Springer.

Kobayashi, T., Chai, X., Fujii, N., 1999. Ultrasound enhanced cross-flow membrane filtration. Sep. Purif. Technol. 17, 31–40.

Kobayashi, T., Kobayashi, T., Hosaka, Y., Fujii, N., 2003. Ultrasound-enhanced membrane-cleaning processes applied water treatments: influence of sonic frequency on filtration treatments. Ultrasonics 41, 185–190.

Koh, L.L.A., Nguyen, H.T.H., Chandrapala, J., Zisu, B., Ashokkumar, M., Kentish, S.E., 2014. The use of ultrasonic feed pre-treatment to reduce membrane fouling in whey ultrafiltration. J. Membr. Sci. 453, 230–239.

Kornfeld, M., Suvorov, L., 1944. On the Destructive Action of Cavitation. J. Appl. Phys. 15, 495–506.

Krefting, D., Mettin, R., Lauterborn, W., 2004. High-speed observation of acoustic cavitation erosion in multibubble systems. 4th Conf. Appl. Power Ultrasound Phys. Chem. Process. 11, 119–123.

Kristo, E., Biliaderis, C.G., 2007. Physical properties of starch nanocrystal-reinforced pullulan films. Carbohydr. Polym. 68, 146–158.

Kromkamp, J., Rijnsent, S., Huttenhuis, R., Schroën, K., Boom, R., 2007. Differential analysis of deposition layers from micellar casein and milk fat globule suspensions onto ultrafiltration and microfiltration membranes. J. Food Eng. 80, 257–266.

Kroon, M., Vos, W.L., Wegdam, G.H., 1998. Structure and formation of a gel of colloidal disks. Phys. Rev. E 57, 1962–1970.

Krstić, D.M., Tekić, M.N., Carić, M.Đ., Milanović, S.D., 2002. The effect of turbulence promoter on cross-flow microfiltration of skim milk. J. Membr. Sci. 208, 303–314.

Kruif, C.G.D., Holt, C., 2003. Casein Micelle Structure, Functions and Interactions, in: Fox, P.F., McSweeney, P.L.H. (Eds.), Advanced Dairy Chemistry—1 Proteins. Springer US, pp. 233–276.

Kyllonen, H., Pirkonen, P., Nystrom, M., Nuortila-Jokinen, J., Gronroos, A., 2006. Experimental aspects of ultrasonically enhanced cross-flow membrane filtration of industrial wastewater. Ultrason. Sonochem. 13, 295–302.

L

Laguna-Camacho, J.R., Lewis, R., Vite-Torres, M., Méndez-Méndez, J.V., 2013. A study of cavitation erosion on engineering materials. Wear Mater. 2013 301, 467–476.

Lamminen, M.O., Walker, H.W., Weavers, L.K., 2004. Mechanisms and factors influencing the ultrasonic cleaning of particle-fouled ceramic membranes. J. Membr. Sci. 237, 213–223.

Lamminen, M.O., Walker, H.W., Weavers, L.K., 2006. Effect of Fouling Conditions and Cake Layer Structure on the Ultrasonic Cleaning of Ceramic Membranes. Sep. Sci. Technol. 41, 3569–3584.

Latt, K.K., Kobayashi, T., 2006. Ultrasound-membrane hybrid processes for enhancement of filtration properties. Ultrason. Sonochem. 13, 321–328.

LeCorre, D., Bras, J., Dufresne, A., 2010. Starch Nanoparticles: A Review. Biomacromolecules 11, 1139–1153.

LeCorre, D., Bras, J., Dufresne, A., 2011. Influence of botanic origin and amylose content on the morphology of starch nanocrystals. J. Nanoparticle Res. 13, 7193–7208.

LeCorre, D., Bras, J., Dufresne, A., 2011a. Evidence of Micro- and Nanoscaled Particles during Starch Nanocrystals Preparation and Their Isolation. Biomacromolecules 12, 3039–3046.

LeCorre, D., Bras, J., Dufresne, A., 2011b. Ceramic membrane filtration for isolating starch nanocrystals. Carbohydr. Polym. 86, 1565–1572.

Lee, D.N., Merson, R.L., 1976. Prefiltration of Cottage Cheese Whey to Reduce Fouling of Ultrafiltration Membranes. J. Food Sci. 41, 403–410.

Legay, M., 2012. Thèse: Intensification des processus de transfert de chaleur par ultrasons, vers un nouveau type d'échangeur de chaleur : l'échangeur vibrant. Ecole Doctorale I-MEP2, Grenoble.

Legay, M., Gondrexon, N., Le Person, S., phane, Boldo, P., Bontemps, A., 2011. Enhancement of Heat Transfer by Ultrasound: Review and Recent Advances. Int. J. Chem. Eng. 2011.

Leighton, T.G., 1994. The Acoustic Bubble. Elsevier.

Leighton, T.G., 2007. What is ultrasound? Prog. Biophys. Mol. Biol. 93, 3–83.

Lelièvre, V., 2005. Thèse : Rhéologie et filtration de dispersions aqueuses de nanoparticules d'hectorite en relation avec la structuration des dépôts. Institut Polytechnique de Grenoble, Grenoble.

Li, H., Fane, A.G., Coster, H.G.L., Vigneswaran, S., 1998. Direct observation of particle deposition on the membrane surface during crossflow microfiltration. J. Membr. Sci. 149, 83–97.

Li, J., Sanderson, R., Jacobs, E., 2002. Ultrasonic cleaning of nylon microfiltration membranes fouled by Kraft paper mill effluent. J. Membr. Sci. 205, 247–257.

Li, X., Yu, J., Nnanna, A.G.A., 2011. Fouling mitigation for hollow-fiber UF membrane by sonication. Desalination 281, 23–29.

Lighthill, S.J., 1978. Acoustic streaming. J. Sound Vib. 61, 391–418.

Lin, H.J., Xie, K., Mahendran, B., Bagley, D.M., Leung, K.T., Liss, S.N., Liao, B.Q., 2009. Sludge properties and their effects on membrane fouling in submerged anaerobic membrane bioreactors (SAnMBRs). Water Res. 43, 3827–3837.

Lindner, P., Zemb, T., 2002. Neutrons, X-rays, and light: scattering methods applied to soft condensed matter. Elsevier, Amsterdam; Boston.

Liu, D., Chen, X., Yue, Y., Chen, M., Wu, Q., 2011. Structure and rheology of nanocrystalline cellulose. Carbohydr. Polym. 84, 316–322.

Lockhart, N.C., 1980. Electrical properties and the surface characteristics and structure of clays. I. Swelling clays. J. Colloid Interface Sci. 74, 509–519.

Loh, B.-G., Hyun, S., Ro, P.I., Kleinstreuer, C., 2002. Acoustic streaming induced by ultrasonic flexural vibrations and associated enhancement of convective heat transfer. J. Acoust. Soc. Am. 111, 875–883.

Lohrberg, H., Stoffel, B., 2001. Measurement of Cavitation Erosive Aggressiveness by Means of Structure Born Noise.

Lu, P., Hsieh, Y.-L., 2010. Preparation and properties of cellulose nanocrystals: Rods, spheres, and network. Carbohydr. Polym. 82, 329–336.

M

Macosko, C.W., 1994. Rheology principles, measurements, and applications. VCH, New York.

Magnin, A., Piau, J.M., 1990. Cone-and-plate rheometry of yield stress fluids. Study of an aqueous gel. J. Non-Newton. Fluid Mech. 36, 85–108.

Marcel Mulder, 2000. Basic principles of Membrane Technology, second edition. ed. Kluwer Academic Publishers.

Marchin, S., Putaux, J.-L., Pignon, F., Léonil, J., 2007. Effects of the environmental factors on the casein micelle structure studied by cryo transmission electron microscopy and small-angle x-ray scattering/ultrasmall-angle x-ray scattering. J. Chem. Phys. 126, 045101.

Marcovich, N. e., Auad, M. l., Bellesi, N. e., Nutt, S. r., Aranguren, M. i., 2006. Cellulose micro/nanocrystals reinforced polyurethane. J. Mater. Res. 21, 870–881.

Marshall, A.D., Munro, P.A., Trägårdh, G., 1993. The effect of protein fouling in microfiltration and ultrafiltration on permeate flux, protein retention and selectivity: A literature review. Desalination 91, 65–108.

Martin, C., Pignon, F., Magnin, A., Meireles, M., Lelièvre, V., Lindner, P., Cabane, B., 2006. Osmotic Compression and Expansion of Highly Ordered Clay Dispersions. Langmuir 22, 4065–4075.

Martin, C., Pignon, F., Piau, J., Magnin, A., Lindner, P., Cabane, B., 2002. Dissociation of thixotropic clay gels. Phys. Rev. E 66, 021401.

Marty, A., Causserand, C., Roques, C., Bacchin, P., 2014. Impact of tortuous flow on bacteria streamer development in microfluidic system during filtration. Biomicrofluidics 8, -.

Maskooki, A., Kobayashi, T., Mortazavi, S.A., Maskooki, A., 2008. Effect of low frequencies and mixed wave of ultrasound and EDTA on flux recovery and cleaning of microfiltration membranes. Sep. Purif. Technol. 59, 67–73.

Mason, T.J., 1991. Practical sonochemistry: user's guide to applications in chemistry and chemical engineering. E. Horwood.

Mason, T.J., 1999. Sonochemistry. Oxford University Press.

Mason, T.J., Lorimer, J.P., 1988. Sonochemistry: Theory, Applications and Uses of Ultrasound in Chemistry. Ellis Horwood.

Masselin, I., Chasseray, X., Durand-Bourlier, L., Lainé, J.-M., Syzaret, P.-Y., Lemordant, D., 2001. Effect of sonication on polymeric membranes. J. Membr. Sci. 181, 213–220.

McLachlan, D.S., Koen, D., Sanderson, R.D., 2010. Flux flow and cleaning enhancement in a spiral membrane element, using continuous infrasonic backpulsing. Water SA 36, 0–0.

Mendret, J., Guigui, C., Schmitz, P., Cabassud, C., Duru, P., 2007. An optical method for in situ characterization of fouling during filtration. AIChE J. 53, 2265–2274.

Meng, F., Zhang, H., Yang, F., Liu, L., 2007. Characterization of Cake Layer in Submerged Membrane Bioreactor. Environ. Sci. Technol. 41, 4065–4070.

Michaels, A.S., Bixler, H.J., 1968. Membrane permeation: theory and practice. Prog. Sep. Purif. 1, 143–186.

Michot, L.J., Bihannic, I., Maddi, S., Funari, S.S., Baravian, C., Levitz, P., Davidson, P., 2006. Liquid–crystalline aqueous clay suspensions. Proc. Natl. Acad. Sci. 103, 16101–16104.

Michot, L.J., Bihannic, I., Porsch, K., Maddi, S., Baravian, C., Mougel, J., Levitz, P., 2004. Phase Diagrams of Wyoming Na-Montmorillonite Clay. Influence of Particle Anisotropy. Langmuir 20, 10829–10837.

Michot, L.J., Paineau, E., Bihannic, I., Maddi, S., Duval, J.F.L., Baravian, C., Davidson, P., Levitz, P., 2013. Isotropic/nematic and sol/gel transitions in aqueous suspensions of size selected nontronite NAu1. Clay Miner. 48, 663–685.

Mirzaie, A., Mohammadi, T., 2012. Effect of ultrasonic waves on flux enhancement in microfiltration of milk. J. Food Eng. 108, 77–86.

Mores, W.D., Davis, R.H., 2001. Direct visual observation of yeast deposition and removal during microfiltration. J. Membr. Sci. 189, 217–230.

Morvan, M., Espinat, D., Lambard, J., Zemb, T., 1994. Ultrasmall- and small-angle X-ray scattering of smectite clay suspensions. Colloids Surf. Physicochem. Eng. Asp. 82, 193–203.

Moulin, P., Manno, P., Rouch, J.., Serra, C., Clifton, M.., Aptel, P., 1999. Flux improvement by Dean vortices: ultrafiltration of colloidal suspensions and macromolecular solutions. J. Membr. Sci. 156, 109–130.

Mourchid, A., Delville, A., Lambard, J., LeColier, E., Levitz, P., 1995. Phase Diagram of Colloidal Dispersions of Anisotropic Charged Particles: Equilibrium Properties, Structure, and Rheology of Laponite Suspensions. Langmuir 11, 1942–1950.

Mourchid, A., Lécolier, E., Van Damme, H., Levitz, P., 1998. On Viscoelastic, Birefringent, and Swelling Properties of Laponite Clay Suspensions: Revisited Phase Diagram. Langmuir 14, 4718–4723.

Mourchid, A., Levitz, P., 1998. Long-term gelation of laponite aqueous dispersions. Phys. Rev. E 57, R4887–R4890.

Munir Cheryan, 1998. Ultrafiltration and Microfiltration Handbook, second edition. ed. Technomic Pub.Co.(Lancaster,Pa.).

Muthukumaran, S., Kentish, S.E., Ashokkumar, M., Stevens, G.W., 2005. Mechanisms for the ultrasonic enhancement of dairy whey ultrafiltration. J. Membr. Sci. 258, 106–114.

Muthukumaran, S., Kentish, S.E., Stevens, G.W., Ashokkumar, M., 2006. Application of ultrasound in membrane separation processes: A review. Rev. Chem. Eng. 22, 155–194.

Muthukumaran, S., Kentish, S.E., Stevens, G.W., Ashokkumar, M., Mawson, R., 2007. The application of ultrasound to dairy ultrafiltration: The influence of operating conditions. J. Food Eng. 81, 364–373.

N

Narayanan, T., 2008. Synchrotron Small-Angle X-Ray Scattering, in: Borsali, R., Pecora, R. (Eds.), Soft Matter Characterization. Springer Netherlands, pp. 899–952.

Narayanan, T., Diat, O., Bösecke, P., 2001. SAXS and USAXS on the high brilliance beamline at the ESRF. Nucl. Instrum. Methods Phys. Res. Sect. Accel. Spectrometers Detect. Assoc. Equip. 467–468, Part 2, 1005–1009.

Neppiras, E.A., 1968. Measurement of Acoustic Cavitation. IEEE Trans. Sonics Ultrason. 15, 81–88.

Neppiras, E.A., 1980. Acoustic cavitation. Phys. Rep. 61, 159–251.

Ng, K.-K., Wu, C.-J., Yang, H.-L., Panchangam, C., Lin, Y.-C., Hong, P.-K.A., Wu, C.-H., Lin, C.-F., 2012. Effect of Ultrasound on Membrane Filtration and Cleaning Operations. Sep. Sci. Technol. 48, 215–222.

Nomura, S., Yamamoto, A., Murakami, K., 2002. Ultrasonic Heat Transfer Enhancement Using a Horn-Type Transducer. Jpn. J. Appl. Phys. 41, 3217–3222.

Noordman, T.R., de Jonge, A., Wesselingh, J.A., Bel, W., Dekker, M., Voorde, E.T., Grijpma, S.D., 2002. Application of fluidised particles as turbulence promoters in ultrafiltration: Improvement of flux and rejection. J. Membr. Sci. 208, 157–169.

Norrish, K., 1954. The swelling of montmorillonite. Discuss. Faraday Soc. 18, 120–134.

Nyborg, W.L., 1982. Ultrasonic microstreaming and related phenomena. Br. J. Cancer. Suppl. 5, 156–160.

Nyborg, W.L., 2005. Acoustic Streaming near a Boundary. J. Acoust. Soc. Am. 30, 329–339.

O - P

Okahata, Y., Noguchi, H., 1983. Ultrasound-responsive permeability control of bilayer-coated capsule membranes. Chem. Lett. 1517–1520.

Paineau, E., Bihannic, I., Baravian, C., Philippe, A.-M., Davidson, P., Levitz, P., Funari, S.S., Rochas, C., Michot, L.J., 2011. Aqueous Suspensions of Natural Swelling Clay Minerals. 1. Structure and Electrostatic Interactions. Langmuir 27, 5562–5573.

Peng, B.L., Dhar, N., Liu, H.L., Tam, K.C., 2011. Chemistry and applications of nanocrystalline cellulose and its derivatives: A nanotechnology perspective. Can. J. Chem. Eng. 89, 1191–1206.

Pétrier, C., Gondrexon, N., Boldo, P., 2008. Ultrasons et sonochimie. Tech. Ing. AF6310.

Piau, J.M., 2007. Carbopol gels: Elastoviscoplastic and slippery glasses made of individual swollen sponges: Meso- and macroscopic properties, constitutive equations and scaling laws. J. Non-Newton. Fluid Mech. 144, 1–29.

Pieracci, J., Crivello, J.V., Belfort, G., 2002. Increasing membrane permeability of UV-modified poly(ether sulfone) ultrafiltration membranes. J. Membr. Sci. 202, 1–16.

Pignon, F., Abyan, M., David, C., Magnin, A., Sztucki, M., 2012. In Situ Characterization by SAXS of Concentration Polarization Layers during Cross-Flow Ultrafiltration of Laponite Dispersions. Langmuir 28, 1083–1094.

Pignon, F., Alemdar, A., Magnin, A., Narayanan, T., 2003. Small-Angle X-ray Scattering Studies of Fe-Montmorillonite Deposits during Ultrafiltration in a Magnetic Field. Langmuir 19, 8638–8645.

Pignon, F., Belina, G., Narayanan, T., Paubel, X., Magnin, A., Gésan-Guiziou, G., 2004. Structure and rheological behavior of casein micelle suspensions during ultrafiltration process. J. Chem. Phys. 121, 8138–8146.

Pignon, F., Magnin, A., Piau, J., Cabane, B., Lindner, P., Diat, O., 1997. Yield stress thixotropic clay suspension: Investigation of structure by light, neutron, and x-ray scattering. Phys. Rev. E 56, 3281–3289.

Pignon, F., Magnin, A., Piau, J.-M., 1996. Thixotropic colloidal suspensions and flow curves with minimum: Identification of flow regimes and rheometric consequences. J. Rheol. 1978-Present 40, 573–587.

Pignon, F., Magnin, A., Piau, J.-M., 1998. Thixotropic behavior of clay dispersions: Combinations of scattering and rheometric techniques. J. Rheol. 42, 1349–1373.

Pignon, F., Magnin, A., Piau, J.-M., Cabane, B., Aimar, P., Meireles, M., Lindner, P., 2000. Structural characterisation of deposits formed during frontal filtration. J. Membr. Sci. 174, 189–204.

Pignon, F., Piau, J., Magnin, A., 1996. Structure and pertinent length scale of a discotic clay gel. Phys. Rev. Lett. 76, 4857–4860.

Pontié, M., Rapenne, S., Thekkedath, A., Duchesne, J., Jacquemet, V., Leparc, J., Suty, H., 2005. Tools for membrane autopsies and antifouling strategies in seawater feeds: a review. Desalination 181, 75–90.

Putaux, J.-L., Molina-Boisseau, S., Momaur, T., Dufresne, A., 2003. Platelet Nanocrystals Resulting from the Disruption of Waxy Maize Starch Granules by Acid Hydrolysis. Biomacromolecules 4, 1198–1202.

R

Rabiller-Baudry, M., Bégoin, L., Delaunay, D., Paugam, L., Chaufer, B., 2008. A dual approach of membrane cleaning based on physico-chemistry and hydrodynamics: Application to PES membrane of dairy industry. Chem. Eng. Process. Process Intensif. 47, 267–275.

Ramsay, J.D.., 1986. Colloidal properties of synthetic hectorite clay dispersions: I. Rheology. J. Colloid Interface Sci. 109, 441–447.

Ramsay, J.D.F., Lindner, P., 1993. Small-angle neutron scattering investigations of the structure of thixotropic dispersions of smectite clay colloids. J. Chem. Soc. Faraday Trans. 89, 4207–4214.

Ramsay, J.D.F., Swanton, S.W., Bunce, J., 1990. Swelling and dispersion of smectite clay colloids: determination of structure by neutron diffraction and small-angle neutron scattering. J. Chem. Soc. Faraday Trans. 86, 3919–3926.

Rayleigh, Lord, 1917. VIII. On the pressure developed in a liquid during the collapse of a spherical cavity. Philos. Mag. Ser. 6 34, 94–98.

Redkar, S., Kuberkar, V., Davis, R.H., 1996. Modeling of concentration polarization and depolarization with high-frequency backpulsing. J. Membr. Sci. 121, 229–242.

Revol, J.-F., Bradford, H., Giasson, J., Marchessault, R.H., Gray, D.G., 1992. Helicoidal self-ordering of cellulose microfibrils in aqueous suspension. Int. J. Biol. Macromol. 14, 170–172.

Revol, J.-F., Godbout, L., Dong, X.-M., Gray, D.G., Chanzy, H., Maret, G., 1994. Chiral nematic suspensions of cellulose crystallites; phase separation and magnetic field orientation. Liq. Cryst. 16, 127–134.

Romero, C., Davis, R., 1988. Global-Model of Cross-Flow Microfiltration Based on Hydrodynamic Particle Diffusion. J. Membr. Sci. 39, 157–185.

Rooney, J.A., 2005. Shear as a Mechanism for Sonically Induced Biological Effects. J. Acoust. Soc. Am. 52, 1718–1724.

Rosta, L., von Gunten, H.R., 1990. Light scattering characterization of laporite sols. J. Colloid Interface Sci. 134, 397–406.

Ruzicka, B., Zaccarelli, E., 2011. A fresh look at the Laponite phase diagram. Soft Matter 7, 1268.

S

Saboyainsta, L.V., Maubois, J.-L., 2000. Current developments of microfiltration technology in the dairy industry. Le Lait 80, 541–553.

Sandra, S., Cooper, C., Alexander, M., Corredig, M., 2011. Coagulation properties of ultrafiltered milk retentates measured using rheology and diffusing wave spectroscopy. Food Res. Int. 44, 951–956.

Schuck, P., Piot, M., Méjean, S., Le Graet, Y., Fauquant, J., Brulé, G., Maubois, J.L., 1994. Déshydratation par atomisation de phosphocaséinate natif obtenu par microfiltration sur membrane. Le Lait 74, 375–388.

Shafiei-Sabet, S., Hamad, W.Y., Hatzikiriakos, S.G., 2012. Rheology of Nanocrystalline Cellulose Aqueous Suspensions. Langmuir 28, 17124–17133.

Shanmugam, A., Chandrapala, J., Ashokkumar, M., 2012. The effect of ultrasound on the physical and functional properties of skim milk. Innov. Food Sci. Emerg. Technol. 16, 251–258.

Shim, J.K., Na, H.S., Lee, Y.M., Huh, H., Nho, Y.C., 2001. Surface modification of polypropylene membranes by γ-ray induced graft copolymerization and their solute permeation characteristics. J. Membr. Sci. 190, 215–226.

Shirato, M., Aragaki, T., Iritani, E., 1979. Blocking filtration laws for filtration of power-law non-Newtonian fluids. J. Chem. Eng. Jpn. 12, 162–164.

Shukla, A., Narayanan, T., Zanchi, D., 2009. Structure of casein micelles and their complexation with tannins. Soft Matter 5, 2884.

Simon, A., 1999. Thèse: Contribution à l'étude de l'ultrafiltration en présence d'un champ ultrasonore basse fréquence. Ecole National Supérieure de Chimie.

Simon, A., Gondrexon, N., Taha, S., Cabon, J., Dorange, G., 2000. Low-frequency ultrasound to improve dead-end ultrafiltration performance. Sep. Sci. Technol. 35, 2619–2637.

Simon, A., Penpenic, L., Gondrexon, N., Taha, S., Dorange, G., 2000. A comparative study between classical stirred and ultrasonically-assisted dead-end ultrafiltration. Ultrason. Sonochem. 7, 183–186.

Siqueira, G., Bras, J., Dufresne, A., 2010. Cellulosic Bionanocomposites: A Review of Preparation, Properties and Applications. Polymers 2, 728–765.

Smilgies, D.-M., Busch, P., Papadakis, C.M., Posselt, D., 2002. Characterization of polymer thin films with small‐angle X‐ray scattering under grazing incidence (GISAXS).

Song, L., Elimelech, M., 1995. Theory of concentration polarization in crossflow filtration. J. Chem. Soc. Faraday Trans. 91, 3389–3398.

Spengler, J.F., Coakley, W.T., Christensen, K.T., 2003. Microstreaming effects on particle concentration in an ultrasonic standing wave. AIChE J. 49, 2773–2782.

Spitzer, J.J., 1989. Electrostatic calculations on swelling pressures of clay-water dispersions. Langmuir 5, 199–205.

Steffe, J.F., 1996. Rheological Methods in Food Process Engineering. Freeman Press.

Stroobants, A., Lekkerkerker, H.N.W., Odijk, T., 1986. Effect of electrostatic interaction on the liquid crystal phase transition in solutions of rodlike polyelectrolytes. Macromolecules 19, 2232–2238.

Šturcová, A., Davies, G.R., Eichhorn, S.J., 2005. Elastic Modulus and Stress-Transfer Properties of Tunicate Cellulose Whiskers. Biomacromolecules 6, 1055–1061.

Suslick, K.S., 1988. Ultrasound: its chemical, physical, and biological effects. VCH Publishers.

T

Ten Brinke, A.J.W., Bailey, L., Lekkerkerker, H.N.W., Maitland, G.C., 2007. Rheology modification in mixed shape colloidal dispersions. Part I: pure components. Soft Matter 3, 1145–1162.

Thekkedath, A., 2007. Thèse: Etude du colmatage de membranes d'ultrafiltration (UF) par les matières organiques naturelles (MON). Ecole Doctorale d'Angers.

Thompson, D.W., Butterworth, J.T., 1992. The nature of laponite and its aqueous dispersions. J. Colloid Interface Sci. 151, 236–243.

Tingaut, P., Zimmermann, T., Lopez-Suevos, F., 2010. Synthesis and Characterization of Bionanocomposites with Tunable Properties from Poly(lactic acid) and Acetylated Microfibrillated Cellulose. Biomacromolecules 11, 454–464.

Tracey, E.M., Davis, R.H., 1994. Protein Fouling of Track-Etched Polycarbonate Microfiltration Membranes. J. Colloid Interface Sci. 167, 104–116.

Trägårdh, G., 1989. Membrane cleaning. Desalination 71, 325–335.

U - Z

Ureña-Benavides, E.E., Ao, G., Davis, V.A., Kitchens, C.L., 2011. Rheology and Phase Behavior of Lyotropic Cellulose Nanocrystal Suspensions. Macromolecules 44, 8990–8998.

Van den Berg, G.B., Smolders, C.A., 1990. Flux decline in ultrafiltration processes. Desalination 77, 101–133.

Villamiel, M., de Jong, P., 2000. Influence of High-Intensity Ultrasound and Heat Treatment in Continuous Flow on Fat, Proteins, and Native Enzymes of Milk. J. Agric. Food Chem. 48, 472–478.

Wagner, N.J., Brady, J.F., 2009. Shear thickening in colloidal dispersions. Phys. Today 62, 27.

Walstra, P., 1999. Casein sub-micelles: do they exist? Int. Dairy J. 9, 189–192.

Wang, N., Ding, E., Cheng, R., 2008. Preparation and Liquid Crystalline Properties of Spherical Cellulose Nanocrystals. Langmuir 24, 5–8.

Wemsy Diagne, N., Rabiller-Baudry, M., Paugam, L., 2013. On the actual cleanability of polyethersulfone membrane fouled by proteins at critical or limiting flux. J. Membr. Sci. 425–426, 40–47.

Williams, A.R., Slade, J.S., 1971. Ultrasonic dispersal of aggregates of Sarcina lutea. Ultrasonics 9, 76–80.

Winzeler, H.B., Belfort, G., 1993. Enhanced performance for pressure-driven membrane processes: the argument for fluid instabilities. J. Membr. Sci. 80, 35–47.

Yao, S., Costello, M., Fane, A.G., Pope, J.M., 1995. Non-invasive observation of flow profiles and polarisation layers in hollow fibre membrane filtration modules using NMR micro-imaging. J. Membr. Sci. 99, 207–216.

Zeqiri, B., Hodnett, M., Carroll, A.J., 2006. Studies of a novel sensor for assessing the spatial distribution of cavitation activity within ultrasonic cleaning vessels. Ultrasonics 44, 73–82.

Zhang, J., Elder, T.J., Pu, Y., Ragauskas, A.J., 2007. Facile synthesis of spherical cellulose nanoparticles. Carbohydr. Polym. 69, 607–611.

Zick, A.A., Homsy, G.M., 1982. Stokes flow through periodic arrays of spheres. J. Fluid Mech. 115, 13–26.

List of publications arising from this thesis

Journal papers

[1] **Y. Jin**, N. Hengl, S. Baup, F. Pignon, N. Gondrexon, A. Magnin, M. Sztucki, T. Narayanan, L. Michot, B. Cabane. **(2014)**. *Effects of ultrasound on colloidal organization at nanometer length scale during cross-flow ultrafiltration probed by in-situ SAXS*. **Journal of Membrane Science.** 453, 624–635.

[2] **Y. Jin**, N. Hengl, S. Baup, F. Pignon, N. Gondrexon, M. Sztucki, G. Gésan-Guiziou, A. Magnin, M. Abyan, M. Karrouch, D. Blésès. **(2014).** *Effects of ultrasound on cross-flow ultrafiltration of skim milk: Characterization from macro-scale to nano-scale.* **Journal of Membrane Science.** *470*(0), 205–218

[3] **Y. Jin,** N. Hengl, S. Baup, F. Pignon, N.Gondrexon, M. Sztucki, A. Romdhane, A. Guillet, M. Aurousseau. **(2015)**. *Ultrasonic assisted cross-flow ultrafiltration of starch and cellulose nanocrystals suspensions: characterization at multi-scales.* **Carbohydrate polymers.** (Accepted)

[4] N. Hengl, **Y. Jin,** F. Pignon, S. Baup, R. Mollard, N. Gondrexon, A. Magnin, L. Michot, E. Paineau. **(2014)**. *A new way to apply ultrasound in cross-flow ultrafiltration: Application to colloidal suspensions.* **Ultrasonics Sonochemistry**. *21*(3), 1018–1025.

[5] N. Gondrexon, L. Cheze, **Y. Jin,** M. Legay, Q. Tissot, N. Hengl, S. Baup, P. Boldo, F. Pignon, E. Talansier. **(2014)**. *Intensification of heat and mass transfer by ultrasound: application to heat exchangers and membrane separation processes.* **Ultrasonics Sonochemistry**. (Publishing).

Oral presentations

[1] **Y. Jin**, N. Hengl, S. Baup, F. Pignon, N. Gondrexon, M. Sztucki, T. Narayanan, L. Michot, G. Gésan-Guiziou, B. Cabane. *Ultrasonic assisted fouling control during ultrafiltration of colloidal dispersions: characterization from macro-scale to nano-scale.* The 10th International Congress on Membranes and Membrane Processes (**ICOM 2014**), 20-25 July 2014, Suzhou, China.

[2] **Y. Jin**, N. Hengl, S. Baup, F. Pignon, N. Gondrexon, M. Sztucki, T. Narayanan, G. Gésan-Guiziou. Cross flow ultrafiltration of skim milk assisted by ultrasound: multi-scale characterization. 14th Meeting of European Society of Sonochemistry (**ESS 2014**), 2-6 Juin 2014, Avignon, France.

[3] **Y. Jin**, N. Hengl, S. Baup, F. Pignon, N. Gondrexon, A. Magnin, M. Sztucki, T. Narayanan, L. Michot, B. Cabane. *Effects of ultrasound on colloidal organization at nanometer length scale during cross-flow ultrafiltration probed by in-situ SAXS*. **ESRF Users' Meeting 2014**. 3-5 February 2014, Grenoble, France.

[4] F. Pignon, **Y. Jin**, N. Hengl, S. Baup, N. Gondrexon, A. Magnin, A. Romdhane, A. Guillet, E. Mauret, M. Sztucki, T. Narayanan. *In-situ SAXS characterization of SNC and CNC dispersions submitted to simultaneous ultrasonication, shear flow and pressure during cross-flow membrane separation process.* International Polysaccharide Conference (**EPNOE 2013**), 21-24 October 2013, Nice, France.

[5] **Y. Jin**, N. Hengl, S. Baup, F. Pignon, N. Gondrexon, A. Magnin, M. Sztucki, T. Narayanan, L. Michot, B. Cabane. Nouvelle méthodologie d'intensification par ultrasons du procédé d'ultrafiltration : caractérisation *in-situ* des couches de polarisation de concentration par diffusion de rayons x aux petits angles. 14ème Congrès de la Société Française de Génie des Procédés (**SFGP 2013**), 3-5 October 2013, Lyon, France. **Keynote.**

[6] **Y. Jin**, N. Hengl, S. Baup, F. Pignon, N. Gondrexon, A. Magnin, M. Sztucki, T. Narayanan, L. Michot, B. Cabane. *In-situ characterization of concentrated layer at nanometer length scale by SAXS during ultrasonic-assisted cross-flow ultrafiltration.* Engineering with Membranes (**EWM 2013**), 3-7 September 2013, Saint-Pierre d'Oléron, France. **Best oral presentation award.**

[7] **Y. Jin**, N. Hengl, S. Baup, F. Pignon, N. Gondrexon, A. Magnin, L. Michot, E. Paineau. *Effet des ultrasons aux interfaces membranaires lors de l'ultrafiltration de colloïdes : intensification du procédé.* 47ème Colloque National du Groupe Français de Rhéologie (**GFR 2012**). 29-31 October 2012, Pau, France.

[8] **Y. Jin**, A. Romdhane, N. Hengl, S. Baup, F. Pignon, A. Guillet, E. Mauret. *Production de nanocristaux de polysaccharide en continu par séparation membranaire sous ultrasons.* Journée Scientifique du Comité de Développement du Génie des Procédés en Rhône-Alpes (**CODEGEPRA 2012**). 18 October 2012, St Etienne, France.

Poster presentations

[1] N. Hengl, **Y. Jin**, S. Baup, F. Pignon, N. Gondrexon, M. Sztucki, T. Narayanan, G. Gésan-Guiziou. *Intensification de l'ultrafiltration tangentielle du lait assistée par ultrasons : De l'échelle nanométrique au procédé.* Intégration des membranes dans les procédés (**MEMPRO 5**). 9-11 April 2014, Toulouse, France.

[2] **Y. Jin**, N. Hengl, S. Baup, F. Pignon, N. Gondrexon, A. Magnin, M. Sztucki, T. Narayanan, L. Michot, B. Cabane, A. Romdhane, A. Guillet, E. Mauret. *Effet des ultrasons sur l'organisation colloïdale à l'échelle nanométrique en ultrafiltration.* Journée Des Doctorants 2013, Ecole Doctorale I-MEP^2, 21 June 2013, Grenoble, France. **1er Prix du Poster (First Prize of poster)**.

[3] **Y. Jin**, N. Hengl, S. Baup, F. Pignon, N. Gondrexon, A. Magnin, M. Sztucki, T. Narayanan, L. Michot, B. Cabane. *Effet des ultrasons sur l'organisation colloïdale a l'echelle*

nanometrique en ultrafiltration. 2ndes Journées Sonochimie : Ultrasons et Procédés (**J-SUP 2013**). 11-12 June 2013, Chambéry, France. **Prix du Meilleur Poster (Best poster award).**

[4] **Y. Jin**, N. Hengl, S. Baup, F. Pignon, N. Gondrexon, A. Magnin, M. Sztucki, T. Narayanan, L. Michot, B. Cabane, A. Romdhane, A. Guillet, E. Mauret. *In-situ SAXS characterization of colloids submitted to simultaneous ultrasonication, shear flow and pressure during cross-flow membrane separation processes.* **ESRF Users' Meeting 2013**. 4-6 February 2013, Grenoble, France.

[5] **Y. Jin**, A. Romdhane, N. Hengl, S. Baup, F. Pignon, A. Guillet, E. Mauret. *Cross-flow Membrane Separation Process Of Starch Nanocrystals: Application To The Production Of Bio-based Product And Improvements.* **Euromembrane 2012**. 23-27 September 2012, London, UK.

[6] **Y. Jin**, A. Romdhane, N. Hengl, S. Baup, F. Pignon, A. Guillet, E. Mauret. *Production de nanocristaux de polysaccharide en continu par séparation membranaire sous ultrasons.* Journée Scientifique du Comité de Développement du Génie des Procédés en Rhône-Alpes (**CODEGEPRA 2012**). 18 October 2012, St Etienne, France.

*Underlined name indicates the presentator.

Résumé

I Introduction

I-1 Procédés de séparation membranaire

La séparation membranaire est un procédé dans lequel une force comme le gradient de pression, un potentiel chimique ou électrique engendre une séparation au travers de membranes semi-perméables. Le composé qui traverse la membrane, constituée des fluides (des liquides ou des gaz) et des solutés de faible masse moléculaire, s'appelle perméat, alors que la matière qui est maintenue par la barrière sélective, constituée des solides et des solutés suspendus du poids, s'appelle le rétentat. Ce procédé de séparation est purement physique et les deux fractions séparées (perméat et rétentat) peuvent servir à différentes applications. Ce procédé est souvent employé dans l'industrie et la recherche pour épurer ou concentrer une solution diluée. Parmi les différentes forces motrices applicables, c'est le gradient de pression qui est le plus utilisé dans différents secteurs d'activités. Par conséquent, cette thèse a portée sur ce type de force motrice.

Le procédé de séparation membranaire a gagné une place importante dans les domaines de l'agroalimentaire, de la pharmaceutique, de la purification de l'eau ainsi que du traitement des effluents industriels et est efficace pour une large gamme d'applications. L'ultrafiltration tangentielle est l'un des développements les plus courants en technologie membranaire pour séparer et/ou concentrer les particules colloïdales (acide humique, colloïdes minéraux, macromolécules, protéines, etc.). C'est un procédé complexe dans lequel des particules colloïdales sont simultanément soumises à l'écoulement de cisaillement et de compression, induit respectivement par le débit tangentiel (Q_v) et la pression transmembranaire (PTM). Un tel procédé est principalement limité par l'accumulation de la matière sur la surface de la membrane qui entraine deux phénomènes : la polarisation de concentration et le colmatage de membrane. Les événements menant à la formation d'une couche concentrée près de la surface de la membrane ont lieu à des échelles de longueur allant du nanomètre à la centaine de micromètre. Les interactions entre les particules à ces échelles sont très importantes, ce qui exige une compréhension fine des interactions colloïdales pendant un tel procédé.

Provenant de diverses forces, les interactions colloïdales sont grandement responsables des propriétés de transport des colloïdes, telles que le gradient de diffusivité, les propriétés

d'écoulement et les propriétés thermodynamiques telles que la pression osmotique. Ces propriétés sont considérées comme des facteurs principaux pendant l'ultrafiltration des colloïdes. En conséquence, un effort de recherche considérable a été mené pour comprendre les mécanismes mis en jeu lors de ce procédé et en les identifiant convenablement.

Cependant, la compréhension des mécanismes gouvernant le procédé ultrafiltration tangentielle n'est pas encore parfaitement atteinte jusqu'à présent. La modélisation de ce procédé a été étudiée depuis vingt ans, plusieurs approches ont été proposés mais sont très souvent limitées aux colloïdes de sphères dures mono disperses, alors que les colloïdes traités dans le monde réel sont souvent poly disperses, déformables avec divers caractères morphologiques. En outre, de nombreuses techniques ont été utilisées pour caractériser ce procédé mais à l'heure actuelle aucun résultat ne peut fournir une version globale des phénomènes qui s'établissent au cours de l'ultrafiltration tangentielle des divers colloïdes, et particulièrement à proximité de la paroi de la membrane. Afin de progresser sur la modélisation et la compréhension fondamentale de ce procédé il est nécessaire d'atteindre une caractérisation précise, non destructive, en temps réel et *in-situ* de la couche concentrée de particules pendant la filtration.

En conséquence, un des premiers buts de cette thèse est de caractériser *in-situ* et en temps réel les couches de colloïdes déposés et concentrés sur les membranes lors de leur ultrafiltration tangentielle et ceci aux échelles pertinentes des colloïdes traités, c'est à dire aux échelles mésoscopiques (du nanomètre à la fraction de micromètre).

I-2 SAXS

Pour atteindre un tel but, des mesures de diffusion des rayons X aux petits angles (SAXS) ont été effectuées à l' « European Synchrotron Radiation Facility » (ESRF) avec une cellule de filtration spécialement conçue. Basée sur la diffusion élastique, la diffusion de rayons X aux petits angles est souvent utilisée pour sonder la dynamique des micro-structure à l'équilibre et hors-équilibre de la matière molle. Elle peut donner accès à la taille moyenne de particules, à la forme et à l'organisation structurelle des dispersions de colloïdes. En plus de cela, elle peut

également fournir des informations sur la concentration en colloïdes par une analyse appropriée, ce qui est directement en relation avec la problématique posée dans ce travail.

I-3 Ultrasons

Pour un procédé couramment utilisé en industrie, l'augmentation de la productivité exige une amélioration de leur performance, notamment dans leur mise en œuvre pour les procédés de séparation membranaire. Une grande variété d'approches ont été proposées pour améliorer l'ultrafiltration tangentielle par une maîtrise de l'accumulation de matière (souvent appelée contrôle de colmatage). Parmi ces nombreuses techniques de contrôle de colmatage, l'approche liée aux ultrasons a gagné une grande attention. À ce jour, un certain nombre de travaux mettent en évidence l'efficacité de l'application d'ultrason dans le nettoyage de membrane et le contrôle du colmatage.

Les ultrasons (US) sont définis comme des ondes sonores dont les fréquences sont au-delà de 18 kHz jusqu'à la gamme du MHz voir au GHz. Les ondes ultrasonores se propagent par un mouvement longitudinal (compression/décompression), qui induit simultanément une variation de pression spatiale et temporelle dans les milieux qu'ils traversent. De la propagation d'une onde ultrasonore dans un milieu liquide, de nombreux phénomènes peuvent survenir. Les principaux phénomènes connus sont les courants acoustiques, l'agitation locale ou « micro-streaming », la cavitation et les effets thermiques, comme présenté par Fig.1.11.

Les courants acoustiques correspondent à un écoulement induit par la propagation de l'onde acoustique dans un milieu. L'étendue effective du courant acoustique est sur l'ordre du centimètre à la dizaine de centimètres (Lamminen *et al*., 2004), avec une vitesse d'écoulement entre 1 à 100 $cm.s^{-1}$ qui peut varier légèrement avec la puissance et la fréquence ultrasonore (Loh *et al*., 2002; Nomura *et al*., 2002).

La cavitation acoustique se manifeste par la formation, la croissance, l'oscillation et l'effondrement des bulles de gaz sous l'influence d'un champ ultrasonore dans les liquides. L'effondrement des bulles de cavitation conduit à la formation d'une micro-échelle « point chaud » qui s'exprime à haute température (jusqu'à 6000 K) et pression élevée (jusqu'à 200 MPa)

(Neppiras, 1980). Ces points chauds transitoires ont des conséquences comme la formation de radicaux qui pourraient servir à de nombreuses applications chimiques, par exemple la lyse et la dégradation de molécules en solution. On estime que l'implosion des bulles a lieu à des échelles de temps de l'ordre de la micro-seconde, et des échelles de longueurs de taille de bulle d'environ 10^{-4} m, selon la fréquence. Par conséquent, l'ordre de grandeur de vitesse de déplacement de particules pendant l'implosion des bulles, peut être estimé à un ordre de grandeur de 100 $m.s^{-1}$. Sans surprise, ce mouvement de liquide de vitesse élevée s'il se produit à l'interface solide-liquide, peut perturber les couches limites thermiques ou de matière entrainant une réduction de la résistance du transfert de chaleur et du transfert de masse (Legay *et al*., 2011).

Il existe aussi un autre type de courant se produisant près de petits obstacles (bulle de gaz ou surface solide) placés dans un champ acoustique qui proviennent des forces de friction entre la frontière et le milieu (Leighton, 1994). Différents des courants acoustiques, cette circulation indépendante du temps, se produit seulement dans une petite région du fluide, souvent dans le voisinage de la couche limite, il se nomme donc micro-streaming. Spengler *et al.* ont mis en évidence le champ de vitesse de micro-streaming d'une suspension de latex par des mesures de vélocimétrie par images de particules (PIV) et ont trouvé une vitesse de micro-streaming moyenne de 450 $\mu m.s^{-1}$ pour une onde ultrasonore de 3,2 MHz avec une pression acoustique d'environ 0,5 MPa (d'amplitude) (Spengler *et al*., 2003).

L'absorption de l'onde ultrasonore par un milieu peut convertir l'énergie acoustique finalement en chaleur, ce qui peut conduire à l'effet thermique : chauffage du milieu. Cet effet est le principe fondamental des mesures calorimétriques proposées par Mason (Mason, 1991) pour la détermination de puissance dissipée par ultrasons.

I-4 Ultrasons-assistés filtration

A partir de 1980, quand les US ont été appliqués pour la première fois pour intensifier le procédé de séparation membranaire (Okahata and Noguchi, 1983), de plus en plus d'investigations ont été rapportées dans la littérature qui mettent en évidence : *i)* l'efficacité du nettoyage des membranes (Ahmad *et al*., 2012; Chai *et al*., 1999; Gonzalez-Avila *et al*., 2012;

Lamminen *et al*., 2006) *ii)* le contrôle du colmatage (Ahmad *et al.*, 2012; Mirzaie and Mohammadi, 2012; Muthukumaran *et al*., 2007), grâce aux actions induites par sa propagation, telle que les vibrations de particules, la cavitation et les courants acoustiques (Lamminen *et al.*, 2004). La plupart de ces travaux de recherches couplant US et filtration, ont utilisés un bain ultrasonore pour la filtration tangentielle ou une onde acoustique pour la filtration frontale. Ces deux types de méthodologies présentent des limitations, telles que la perte d'énergie de haut niveau, aucun accès aux effets à proximité du champ ultrasonore (cas de filtration tangentielle) ou un potentiel limité pour l'application industrielle (cas de filtration frontale). Par conséquent, une étude plus approfondie basée sur les besoins industriels rend nécessaire une conception nouvelle d'un module permettant de coupler les ultrasons avec la filtration tangentielle directement appliquée aux fluides à traiter.

Une cellule de filtration spécialement conçue pour ce travail de thèse a ainsi été développée au Laboratoire Rhéologie et Procédés en couplant un système ultrasonore adapté à une cellule d'ultrafiltration tangentielle sous SAXS. Elle permet, d'une part, d'appliquer les ondes ultrasonores au voisinage de la membrane ; d'autre part, d'accéder en temps réel, à l'organisation structurale *in-situ* de la couche concentrée à l'échelle nanométrique par des mesures de SAXS.

Un des objectifs principaux de cette thèse est donc d'examiner l'effet de l'application des ultrasons sur la performance de filtration et les changements structurels associés dans la couche concentrée pendant l'ultrafiltration tangentielle assisté par ultrasons.

Avec cet objectif, nous avons décidé d'étudier plusieurs colloïdes de divers caractères (nature, taille, forme, propriété physico-chimique) pour élargir la gamme explorée et pour approfondir la compréhension de ce procédé. Deux dispersions d'argile (des dispersions d'argile synthétique et deux dispersions d'argile naturelles) et deux suspensions colloïdales ayant un grand intérêt pour l'industrie (des suspensions nano-cristaux de polysaccharides et des suspensions de micelles de caséines : lait écrémé) ont été mise en œuvre dans cette étude. Il est important de souligner que le procédé d'ultrafiltration tangentielle devient plus complexe en rajoutant les US : hormis les interactions internes qui peuvent fortement influencer la performance de filtration, les colloïdes dans ce cas sont simultanément soumis à la compression, à l'écoulement de cisaillement aussi bien qu'à une force ultrasonore, comme montré dans la figure ci-dessous :

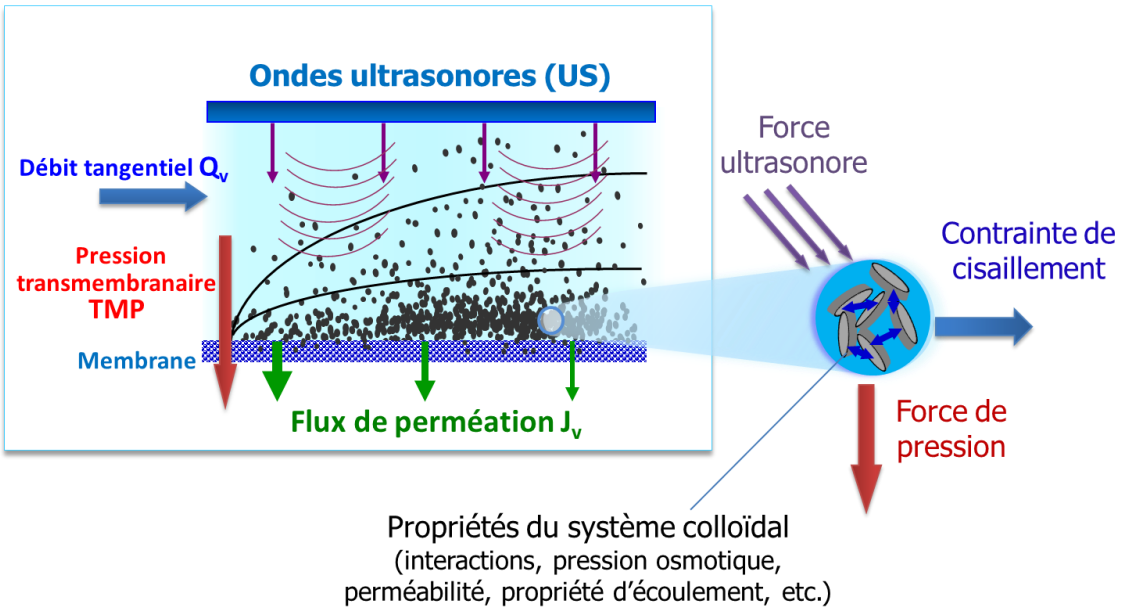

Fig.R.1 *Suspensions colloïdales dans l'ultrafiltration tangentielle sous US*

II Matériel et méthodes

II-1 Colloïdes étudiés

Comme indiqué précédemment, des suspensions colloïdales de différentes structures sont étudiées dans cette étude. La Fig. R.2 schématise leurs propriétés de structure. A et B représentent les suspensions synthétiques d'argile, Laponite, se composant de petites disquettes avec un diamètre environ de 30 nm et une épaisseur de 1 nm. La structure des dispersions au repos se compose des sous-unités mesurant quelques dizaines de nanomètres, qui s'organisent sous l'effet des forces d'attraction et de répulsion agissant entre les particules. Elles se combinent alors pour former des agrégats denses mesurant environ 1 µm. À de plus grandes échelles de longueurs, ces agrégats de taille d'un micromètre sont réarrangés pour former une structure isotrope tridimensionnelle continue, donnant au gel sa structure tridimensionnelle qui est responsable de l'apparition d'une contrainte seuil (Pignon *et al*., 1998).

Des peptisants sont utilisé généralement pour contrôler les interactions entre particules (Martin *et al*., 2002). Le peptisant utilisé dans cette étude est le diphosphate tétrasodium (abrégé

tspp ci-après). Deux concentrations de peptisant (C_{tspp}) ont été étudiées (0 % et 6 %) de la masse d'argile sèche. L'addition du tspp dans ce travail a permis de réduire les interactions du réseau de particules et a conduit à une modification des propriétés d'écoulement depuis un comportement de gel à seuils de contrainte (C_{tspp} = 0 %) vers un fluide rhéo-fluidifiant (C_{tspp} = 6 %).

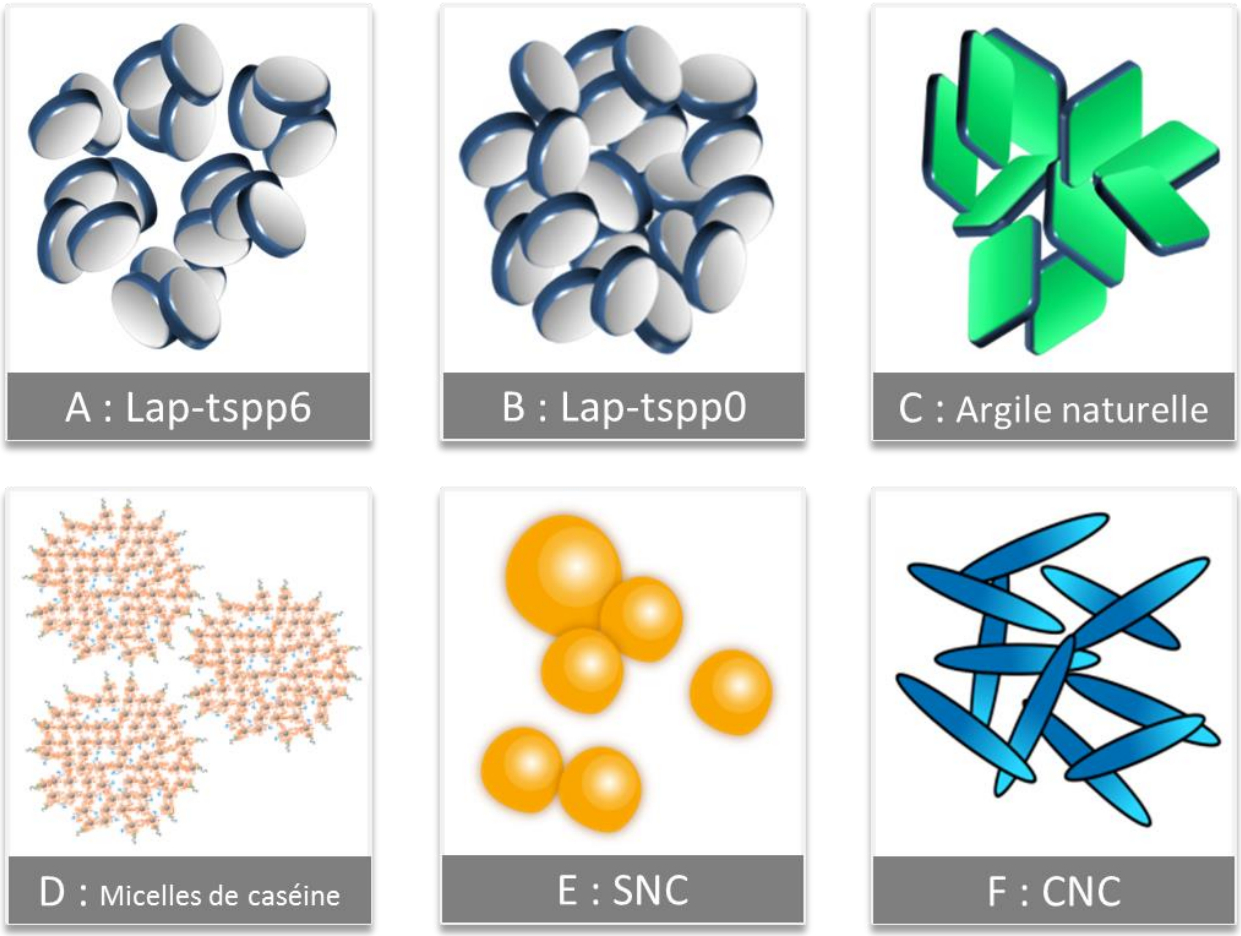

Fig.R.2. *Représentations schématiques de la structure des colloïdes étudiés*

Deux types d'argile gonflantes ont été étudiées. Toutes les deux sont des smectites dioctahedrales : (I) une Montmorillonite du Wyoming (SWy-2), (ii) une Nontronite d'Australie (NAu-1). Elles se composent des plaquettes qui ont des rapports d'aspect élevés (20-1000). Les composés d'aluminosilicate sont typiquement formés de deux couches tétraédriques entourant une couche octaédrique. Il est admis que la structure de gel se stabilise par les répulsions électrostatiques entre les doubles couches des plaquettes. Une des propriétés les plus importantes des minéraux d'argile naturellement gonflés est leur capacité de former des matériaux à seuils de

contraintes une fois dispersée dans l'eau. Ces suspensions aqueuses peuvent avoir une transition isotrope/nématique, à concentration élevée, la phase nématique présente une forte orientation de particules qui peuvent s'alignées sous des champs magnétiques, une caractéristique distinctive de la phase cristal liquide. (Michot *et al*., 2006).

Le lait écrémé contient les particules colloïdales qui se composent d'associations complexes de protéine et de phosphate de calcium. Ces protéines associées en structures hétérogènes sont appelés les micelles de caséine, elles sont constituées de quatre caséines distinctes (α_{s1}, α_{s2}, β et κ). Il a été montré (Brans *et al*., 2004; Holt *et al*., 2003; Pignon *et al*., 2004; Shukla *et al*., 2009) que l'intérieur de la micelle se compose d'une association des caséines et du phosphate de calcium colloïdal alors que l'extérieur de la micelle est principalement composé de la κ-caséine hydrophile. Cette couche externe négativement - chargée s'appelle « la couche velue » qui fournit une stabilité stérique à la micelle de caséine et par conséquent empêche leur agrégation (Fig.R.2.D).

Les nanocristaux d'amidon (SNC) résultent de la rupture des granules cireux de fécule de maïs par hydrolyse acide. Pour des suspensions de SNC, une poly-dispersité élevée a été mise en évidence avec des particules/agrégats ronds s'étendant de la centaine de nanomètres à quelques micromètres. Les nanocrystaux de cellulose (CNC) dérivés de l'hydrolyse acide de la cellulose naturelle possèdent différentes morphologies selon les origines et les conditions d'hydrolyse. Généralement, ce sont des cristaux de bâtonnets rigides d'un diamètre de l'ordre de 10 – 20 nm et de longueurs de quelques centaines de nanomètres. Il est à noter que les CNC sont très polaire et peuvent s'attirer par liaison d'hydrogène ; ils ont ainsi tendance à former des paquets ou des agrégats (Lu and Hsieh, 2010; Marcovich *et al.*, 2006). À basse concentration, les particules de CNC sont aléatoirement orientées dans la suspension aqueuse formant une phase isotrope, mais quand la concentration atteint une valeur critique, elles forment une structure chirale nématique où les suspensions de CNC passent d'une phase isotrope à une phase cristalline anisotrope (Revol *et al*., 1992). À concentration croissante il a été montré que les suspensions aqueuses de CNC présentent une biréfringence sous écoulement de cisaillement.

II-2 Installation expérimentale

« Une cellule d'ultrafiltration tangentielle sous SAXS couplée aux ultrasons » (Fig.2.8) a été développée pour d'une part, appliquer des ondes ultrasonores près de la membrane en positionnant dans le compartiment d'alimentation une lame vibrante en titane et d'autre part, pour suivre *in-situ* l'organisation de structure de la couche concentrée par SAXS. Cette cellule est faite de polycarbonate transparent et contient une membrane plate d'ultrafiltration en polyethersulfone (MWCO = 100 kD, PleyadeRayflow x100, Rhodia Orelis). Placée au-dessus de la membrane plate à une distance de 8 mm, cette lame vibrante est reliée à un sonotrode se composant d'un transducteur piézoélectrique fixé à une tige en métal, qui produit des ondes ultrasonores à une fréquence de 20 kHz et à une amplitude appliquée de 1,6 µm (SODEVA TDS, France). La puissance électrique d'alimentation s'étend de 2 à 10 W, correspondant à l'intensité ultrasonore de 0,6 à 2,9 $W.cm^{-2}$ (la puissance d'alimentation par unité de surface de la lame). Le canal d'alimentation est de 100 mm de long dans la direction de flux tangentiel et de 4 × 8 mm (largeur × hauteur) dans la section d'écoulement. Trois fenêtres de 3 × 5,5 × 0,3 mm (hauteur × largeur × épaisseur) sont ouvertes localisées en amont, au milieu et en aval dans le compartiment d'alimentation avec une distance de 43 mm entre elles. La cellule de filtration a été montée sur une table motorisée, ce qui permet de déplacer la cellule devant le faisceau de rayons X et de suivre par SAXS la concentration et l'organisation structurale des suspensions à des distances différentes de la membrane aussi bien qu'à différentes positions le long de la membrane.

Comme montré par Fig.2.9, lors des essais, la suspension d'alimentation est pompée (LF series, MONO PUMPS, UK) depuis un récipient haute pression (MILLIPORE, France) en direction de la cellule de filtration, et le débit tangentiel est mesuré en continu par un débitmètre magnétique (Optiflux 6300C, KROHNE, France). La pression est appliquée par de l'air comprimé purifié, et est enregistrée en continu par 2 sondes de pression (FP110, FGP SENSORS & INSTRUMENT, France) à l'entrée et à la sortie de la cellule de filtration. La température est maintenue à 25±1°C par le biais d'un cryo-thermostat (Thermo &Scientific SC 150 A25, HAAKE, Germany) et est vérifiée en continu par 2 capteurs (YC-747D with K thermocouples, YU CHING TECHNOLOGY, Taiwan) disposés à l'entrée et à la sortie de la cellule de filtration. Le flux de perméat J_v ($L.h^{-1}.m^{-2}$) est enregistré via la mesure de la masse de perméat toutes les 5 secondes, avec une précision de 0,001 g (Balance 400M, PRECISA, France).

II-3 Caractérisation du système ultrasonore

La vibration, l'intensité et l'activité de cavitation du système ultrasonore utilisé ont été caractérisées.

La vibration de la lame est mesurée par vibrométrie laser. D'après la Fig.2.13, la vibration de la lame n'est pas homogène, et peut être distinguée par quatre zones. La zone zéro (B0) correspond au bloc au-dessous du sonotrode qui ne pouvait pas être mesuré pendant la filtration. B1 représente les zones près de B0 où l'amplitude de déplacement est presque constante avec une valeur de 1,6 µm (commande d'amplitude des US = 100%). Au milieu de chaque côté de la lame, B2, il apparaît une faible vibration. À l'extrémité de cette zone, on revient au même niveau que B1, ensuite le système présente alors un délabrement progressif aux extrémités de la lame, dénotées B3.

L'intensité ultrasonore a été estimée par la méthode de calorimétrie (Mason, 1999). comme indiqué dans la Fig.2.16 et le Tab.2.5, la puissance acoustique effective (dissipée) augmente avec l'alimentation électrique, et le rendement d'énergie (dénoté comme η_E, puissance dissipée/ alimentation électrique, %) varie de 35 % à 83 %. La perte de puissance semble être plus importante à alimentation électrique élevée (η_E= 35 % quand la puissance d'alimentation est 10±1 W ; 83 % quand la puissance d'entrée est 2±1 W). Dans cette étude, l'amplitude ultrasonore est souvent réglée à 80 % (7±1 W) et le rendement d'énergie est d'environ 36 % dans ces conditions.

L'activité de cavitation a été évaluée par des essais d'érosion par cavitation. Les résultats affichés dans Fig.2.17 – 2.19 suggèrent que la zone principale d'action de la cavitation se situe dans le volume plutôt que sur la surface de la membrane pendant la filtration, et plutôt dans la zone située au-dessous de la sonotrode. Combiné avec l'évaluation de vibration, on peut déclarer que la puissance ultrasonore est plus élevée au milieu du canal que sur les deux extrémités où la perte d'amplitude est plus prononcée.

II-4 Mesures SAXS et analyses

Des mesures de SAXS ont été effectuées au ID2 High Brilliance SAXS/WAXS/USAXS Beamline (Narayanan *et al*., 2001), à the European Synchrotron Radiation Facility (ESRF, Grenoble, France). Le faisceau incident de rayons X de longueur d'onde (λ) 0,1 nm, a été collimaté à 20 µm verticalement et 200 µm horizontalement en utilisant des fentes. On a employé deux distances d'échantillon/détecteur qui ont fourni une gamme de vecteur de diffusion q de 0,01 nm^{-1} à 6 nm^{-1}, où $q = (4\pi/\lambda) \sin(\theta/2)$ avec θ l'angle de diffusion, qui correspond à une gamme d'échelle de longueur ($l = 2\pi/q$) de 1 à 600 nm. Le rayon incident a traversé l'échantillon et l'intensité diffusée a été enregistrée sur un détecteur CCD de haute résolution sous forme de spectre de diffusion bidimensionnel. Ces spectres obtenus ont été ensuite normalisés à une échelle d'intensité absolue après application de la correction standard du détecteur puis ramenés à une moyenne radiale pour obtenir le profil d'intensité $I(q)$.

La diffusion du milieu suspendant des différentes cellules remplies d'eau distillée a été systématiquement soustraite (David *et al*., 2008; Pignon *et al*., 2012) de l'intensité diffusée par l'échantillon correspondant. Tandis que de l'information qualitative pourrait être directement obtenue à partir des spectres bidimensionnels tels que l'anisotropie et l'orientation des particules, la modélisation quantitative d'$I(q)$ fournit la taille moyenne, la forme des particules et leur organisation structurelle (David *et al*., 2008). Des mesures *in-situ* ont été effectuées utilisant la cellule de filtration tangentielle représentée dans la fig. 2.8. La distance z de la surface de la membrane (David *et al*., 2008) a été exactement évaluée par des mesures d'intensité transmises. La distance minimum pour obtenir des données exploitables de SAXS au-dessus de la membrane était de 20 µm.

Afin de déterminer les concentrations d'échantillon dans la couche concentrée pendant la filtration, une courbe d'étalonnage a été premièrement établie. Deux approches ont été employées pour obtenir cette courbe d'étalonnage : à l'aide des profils $I(q)$ ou des profils $S(q)$.

Courbe d'étalonnage depuis profils I(q)

L'intensité diffusée provient du contraste qui représente la différence de densité d'électrons entre la particule et le milieu dans l'échantillon liquide. Par conséquent, pour un système défini de particule-solvant, l'intensité diffusée est proportionnel au nombre de particules par volume unitaire pour les valeurs de q correspondantes à $S(q) = 1$. Autrement dit, la concentration de la solution peut être déterminée à partir de l'intensité diffusée dans la gamme de valeurs q élevées.

Pour caractériser les suspensions initiales, des mesures de SAXS sur plusieurs dispersions des fractions volumiques connues ont été effectuées dans une cellule capillaire à température contrôlée à 25±1 °C (diamètre ~ 2 mm). Ceci nous a permis d'établir des relations entre les intensités diffusées et les fractions volumiques, menant à une courbe d'étalonnage. Avec les courbes d'étalonnage obtenues, la concentration des échantillons colloïdaux filtrés a pu être déterminée en comparant leur intensité diffusée absolue à un vecteur de diffusion donné. Comme mentionné avant, l'intensité de la diffusion du milieu suspendant a été systématiquement soustraite. Le Tableau 2.6 résume les vecteurs de diffusion choisis ainsi que les relations d'intensité-concentration pour les dispersions colloïdales étudiées dans cette thèse. Les courbes d'étalonnage sont présentées dans la Fig. 2.25. Ces équations ont été établies dans la partie correspondante au facteur de forme $P(q)$ des particules qui n'est pas affecté par le changement des interactions inter-particulaires (décrites par le facteur de structure $S(q)$) et donc valide même à des concentrations plus élevées.

Courbe d'étalonnage depuis profils S(q)

Les spectres 2D de SAXS des suspensions naturelles d'argile sont anisotropes dus à l'alignement mutuel des particules. A partir du $S(q)$ il apparaît un pic de diffusion marqué qui corresponde à l'ordre de position à courte portée des plaquettes. Une évaluation de la distance inter-particulaire moyenne expérimentale peut être déduite de la position de ce pic dans les oscillations de l'intensité diffusée, permettant une estimation de la loi de gonflement qui relie la distance inter-particulaire à la fraction volumique.

Pour accéder à la fraction volumique dans les couches concentrées pendant la filtration, les profils S(*q*) correspondant aux spectres enregistrés dans la « cellule d'ultrafiltration tangentielle sous SAXS couplée aux ultrasons » sont tracés pour chaque position de z. La distance inter-particulaire correspondante $d(z) = 2\pi/q_{pic}$ est extraite à chaque position de z dans les couches concentrées. Le profil de concentration $\phi_v(z)$ peut être donc déduit en utilisant la loi de gonflement.

III Ultrafiltration assistée par US de suspensions d'argile

III-1 Dispersions de Laponite

III-1.1 Propriétés d'écoulement des dispersions de Laponite

Des dispersions de Laponite de ϕ_v = 1-3 % ont été spécifiquement préparées pour l'étude et leurs propriétés d'écoulement après différents traitements (par exemple pré-cisaillement et traitement ultrasonore) ont été analysées. Une bonne concordance de la dépendance entre la contrainte seuil et la fraction volumique des dispersions de Laponite est trouvée entre la littérature et nos résultats. L'effet du pré-cisaillement et du traitement des US sur la contrainte seuil de l'échantillon de Laponite est mis en évidence. Les deux traitements réduisent leurs niveaux de contrainte de seuil. La réduction est plus importante pour les suspensions de Laponite avec peptisant dont les contraintes seuil sont inférieures à celles sans peptisant. Ceci suggère que les dispersions de Laponite avec peptisant (6%) soient plus sensibles aux forces de cisaillement ou ultrasonores que celles sans peptisant, résultant de la réduction des forces attractives entre les particules. Cette différence dans le comportement aura quelques conséquences sur l'accumulation de particules près de la surface de la membrane pendant le procédé d'ultrafiltration.

III-1.2 Effet des US sur les propriétés de dispersion de Laponite pendant la filtration

Les propriétés des dispersions de Laponite traitées dans la filtration ont été caractérisées par deux approches : mesures rhéomètriques et SAXS *in-situ*. Les résultats suggèrent que les US permettent de faire couler plus facilement les dispersions de Laponite traitées comme le fait la force de cisaillement, mais son effet est moins prononcé que la force de cisaillement (ex. la

pompe). Quant aux mesures de SAXS *in-situ*, on n'observe aucune influence significative des US sur la structure des suspensions de Laponite aux échelles de longueur de 3 à 600 nm. En outre, aucune modification de la taille et de la forme des particules provoquées par les US ne peut être observée puisque les intensités diffusée de tous les échantillons sont exactement identiques aux échelles de longueur des particules (au-dessus de 0,4 nm^{-1}, correspondant à une longueur de 15 nm, dans l'ordre grandeur du diamètre moyen des disques de Laponite).

III-1.3 Effet des US sur l'ultrafiltration à l'échelle macroscopique

Selon la procédure de filtration proposée par Espinasse et *al.* (2002), des paliers alternant des augmentations et des diminutions de pression transmembranaire ont été effectués, afin de déterminer les phénomènes de polarisation de concentration et de colmatage lors de la filtration. 6 filtrations ont été effectuées avec différent Q_v avec ou sans US. Les résultats indiquent que la polarisation de concentration réversible est le phénomène dominant plutôt que la formation de dépôt irréversible dans la filtration des dispersions de Laponite. Un flux limite est atteint très rapidement au tout début de la filtration, puisque le flux de perméation augmente à peine quelque soit la PTM appliquée. L'apparition de flux limite implique que la couche concentrée de particules est dense bien qu'elle soit réversible.

Généralement l'application des US mène à une augmentation immédiate et significative du flux de perméation, de 3 à 5 fois. D'ailleurs, on a observé différents comportements de filtration : au lieu d'être limité, le flux de perméation continue à augmenter avec PTM jusqu'à 1,4 $\times 10^5$ Pa pour chacune des trois filtrations sous US. Puisque ce flux limite dépend fortement de la couche des particules accumulées concentrée, ceci implique que les ondes ultrasonores appliquées permettent de réduire cette couche concentrée dense. Pour résumer, les US sont efficaces pour intensifier la performance de filtration des dispersions de Laponite, dans le cas où ils sont appliqués directement aux dispersions du côté rétentat. En outre, on n'a observé aucun endommagement de membrane puisque la perméabilité de la membrane demeure stable après chaque filtration sous US. Aucun effet thermique n'a été observé à l'application d'US, puisque les températures moyennes à l'entrée et à la sortie de la cellule de filtration étaient toujours environ 25 °C. En mesurant le pourcentage de poids sec de l'alimentation et du perméat, le taux de

rétention de membrane a été également déterminé. L'application des US n'a pas changé le taux de rétention de la membrane PES utilisée.

III-1.4 Effet des US sur l'ultrafiltration à l'échelle nanométrique

Trois dispersions, de fractions volumiques et de concentrations différentes de peptisant sont concernées : Lap1-tspp6, Lap0.48-tspp6 et Lap1-tspp0 (voir le Tab.3.1 pour la nomenclature). Toutes les filtrations présentées dans cette section ont été effectuées à ESRF, avec des mesures de SAXS *in-situ*, en temps réel. Les profils de concentration et l'organisation structurelle des dispersions de Laponite près de la surface de la membrane pendant la filtration ont été mis en évidence grâce à cette technique puissante.

Lap1-tspp6

Plusieurs paramètres hydrodynamiques ont été explorés et les US étaient appliqués pendant certaines étapes de filtration après l'introduction de la dispersion d'alimentation dans le réservoir, présenté dans la fig. 3.9. En accord avec les résultats aux échelles macroscopiques, on a observé une augmentation significative du flux de perméation avec les US. La couche concentrée a disparu à la fin des étapes avec US, comme indiqué par les mesures de SAXS *in-situ*.

L'application des US semble mener à une rupture de couche concentrée de particules induisant une augmentation de flux de perméation. Il est alors particulièrement important de savoir comment cette couche concentrée a été perturbée. L'évolution des profils de concentration au fil du temps a été étudiée pour chaque étape de filtration, présenté dans la Fig.3.12. Il semble que les US appliqués peuvent désagréger le réseau de Laponite comme une force supplémentaire mais cela prend du temps car l'effet dépend de la résistance de la structure de la Laponite. Par conséquent, les temps de déstructuration d'une couche concentrée ont été réduits pour des étapes consécutives avec les US. En outre, l'étude cinétique de la déstructuration de la couche concentrée sous US (Fig.3.13) suggère que le bas de la couche concentrée de particules (près de la membrane) est la zone cible de la rupture sous US.

La croissance de la couche concentrée sans US a été également étudiée. À l'état transitoire, la matière colloïdale s'accumule à la membrane progressivement. Le profil des couches accumulées suivent une forme exponentielle au-dessus de la membrane à un moment donné pendant la filtration. Les résultats indiquent également que l'effet des US sur la filtration est presque instantané : l'accumulation de la matière sur la surface de la membrane ne peut pas être atténuée quand les US sont coupés. D'ailleurs, des profils de concentration en fonction de Q_v ont été comparés, et ils suggèrent que ce ne soit pas le moyen le plus efficace pour enlever la couche de polarisation de la surface de la membrane.

Enfin, les profils de concentration le long de la membrane en régime permanent de la filtration ont été obtenus (Fig.3.16) puisque trois fenêtres sont disponibles situées à 7 mm, 50 mm et 93 mm de l'entrée de la cellule de filtration. Un profil de concentration x-dépendant a été mis en évidence sans US, qui sont en accord avec les prévisions théoriques (Bhattacharjee *et al*., 1999; Davis and Leighton, 1987; Elimelech and Bhattacharjee, 1998; Romero and Davis, 1988). Une application des US durant 1 heure a alors induit une rupture significative de cette couche concentrée.

Lap0.48-tspp6

Les dispersions de Lap0.48-tspp6 sont moins concentrées et les interactions entre les particules dans la couche concentrée sont plus faibles qu'avec Lap1-tspp6. Ainsi les US ont perturbé immédiatement la partie moins concentrée (partie haute) de la couche accumulée, présenté dans la Fig.3.19b.

L'effet des US sur le système au repos a été également étudié. A PTM et Q_v nuls, aucun flux de perméation n’a été obtenu sous US, ce qui suggère que les US ne provoquent pas de flux de convection vers la membrane (du moins pas aussi fort que celui dû à la PTM). Ensuite une couche concentrée a été préformée et rompue suite à l’application d’US à PTM et Q_v nuls. La partie inférieure de cette couche devient de moins en moins concentrée au fil du temps. Cependant, contrairement à ce qui s’est produit pendant la filtration, les US n'ont pas enlevé cette couche concentrée puisqu'après 10 minutes la réduction de concentration induite par les US est

ralentie et elle commence à suivre un régime de faible oscillation. Ainsi les US appliqués ne peuvent pas à eux-seuls enlever la couche concentrée et l'érosion pendant la filtration est le résultat des actions combinées des US et de des forces hydrodynamiques.

Lap1-tspp0

Les dispersions de Laponite sans peptisant se composent d'un réseau très attractif qui facilite la formation d'agrégats. Dans ce cas, on a observé l'orientation de particules près de la surface de la membrane pendant la filtration. Les US ont augmenté le flux de perméation immédiatement et de manière significative. Cependant, la couche concentrée n'a pas été du tout perturbée par les US comme l'indique les mesures de SAXS, même aux échelles inter-particules.

III-2 Dispersions d'argile naturelle

Cette section concerne deux types de suspensions d'argile naturelle: SWy-2 T3 and NAu-1 T3. Elles se composent des plaquettes de tailles plus grandes que la Laponite, formant un réseau répulsif dû aux forces électrostatiques de double-couche. En raison de l'alignement mutuel des particules, leurs spectres de diffusion par SAXS sont anisotropes. Deux ultrafiltrations sous US ont été effectuées. Pendant la filtration, ces particules sous forme de plaquettes peuvent former une structure fermée dans la couche concentrée que les US appliqués modifieraient à peine. Cependant, une augmentation significative du flux de perméation a toujours été observée sous US, comme le cas de Lap1-tspp0. D'ailleurs, l'augmentation de l'écoulement a réduit la couche concentrée, ce qui conduit à une intensification importante de la performance de la filtration combinée avec les US.

IV Ultrafiltration sous US de colloïdes d'intérêt industriel

IV-1 Lait écrémé

IV-1.1 Propriétés d'écoulement des suspensions de micelles de caséine

Les suspensions montrent un comportement newtonien au-dessous de 4,00*C_o (108 g.L^{-1}) et un comportement rhéo-fluidifiant de 4,00*C_o à 6,80*C_o (183,6 g.L^{-1}). Pour les suspensions de concentrations plus élevées, de 7,00*C_o à 8,00*C_o (de 189 g.L^{-1} à 216 g.L^{-1}), les contraintes seuil apparaissent. Cette évolution du comportement rhéologique ne dépend pas de la nature de la phase aqueuse (l'eau déminéralisées, ultrafiltrat et microfiltrat) pour les suspensions à C_o<C<6*C_o. La transition sol-gel de la suspension de micelles de caséine a été également estimée à 185 g.L^{-1}, au-delà de laquelle la suspension se comporte comme un gel élastique.

IV-1.2 Effet des US sur les propriétés des suspensions d'alimentation pour la filtration (lait écrémé)

Les mesures rhéologiques indiquent que les US appliqués dans notre expérience n'ont exercé aucun effet sur la viscosité d'un lait écrémé concentré (4*C_o). Les profils de SAXS suggèrent également que la structure interne du lait écrémé (vecteur de diffusion *q* de 1 à 0,1 nm^{-1}) n'a pas été affectée par les US.

IV-1.3 Effet des US sur l'ultrafiltration à l'échelle macroscopique

Des ultrafiltrations tangentielles ont été effectuées à trois Q_v différents avec ou sans US. Une procédure de montée-en-escalier de PTM a été employée : une filtration pendant 30 minutes à chaque étape de PTM avec un intervalle de 5 minutes entre les étapes. Sans US, on a observé un flux limite et la performance de filtration a été améliorée par l'augmentation du Q_v. Avec US, le flux limite disparaît et continue à augmenter avec PTM jusqu'à 1,4 $\times 10^5$ Pa. Les résultats impliquent également que les US peuvent augmenter la force hydrodynamique du fluide, similaire à un agitateur mécanique classique. La perméabilité de membrane et le taux de rétention ont été mesurés avant et après chaque filtration ; les US n'ont pas changé la sélectivité de la membrane.

En plus de la filtration de la suspension standard de lait écrémé (C_o), une suspension plus concentrée ($4*C_o$) a été filtrée ; le flux de perméation est devenu assez bas et presque nul pour les PTM faibles, même avec US. On spécule qu'une couche de colmatage fortement cohésive a été formée dès que la filtration a commencé ainsi la membrane a été totalement colmatée quand l'alimentation est concentrée. Dans ce cas, US n'ont apporté aucun changement au comportement de la filtration, ce qui indique que les US n'ont pas perturbé cette couche de colmatage cohésive. Donc, une intensité ultrasonore plus élevée serait nécessaire pour produire de la rupture prévue de cette couche de colmatage.

En outre, différentes intensités ultrasonores étaient appliquées pendant la filtration des suspensions de lait écrémé à C_o. Les facteurs d'amélioration d'US étaient environ 2 pour toutes les intensités appliquées, ce qui indique que l'intensité d'US en conditions de fonctionnement choisies n'a presque pas affectée les performances.

IV-1.4 Effet des US sur l'ultrafiltration à l'échelle nanométrique

Les mesures *in-situ* de SAXS ont mis en évidence pour la première fois l'évolution des profils de concentration sur la surface de la membrane au fil du temps pendant le procédé d'ultrafiltration tangentielle de lait écrémé. L'épaisseur des couches concentrées de lait écrémé en régime permanent est de 120 à 160 µm dans nos conditions opératoires. En outre, l'application d'US a conduit à une rupture partielle de la couche concentrée qui a mené à une augmentation de flux de perméation par un facteur de 2,0 à 4,7. Quand la concentration d'alimentation augmente (de C_o à $2*C_o$), l'effet des US sur la couche concentrée s'est affaibli, ce qui peut s'expliquer par l'équilibre entre les interactions internes dans des suspensions de micelles de caséine et la force ultrasonore.

IV-2 Suspensions des nanocristaux de polysaccharide : SNC et CNC

IV-2.1 Caractérisation des nanocristaux

Différentes approches ont été utilisées pour caractériser les échantillons de nanocristaux de polysaccharide (SNC et CNC). Pour des suspensions de SNC, l'échantillon analysé a mis en évidence une polydispersité élevée avec des particules rondes, s'étendant de la centaine de nanomètres à quelques micromètres. Le diamètre moyen des suspensions utilisées était 1600 ± 80 nm. Quant aux suspensions de CNC utilisées pour la filtration, les différentes analyses ont mis en évidence des particules en forme de bâtonnets, de 10 ± 3 nm d'épaisseur 125 nm et de 270 ± 90 nm de longueur.

Les profils de SAXS des deux suspensions dans différentes conditions ont été tracés. Il en ressort que les ultrasons n'ont pas affecté leur structure interne. Pour la suspension de CNC, l'accumulation de particules a conduit à un léger changement de profil sur la gamme basse de vecteur de diffusion ($q < 0.3$ nm^{-1}), probablement dû à l'orientation de ces nanocristaux lorsque la suspension se concentre à proximité de la membrane.

Les propriétés d'écoulement des suspensions de SNC ont également été étudiées. Tous les échantillons ont montré un comportement de fluide rhéo-fluidifiant. Avec l'augmentation de la concentration d'échantillon, ce comportement de fluide rhéo-fluidifiant est devenu de plus en plus prononcé, jusqu'à apparition de la contrainte de seuil au-delà d'une concentration de 9,6 % (w/w). Aucun effet de la température n'a été observé entre 20°C et 30°C, de même qu'aucun changement de viscosité n'est notable lors de la filtration, même en présence d'ultrasons pendant 280 mn.

IV-2.2 Ultrafiltration des SNC

Pendant l'ultrafiltration, l'accumulation de particules de SNC est susceptible de créer une couche de colmatage, entrainerait un flux limite. Dans nos expériences, la couche de particules de SNC accumulées s'est révélée peu concentrée et ouverte, de telle sorte que les ultrasons l'ont enlevée très rapidement, provoquant ainsi une amélioration de la performance de filtration qui s'est traduit par une augmentation de flux de perméation à macro-échelle. En outre, pour la

membrane utilisée, les particules de SNC étaient retrouvées dans le perméat, avec et sans US. Un autre point à noter est que le taux de rétention en présence d'ultrasons était légèrement inférieur à celui en absence d'ultrasons.

IV-2.3 Ultrafiltration des CNC

L'accumulation de particules de CNC près de la membrane était importante pendant l'ultrafiltration : la concentration des particules de CNC à l'interface de la membrane peut ainsi être 10 fois plus concentrée que la suspension d'alimentation, avec une anisotropie 5 fois plus élevée que celle de l'alimentation. Pendant la filtration, l'organisation structurelle anisotrope des particules de CNC a donc rendu la couche accumulée plus dense par rapport à la structure « fragile » et ouverte des particules de SNC, de sorte que les ultrasons ne pouvaient déstabiliser la couche accumulée de CNC. Néanmoins, l'application des ultrasons a diminué l'anisotropie et à la concentration dans l'épaisseur entière de la couche concentrée à partir de la surface de la membrane au volume, le flux de perméation étant augmenté d'un facteur de 3.

V Analyse des profils de concentration et approche de modélisation

V-1 Résumé de résultats

Cette étude se concentre sur les ultrafiltrations assistées par ultrasons des suspensions colloïdales. Afin d'élargir la gamme d'étude et de fournir une compréhension du procédé et de l'interaction colloïde/procédé aussi complet que possible, quatre types de colloïdes ont été étudiés.

La figure présente le facteur d'intensification par ultrasons (E_{US}) pour tous les colloïdes étudiés, qui varie de 1,6 à 13,5, ce qui indique une grande différence d'intensification. Le facteur d'intensification par ultrasons pour les SNC est relativement faible puisque la chute de flux de perméation n'est pas élevée pour cette suspension comme discuté dans la section 2.3 du chapitre 4. A contrario, le facteur d'intensification par ultrasons des dispersions de Laponite sans tspp est très élevé, entre 10 et 13,5. Cette grande différence d'E_{US} pour les différentes suspensions a pu être expliquée par différents mécanismes d'action dépendant de la couche concentrée. Elles

peuvent être classifiées en trois groupes, présentés à la Fig.5.2. Les ultrasons appliqués ont induit une érosion complète de la couche accumulée de particules, comme dans le cas de Laponite en présence de tspp (Lap1-tspp6 et Lap0.48-tspp6) et de SNC ; ils ont mené à une rupture partielle de la couche concentrée, comme dans le cas du lait écrémé et de CNC ; ou aucun changement (nanométrique) de la couche concentrée n'a été détecté par la mesure utilisée de SAXS mais toujours une augmentation importante de flux de perméation dans le cas de Lap1-tspp0, SWy-2 T3 et de NAu-1 T3.

Sur ces résultats, nous avons émis l'hypothèse de deux principaux phénomènes induits par les ultrasons pendant l'ultrafiltration : i) les ultrasons induisent une contrainte de cisaillement via les courants à haute vitesse générés localement dans le réseau des particules accumulées. Si cette contrainte de cisaillement est supérieure à la contrainte seuil de la suspension, une désagrégation est susceptible de se produire, menant à une érosion progressive de la couche accumulée. On observe principalement ce phénomène dans le cas d'une organisation structurelle ouverte des particules (agrégation des particules dues aux forces attractives entre elles et/ou à l'organisation fractale). ii) Dans le second cas en présence d'un réseau plus dense où les particules interagissent d'une manière répulsive et/ou sont assemblées d'une manière anisotrope, la structure (à l'échelle nanométrique) du réseau de particules demeure sans changement sous ultrasons. Néanmoins, les ultrasons créent toujours une circulation localisée supplémentaire de l'eau à l'intérieur du réseau, à la base de l'augmentation de flux de perméation.

V-2 Analyse globale des résultats

Les résultats présentés dans les précédentes parties ont été obtenus à partir de la fenêtre creusée au milieu (x = 50 mm) de notre cellule de filtration. Afin de fournir une vision globale et de mettre en évidence le mécanisme général du procédé, les résultats obtenus par les mesures de SAXS à travers les trois fenêtres ont été analysés par des calculs intégrés. Le logiciel Matlab a été employé pour effectuer cette étude numérique. Nous sommes intéressés aussi bien à l'accumulation de matière qu'aux contraintes de seuil, aux différentes positions à l'intérieur de la couche concentrée de particules. Quelques modèles théoriques ont été pris en considération pour prévoir le flux de perméation local le long de la surface de la membrane. Dans cette section, les

dispersions de Laponite et le lait écrémé sont choisis puisqu'ils représentent des familles colloïdales qui ont des performances très différentes.

V-2.1 Accumulation de matière au sein de la couche concentrée

En se basant sur le profil de concentration le long de la membrane obtenu par analyse SAXS, l'intégration a été effectuée afin de calculer l'accumulation de matière dans la couche concentrée. Une bonne corrélation entre accumulation de matière et profil de concentration a été trouvée dans tous les cas. Pour le lait écrémé à $2*C_o$, certains résultats se révèlent tout particulièrement intéressants. Un profil d'accumulation de matière en forme de U pourrait être lié à l'inhomogénéité de l'activité ultrasonore dans le canal de filtration. Par ailleurs, cette forme de U a semblé être « une base solide » correspondant à la couche cohésive à la surface de la membrane pendant la filtration du lait écrémé concentré.

En outre, un essai a été fait pour corréler la masse accumulée en total au le flux de perméation. Les résultats suggèrent que l'accumulation de matière seule ne pourrait pas déterminer le flux de perméation dans un procédé de filtration tangentielle pour les suspensions colloïdales.

V-2.2 Propriétés d’écoulement au sein de la couche concentrée

Les propriétés d'écoulement de Lap-tspp0 et de Lap-tspp6 sont extrêmement différentes du fait de la résistance mécanique du réseau de particules. Avec les profils de concentration obtenus, les cartographies de contrainte seuil dans le canal expérimental pendant la filtration ont été dressées. La contrainte seuil de la couche concentrée ne dépasse pas 100 Pa pour le système Lap1-tspp6 tandis qu'il peut atteindre 2500 Pa pour le système Lap1-tspp0. Or une valeur de la contrainte seuil a été mise en évidence lors de l'étude des propriétés d'écoulement de la Laponite : au-delà de 100 Pa (chapitre 3, section 1.2), les ultrasons ne peuvent détruire son réseau mécanique. Il a donc été confirmé que la consistance du gel de Lap1-tspp0 concentré est si élevée

que le cisaillement induit par les ultrasons est incapable de déstructurer son réseau, alors que la contrainte seuil du système Lap1-tspp6 concentré permet aux ultrasons de déstructurer son réseau.

V-2.3 Prédiction de flux de perméation le long de la membrane

A partir de nos profils de concentration obtenus pendant la filtration, des prédictions de flux de perméation ont été effectuées, s'appuyant sur des facteurs accessibles expérimentalement. Cette approche intégrée de la modélisation démontre la corrélation entre les facteurs clé du modèle (perméabilité et pression osmotique de couche concentrée) et de la performance de filtration (flux de perméation). Généralement, ces deux facteurs peuvent fournir une description globale de la performance de filtration. Cependant, l'effet des ultrasons n'est pas pris en compte. Par conséquent, la loi de perméabilité et de pression osmotique (ou au moins la loi de perméabilité) devrait être déterminée à nouveau par des expériences pour des suspensions en présence d'ultrasons à l'avenir. Le modèle pourrait également être amélioré en intégrant d'autres facteurs, tels que le coefficient de diffusion D qui pourrait être réinterprété en prenant en considération la propriété d'écoulement de la couche concentrée. Par ailleurs, la caractérisation du profil de vitesse au sein du canal de filtration peut être est envisagé pour de prochaines études.

Conclusions

Cette étude a caractérisé à plusieurs échelles l'ultrafiltration tangentielle assistée par ultrasons. Grâce aux mesures non destructives de SAXS, des observations de la couche concentrée de particules, en temps réel et *in-situ* ont pu avoir lieu. Ainsi, ce travail a combiné des résultats macroscopiques (flux de perméation) avec des observations nanométriques (profils de concentration) simultanées du procédé. Les résultats obtenus peuvent être récapitulés via trois conclusions principales.

Premièrement, les modifications induites par les ultrasons sur les propriétés d'écoulement de différentes suspensions colloïdales ont été étudiés.

Deuxièmement, l'effet des ultrasons sur la performance de filtration a été étudié de l'échelle nanométrique à l'échelle macroscopique. En termes d'intérêt industriel (à l'échelle macroscopique), nos résultats démontrent qu'une application simultanée des ultrasons (20 kHz, 0,6-2,9 $W.cm^{-2}$) peut être un moyen efficace d'intensifier le procédé d'ultrafiltration. Les ultrasons ont augmenté de manière significative le flux de perméation de l'ultrafiltration : pour les 9 suspensions étudiées, le facteur d'intensification E_{US} varie de 1,6 à 13,5. En outre, l'intensité des ultrasons variant de 0,6 $W.cm^{-2}$ à 2,9 $W.cm^{-2}$ ne semblait pas affecter ce facteur E_{US}, comme montré dans le cas de la filtration du lait écrémé. Mise en exergue par les mesures *in-situ* en temps réel de SAXS, à l'échelle nanométrique, nos résultats illustrent que les ultrasons appliqués pendant ultrafiltration n'ont pas affecté la structure des particules de toutes les suspensions étudiées**.** Trois mécanismes importants liés à la couche concentrée ont été identifiés, qui impliquent deux principaux phénomènes induits par les ultrasons pendant la filtration, comme discuté dans la section V-1 de ce résumé.

Troisièmement, une analyse numérique a été effectuée pour trois suspensions représentatives, afin de fournir une interprétation globale intégrant l'ensemble des phénomènes dans le canal de filtration, grâce aux profils de concentration obtenus par les mesures *in-situ* en temps réel de SAXS. L'accumulation de matière au sein des couches concentrées a été calculée, de même que les cartographies de contrainte seuil au sein du canal de filtration. En s'appuyant sur les facteurs accessibles expérimentalement (perméabilité et pression osmotique dans la

couche concentrée), les flux de perméation localisés le long de la membrane ont été prédits pour différent paramètres opératoires.